

Investigation of low-temperature-grown GaAs photoconductive antennae for continuous-wave and pulsed terahertz generation

Dissertation zur Erlangung des Doktorgrades der Naturwissenschaften

Vorgelegt beim Fachbereich Physik
der Johann Wolfgang Goethe-Universität
in Frankfurt am Main

von Gabriel C. Loata
aus Onesti, Rumänien

Frankfurt am Main 2007
(D 30)

vom Fachbereich der
Johann Wolfgang Goethe-Universität als Dissertation angenommen.

Dekan:

Gutachter:

Datum der Disputation:

Contents

1. Introduction	1
1.1. Outline	5
1.2. Publications	7
1.3. Zusammenfassung	9
2. Low-temperature-Grown GaAs material system	15
2.1. Growth and morphology	15
2.2. Optical and electrical properties of LTG-GaAs	19
2.2.1. Band structure and electronic properties of LTG-GaAs	19
2.2.2. Considerations on the dynamics of photogenerated carriers	20
2.3. Electrical and carrier transport properties of LTG-GaAs	26
2.3.1. Carrier mobility in LTG-GaAs	32
2.4. Characterization of LTG material used in the current work	35
2.4.1. Growth and annealing	35
2.4.2. Electrical characterization of the LTG-GaAs substrates	35
2.4.3. Optical characterization of the LTG-GaAs material	39
3. Continuous wave THz generation by photomixing in LTG GaAs	43
3.1. Fundamentals of photomixing	43
3.2. Experimental setup for generation and detection of CW THz	47
3.2.1. Laser system	50
3.2.2. Probe station	53
3.2.3. Detector characterization	56
3.2.4. Silicon substrate lens	58
3.3. State of affairs in photomixing	60
3.4. Design and fabrication of photomixers	64
3.5. Analysis of photocurrent and THz emission characteristics	69
3.5.1. DC photocurrent vs. applied bias voltage	69
3.5.2. THz photocurrent	72
3.5.3. THz power dependence on the applied bias	72
3.5.4. Determination of carrier lifetime vs. electric field dependence	77
3.5.5. Determination of electron drift velocity vs. electrical field. Velocity overshoot in LTG-GaAs.	81

3.5.6.	Optical power dependence of the emitted THz power and DC photocurrent	85
3.5.7.	Frequency response from two types of antenna and the influence of LTG-GaAs material parameters	86
4.	Pulsed THz radiation generated with photoconductive antennas	89
4.1.	Principles of THz pulse generation with photoconductive antennas	89
4.2.	Experimental setup for pulsed THz generation and detection	94
4.3.	Emission characteristics of LTG-GaAs-based photoconductive antennas	97
4.3.1.	Voltage bias dependence of the emitted THz field	97
4.3.2.	Optical power dependence of the emitted THz field	99
4.4.	Saturation behavior and radiation field screening in small-size LTG-GaAs photoconductive antennas	102
4.4.1.	Antenna impedance and radiation resistance	102
4.4.2.	Equivalent circuit of a small-size photoconductive antenna	105
4.4.3.	DC photocurrent	107
4.4.4.	Calculated THz waveforms and transient photocurrent	108
4.4.5.	Experimental saturation data and agreement with the equivalent circuit model of radiation field screening	110
5.	Double-pump pulse THz spectroscopy on LTG-GaAs-based PC antenna	115
5.1.	Why double-pump pulse experiments?	115
5.2.	Principle and experimental realization of the double-pulse experiment	117
5.3.	Double-pump pulse experimental results and their preliminary interpretation	121
5.3.1.	Double-pulse characteristics from the PC1 antenna	121
5.3.2.	A review of the literature on double-pulse measurements	124
5.3.3.	Experimental evidence for the radiation field screening effects	128
5.3.4.	Double-pulse traces on PC emitters with Bragg reflectors: no evidence for carriers generated in the GaAs substrate	129
5.4.	Modeling the double-pump pulse experiment	130
5.4.1.	Extended equivalent circuit model and the response to single-pulse excitation	130
5.4.2.	Validation of the equivalent circuit model for single-pulse excitation	136
5.4.3.	Temporal evolution of the field in the photogap	137
5.4.4.	Photoswitch response to double-pulse excitation	141
5.4.5.	Validation of the equivalent circuit model for double-pulse excitation	142

5.5. Double-pulse measurements on emitters with different LTG-GaAs materials	146
5.6. Bias dependence of the double-pulse traces	148
6. Evidence of long-living screening fields in LTG-GaAs-based photoconductive switches	151
6.1. Long-living transients observed in the double-pulse measurements . .	152
6.1.1. THz-pump power dependence of the incomplete THz-probe signal recovery	153
6.1.2. Evaluation of the de-screening time from double-pulse data . .	155
6.2. THz-pulsed emission from a PC emitter with CW background illumination	158
6.2.1. Experimental realization of the pulsed-THz with CW background experiment	158
6.2.2. Experimental observation of THz-field reduction due to CW background illumination	159
6.2.3. Evaluation of the de-screening time for the case of CW background illumination	161
6.3. Discussion: long-lived screening in LTG-GaAs	163
7. Conclusions and Overview	167
A. Auxiliary theoretical derivations	173
A.1. Analytic expression for the carrier density generated by a single Gaussian pulse excitation in a photoconductor with traps	173
A.2. Derivation of the differential equation describing the temporal evolution of the electric field in the photogap	174
A.3. Derivation of the differential equation describing the temporal evolution of the polarization due to the separation of carriers	175
B. Overview of the THz emitters used in the present work	177
C. Auxiliary publications	179
Bibliography	193
Curriculum Vitae	211
Acknowledgments	215

List of abbreviations and symbols

Frequently used acronyms

THz	terahertz
CW	continuous-wave
LTG-GaAs	low-temperature-grown gallium arsenide
VIS	visible
IR	infrared
NIR	near-infrared
MSM	metal-semiconductor-metal
MBE	molecular beam epitaxy
VB	valence band
CB	conduction band
SCLC	space-charge-limited current
DC	direct current
AC	alternating current
DUT	device under test
SI	semi-insulating
SOR	system optical response
NEP	noise equivalent power
EHP	electron-hole pair
VO	velocity overshoot
PC	photoconductive
EO	electro-optical
OPTP	optical-pump-THz-probe
SNR	signal to noise ratio
FFT	fast-Fourier transform
TPP	terahertz pump-and-probe
DPP	double-pump pulse
SRH	Shockley-Read-Hall
SCL	space-charge-limited

Physical Constants

c	$= 2.997925 \times 10^8$ m/s	velocity of light in vacuum
e	$= 1.60219 \times 10^{-19}$ C	electronic charge
m_0	$= 9.10956 \times 10^{-31}$ g	electron rest mass
h	$= 6.62620 \times 10^{-34}$ Js	Planck's constant
ε_0	$= 8.85 \times 10^{-12}$ F/m	permittivity of free space
k_B	$= 1.3807 \times 10^{-23}$ J/K	Boltzmann's constant

Photon energy: 1 eV = 1.60219×10^{-19} J

LTG-GaAs material parameters:

n_{LTG}	$= 3.62$	refractive index (850 nm)
ε_r	$= 12.9$	relative dielectric permittivity
α_{LTG}	$= 1.5 \times 10^4$ cm ⁻¹	absorption coefficient (850 nm)
E_g	$= 1.42$ eV	band gap energy

Definition of commonly used symbols

A	elementary photogap area
A_c	contact (active region) area
As_{Ga}	As antisite defect
As_i	interstitial As defect
$A(V_b, Z_a, \tau_c, \mu_e)$	parametric function
$B(\mu_e)$	function of electron mobility
C	capacitance
\mathcal{C}	heat capacity
d	distance between the electrodes
\mathcal{D}	space-charge geometrical factor
E	electrical field
$E_{\text{opt}}(t)$	time-dependent optical electrical field
$E(r, \theta, t)$	radiated field due to time-dependent dipole
E_b	(applied) bias field
$E_g(t)$	effective electrical field in the photogap
$E_r(t)$	radiated near-field
$E_{\text{rad}}(t)$	electrical field across the photogap produced by the radiation process
$E_{\text{sc}}(t)$	screening field due to space-charge

ΔE_{sc}	space-charge field screening due to THz-pump pulse only
$E_{sc}(t < 0)$	level of space-charge screening that survives the pulse interspac- ing
E_{sc}^{CW}	relative amplitude of space-charge field screening (CW case)
$E_{THz}(t)$	radiated instantaneous THz field
E_{ff}	emission efficiency
E	complex electrical field
f_n	antenna resonant frequency
f_{eff}	effective resonant frequency
f_{3dB}^{RC}	3dB cut-off frequency
Φ_B	Schottky barrier height
g	photoconductive gain
g_0	total photogeneration rate under steady-state illumination
g_0'	elementary photogeneration rate under steady-state illumina- tion
$g(\vec{r}, t)$	photocarrier generation rate
G_0	maximum photoconductance
$G(t)$	instantaneous photoconductance
H	complex magnetic field intensity
$i(t)$	time-dependent current
$i_{pc}(t)$	instantaneous photocurrent in the photogap
I_{in}	antenna input current
$I_{opt}(t), I_{opt}(\vec{r}, t)$	instantaneous optical intensity
I_{DC}	DC photocurrent (pulsed case)
I'_{ph}	elementary photocurrent
I_{ph}	total photocurrent
I_{ph}^{DC}	DC photocurrent (CW case)
I_{ph}^p	primary photocurrent
I_{ph}^{THz}	THz-modulated (AC) photocurrent
$I_{s,p}$	intensity of s and respectively p polarized light
I_0	incident intensity (EO detection)
$j_{pc}(t)$	instantaneous photocurrent density
J	current density
J_n	electron current density
J_h	hole current density
$J_{pump(probe)}$	optical pump (probe) pulse energy
J_s	surface current density
J_{SCLC}	space-charge-limited-current density
J_d	displacement current density
l	electrode length (MSM)
l_c	active area length
l_e	dipole length

(M)	preamplifier gain (detector)
$N(t)$	instantaneous carrier density (photogenerated)
n_0	density of thermally generated electrons
n	free electron density
$n(t)$	instantaneous carrier density
$n_f(t)$	instantaneous free-carrier density
N_d	total density of deep donor states (SCLC)
N_{d0}^+	density of ionized deep donor states
N_a	density of acceptor states
N_A	concentration of acceptors
N_D	density of defect states (donors)
$\Delta n(t)$	change in the real part of the refractive index
n	refractive index
N_g	number of gaps between electrodes (MSM)
N_e	number of electrodes (MSM)
p	hole density
$p(t)$	dipole moment
\bar{P}	average optical pulse power
$P(t)$	time-dependent polarization
$P_{1,2}$	average optical power level
P_{abs}	absorbed optical power
P_{inc}	incident optical power
P_{ch}	chopped incident power
$P_{opt}(t)$	instantaneous optical power
$P_{pulse}(t)$	instantaneous optical pulse power
P_{pulse}^0	optical pulse peak power
P_{rad}	time-averaged radiated power
P_0	total incident optical power (DC illumination)
P'_0	optical power incident on the elementary area
P_T	transmittable power (transmission line)
$P_{THz}(\omega)$	radiated THz power
\mathcal{P}	Poynting vector
r	responsivity of the detection system
R	carrier recombination rate
\mathcal{R}	reflectivity coefficient
R_a	radiation resistance
R^H	Hall coefficient
R_{in}	antenna input resistance
R_{rad}	antenna radiation resistance
r_n, R_n	inner and outer radius of a log-periodic antenna
$\frac{\Delta R}{R_0}$	relative change in reflectance
Q^{cont}	electric charge flowing into the contacts

Q^{gen}	total amount of generated electric charge
$Q_{\text{avg}}^{\text{pulse}}$	amount of space-charge generated by a single laser pulse
$S(V_b)$	photoswitch responsivity
S_f	shadowing factor
ΔS	relative change in THz (double-pulse) signal
t	time
t_{tr}	carrier transit time
t_{tr}^h	hole transit time
t_{LT}	thickness of the LTG-GaAs layer
T	temperature
T_0	pulse duration
T_{FWHM}	full-width half-maximum pulse duration
\mathcal{T}	transmission coefficient
T_a	anneal temperature
T_g	growth temperature
T_{rep}	laser repetition period
U	net recombination rate in SRH model
U_t	energy depth of trap level
U_i	energy level at mid-gap
$v(t)$	time-dependent carrier drift velocity
v_e	electron drift velocity
v_h	hole drift velocity
v_{sat}	carrier saturation velocity
$V(t)$	time-dependent voltage
v_{th}	thermal velocity of electrons
V	voltage
V_a	voltage drop at antenna terminals
V_b	(applied) bias voltage
V_{Ga}	Ga vacancy defect
V_{out}	output voltage (detector)
V_{in}	antenna input voltage
$V_{sc}(t)$	instantaneous voltage drop due space-charge screening
V_{TFL}	trap filling limit voltage
\mathcal{V}	volume of active region of the photomixer
\mathcal{V}'	elementary volume of the active area
w	electrode width
w_c	active area width
\tilde{W}_e	time-averaged electric energy density
\tilde{W}_m	time-averaged magnetic energy density
Z_a	antenna impedance
Z_g	photogap impedance
$Z_g(t)$	instantaneous photogap impedance

Z_{in}	driving point (input) antenna impedance
Z_0	intrinsic medium impedance
X_{in}	input antenna reactance
ε_{eff}	effective dielectric constant of the substrate
η	total quantum efficiency
η_{opt}	optical quantum efficiency
γ_{41}	EO coefficient of ZnTe
η_0	free-space impedance
κ	space-charge screening factor
λ_i	wavelength $i = 1, 2, \dots$
μ	carrier mobility
μ_b	conduction band mobility
μ_e	electron mobility
μ_h	hole mobility
$\nu_{1,2}$	frequency
ν_{rep}	laser repetition rate
ω	angular frequency
ρ	resistivity
σ	electrical conductivity
σ_e	capture cross-section for electrons
σ_s	surface conductivity
$\sigma(t)$	instantaneous conductivity
σ_0	steady-state photoconductivity
θ	thermal conductance
τ	period of a log-periodic antenna
τ_c	carrier trapping time
τ_e	free-carrier (mobility) lifetime
τ_i	carrier decay time ($i = 1, 2, \dots$)
τ_s	carrier momentum relaxation (scattering) time
τ_d	dielectric relaxation time
τ_h	hole (mobility) lifetime
$\tau_e(E_0)$	field-dependent free-carrier lifetime
τ_{e0}	field-independent free-carrier lifetime
τ_R	carrier recombination time
τ_{RC}	RC time constant
θ_c	detection correction factor
χ	electric field non-homogeneity factor
Γ	THz-induced phase change (EO detection)

1. Introduction

With wavelengths between 1000-30 μm (300 GHz-10 THz), the terahertz¹ (THz) range bridges the gap between microwave (mm-wave region) and infra-red frequencies, being until recently one of the least explored regions of the electromagnetic spectrum. The reason for this could be attributed to the lack of practical sources of THz radiation. For approximately 20 years (1970-1990), the only driving force for THz science were the fields of high-resolution spectroscopy and remote sensing [1]. Based on heterodyne and Fourier transform techniques, these methods offered astronomers, chemists and space scientists a tool for investigating the thermal emission lines of a wide diversity of light-weight molecules, since “approximately one-half of the total luminosity and 98 % of the photons emitted since the Big Bang fall into the submillimeter and far-infrared” (P. Siegel, Jet Propulsion Laboratory).

During the last decade, the general interest in THz radiation rose significantly, mainly due to its ability to penetrate many organic materials, without the damage associated with ionizing radiation such as X-rays (albeit without the spatial resolution). Since THz radiation is strongly absorbed by water molecules, it can be used to distinguish between materials with varying water content. All these properties laid the grounds for extensive applications in process and quality control [2] as well as biomedical imaging (“T-ray imaging”) [3]. Tests are currently under way to determine whether terahertz tomographic imaging can augment or replace mammography [4], and some scientists have proposed terahertz imaging as a method of screening passengers for explosives at airports [5].

In its early stages, the generation (and partly the detection) of THz pulses was conditioned by the availability of short laser pulses and was based on photoconductive switching, as pioneered by Auston in 1975 [6]. Implementing new photoconductive materials with ultrashort carrier lifetimes, like for example, radiation-damaged silicon-on-sapphire (rd-SOS) [7], the generation of very fast electromagnetic transients (~ 1.6 ps) in the mm and sub-mm wave range were demonstrated [8]. A major breakthrough came with the introduction of mode-locked Ti:sapphire lasers, which could deliver sub-100 fs pulses [9] and from there on the “THz-pulse” was chosen as a generic name for ultrafast EM transients. The refinement of antennas and transmission lines [10, 11] as well as the introduction of photoconductive materials with better properties (like low-temperature-grown-GaAs, for instance), enabled the realization of a THz generation and detection system which was shown to be a

¹1 THz = 10^{12} Hz = 1 ps = 300 μm = 33 cm^{-1} = 4.1 meV = 47.6 K.

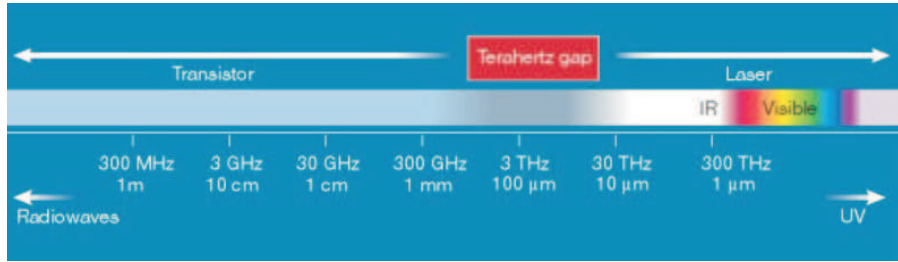


Figure 1.1.: The Terahertz gap.

useful spectroscopic tool and so Terahertz Time-Domain Spectroscopy (TDS) came into being [12]. Besides ultrafast photoconductors, the THz pulses were also generated using optical rectification in non-linear crystals [13], from semiconductor's surfaces [14], in semiconductor quantum structures [15], by the photo-Dember effect, from Bloch oscillations in a semiconductor superlattice [16], and more recently from coherent phonons in semiconductors [17]. Nowadays, there is an imperious need for coherent, tunable continuous-wave (CW) THz sources for applications such as heterodyne receiver systems, local area networks and high-resolution spectroscopy. Among the existing sources available for generation of CW THz radiation are back-wave oscillators [18], gas lasers based on molecular transitions [19], Schottky diode up-converters (frequency multipliers) [20], parametric down-converters [21]. Coming from the lower end of the THz region, the solid-state electronics-based approach is limited to below 1 THz by the high parasitic resistance and capacitance present in such devices, while new hybrid technologies like the THz quantum cascade laser (QCL), based on a fundamentally different approach, require operation at cryogenic temperatures. In particular, with the recent demonstration of low-frequency QCL operation around 1.7 THz with pulsed and CW operation up to 95 and 80 K [22], this technology shows great potential as a compact, high-power, high-efficiency coherent solid-state terahertz source.

An alternative way for generating coherent CW THz radiation is photomixing [23], which can be generally defined as the optical heterodyne down-conversion of two slightly-detuned optical laser beams on a photoconductive material, such as low-temperature-grown GaAs. The optical beats obtained by the interference of the two optical beams modulate the photoconductance of a semiconductor material, where the photogenerated carriers (mainly electrons) are accelerated by an applied bias field, thus generating a current oscillating at a frequency corresponding to the beat note between the two laser lines. The time-dependent current is fed to a planar antenna, generating CW THz emission (in a similar way to its pulsed counterpart - the Auston switch).

Due to the fact that, primarily, the efficiency of the photomixing process is dictated by the ability of the photogenerated carriers (electrons) to follow the optical-

beat signal, a material with an ultra-short carrier lifetime is desired. The pursuit of such a material was aided by the fact that, nowadays, epitaxial growth techniques enable the growth of materials with no bulk analog. Among them, low temperature growth of semi-insulating GaAs material attracted a lot of attention beginning with the work by Smith et al. [24], who found that back-gating of metal-semiconductor-field-effect transistor (MESFET) devices could be eliminated when grown on low-temperature-grown GaAs (LTG-GaAs). For more than one decade now, LTG-GaAs, also referred to as non-stoichiometric (NS) GaAs, has become one of the most widely used and explored optoelectronic materials. It meets almost all requirements that would make an efficient active layer for an ultra-fast device: ultra-short carrier lifetime (~ 0.2 ps), relatively high carrier mobility (~ 1000 cm²/Vs), high electrical field breakdown (~ 300 kV/cm), high dark resistivity ($\sim 10^6$ Ω cm) and large nonlinear optical coefficients [25].

Among all of the all-solid-state sources mentioned above, photomixers combine the advantages of both electronic and optical technologies: room temperature operation, wide-range tunability, compactness and narrow linewidths (limited by the stabilization of the lasers used). With the photomixer expected to serve as a local oscillator (LO) in heterodyne receiver systems for astronomy, it meets the requirements for tunability, compactness and ease of operation. However, LTG-GaAs photomixers fulfill only marginally the power requirements for superconducting and semiconductor mixers (hot-electron-bolometer (HEB), semiconductor-insulator-semiconductor (SIS)), which lie between 1 to 10 μ W [26].

The relatively modest THz power level (1-2 μ W [27]) measured so far from LTG-GaAs photomixers has a couple of reasons behind it, mainly related to the challenge imposed by integrating the photoconductor with a planar antenna. An extensive overview of these limitations are exposed in Chapter 3 of this work. The limitations of photomixers can be divided in two distinct categories: the first one is connected with the device aspect, while the second one is exclusively related to the intrinsic properties of the active layer used (LTG-GaAs). A low photoconductive gain (and hence a low quantum efficiency), the impedance mismatch between the photogap and THz antenna, high RC time-constants which limit the photomixer bandwidth, electric field inhomogeneity, and the poor thermal conductivity of the GaAs substrate belong to the first category.

Although a series of optimization steps and procedures have been implemented, the emitted THz power still remains relatively low. To outline the most relevant developments: (i) advanced impedance matching techniques (inductive chokes) and resonant antenna (twin-dipoles) (Duffy et al. [27]); (ii) a traveling-wave design (free of the RC time constant roll-off) (Matsuura et al. [28]); (iii) recessed contacts (Mikulics et al [29]) and a vertical structure (Lippens et co. [30]); (iv) a AlGa buffer layer with twice the thermal conductivity of GaAs substrate [31].

On the material system side, most of the optimization work was aimed at the reduction of the carrier lifetime (in order to increase the achievable THz bandwidth). At the same time, unwanted effects like the elongation of the electron trapping time at high values of applied field ([32]) proved to thwart an increase in the output power. Although an impressive amount of literature exists on the transport and carrier dynamics properties of LTG-GaAs under illumination, only a few studies try to relate the material properties with the emission efficiency of the photomixer (or photoswitch, in the case of pulsed-THz emitters). Despite the numerous studies on LTG-GaAs, very little is known about the photogenerated carrier recombination dynamics (carrier lifetime) as well as about the magnitude of the field-screening due to space-charge effects. Moreover, the vast majority of these experiments (mainly optical pump-probe [33] or optical pump-THz-probe [34]) were not performed under conditions that reproduce the device operating conditions, that is, under applied bias.

Therefore, it is the aim of the present study to try and shed some light on the material and device properties as a whole. With this purpose in mind, besides an extensive study of carrier transport and device characteristics (obtained by correlating the information on the emitted CW THz power and DC photocurrent versus applied bias), we have also implemented specialized THz-emission spectroscopy techniques and applied them to LTG-GaAs photoswitches. Among them, the so-called “double-pulse” technique is capable of revealing the temporal evolution of the local electrical field in the photogap, and hence important aspects of the ultrafast carrier dynamics, providing at the same time direct access to, and a quantitative evaluation of the impact of field screening on the operation of photoconductive switches.

Very recently, an alternative material to LTG-GaAs, namely high-energy nitrogen ion-implanted GaAs was integrated with a traveling-wave photomixer [35]. The authors reported increased responsivity, lower dark currents and higher THz output power (2.6 μW at 850 GHz). Despite the fact that some of the THz emission features (saturation of the THz power at high fields) observed for LTG-GaAs-based photomixers were no longer observed, the inherent problems caused by the presence of carrier traps are believed to have a harmful impact upon the photomixer’s performance. In a totally different approach to the lifetime limited metal-semiconductor-metal (MSM) photomixers, a great deal of the research work I carried out was also related to the investigation a new photomixer design [36] which, as opposed to LTG-GaAs photoswitches, turns the hampering field-screening effect into an advantage. The *nipnip* emitter [37], as conceived by Prof. Döhler in Erlangen, is based on quasi-ballistic transport in an asymmetric modulation-doped n-i-p-n superlattice. The new concept exploits some of the advantages of pin photodiodes but through its clever design is freed from the high-frequency limitations of the pin diodes, by that one should understand the restrictions imposed by the trade-off between the

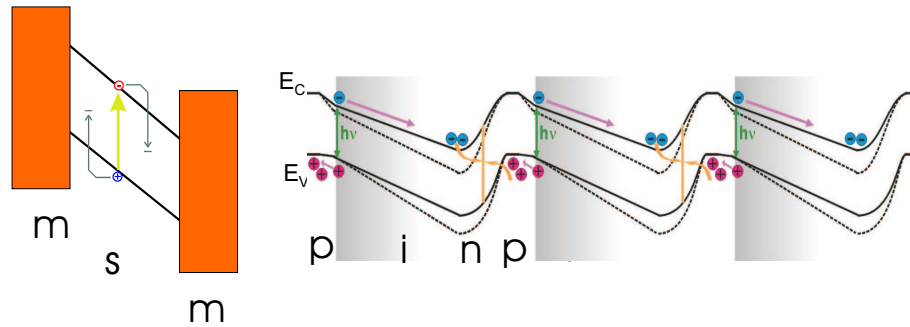


Figure 1.2.: Conventional MSM photomixer (left) and the novel nipinip design (right).

transit-time and capacitance. The capacitance problem is circumvented by cascading a number of N periods of nano-pin diodes, while the transit-time problem is solved by using the ballistic transport of photogenerated carriers in the intrinsic layer. For a target operation frequency the optimum length of the transport path (i-layer) corresponds to the distance over which an electron can propagate quasi-ballistically during half the oscillation period. The optimum field for ballistic transport is tuned for each optical pump level by applying a voltage bias. Indeed, measured frequency spectra for a 4- and 7-period device indicate that the device is free of the RC time-constant roll-off. Details on the photomixer design as well as on the experimental results obtained on the THz emission performance can be found in the auxiliary publication included in Appendix C. Most of the work presented here was a part of a joint European Space Agency project (“Far-IR Wave Generation” – ESA Ref. Nr. TOS-MMR/2002.01/BL/BL). Besides designing and developing the photomixer test bed (see Section 3.2, “The Probe Station”), an activity which also comprised the construction of a laser source and the calibration of detectors for absolute power measurements, we performed all the characterization work on the various photomixer devices which included a range of measurements from simple I-V characteristics to fully-automatic frequency scans. One of the most important features of the CW-THz experimental setup we designed is given by the possibility to record the emitted THz power and the DC photocurrent simultaneously, as a function of the applied bias. For the case of LTG-GaAs photomixers, this allowed us to gain some meaningful insight into the relationship between the carrier transport and emission performance.

1.1. Outline

The structure of this dissertation is as follows:

Chapter 2 contains a comprehensive review of the most significant structural, optical and electrical properties of LTG-GaAs, with a special emphasis on those

properties which make LTG-GaAs a suitable material for ultrafast optoelectronic devices applications. This chapter also gives an overview of the experimental techniques used in investigating the LTG-GaAs material parameters. The chapter concludes with the experimental results obtained from investigation of the electrical and optical properties of the LTG-GaAs material used in the present work.

Chapter 3 deals with the theoretical and experimental aspects of photomixing in LTG-GaAs. After describing the physics behind the photomixing process, a comprehensive experimental section offers an overview on the most relevant approaches used in establishing a state-of-the-art CW-THz generation and detection setup. Details on the laser source and on the calibrated detectors are given here, as well as a complete description of the photomixer "Probe Station" - an optomechanical approach to a fast and reliable photomixer characterization. The final part of this chapter deals with the particularities of carrier transport (elongation of electron trapping time and velocity overshoot) in LTG-GaAs at high electric fields as derived from the experimental facts.

Chapter 4. This chapter reviews the physics and the experimental techniques used for generation and detection of pulsed-THz radiation from photoconductive (PC) antenna. An investigation of the emitted THz waveform and amplitude as a function of driving optical power and applied bias is presented. The observed saturation behavior at higher optical intensities is attributed to the effect of "radiation field screening" and discussed in terms of the equivalent circuit model used to calculate the response of the photoswitch.

Chapter 5. Based on the pulsed-THz generation described in the previous chapter, here we describe a pump-and-probe THz emission technique (also referred to as "double-pulse") which enables us to gain some insight into the local electrical field dynamics of the photoswitch, and by that into the ultrafast carrier dynamics under applied bias, subsequent to the photogeneration. The qualitative and quantitative evaluation of experimental findings is carried out by extending the equivalent circuit model implemented in Chapter 4, such that besides the effect of the radiation field screening discussed already, it accommodates the space-charge field screening effects produced by photogenerated carriers moving in the external bias field, an effect which is important in photoconductors at high excitation densities.

Chapter 6. The incomplete recovery of the double-pulse traces observed at different levels of optical excitation power observed in Chapter 5 are discussed here and attributed to the effect of space-charge screening outliving the repetition period of the laser system employed. We proceed to a quantitative analysis of these effects, the outcome of which is the screening relaxation time (recombination or de-screening time). Additionally, by measuring the change of the THz amplitude when a background CW illumination is incident on the photogap, we obtain very useful information on the field-screening due to space-charge in the CW operation mode.

Chapter 7. The concluding chapter summarizes the main results, suggesting possible directions to be followed when designing an efficient photomixer.

1.2. Publications

The research work presented in this dissertation resulted also in a number of publications which are listed below:

1. C. Sydlo, J. Sigmund, H.L. Hartnagel, **G. Loata**, K.J. Siebert, and H.G. Roskos, "*Efficient THz-emitters for low-temperature-grown GaAs photomixers*" Terahertz Electronics Proceedings IEEE 10th International Conference on, 2002 Page(s): 60 - 62
2. B. Leone, V. Krozer, M. Feiginov, H.G. Roskos, H. Quast, T. Löffler, **G. Loata**, G. Döhler, P. Kiesel, M. Eckardt, A. Schwanhäußer, T.O. Klaassen, and P. Lugli, "*Optical far-IR wave generation - an ESA review study*" 3rd ESA Workshop on Millimetre Wave Technology and Applications, May 2003
3. F. Renner, M. Eckardt, Ö. Yüsekdağ, S. Malzer, D. Driscoll, M. Hanson, A.C. Gossard, **G. Loata**, T. Löffler, H.G. Roskos, and G.H. Döhler, "*Novel THz-Photomixer based on vertical quasi-ballistic transport in p-i-n-p-superlattices*" Proceedings of ITQW 2003 (2003)
4. **G. Loata**, T. Löffler, H.G. Roskos, F.H. Renner, O. Klar, M. Eckardt, A. Schwanhäußer, G.H. Döhler, D. Driscoll, M. Hansen, A.C. Gossard, V. Krozer, "*A New THz-Photomixer Based On a n-i-p-n Doping Superlattice*" Proceedings of the 29th International Conference on Infrared and Millimeter Waves, Karlsruhe, Germany, September 27-October 1 (2004), p. 495
5. V. Krozer, B. Leone, H.G. Roskos, T. Löffler, **G. Loata**, G. H. Döhler, F. Renner, S. Eckardt, S. Malzer, A. Schwanhäußer, T.O. Klaassen, A. Adam, P. Lugli, A. Di Carlo, M. Manenti, G. Scamarcio, M.S. Vitiello, and M. Feiginov, "*Optical far-IR wave generation - state-of-the-art and advanced device structures*" Proc. SPIE Int. Soc. Opt. Eng. 178 (2004) 5466
6. T. Löffler, K. J. Siebert, H. Quast, N. Hasegawa, **G. Loata**, R. Wipf, T. Hahn, M. Thomson, R. Leonhardt, and H. G. Roskos, "*All-optoelectronic continuous-wave terahertz systems*" The Royal Society Philosophical Transactions, 362 (2004) 263 - 281
7. F. H. Renner, O. Klar, S. Malzer, D. Driscoll, M. Hanson, A.C. Gossard, **G. Loata**, T. Löffler, H.G. Roskos, and G.H. Döhler, "*The nipnip-THz-emitter: photomixing based on ballistic transport*" AIP Conf. Proc. 772, 1220 (2005)

8. T. Löffler, K.J. Siebert, N. Hasegawa, T. Hahn, **G. Loata**, R. Wipf, M. Kress, M. Thomson, and H.G. Roskos, "*Terahertz surface and interface characterization*" Microwave Symposium Digest, 2005 IEEE MTT-S International Volume, Issue, 12-17 June 2005, Page(s): 633 - 636
9. G.H. Döhler, F. Renner, O. Klar, M. Eckardt, A. Schwanhäußer, S. Malzer, D. Driscoll, M. Hanson, A.C. Gossard, **G. Loata**, T. Löffler, and H.G. Roskos, "*THz photomixer based on quasi-ballistic transport*" Semiconductor Science and Technology 20, S178-S190 (2005)
10. F. Renner, M. Eckardt, A. Schwanhäußer, O. Klar, S. Malzer, G. H. Döhler, **G. Loata**, T. Löffler, H.G. Roskos, M. Hanson, D. Driscoll, and A.C. Gossard: "*THz-emitter based on ballistic transport in nano-pin diodes*" phys. stat. sol. (a) 202 (6), 965 (2005)
11. G.H. Döhler, M. Eckardt, A. Schwanhäußer, F. Renner, S. Malzer, S. Trumm, M. Betz, F. Sotier, A. Leitenstorfer, **G. Loata**, T. Löffler, H.G. Roskos, T. Müller, K. Unterrainer, D. Driscoll, M. Hanson, and A.C. Gossard, "*Ballistic transport in semiconductor nanostructures: From quasi-classical oscillations to novel THz-emitters*" Pramana - Journal of Physics 67 (1): 199-205, July 2006
12. **G. Loata**, T. Löffler, and H.G. Roskos, "*Evidence for long-living charge carriers in electrically biased low-temperature-grown GaAs photoconductive switches*" accepted for publication in Applied Physics Letters (2007).

1.3. Zusammenfassung

Photomischen ist eine Möglichkeit um Dauerstrich (CW) THz-Strahlung mit Hilfe von Laserstrahlung zu erzeugen. Dabei vereint das Photomischen viele Vorteile welche aus den Bereichen der Optik und der Elektronik bekannt sind: Kompaktheit, breitbandige Abstimmbarkeit und Betrieb bei Raumtemperatur. Zum Photomischen werden bevorzugte so genannte Metall-Halbleiter-Metall Strukturen (MSM) verwendet. Dabei wird als Halbleitermaterial bevorzugt bei tiefen Temperaturen gewachsenes GaAs (LTG-GaAs) verwendet. LTG-GaAs ist das wohl am intensivsten untersuchte Material für derartige Anwendungen und zeigt alle gewünschten Eigenschaften (relativ hohe Mobilität, niedriger Dunkelstrom und ultraschnelle Ladungsträgereinfangzeit). Es gibt jedoch noch keine zufriedenstellende tiefergehende theoretische Beschreibung für die Ladungsträger-Rekombinationsdynamik bei angelegter Vorspannung und die Feldabschirmung, welche durch die freien Ladungsträger erzeugt wird. Die hier vorgelegte Arbeit beinhaltet Resultate, die mit Hilfe gepulster und CW Laserstrahlung an photoleitenden LTG-GaAs Schaltern erzielt wurden. Die Studie zielt darauf ab den Einfluss der Materialeigenschaften auf die THz-Erzeugung zu untersuchen, um ein Verständnis für die bislang noch sehr niedrige Effizienz der THz-Abstrahlung zu entwickeln.

Die Messungen wurden an zwei verschieden präparierten Materialien durchgeführt. Die erste Probe (G420) wurde unter Bedingungen prozessiert, welche für die THz-Erzeugung in photoleitenden Schaltern optimiert wurde. Die zweite Probe (TP983) wurde zwar auch bei tiefen Temperaturen gewachsen, zeigte aber eine längere Einfangzeit der freien Ladungsträger und gilt damit als nicht optimal für die Anwendung in einem ultraschnellen Schalter. Beide Proben wurden zuerst mit Hilfe einer optischen Anrege- und Abfrage-Technik (engl. Pump-Probe) auf die Lebensdauer der photoerzeugten Ladungsträger untersucht. Diese Messungen sind allerdings nicht eindeutig interpretierbar, da mehrere Ladungsträgerrelaxierungs-Phänomene gleichzeitig stattfinden und sich überlagern. Diese Messungen alleine reichen daher nicht aus, um den Einfluss der Ladungsträgerrekombinationsdynamik und die Feldabschirmung, welche durch die an den Arsen-Defekten eingefangenen Ladungsträger erzeugt wird, auf die Effizienz der THz-Erzeugung, zu untersuchen und erklären. Deshalb wurden im Rahmen dieser Arbeit weiterführende Untersuchungen, in Bezug auf die Erzeugung CW THz-Strahlung, an einer logarithmisch-periodischen Antennenstruktur, durchgeführt.

Damit konnte die THz-Emissionseffizienz bei diskreten Frequenzen und hohen Vorspannungen untersucht werden. Zusätzlich wurde eine Probe (TP984) unter den gleichen Bedingungen wie TP983 prozessiert, jedoch zusätzlich mit einem so genannten Bragg-Reflektor versehen, welcher aus einer Sequenz von 20 Folgen AlGaAs/AlAs besteht. Mit Hilfe des Bragg-Reflektors wurde der Einfluss von eventuell

im halbleitenden Substratmaterial GaAs erzeugten Ladungsträgern auf die THz-Erzeugung untersucht.

Dazu wurden gleichzeitig der DC-Photostrom und die emittierte THz-Leistung, als Funktion der angelegten Vorspannung, bei verschiedenen optischen Leistungen und Mischfrequenzen, aufgenommen. Einige Trends konnten dabei bereits isoliert betrachtet und erklärt werden. Insbesondere konnte die Abweichung in der Strom-Spannungscharakteristik von dem erwarteten linearen ohmschen Verhalten unter Beleuchtung bei hohen Vorspannungen, um die 100 kV/cm, zu dem tatsächlich beobachteten nahezu quadratischen Verhalten ansatzweise erklärt werden. Im Gegensatz zu den verschiedenen Effekten, welche in der Literatur dazu herangezogen werden, um diese Beobachtung zu erklären (bspw. durch einen raumladungslimitierten Strom oder durch Ladungsträger, welche im GaAs-Substrat erzeugt werden), führen wir dieses nichtlineare Verhalten hauptsächlich auf die Verlängerung der Einfangzeit der Elektronen bei höheren Vorspannungen aufgrund einer Verringerung der Coulombbarriere und auf eine Erhöhung der Elektronentemperatur zurück. Aber auch die beiden erwähnten Effekte reichen nicht zu einer vollständigen Beschreibung des beobachteten nahezu quadratischen Verhaltens in der Strom-Spannungscharakteristik aus. Auch die beobachtete Sättigung in der THz-Erzeugung, bei hohen Vorspannungen, kann durch diese Effekte allein nicht ausreichend gut beschrieben werden.

Daraufhin haben wir in unseren Modellierungen eine Prozedur entwickelt, welche uns erlaubt Werte für die Einfangzeit der Elektronen, aus den gemessenen DC-Photoströmen und THz-Leistungen, zu extrahieren. Die damit erhaltene Abhängigkeit zeigt bei einer Vorspannung von 200 kV/cm die dreifache Ladungsträgereinfangzeit, im Vergleich zu der Einfangzeit, welche zuvor aus den Anrege-Abfrage-Experimenten bestimmt wurde und welche der durch die Theorie vorrausgesagten $E^{3/2}$ Abhängigkeit nach Zamdmer et. al folgt. Eine zentrale Annahme, die wir in der weiterentwickelten Analyse verwendet haben ist, dass nur die Elektronen zum gemessenen Photostrom und THz-Signal beitragen. Die Tatsache, dass die Sättigung der THz-Abstrahlung bei zwei verschiedenen Mischfrequenzen zu beobachten war, deutet daraufhin, dass sich der Elektronentransport bei hohen Vorspannungen wesentlich ändert. Daraufhin haben wir in unseren Modellierungen, basierend auf den experimentell erhaltenen Werten für die Ladungsträgereinfangzeit, eine Methode entwickelt die Driftgeschwindigkeit der Elektronen als Funktion der angelegten Vorspannung zu beschreiben. Dabei haben wir in den Modellierungen ein Überschwingen in der Driftgeschwindigkeit festgestellt. Bislang wurde in der Literatur noch nicht über einen experimentellen Beweis eines solchen Überschwingens in der Driftgeschwindigkeit der Elektronen berichtet. Es gibt jedoch Monte Carlo Rechnungen von Arifin et. al., welche ein solches Phänomen zumindest nicht ausschließen. Die Stärke des Überschwingens muss jedoch anhand der Ergebnisse aus Kapitel 6

noch einmal überdacht werden.

Der zentrale Teil dieser Arbeit beginnt mit einem Kapitel, in welchem THz-Transienten, welche von photoleitenden LTG-GaAs Antennen, mit Hilfe von Femtosekunden Laserpulsen erzeugt wurden, untersucht wurden. Die Antennenstrukturen, welche hierbei verwendet wurden, waren resonante H-Dipole, die eine photoleitende Lücke besitzen. Basierend auf der Idee, dass man aus der THz-Wellenform und Amplitude Informationen über die Ladungsträgerdynamiken und den Einfluss des "THz Stromkreises" erhalten kann, haben wir eine systematische Untersuchung der THz-Wellenformen in Abhängigkeit der angelegten Vorspannung und der optischen Leistung durchgeführt. Dabei haben wir eine kleine Änderung in der THz-Wellenform entdeckt, wobei das Maximum bei höheren Vorspannungen (60 kV/cm) in Richtung früherer Zeiten verschoben ist. In der Literatur wurde dieses Phänomen in Zusammenhang mit dem Überschwingen der Elektronendriftgeschwindigkeit gebracht. Unter Berücksichtigung der im Rahmen dieser Arbeit erhaltenen CW Eigenschaften, erwarten wir kein Überschwingen in der Driftgeschwindigkeit bei derart niedrigen Vorspannungen. Dies bestätigt sich auch in der linearen Abhängigkeit der THz-Amplitude von der angelegten Vorspannung, welche eine lineare Abhängigkeit zwischen Driftgeschwindigkeit und elektrischem Feld suggeriert.

Wie auch schon bereits oft in der Literatur darüber berichtet wurde, haben wir auch ein Sättigungsverhalten der emittierten THz-Feldstärke und dem DC-Photostrom, bei zunehmender optischer Leistung, gefunden. Das gleiche Verhalten wurde auch in großflächigen photoleitenden Emittern gefunden und wurde auf eine durch das THz-Nahfeld erzeugte Abschirmung der Vorspannung zurückgeführt. Um die Möglichkeit eines solchen Effektes auch für die kleinen Antennenstrukturen zu untersuchen, haben wir ein äquivalentes Stromkreismodell entwickelt, welche eine zeitabhängige Leitfähigkeit beinhaltet, während die Antenne als einfacher ohmscher Widerstand simuliert wird. Dabei hat sich gezeigt, dass tatsächlich durch die Berücksichtigung der Dipolantenne eine Feldabschirmung bei der Abstrahlung erzeugt wird. Dies kann durch einen Spannungsabfall an den Antennenenden durch die Abstrahlung (Konzept des Strahlungswiderstandes) erklärt werden, welcher die effektive Vorspannung über die Photolücke verkleinert. Im Modellbild des äquivalenten Stromkreises kann dieses Phänomen als eine Art "Spannungsteilereffekt" angesehen werden, welcher für die beobachteten Nichtlinearitäten im Photostrom und der THz-Amplitude bei hohen optischen Leistungen verantwortlich ist.

Um weitere Informationen über den Zusammenhang zwischen dem ultraschnellen Ladungsträgerrelaxationsprozess und dem Abschirmungseffekt, erzeugt durch die photogenerierten Ladungsträgern, welche beide über die Dynamik des lokalen elektrischen Felds in der Photolücke identifiziert werden können, zu erhalten, haben wir die so genannte "Doppelpuls THz Technik" angewendet. Bei dieser Methode wird die Photolücke durch zwei aufeinanderfolgende Femtosekundenlaserpulse, zwischen

welchen der zeitliche Abstand variiert werden kann, angeregt. Dabei erzeugt der erste Puls (Pump-THz) die freien Ladungsträger in der Photolücke und mit Hilfe des zweiten Pulses (Probe-THz) kann die zeitliche Entwicklung des elektrischen Feldes in der Photolücke abgetastet werden.

In diesen Messungen des Doppelpulsexperimentes haben wir 3 verschiedene charakteristische zeitliche Regime identifiziert. Das konstante Signal während negativer Verzögerungszeiten zwischen Anrege- und Abfragepuls entspricht einem dem Anregepuls vorausseilenden Abfragepuls. Im Nullverzögerungszeitpunkt zeigt das Signal einen abrupten Abfall, gefolgt von einem schnellen exponentiellen Wiederanstieg, der nahezu auf der Zeitskala der Ladungsträgereinfangzeit liegt. Für längere positive zeitliche Verschiebungen zeigt das Signal eine Verschiebung auf einen konstanten negativen Wert.

Um das Doppelpulsexperiment mit Hilfe des äquivalenten Stromkreismodells zu beschreiben, musste dieses so modifiziert werden, dass es neben der bereits implementierten Feldabschirmung durch die Abstrahlung, auch Raumladungsträger Abschirmungseffekte, welche durch die Bewegung der photoerzeugten Ladungsträger im elektrischen Feld erzeugt werden, berücksichtigt. Mit dieser Erweiterung war es uns möglich sowohl die zeitliche Entwicklung, als auch die Größe der beteiligten Feldabschirmungseffekte zu identifizieren. Dabei haben wir zu Beginn nur die Einzelpulsanregung simuliert und festgestellt, dass das Antwortsignal zu frühen Zeiten durch die Strahlungsfeldabschirmung dominiert wird, auf einer Zeitskala die der Einfangzeit der Ladungsträger entspricht, und das spätere Antwortsignal ist über Raumladungseffekte durch die eingefangenen Ladungsträger dominiert. Das Doppelpulsexperiment konnte durch die Modellierung, in der die Ladungsträgereinfangzeit, ein Abschirmungsparameter und die Elektronenbeweglichkeit als Anpassungsparameter gewählt wurden, bei niedrigen Anregungsdichten sehr gut reproduziert werden.

Bei der Untersuchung des Doppelpulsexperiments in Abhängigkeit der Pump-THz-Leistung haben wir eine weitere Bestätigung für die Richtigkeit unserer theoretischen Näherung bekommen, da die Stärke des relativen THz-Signals bei Nullzeitverzögerung der gleichen Abhängigkeit von der optischen Leistung folgt, wie die Einzelpulsemission.

Allerdings haben wir auch einen Widerspruch zu unserer entwickelten Theorie gefunden, da das THz Signal bei negativen Zeitverzögerungen nicht konstant war, sondern mit der THz-Pumpleistung zugenommen hat. Dieses könnte durch eine unvollständige Relaxation der Ladungsträger bei negativer Zeitverzögerung begründet sein.

Entsprechend zu der konstanten negativen Verschiebung bei großen Zeitverzögerungen, wird der im vorangegangenen beschriebene Effekt in nahezu der gesamten Literatur auf mögliche langlebige Ladungsträger, welche im halbleitenden GaAs-Substrat erzeugt werden, zurückgeführt. Diese These konnten

wir widerlegen, da wir identische Doppelpulssignale für eine Probe mit und eine Probe ohne Bragg-Reflektor zwischen der aktiven Schicht und dem GaAs-Substrat erhalten haben. Deshalb haben wir die negative konstante Verschiebung bei großen Zeitverzögerungen auf Raumladungseffekte, erzeugt durch die eingefangenen Ladungsträger, zurückgeführt. Unsere Hypothese wird des Weiteren durch die Skalierung der negativen Verschiebung mit der Vorspannung, welche experimentell bestätigt wurde, unterstützt. Das Doppelpulsexperiment wurde auch dazu verwendet, um die Tauglichkeit eines bestimmten Materials für die Anwendung in einem ultraschnellen Schalter zu überprüfen.

Dies geschah unter der Verwendung identischer Antennenstrukturen auf unterschiedlich prozessiertem LTG-GaAs Material (G420 und TP983). Dabei zeigten die Messungen an der Probe TP983 ein weniger optimales Verhalten, d.h. eine deutlich längere Erholungszeit nach der Anregung (im Vergleich zu den transienten Reflektivitätsmessungen) und eine starke Feldabschirmung durch Raumladungseffekte. Die beobachtete Abhängigkeit des THz-Signals von der THz-Pumpleistung im Doppelpulsexperiment, bei negativen Zeitverzögerungen, deutet auf langlebige Raumladungseffekte hin, welche die Wiederholrate des Lasers überdauern. Diese langlebigen Ladungsträger, Elektronen und Löcher, werden dabei einer Untergruppe der Gesamtladungsträger zugeordnet, welche in nächster Nähe zu den Elektronen eingefangen sind, wobei (aufgrund des unterschiedlichen Ladungsträgertransports in die Elektroden) an der jeweiligen Elektrode die entgegengesetzte Polarität der Ladungsträger vermindert ist. Wir haben die Berechnung dahingehend erweitert, die Raumladungseffekte und deren Relaxation auf der Nanosekundenzeitskala zu berechnen. Dabei zeigen die experimentellen Daten, dass aufgrund der erhöhten Anzahl an Rekombinationsmöglichkeiten bei höheren optischen Intensitäten der Rekombinationsprozess verbessert abläuft.

Zusätzlich haben wir durch die Messung der THz-Transienten erzeugt mit einem konstanten Laserpuls und mit und ohne zusätzlicher CW Hintergrundbeleuchtung eine Reduzierung der THz-Amplitude um ca. 40 % beobachtet, welches einer Reduzierung der Leistung um etwa 64 %, bei einer CW Leistung von etwa 10-20 mW, entspricht. Dieses Phänomen konnte ebenfalls auf die Existenz von langlebigen Ladungsträgern zurückgeführt werden.

In prinzipieller und kurzer Zusammenfassung dieser Studie kann die Aussage getroffen werden, dass Photomischer, basierend auf Materialien mit Ladungsträgererfangdefekten, stark zu langlebigen Raumladungseffekten neigen, welche die gewünschte Abstrahlungsleistung der Bauelemente deutlich reduzieren. Eine Alternative bieten damit Übergangslimitierte Materialien, bei welchen die Antwortzeit auf eine Anregung durch die Ladungsträgersammelungszeit gegeben ist, wobei es möglich ist, dass nur eine Sorte der Ladungsträger zum THz-Signal beiträgt.

2. Low-temperature-Grown GaAs material system

The present chapter gives a somewhat detailed and comprehensive overview of the main structural, optical and electrical properties of low-temperature-grown (LTG) GaAs, with respect to its applications as an active layer in ultrafast optoelectronic components. However, there is an overwhelming amount of literature produced as a result of LTG-GaAs investigations, therefore, in the following, we will only review/focus on those properties relevant for the work presented here. In close relation with the double-pulse technique presented in Chapter 5, we also review the main experimental techniques used in determining the material parameters. In Section 2.4 we present the electrical and optical (transient reflectivity) characteristics of the LTG-GaAs material used in the present study.

2.1. Growth and morphology

The high quality GaAs grown by molecular beam epitaxy (MBE) is usually grown at a substrate temperature of 600 °C with an As₄-to-Ga beam equivalent pressure (bep) ratio of 15-20 and a growth rate of 1 μm/h. LTG-GaAs differs from the standard, highly stoichiometric GaAs through its low growth temperature - between 200 °C and 300 °C. It is worth mentioning that despite its high non-stoichiometry LTG-GaAs can be grown as high quality mono-crystals [38]. If the temperature is lowered below 180 °C the epi-layer becomes polycrystalline or amorphous. During the growth process, excess As is incorporated leading to the formation of a relatively high density of *point defects* with density values spread over a wide range, depending on the growth conditions ($10^{17} - 10^{20} \text{ cm}^{-3}$), such as arsenic antisites As_{Ga} and possibly arsenic interstitials As_i as well as gallium vacancy point defects (V_{Ga}), as depicted in Figure 2.1. The substrate temperature controls the amount of excess arsenic which can be as high as 2% during the molecular beam epitaxy (MBE), the defect density decreasing exponentially with the growth temperature (T_g) in the range 250-300 °C [39]. Yu et al. [40] and Liu et al. [41] found an amount of excess arsenic of only 0.1% for $T_g > 280$ °C. Also, the arsenic defect density will be high if the arsenic pressure during molecular beam epitaxial (MBE) crystal growth is high; with decreasing growth temperature both the lattice parameter and the concentration of As_{Ga} increase, the dominant effects for the lattice expansion in LTG-GaAs being the As_{Ga} defects.

Due to the excess As atoms embedded in the lattice and subsequent formation

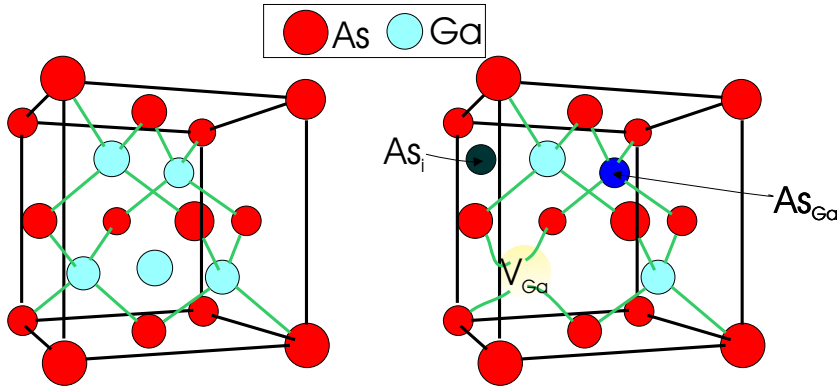


Figure 2.1.: The lattice of SI GaAs (left) and LTG-GaAs (right) with point defects indicated.

of the As_{Ga} antisite defects, an isotropic expansion up to 0.15% of the lattice was observed [38]. This can be easily understood since the As-As bond is slightly longer than the Ga-As bond. If one takes the interatomic distance between the nearest neighbors $r = 2.51 \text{ \AA}$ in a rhombohedral As crystal, then this is larger than the nearest Ga-As interatomic distance ($r_0 = 2.45 \text{ \AA}$) in the GaAs crystal. It was suggested that the length of the As_{Ga} -As bond might be even longer in LTG-GaAs. Based on the fact that the LTG-GaAs crystal is tetragonally strained, Liu et al. [42] found that the increase in the lattice parameter can be linked to the concentration of As_{Ga} defects (from hereon denoted as $[As_{Ga}]$) :

$$\frac{\Delta a}{a_0} = \frac{r^3 - r_0^3}{r_0^3} \frac{1}{2.2 \times 10^{22}} [As_{Ga}], \quad (2.1)$$

where r_0 and r are the interatomic distance between Ga-As in normal GaAs and As_{Ga} -As in LTG-GaAs, respectively. From Eq. 2.1 together with a measured defect density of $1.6 \times 10^{19} \text{ cm}^{-3}$ a distance $r = 2.65 \text{ \AA}$ was derived. With increasing T_g a decrease of the lattice strain is observed - according to Ref. [42] for $T_g > 280 \text{ }^\circ\text{C}$ the expansion of the lattice amounts to only 0.01%.

For layers grown at $200 \text{ }^\circ\text{C}$ the as-grown antisite concentrations are approximately 10^{19} cm^{-3} . The gallium vacancy V_{Ga} is believed to be the dominant native acceptor taking part in the carrier compensation. The gallium vacancy concentration is lower by a factor of 10 for this growth temperature, but still far above equilibrium values, leading to an interesting annealing behavior. The presence of the gallium vacancies in LTG-GaAs results in very important effects on device thermal stability and operation lifetimes, due to the fact that the vacancy is mobile, being the main mechanism for superlattice intermixing as well as impurity diffusion. For example, the high as-grown vacancy concentration can lead to *transient enhanced diffusion*, phenomenon that can degrade the optical and electronic device properties [25]. It was found that there is a critical thickness beyond which the film turns amorphous,

with the critical thickness being a function of the amount of excess arsenic incorporated in the epilayer, the arsenic species-to-Ga flux ratio, and of the arsenic species used (the dimer As_2 or the tetramer As_4). For an excess arsenic of 1.5%, layers as thick as $1.5\ \mu\text{m}$ were grown [43]. It was found that As-rich LTG-GaAs possesses a relatively low dark resistivity ($\rho=0.2\text{-}2\ \Omega\text{m}$) [44]. The need for a material with a high dark resistivity led to further treatment of the material following the growth process. Melloch et al. [45] discovered that if the LTG-GaAs material undergoes a *post-growth annealing process* at higher temperatures between $\sim 600\text{-}800\ ^\circ\text{C}$, the crystallinity of the epi-layers improves considerably - the structural distortion and hence the strain in the lattice induced by the excess As antisites relaxes. Most of the strain in LTG-GaAs relaxes with modest annealing temperatures - $600\ ^\circ\text{C}$ for 10 or 30 min or $700\ ^\circ\text{C}$ or higher for 30 sec or less. The excess arsenic forms As metallic precipitates - round metallic clusters with a radius on the order of couple of nm. In LTG material grown at a substrate temperature of $250\ ^\circ\text{C}$ and an As_4 to Ga bep of 16, the precipitates ranged in size from 20 to $100\ \text{\AA}$ with a density of $10^{17}\text{-}10^{18}\ \text{cm}^{-3}$ [43]. Due to the As precipitate formation, the density of As point defects decreases during the annealing process. The precipitate size distribution is not homogeneous, but does have well-defined average sizes and spacings that increased with increasing annealing temperature (T_a) and annealing time. Thus, the density of the As precipitates could also be controlled through the annealing temperature. Luo et. al [39] reported a decrease in the As-cluster density from 10^{19} to $10^{16}\ \text{cm}^{-3}$ together with an increase in the cluster diameter from 1 to 20 nm by an increase in T_a from $250\ ^\circ\text{C}$ to $900\ ^\circ\text{C}$ with 10 min annealing time. Numerous studies performed on the precipitation process showed that it could be controlled by a high degree of specificity, leading to the term of “precipitate engineering”. For example, by combining different doping and compositional layers in a heterostructure, and by controlling the growth and the annealing temperatures, the precipitates could be induced to grow only in the preferred regions or planes. Yano et al. [46] found that during the annealing process the As_{Ga} antisite defects diffuse via site exchange with V_{Ga} vacancies and hence the annealing dynamics of As_{Ga} antisite defects is dominated by the V_{Ga} vacancy diffusion; the annealing is considered to relax the structural distortion of the GaAs. For a high annealing temperature more defects in the sample will be thermally activated and the diffusion of the defects will be enhanced; samples annealed at higher temperature thus have a smaller defect density. If each As defect is annealed and annihilated with the same probability, a sample grown under high arsenic pressure will have a large arsenic defect density after the annealing. However, the dynamics of the annealing process is far from being elucidated, due to its great complexity. An insight into the precipitate formation on a microscopic level is offered in Ref. [47]. Using calculations based on the self-consistent-charge density-functional-based tight-binding (SCC-DFTB) method, the authors showed that agglomerates of the

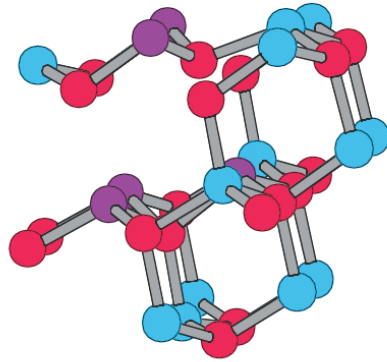


Figure 2.2.: As precipitate.

spherical shape are not necessarily the most stable configuration for a given number of As antisites, and that the primary nucleus that triggers the precipitate formation is the binding of two closest As antisites, from the neighboring Ga sublattice, an event which seems to be energetically favored due to the more metallic bonding of As and its associated charge delocalization. Hence, the nucleation and growth processes start on the atomic scale by re-arranging the atomic bonds in the most energetically favorable fashion. The energy gain due to the precipitate formation is much larger than that obtained by straining the layer in the growth direction, therefore the mobile As_{Ga} will tend to agglomerate.

The annealing process can occur *in-situ* if carried out without exposing the sample to external conditions, or *ex-situ* when the process takes place in a furnace exterior to the growth chamber. Usually, the annealing process is carried out in a gaseous environment (N_2 , H_2/Ar , As), such that the As losses through diffusion are minimized. For the *ex-situ* procedure, good results were obtained with the so-called “face-to-face” condition, where the LTG sample was covered with an undoped GaAs wafer, so that a chemical balance of the As-pressures between the wafer and the sample is established, analogous to the *in-situ* situation, minimizing the outdiffusion of As.

A very thorny problem, which no doubt contributes to that of the wide dispersion of experimental data on LTG-GaAs in the literature, is related to the problem of measuring low growth temperatures (around $200\text{ }^\circ\text{C}$). Since they operate mostly at temperatures between $400\text{--}800\text{ }^\circ\text{C}$ the MBE growth chambers are equipped with infrared pyrometers which, in the low temperature regime are replaced by thermoelements, and therefore the precision and the reproducibility of the temperature measurements depends on the coupling between the substrate and the thermocouple. Another practice consists of linear extrapolation of the pyrometer calibration for low temperatures, again, rendering a large degree of uncertainty. Yu et al. [40] report a reproducibility range of $10\text{--}20\text{ }^\circ\text{C}$ whereas Look [48] speaks of uncertainties of $\sim 30\text{ }^\circ\text{C}$

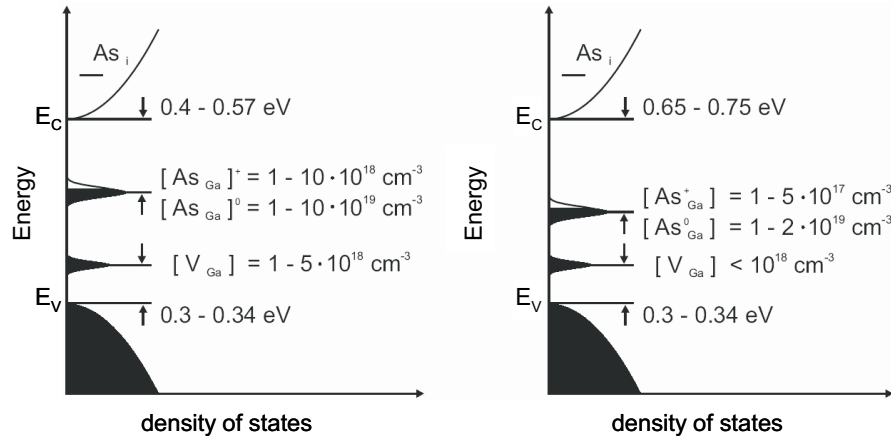


Figure 2.3.: Distribution of point defect energies as a function of density of states in non-annealed (left) and annealed (right) LTG-GaAs.

in comparing results from different MBE installations.

2.2. Optical and electrical properties of LTG-GaAs

The LTG-GaAs material has been surrounded by quite a large number of controversies, the initial controversy being concerned with what happens to the excess As after the annealing process, now it is known that the excess arsenic precipitates during annealing. One of the most disputed issues is still related to the role played by the residual effects vs. arsenic cluster in controlling the material electronic and optical properties. The LTG-GaAs material used commonly in optoelectronics nowadays is annealed, however, looking at the properties of the non-annealed material could be helpful in trying to understand the properties of the annealed one.

2.2.1. Band structure and electronic properties of LTG-GaAs

The concentrations of the As_{Ga} defects in both as-grown and annealed LTG-GaAs were quantified using electron paramagnetic resonance (EPR) [38], near-infrared absorption [49], magnetic circular dichroism of absorption (MCDA) [41], and scanning tunneling microscopy (STM) [50]. Shen et al. [51] performed photorefectance (PL) measurements of the Fermi level position, finding it in both cases (annealed and non-annealed) pinned at different levels.

In the non-annealed state, the As_{Ga} point defect acts as a double donor, being present in a neutral charge state As_{Ga}^0 and in a single positive charge state As_{Ga}^+ . Typical concentrations are $[As_{Ga}^0] \cong 10^{20} \text{ cm}^{-3}$ and $[As_{Ga}^+] \cong 10^{19} \text{ cm}^{-3}$ $T_g \sim 200 \text{ }^\circ\text{C}$ [52]. The As_{Ga} create a deep donor level, partially ionized and situated at 0.4-0.57 eV [53, 54, 55, 56] below the conduction band edge, as depicted in Figure 2.3. It

is believed that the positively charged As_{Ga}^+ defects act as electron traps since the properties of As_{Ga} defects in LTG-GaAs and EL-2 defects in semi-insulating (SI) GaAs are very similar, the EL2 defects being well known as electron traps. The positive As_{Ga}^+ are compensated by native acceptors - the gallium vacancies V_{Ga} . The V_{Ga} states are located in the lower half of the bandgap with a concentration lower by a factor of three than the As_{Ga}^+ concentration [57]. They create a deep acceptor level, fully ionized placed 0.3-0.34 eV above the valence band [48]. The annealing process causes the deep donor level to shift towards the middle of the band gap around 0.65-0.75 eV, consistent with a substantial reduction in the concentration of the As_{Ga} point defects. In Refs. [41, 58] the authors report a strong dependence of the defect concentration on the annealing temperature: $[\text{As}_{\text{Ga}}^0]$ decreases from 3×10^{19} to approximately 10^{18} cm^{-3} while $[\text{As}_{\text{Ga}}^+]$ decreases from 3×10^{18} to $2 \times 10^{17} \text{ cm}^{-3}$ when the annealing temperature is increased from 200 °C to 600 °C. While the concentration of EL2 defects in SI GaAs is on the order of 10^{16} cm^{-3} , due to the several orders of magnitude higher concentration of As_{Ga} defects the non-annealed material loses its semi-insulating properties.

2.2.2. Considerations on the dynamics of photogenerated carriers

With the advent of ultrafast photoconductive switches based on LTG-GaAs there was an on-going interest in the dynamics of the photogenerated carries, with numerous investigation methods being employed. Among them, optical techniques based on femtosecond lasers and the pump-and-probe approach have been widely used. Here, changes in the physical properties of the sample induced by the pump pulse are recorded by using a subsequent probe pulse arriving at the sample at different time delays. Thus it provides perhaps the best tool for investigation of the ultrafast carrier relaxation processes. One of the most effective, hence, most frequently employed ways to obtain information about photogenerated carriers in LTG-GaAs is based on transient reflectance/transmission measurements. Other methods employed in investigating carrier dynamics in LTG-GaAs were based on measuring photocurrent transients [59], time-resolved photoluminescence [60] and optical-pump-THz-radiation probe experiments [61]. In the following we will briefly discuss the principles as well as some of the most relevant results obtained with these methods. For instance, in a typical pump-probe experiment that measures the time-dependent changes in reflectivity, the above-band-gap photons in the pump beam induce absorption nonlinearities ($\Delta\alpha$) due to photogenerated electrons and holes, through the mechanism of band-filling, bandgap renormalisation and free-carrier absorption [62]. The change in absorption is related through the Kramer-Konig relations to the changes in the

refractive index - directly related to a change in reflectivity:

$$\frac{\Delta R}{R_0} \cong \frac{4\Delta n(t)}{(n^2 - 1)}, \quad (2.2)$$

where $\Delta n(t)$ is the change in the real part of the refractive index (since the imaginary part of the refractive index can be typically neglected). The Δn factor for each of these three processes mentioned above depends on the probe-photon energy and photocarrier density. For probe energies above the bandgap and for typical injected carrier densities of $\sim 10^{18} \text{ cm}^{-3}$, the change in refractive index and hence in reflectivity is mainly caused by the band-filling (as long as the contribution of the absorbed carrier to a change in absorption can be discarded). If the initial changes in the reflectivity are due to the rate at which photogenerated electrons fill up the lowest available state near the band edge, the subsequent 1/e-decay time is assumed to indicate the rate at which the photogenerated electrons are trapped or recombine at lower energy states/deep levels below the band edge.

The first investigations of the ultrafast carrier relaxation in LTG-GaAs, are from Gupta et al. [63]. They reported a carrier trapping time of $\sim 0.4 \text{ ps}$ for a material grown at $200 \text{ }^\circ\text{C}$ and annealed at $600 \text{ }^\circ\text{C}$. From a very early stage it was admitted that the exact determination of the trapping time is a cumbersome procedure mainly due to the fact that for such short times, one would rather probe the *intraband* dynamics, than the decay of the mobile carriers. One way to obtain reliable data is to use photon pump energies resonant or very close to the bandgap. For optimized growth and annealing temperatures carrier trapping times between 100 fs and 400 fs for the non-annealed material [63, 33, 64, 61, 65, 66] as well as between 300 fs and 500 fs for the annealed LTG-GaAs [64] were reported.

The analysis of the experimental data was mainly conducted around two models. Within the first model, Loka et al. [67, 68, 69] describe the dynamics of the photogenerated carriers neglecting the role played by the gallium vacancies - the main processes being generation, electron capture and recombination, as sketched in Figure 2.4. The photogeneration of the electron hole pairs takes place not only by single photon absorption (SPA) but also through a two-photon absorption (TPA) process, (i.e. when the incident field wavelength is such that $E_g/2 < h\nu < E_g$, and electrons make the transition from the valence band (VB) to the conduction band (CB) by simultaneously absorbing two photons). Depending on the photon energy used in the pump beam, the photogenerated electrons possess an supplement of energy with respect to the conduction band edge. A third possibility to generate free carriers is to excite electrons from the As_{Ga}^0 defects (process denoted with TA in Figure 2.4). Due to the smaller concentrations and the absorption cross-section, the excitation of holes from the valence band to the As_{Ga}^+ defects is discarded [70, 69]. The decay of the photogenerated carriers takes place through the processes marked with straight

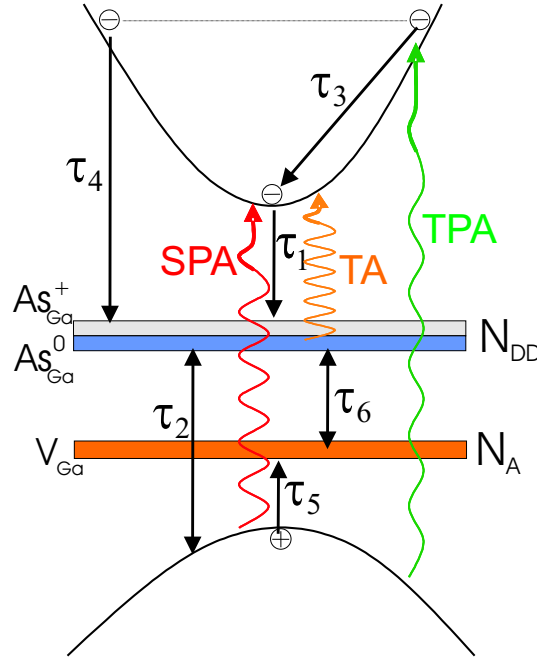


Figure 2.4.: Band diagram for LTG-GaAs showing the different processes involved in the carrier dynamics.

arrows in Figure 2.4, with the corresponding decay times τ_1 through τ_4 , while the excitation processes are depicted with curly arrows. The carriers situated on the bottom of the CB have just one decay channel - here denoted with τ_1 . The hot carriers excited high up in the CB can be directly captured by the ionized defects (As_{Ga}^+) within a time τ_4 , or they might relax to the bottom of the band (τ_3) and then be trapped (τ_1). The electrons trapped in the deep donor level recombine at last with the holes in the VB in a time τ_2 . The above model was implemented for both non-annealed and annealed LTG-GaAs; the interpretation of the experimental data yields values of $\tau_1=1.5$ ps, $\tau_2=3$ ps, $\tau_3=100$ ps and $\tau_4=0.3$ ps, for annealed LTG-GaAs material grown at 300 °C. The trapping times for carriers excited higher in the CB are faster than the times for the carriers excited to the bottom of the CB, due to the fact that the trapping time by the mid-gap states should be inversely proportional to the carrier velocity.

Other authors [70, 71], using time-resolved transmission experiments, developed an alternative model whose characteristics are also depicted in Figure 2.4. Here, the carrier photogeneration is due to single photon absorption (SPA) and to the excitation of electrons from neutral As_{Ga} defects, the TPA process being neglected here. The VB- As_{Ga}^+ transition is neglected in this model as well, due to the lower concentration of As_{Ga}^+ defects and their much lower absorption cross-section. With the assumption that the relaxation of the hot-electrons to the bottom of the CB is not relevant, the decay of the photoexcited carriers to the As_{Ga}^+ states is described

by a characteristic time τ_1 . In contrast with the time constant of the other model, here the holes are trapped in the V_{Ga} acceptor states with a time constant of τ_5 . The emptying of the donor trap states takes place through recombination of electrons with the holes in the VB (τ_2) or V_{Ga} acceptor level (τ_6). Siegner et al. [70] proposed the above model based of qualitative considerations on transmission measurements performed on non-annealed LTG-GaAs, whereas Lochtefeld et al. [71] provided some quantitative insight, determining the electron and hole capture cross section ($\sigma_n=7\times 10^{-15}$ cm², $\sigma_p=6\times 10^{-17}$ cm²) for the trapping processes τ_1 and τ_2 , the electron capture cross section being one order of magnitude greater than for the EL-2 defects in GaAs. For the case of non-annealed material, together with a trapping time of around 200 fs for electrons and holes ($\tau_1 \sim \tau_2$), Lochtefeld et al. observed an extremely long time constant for the emptying of the trapping states (assumed to take place through recombination) of more than 1 ns, attributed to the trapping of the electrons and holes at different types of defects (τ_6). If the photo-generated carrier density is high or the density of defects low, a saturation of the As_{Ga}^+ and V_{Ga} states occurs, causing the non-ionized (As_{Ga}^0) states to capture holes (process associated with τ_2 (upwards) in Figure 2.4) and hence causing a bottleneck for the process of emptying the electron trap, resulting in slow time decays: $\tau_1 \sim \tau_5 \ll \tau_2 \ll \tau_6$. For the annealed material, a single exponential decay was found (hence no de-trapping of electrons occurs) consistent with the assumption that for the annealed material the trapping center is a singular entity: most probably the As metallic precipitate, this also explaining the fast recombination of carriers.

Since in most of its ultrafast applications the LTG-GaAs is annealed (due to its higher dark resistivity), the recombination dynamics in the annealed material plays a very important role in device operation. Studies of carrier relaxation times revealed a systematic increase of the trapping time with increasing both the growth and annealing temperature [61, 66]. McIntosh et al. [64] reported carrier trapping times as short as 90 fs on a LTG-GaAs material grown at $T_g=195^\circ\text{C}$ and annealed at temperatures below 580°C . Recently, Gregory et al. [72] found that material grown at $\sim 230^\circ\text{C}$ but annealed at lower temperatures ($T_a \simeq 425^\circ\text{C}$) had a very short carrier lifetime ~ 100 fs and a relatively high resistivity, suggesting that a compromise between the T_g and T_a must be sought when choosing a fabrication recipe for specific THz applications. There is still a strong controversy as far as the importance of the As precipitates is concerned: some groups adopt the so-called *point-defect model* claiming that the As precipitates have very little influence on the recombination dynamics. Hence the longer trapping times observed for annealed materials is associated with a decrease in As_{Ga} point defect density [61], while other groups outline the importance of As clusters as effective trapping and recombination centers [71]. In the *point defect model*, a single defect level (denoted with N_{DD} in Figure 2.4), lying within the bandgap is assumed, the carrier capture time being controlled through

the density of defects, as seen from the standpoint of the Shockley-Read-Hall (SRH) theory:

$$\tau_c = \frac{1}{N_D v_{th} \sigma_e}, \quad (2.3)$$

where N_D is the defect density, v_{th} thermal velocity of electrons and σ_e the capture cross section. On the other hand, Melloch et al. [43] suggested that the trapping mechanism should be considered to be diffusive transport followed by impact on a As precipitate. They observed a superlinear dependence of the electron trapping time on the As precipitate spacing, using an empirical $\tau \sim R^2$ -law in order to describe their data. More recently, the work of Loukasos et al. [73], based on the model of Ruda and Shik [74], showed that the carrier trapping times depend on the As precipitate size and spacing according to the law $\tau = \frac{R^3}{3D\alpha}$, where D is the diffusion constant, R is the average spacing and α is the mean radius of the As precipitates. Their conclusion was that the transport mechanism of the photoexcited carriers, and hence their relaxation time is influenced by a 3D diffusion transport mechanism together with the density and size of the As precipitates.

A very versatile tool in characterizing the carrier dynamics in LTG-GaAs proved to be the optical-pump THz-probe spectroscopy [61, 34, 75]. It was shown that this technique could circumvent some of the shortcomings present in the conventional optical pump-probe experiments: photoinduced absorption, Auger effect, bandgap renormalization, TPA, re-excitation of trapped and un-trapped carriers. It can be used with rather low pump carrier densities as well as a unique probe interaction, with energies situated in the mid-infrared (MIR) or far-infrared (FIR), where only intra-band transitions are important (only the free carriers influence the signal). Besides the insight into the ultrafast carrier dynamics, this method offers also quantitative information on the electrical properties of the LTG-GaAs material (the electron scattering time τ_S and mobility). Segsneider et al. [34] outlined the importance of the As_{Ga}^+ defects as recombination centers, in the same time reporting a fast trap-emptying time for higher excitation densities, explained by either a carrier density-dependent recombination time or by the activation of the neutral As_{Ga}^0 defects as recombination centers (the process denoted with TA in Figure 2.4. However, even for the highest intensity the reported recombination time is on the order 20-25 ps. Beard et al. [75] in the same kind of experiment (but pumping with two different wavelengths) adopts the As cluster model in interpreting the data, stating that there is an interrelation between carrier lifetime and mobility in LTG-GaAs, due to the fact that the carrier lifetime is governed by the average time a photoexcited carrier diffuses before encountering a trap - the diffusion time being determined by the mobility.

So far, the information on the hole trapping processes in LTG-GaAs is very scarce, although it is of the same importance as electron trapping parameters when de-

signing ultrafast optoelectronic devices. The trapping times for holes were mostly inferred from indirect experimental evidence such as the change of the reflectance or transmittance transients at high photoexcited carrier densities, when the electron traps were saturated [76]. Saturation experiments with a sub-bandgap probe have been performed by Grenier et al. [77], and revealed a trap emptying time of several hundreds of picoseconds that was associated with the hole lifetime. Adomavicius et al. [78] were able to directly monitor the hole density dynamics in the valence band of LTG-GaAs using a two-color pump-probe technique. The hole trapping time was determined by photo-exciting the carriers with femtosecond 800-nm pulses while probing the inter-valence band transitions with 9- μm -wavelength optical pulses, the latter wavelength corresponding to resonant transitions between the heavy hole (HH) and the light hole (LH) valence bands. In non-annealed LTG-GaAs the hole trapping time was found to be around 2 ps while after annealing it increases to more than 100 ps.

It is important to mention that shallow defects (also referred to as sub-bandgap states) were observed in LTG-GaAs - in the band edge continuous-wave (CW) absorption spectrum [79]. The presence of the shallow donor states could be best explained in terms of the spatial potential fluctuations due to point defects. The carriers trapped in these states have relatively long lifetimes, hence they might have an impact on the optoelectronic properties of LTG-GaAs since the carriers trapped in shallow potentials could be re-excited thermally or by THz electric fields.

There are also models proposed to explain other specific experiments. For example, in order to model results from a photoconductivity experiment, Stellmacher et al. [80] treated the deep donor levels associated with the arsenic antisite defects as recombination centers. Here, the gallium vacancies influence indirectly the carrier dynamics through the compensation of the As_{Ga}^+ states. In a time-resolved absorption experiment, Grenier et al. [77] used a model with two sets of trapping states and four time constants, suggesting that there could be carriers captured in long-lived trapping states that might recombine after more than 100 ps. However, clearly there is still a lot of controversy as far as the ultrafast carrier dynamics in LTG-GaAs is concerned. It should be outlined that the purpose of the present work is not to reveal the intricate details of the carrier dynamics but to provide the reader with insight into the direct impact some aspects of carrier dynamics have on the efficiency of optoelectronic THz emitters.

2.3. Electrical and carrier transport properties of LTG-GaAs

One of the properties that makes LTG-GaAs a very appealing material for optoelectronic applications is its relatively large dark resistivity. This motivated a large number of authors to investigate the transport mechanisms in LTG-GaAs and its dependence on the point defect density, concentration and size of As clusters.

LTG-GaAs material grown at 200 °C, without any subsequent annealing, presents a rather low resistivity $\rho \sim 10 \text{ } \Omega\text{cm}$ [54, 81, 82]. If the growth temperature is increased from 200 °C to 400 °C, the resistivity increases from 10^1 to approximately $10^5 \text{ } \Omega\text{cm}$ [83, 44, 81]. Temperature-dependent measurements have revealed two conduction mechanisms: at temperatures higher than 300 K the transport is through “nearest-neighbor hopping” (NNH), taking place in the deep donor band created by the As antisite defects and situated around 0.75 eV below the conduction band edge (see Figure 2.3), corresponding to the activation energy of the hopping transport. Thus, according to Look [82], the charge carriers are “holes”, excited from the valence band into a nearby neutral donor state, the hole hopping through the lattice between neighboring donors. The conductivity decreases exponentially with the concentration of defects N_D , due to the necessity of defect wave function overlap: $\sigma \sim \exp\left(1/aN_D^{\frac{1}{3}}\right)$, where a is the extent of the donor wave function, calculated to be 8.67 Å. Accordingly, the observed increase in resistivity with the growth temperature could be explained in terms of a decreasing concentration of point defects reported for higher growth temperatures. For temperatures lower than 250 K, the conduction is mainly attributed to “variable-range hopping”, as derived from a $\exp\left(-\frac{T_0}{T}\right)^{\frac{1}{4}}$ dependence of the conductivity. Here, due to the “freeze-out” of carriers (carriers possess much lower energy), a carrier can hop with an equal probability to any of the donor levels of the same energy, situated within a certain range.

As in the case of ultra-fast photocarrier dynamics, there has been considerable debate concerning the role of point defects vs the role of arsenic precipitates in explaining the electrical properties displayed by the annealed LTG material. It was observed that after annealing the resistivity of the LTG-GaAs material increased tremendously, the material becoming semi-insulating (SI). For example, a sample grown at 200 °C before annealing showed a resistivity of only 10 Ωcm while for the same sample after 10 min annealing at 600 °C the resistivity increased to $10^6 \text{ } \Omega\text{cm}$ [54]. Look et al. showed that for annealing temperatures $T_a < 350 \text{ } ^\circ\text{C}$ there was absolutely no effect of the annealing on the electrical properties of the LTG material, an observation confirmed at a later stage by Luo et al. [81, 39].

Within the "point defect model", Look tried to explain the increase in resistivity by a decrease in the concentration of the As_{Ga} and V_{Ga} defects with annealing, thus the hopping component of the conductivity being strongly reduced. More explicitly, for intermediate annealing temperatures, the number of acceptors N_A decreases in

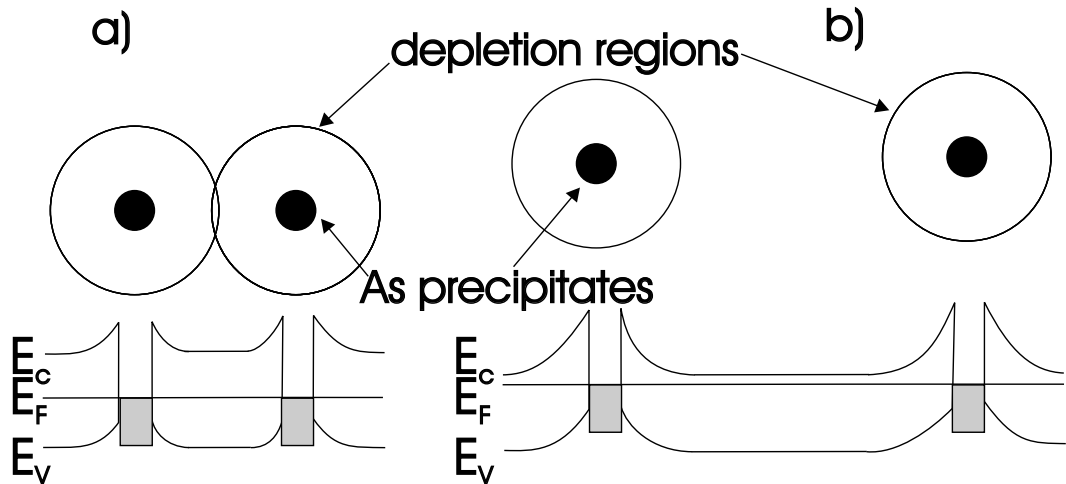


Figure 2.5.: Depletion regions around arsenic precipitates such that the depletion regions just overlap a) or with spacing b) such that there is undepleted material between the clusters.

parallel with the concentration of donors N_D and thus the amount of holes promoting hopping present in the donor band is reduced, the impact of a lower concentration of donors being reflected in the lower hopping probability. The semi-insulating properties of the LTG material were explained by the full compensation of the ionized As_{Ga}^+ donors by the V_{Ga} acceptors. It was established that for an annealing temperature $T_a < 400^\circ\text{C}$, the main contributor to the conduction mechanism is hopping, whereas for $T_a > 500^\circ\text{C}$ the carrier transport is carried out mainly in the conduction band, having a thermally activated component, while the As precipitates were left out of the picture.

Another model proposed for explaining the semi-insulating properties of LTG-GaAs was proposed by Warren et al. [84]. Here, assuming a decreased number of As_{Ga} defects and a relatively high density of As precipitates after annealing, the key role in defining the electrical properties of LTG-GaAs is taken up by the As precipitates. For non-doped LTG-GaAs material, the semi-insulating properties are explained by the overlap of the depletion regions formed due to the Schottky barriers at the metal(As)/semiconductor(GaAs) interfaces for a sufficiently high density of precipitates, as illustrated in Figure 2.5. The As clusters can be regarded as buried Schottky contacts, the formation of which could be explained either by metal-induced gap states (MIGs) [85], or by the effect of the metallic clusters in the compensation mechanism, pinning the interface Fermi level at a value corresponding to the Schottky barrier (SB) height¹. Thus, if the cluster density is low (moderate

¹The values for SB heights reported in the literature for n and p-type GaAs are $\Phi_{n,p}=0.8$, respectively 0.6 eV.

levels of annealing) the depletion regions are isolated (Figure 2.5, a)), the LTG material will be partially compensated but still conducting², whereas for a high density of clusters the material is fully depleted (screened) becoming semi-insulating Figure 2.5 b). The maximum depletion radius r_s is connected to the barrier height Φ_B and the cluster radius r_0 through Poisson's equation:

$$\Phi_B = \left(\frac{qN_D}{6\epsilon} \right) \left[\left(\frac{2r_s^3}{r_0} \right) + r_0^2 - 3r_s^2 \right], \quad (2.4)$$

where the N_D is the doping concentration (or for the undoped case the concentration of the ionized As_{Ga}^+ defects). According to Warren, for a precipitate density $>10^{16} \text{ cm}^{-3}$ the depletion spheres begin to overlap. It was also shown that for a fixed cluster size, the compensation limits are set by the cluster density.

Performing a thorough investigation of LTG materials with a wide range of growth and annealing temperatures, and trying to explain the observed exponential rise of resistivity with the annealing temperature, Luo et al. [39, 81] unified both the point defect and the Schottky barrier model in terms of an As-cluster model. Based on the finding that in annealed material and for low measurement temperatures the transport is dominated by hopping, Luo suggested that the As_{Ga} defects can be regarded as one extreme case of As clusters. This model is supposed to explain the conductivity behavior of both the un-annealed as well as the annealed samples. The model predicts that for un-annealed samples, the high density of As clusters causes the overlapping of the defect wave functions providing an effective path for hopping conduction; during the annealing process, the excess As coalesces forming As precipitates/clusters acting as buried Schottky contacts with overlapping depletion regions. With increasing the annealing temperature the cluster size increases as well as the distance between the clusters, thus rendering the material highly resistive due to the less effective hopping conduction between As clusters, the conduction being taken over by thermionic field-emission from the As precipitates. From I-V-T measurements the activation energy for the hopping process (70 meV) as well as for the thermally activated component (0.7 eV) in the annealed samples was determined. In the later case, the activation energy corresponds to the thermionic emission of electrons over the barrier of As/GaAs clusters. Also, the exponential dependence of the resistivity on T_a yields an activation energy of 2.1 eV which was associated with the activation energy of the arsenic precipitate formation process.

The experimental techniques used to investigate the transport in LTG-GaAs material were Hall and resistivity measurements (Look et al. [82]) taken at different temperatures, and current-voltage (I-V) characteristics versus temperature (Luo et al. [81]). For the case of LTG-GaAs the conductivity σ and the Hall coefficient R^H are

²The conduction in this case will take place through percolation, leading to hopping-like conductivity at low temperatures.

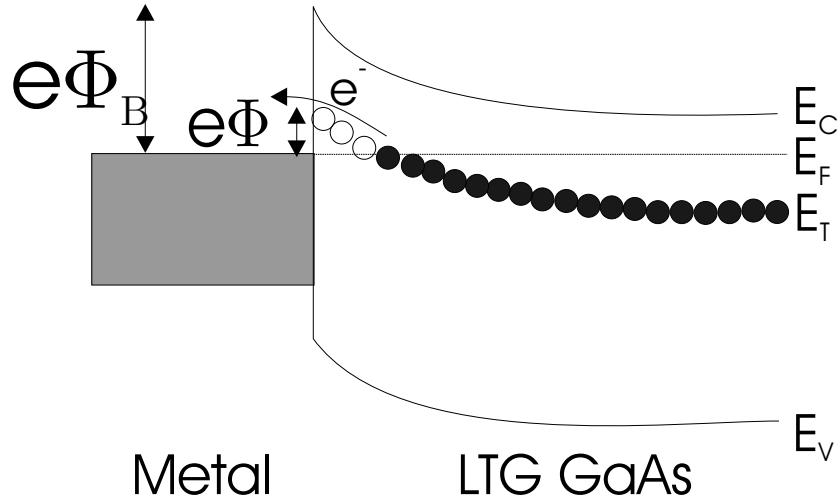


Figure 2.6.: Band diagram for the metal-semiconductor contact.

interrelated through the compensation mechanism, that is, there is a conduction band contribution to mobility, $\sigma_b = en_b\mu_b$ (where the subscript b stands for *band*), and where the mobility μ_b is mainly due to the scattering from neutral deep donors and the Hall coefficient contribution being $R_b = \frac{1}{en_b}$. The analysis of the data was complicated by the two mechanisms contributing to the conductivity: band conduction and hopping in the miniband created by the deep donors, such that the values for measured conductivity and Hall coefficient were given by: $\sigma = \sigma_b + \sigma_h$ and $R = \frac{R_b\sigma_b^2 + R_h\sigma_h^2}{(\sigma_b + \sigma_h)^2} \simeq \frac{R_b\sigma_b^2}{(\sigma_b + \sigma_h)^2}$, assuming $R_h \sim 0$.

Another complication was created by the fact that is almost impossible to obtain good Hall-effect measurements on LTG-GaAs without separating the layers from their SI GaAs substrate. This is because the sheet conductance of a layer grown at 200 °C is less than that of its substrate after a high-temperature anneal ($T_a > 500$ °C).

An important aspect of the electrical measurements is the contacting of the LTG material to the external circuit. It was found by a considerable number of authors [86, 81, 82, 87] that some of the metalization schemes most frequently used in semiconductor device technology (Ti/Au, Au/Ge/Ni) make ohmic contacts on LTG-GaAs material. Indeed, as reported by Luo et al. [81], all the as-grown (non-annealed) samples showed Ohmic behavior, when Au/Ge/Ni contacts were deposited on the LTG material. Yamamoto et al. [87], proposed a carrier transport model in which the electrons travel from metal directly into the deep trap level (E_T) formed by the dense As_{Ga} defects, as depicted in Figure 2.6. With a calculated value of the Fermi level position at ~ 0.4 eV from the conduction band minimum, and a very small density of carriers in the conduction band ($\sim 7 \times 10^{10} \text{ cm}^{-3}$), the authors rule out thermionic emission over the Schottky barrier ($\Phi_B \sim 0.8$ eV), calculating an effective barrier of ~ 0.15 eV. As can be seen in Figure 2.6, due to the band bending

at the interface, there is an unoccupied region in the deep donor band, which in the forward bias regime becomes occupied. Hence, the electrons in the miniband (E_T) have to surmount a lower barrier to enter the metal. In the same fashion, when reverse biased, the electrons in the metal can enter into an unoccupied state of the donor miniband and then move into the bulk with no barrier to overcome. The calculated value for the effective barrier agrees well with the value obtained experimentally (~ 0.12 eV).

For the annealed samples, the $J - V$ characteristics show an ohmic behavior at low temperatures (Luo et al. [81]), while at room temperature the LTG samples exhibited nonlinear characteristics in the medium bias region indicating the existence of a barrier which produces an electron transport response similar to that in a reverse-biased Schottky contact. Ibbetson et al. [88] studied the transport properties of microstructured LTG-GaAs material annealed at different temperatures, revealing a very complex behavior in which the transport mechanism is sensitive to both the annealing and measurement temperature. They confirmed the dominance of hopping processes at low measurement temperatures, whose contribution decreases with increasing the annealing temperature, mainly due to the reduction in the As_{Ga} defect density. For room temperature measurements and high anneal temperatures ($T_a \simeq 700^\circ\text{C}$) they report an almost exponential dependence of current upon the applied bias, pointing towards transport over a potential barrier. The measurements show a strong dependence on the measurement temperature, having an activation energy of 0.6 eV. The $J - V$ characteristics were explained by modeling the LTG-GaAs material as a series of N equivalent metal/semiconductor/metal (MSM) junctions, where N is the total thickness of the LTG layer multiplied with the average number of precipitates per unit length, each junction being represented as pair of back-to-back Schottky diodes. The current flow was calculated as the current flowing through a reverse biased Schottky diode, considering both thermionic emission over the barrier as well as tunneling emission below the barrier tip. The total current density is given by:

$$J = \frac{emk_B T}{2\pi h^3} \int_0^\infty \exp\left(-\frac{E}{k_B T}\right) P(E, \varepsilon) dE, \quad (2.5)$$

where $P(E, \varepsilon)$ is the transmission probability for an electron with the energy E .

Latter on, Ibbetson et al. [89] performed an ample investigation of the dark $J - V$ characteristics of LTG material annealed at 700°C , sandwiched between an ohmic contact and a highly conductive n^+ GaAs layer. The structure was biased such that the electrons flow from the highly doped layer into the LTG material. The observed $J - V$ characteristics display an ohmic behavior for low applied bias fields (0.1–5 kV/cm), followed by a saturation in the current and then, at high voltages, the current has a superlinear dependence (see Figure 2.7). The authors attempt to explain the observed features using the space charge limited current (SCLC) theory

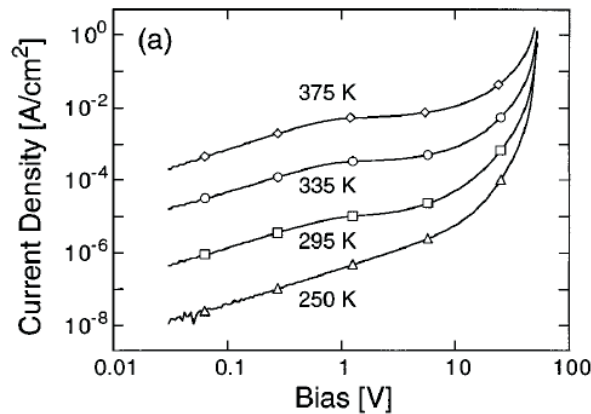


Figure 2.7.: Current-voltage characteristics of LTG-GaAs measured at different temperatures, from Ref. [89].

and electron velocity saturation. Very common in insulators, details of the SCLC theory will be given in the next chapter. In brief, the electrons injected from the highly conductive layer (injecting contact) are transported across the LTG layer in an ohmic regime as long as the number of injected electrons does not exceed the number of electrons n_0 that are thermally generated. The current density in this regime obeys Ohm's law: $J = en_0\mu\frac{V}{L}$, where V is the applied voltage and L is the transport length (thickness) of the sample (LTG-GaAs layer). If the injected electron density n_i is greater than n_0 , or more specifically, the transit time of the injected carriers $t_{tr} = \frac{L^2}{\mu V}$ exceeds the dielectric relaxation time of the material $\tau_d = \frac{\epsilon}{en_0\mu}$ (i.e. the time it takes for the thermally generated charge to relax the excess charge), then the “non-accommodated” charge distributes itself within the insulator creating a space charge domain and setting up an inhomogeneous electric field distribution that controls (limits) the current flow through the insulator. The charge distribution is not uniform within the material, being that one for which the current continuity equation and Poisson's equation can be solved simultaneously and self-consistently. It was first shown by Mott and Gurney (1940) [90] that the current density in the case of SCL current is given by: $J = \frac{9}{8}\epsilon\mu\frac{V^2}{L^3}$, where ϵ is the permittivity of the insulator. There are two important aspects to be mentioned: firstly, the SCLC implies the existence of ohmic contacts with the insulator and secondly, the above equation was deduced for a trap-free insulator. In the case of an insulator with traps, the current density will follow the same quadratic dependence but it will have a much lower magnitude due to the filling of the traps. In implementing the SCLC model for LTG-GaAs, Ibbetson [89] assumed that the electron concentration in the bulk would not change until the electric field across the sample exceeds the value required for electron velocity saturation. At the threshold for injection, the number of the carriers in the conduction band, n_0 , is given by the density of deep

traps N_D , compensated by a deep acceptor N_A (the point defect model), therefore it is the concentration of the compensating species (V_{Ga} in our case) that controls the space charge. While this model works well for low and moderate fields, it fails to fit the $J - V$ characteristics at high bias (100 kV/cm), the authors suggesting that the field ionization of the traps as well as trap-filling come into play at higher bias. Identical features in the I-V curves were observed by Kordos et al. [91]. A striking observation in their study is that the conductivity of the LTG-GaAs layer is different if measured on a vertical vs. a planar structure. Their explanation invokes an inhomogeneous distribution of electric field across the sample that suppresses the hopping conduction at intermediate fields.

2.3.1. Carrier mobility in LTG-GaAs

The carrier mobility has a great impact on the sensitivity and the efficiency of any optoelectronic device. For LTG-GaAs the carrier mobility was investigated using various methods ranging from typical Hall measurements [82], to time integrated efficiency of photoconductive switches as well as THz spectroscopy [34, 65, 75]. In highly stoichiometric MBE GaAs grown at high temperatures, the mobility of free electrons is dominated at room temperature by the interaction with the lattice (phonon scattering), being defined as:

$$\mu_e = \frac{e\tau_s}{m^*}, \quad (2.6)$$

where τ_s is the momentum relaxation (scattering) time, representing the time interval between two consecutive scattering events, and m^* is the reduced mass of the electron, assumed to be the same for LTG-GaAs material as in single-crystalline GaAs. In LTG-GaAs, due to its highly non-stoichiometric characteristics resulting in a high density of lattice imperfections, the carrier mobility should be defined by the elastic carrier scattering on neutral and ionized defects.

Among the first to report on mobility values in LTG-GaAs was Look et al. [54, 82, 92]. The reported Hall-mobility values for non-annealed material at room temperature were below 1 cm²/Vs, the conduction taking place through hopping in the EL2-like defect miniband. One should clearly distinguish in this case between the hopping mobility (seemingly a very complicated effect, disregarded in Look's measurements) and the conduction band mobility. As the conduction band carrier transport becomes predominant for high anneal temperatures, the conduction band mobility increases also with annealing temperature to values of 200-400 cm²/Vs. According to the proposed "point-defect" model, the conduction band mobility has a two-component form, accounting for the lattice and ionized/neutral defect scat-

tering:

$$\mu_b^{-1} = \left(\frac{1}{8500 \left(\frac{300}{T}\right)^{\frac{3}{2}}} + \frac{N_D}{K_1} \right)^{-1}, \quad (2.7)$$

where N_D is the defect concentration and K_1 obtained from fitting the experimental data amounts to $1.02 \times 10^{22} \text{cm}^{-1}/\text{Vs}$. However, Look et al. find the hopping conduction predominant around 300 K even at higher annealing temperatures. Besides, they consider the holes as being responsible for charge transport, and this could offer an explanation for the low mobilities observed. Betko et al. [93], performing DC conductivity and Hall-effect measurements following the van-der-Pauw method on non-annealed LTG-GaAs, separated the band and Hall mobilities. They report a Hall hopping mobility of $\sim 0.14\text{-}0.45 \text{cm}^2/\text{Vs}$. For the band Hall mobility they find an increase from 500 to 6000 cm^2/Vs with increasing growth temperature from 300 °C to 420 °C. Results from Hall measurements on annealed samples can also be found in Ref. [80], here the mobility increasing from 2000 cm^2/Vs for a sample grown at 225 °C to 4000 cm^2/Vs for a growth temperature of 350 °C. The increase in mobility for annealed samples is consistent with the relaxation of the lattice strain and the reduction in defect density, as predicted by Equation 2.7.

Zamdmmer et al. [32] infer rather low mobility values from illuminated $I - V$ characteristics in the low bias region; they assume ohmic conduction and a given carrier lifetime. Here, uncertainties might arise because the holes can have quite a substantial contribution to the measured DC photocurrent. In a pure THz emission spectroscopy experiment, Nemeč et al. [65], report an electron mobility as high as 2250 cm^2/Vs for a sample grown at 250 °C and annealed at 600 °C.

A considerable amount of useful information on mobility was inferred as a by-product of, or in direct relation with, ultrafast carrier dynamics experiments like the optical-pump-THz-probe (OPTP) spectroscopy. Prabhu et al. [61], assuming a semi-classical Drude conductivity model determines a momentum relaxation time τ_s in LTG-GaAs of ~ 180 fs, which points to a rather high mobility $\sim 2000 \text{cm}^2/\text{Vs}$ of the photo-injected carriers, for a sample grown at 300 °C. They make the assumption that the conductivity and THz response of the LTG-GaAs material is dominated by electrons, with the hole mobility being 1 order of magnitude lower. In a similar experiment, Segschneider et al. [34] derive a scattering time of $\sim 15\text{-}20$ fs and an electron mobility with values in the range 450-550 cm^2/Vs .

According to Beard et al. [75], who adopted the As cluster model, the reduced mobility in LTG-GaAs material is due to residual shallow defects, increasing the scattering processes, thereby decreasing the scattering time τ_s . Exciting with two different pump wavelengths, 400 nm and 800 nm, they find a time-dependent mobility which increases from 400 to 1000 cm^2/Vs with a time constant of 2.0 ps. Considering a three-state model (the conduction band is constituted of three sub-

bands - Γ , X and L - with different effective masses), their explanation of the results is found in the large population of phonons produced through the combined inter-valley scattering processes into the low mobility L and X valleys, as well as through exciting carriers higher in the L valley. When exciting with 800 nm, they obtained a time-independent mobility situated around 3000 cm²/Vs, much higher than that obtained from 400 nm measurements, mostly due to the lower amount of scattering taking place. Also, due to the differences in the absorption coefficient dependence on wavelength, at 400 nm the density of photogenerated carriers is higher than at 800 nm, therefore, the carrier-carrier scattering contributes to the reduced mobility. Another interesting aspect pointed out in the work of Bear et al. [75] is that the carrier mobility could influence the trapping time - assuming that the carrier diffuses before encountering a trap, the diffusion time being set by the mobility. Based on this concept, Loukakos et al. [73], determine a diffusion constant $D=43$ cm²s⁻¹, and by using the Einstein relationship $\frac{D}{\mu} = \frac{kT}{e}$, they obtain $\mu=1650$ cm²/Vs.

The reason for the vast dispersion of the reported mobility values on LTG-GaAs can be attributed to the different techniques used for extracting it, as well as in the different growth conditions. For instance, most of the data obtained using the van-der-Pauw method was obtained under no illumination, whereas for the case where data is extracted from illuminated $I - V$ curves the mobility depends on the time-averaged photo-excited electron and hole contributions. If the mobility is extracted from measuring photocurrent transients in photoconductive switches (applicable for THz generation as well), the difficult estimation of the displacement currents introduces a high degree of uncertainty in the results [94]. Last, but not least, the mobility of photo-excited carriers in a material with ultra-short lifetimes do not reach their stationary values during the carrier lifetime, due to the intra-band dynamics.

Another aspect related to the electron mobility in LTG-GaAs - based on the observation that the LTG-GaAs material preserves the band structure of high quality GaAs - is the possibility of velocity overshoot. Numerous workers in the field have claimed the possibility of such a phenomenon, mostly supported by Monte Carlo simulations [95, 96], but there is no direct experimental proof yet for its occurrence. This aspect will be discussed in detail in the following chapter.

2.4. Characterization of LTG material used in the current work

Throughout the remainder of this work, characteristics of THz emitters employing various LTG-GaAs substrates will be analyzed. In this section, details of the growth process for the used LTG-GaAs material, as well as an attempt to characterize their electrical and optical properties, is presented.

2.4.1. Growth and annealing

The G420 LTG-GaAs material was grown at 270 °C and annealed *in situ* at 600 °C for 5 min at TU Vienna³. The layer thickness was around 2 μm . Throughout the work presented here this substrate was used as a reference, representing what is believed to be an optimal LTG-GaAs material for optoelectronic applications.

The substrates which are the main subject of investigation in this work were grown at the University of Erlangen and are denoted TP983 and TP984, respectively. For the TP983 sample a 1.5 μm thick LTG-GaAs layer was grown at 200 °C and annealed at 590 °C for 15 min. In addition to the TP983, the TP984 has a Bragg reflector embedded between the LTG-GaAs layer and the semi-insulating GaAs substrate. The Bragg mirrors were optimized for 850 nm and consist of 20 sequences of $\text{Al}_{0.15}\text{Ga}_{0.85}\text{As}/\text{AlAs}$ alternating layers, each pair of the Bragg reflectors being 60.6 nm, respectively 71.3 nm thick (the total thickness of the Bragg mirror is $\sim 2.6 \mu\text{m}$). Details of growth parameters and layer sequences for each of the substrates used in the current work are presented in the Table 2.1.

2.4.2. Electrical characterization of the LTG-GaAs substrates

The electrical characterization of the LTG-GaAs materials investigated in this work was done by measuring $J - V$ curves under no illumination. The dark $J - V$ characteristics were measured at room temperature on photomixer/photoswitch structures using a Keithley bridge. We manufactured different types of photoconductive switches integrated with two different antenna, in order to meet the requirements of our experiments. A complete overview of the devices processed on the three substrates listed in Table 2.1 is presented in Appendix B. The calculated current density is plotted versus the applied electric field in Figure 2.8 for three different devices, grown on different LTG-GaAs substrates. The contact area for the PC1 emitter grown on the G420 material was around $10 \times 10 \mu\text{m}^2$, and $6 \times 10 \mu\text{m}^2$ for the photomixers CW1 and CW2 grown on TP983/984 materials. The electrode separation was 5 μm for PC1 and only 1 μm for CW1 and CW2. The straight lines are a guide for the eye representing the exponent $n = 1$ and $n = 2$ for the $J \propto E^n$ relation.

³Institut für Festkörperelektronik, Group of Prof. Dr. Strasser.

Substrate	Layers	Thickness (μm)	Al content (%)	T_g ($^{\circ}\text{C}$)	T_a ($^{\circ}\text{C}$)	t_A (min)
G420	LTG-GaAs	2	0	270	600	5
	AlAs	0.1	100			
	SI-GaAs	508	0			
TP983	LTG-GaAs	1.5	0	200	590	15
	AlAs	0.1	100			
	SI-GaAs	500	0			
TP984	LTG-GaAs	1.5	0	200	590	15
	$\text{Al}_{0.15}\text{Ga}_{0.85}\text{As}$ *	0.0712	15			
	AlAs *	0.0606	100			
	SI-GaAs	500	0			
*	repeated 20 times for the Bragg reflectors					

Table 2.1.: Structure and growth parameters for the LTG-GaAs substrates used in the current work.

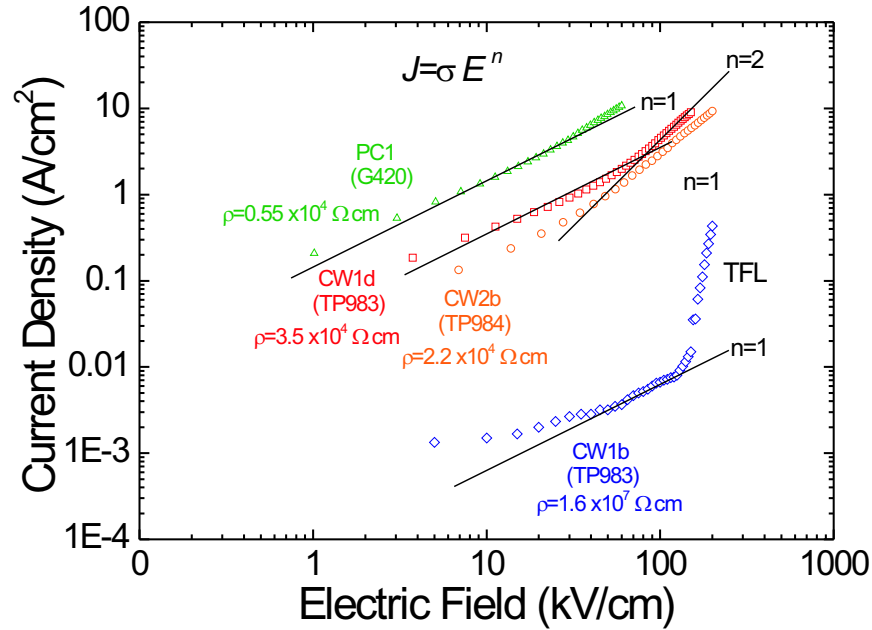


Figure 2.8.: Dark $J - V$ characteristics obtained from photoconductive structures on the LTG-GaAs substrates listed in Table 2.1.

For most of the measured devices, at low applied fields (< 20 kV/cm), the current follows a linear dependence on the applied bias indicating an ohmic transport regime, as frequently reported in literature. In the ohmic region, the electric field inside the structure scales linearly with the applied bias according to $E = \frac{V}{d}$ where d is the distance between the electrodes, whereas in the supralinear region it is only an indication of the electric field applied at the electrodes, since the electric field within the sample is highly non-uniform (due to the probable space-charge effects). Fitting the low bias regime in a linear plot ($n=1$) with Ohm's law $J = \sigma E$, we were able to calculate the conductivity of the substrates. Thus the G420 sample has a conductivity of $1.8 \times 10^{-4} \Omega^{-1} \text{cm}^{-1}$ while the values determined for the TP material are $2.8 \times 10^{-5} \Omega^{-1} \text{cm}^{-1}$ for TP983 and $4.5 \times 10^{-5} \Omega^{-1} \text{cm}^{-1}$ for TP984. For the G420 material the conductivity is one order of magnitude higher than that for the TP983/984 material, in agreement with the reported growth temperature variation. However, the calculated resistivity of the TP984 material is $\rho = 2.2 \times 10^4 \Omega \text{cm}$, being at least one order of magnitude lower than the values reported in the literature, usually $\sim 10^6 \Omega \text{cm}$ at $T_a = 600^\circ \text{C}$. Around 20 kV/cm the structure grown on TP983 shows a slight tendency towards saturation while TP984 displays a strong deviation from ohmic transport, following an almost quadratic dependence ($n = 2$) on the applied bias, suggesting the presence of space-charge-limited (SCL) transport

in the TP983/984 structures. At the same applied field, the structure grown on the G420 material, exhibits almost one order of magnitude higher current density, due to the probable increase in carrier mobility with the growth temperature. The onset of SCLC regime for the G420 sample could be shifted to higher current densities due to the lower density of traps and the implicit higher mobility resulting from the higher growth temperatures. For all characteristics, the departure from the square law can be due to the non-linearity in the velocity-field relation $v \simeq \mu E$. In our case, the features of the $J - V$ curves differ quite substantially from those reported in Ref.s[81, 88]. An important characteristic of the SCL transport in a material with a high density of deep traps, as for the case of LTG-GaAs here, is the presence of the trap-filling process. If one considers a deep donor trap level of density N_d (As_{Ga}), located slightly below the Fermi level (pinned) due to the partial compensation by an acceptor N_a (V_{Ga} in our case), than only a fraction of the electrons (n_0) end up in the conduction band (with many of the electrons filling acceptor states), such that $N_{d0}^+ = n_0 + N_a$. Hence, when the system is at equilibrium, n_0 is very small, and the number of donor states is much larger than the number of electrons in the conduction band ($N_{d0}^+ \gg n_0$). Defining $\gamma = \frac{N_{d0}^+}{n_0} = 1 + \frac{N_a}{n_0}$, it can be seen that γ^{-1} is the fraction of ionized donors which end up in the conduction band, being strongly influenced by the density of acceptor states. When a bias is applied, the injected charge increases the concentration of both mobile and trapped charge. The carrier transport is ohmic until the injected mobile charge density $n_{f,inj} = n_0$, equivalent to E_F moving upwards in the band gap with an amount $0.7 kT$, resulting in all the donor states that were empty at equilibrium N_{d0}^+ to be filled. The total injected trapped charge will be $n_{t,inj} = N_{d0}^+$ and the average space-charge in the material is given by $n_{inj} = n_{t,inj} + n_{f,inj} = N_{d0}^+ + n_0 \simeq N_{d0}^+$. The voltage supported by this charge, according to the capacitance $C = \frac{2\epsilon}{L}$, is named *trap-filled limit* (TFL) voltage, given by:

$$V_{TFL} = \frac{eN_{d0}^+L^2}{2\epsilon} = \frac{en_0L^2}{\epsilon} \left(\frac{\gamma}{2} \right). \quad (2.8)$$

If the bias is increased beyond this limit, since the traps are already filled, the electrons must appear in the conduction band, so that the current increases at a very high rate (usually mistaken for an electrical breakdown). While for SI GaAs, where a density of defects around $10^{15} - 10^{16} \text{cm}^{-3}$ makes it visible at moderate voltages [97], the trap-filling limit was never reported in the case of LTG-GaAs. The characteristic measured for the CW1b (TP983) device in Figure 2.8, shows a steep increase of the dark-current somewhat similar to the signature of the trap-filling limit. This behavior is in strong contrast to the sample CW1d. Although certainly peculiar, since two identical devices grown on the same substrate must exhibit the same characteristics, we were able to reproduce the $J - V$ curve for both devices, that is, the voltage breakdown mechanism for CW1b is excluded. For the present

case, a simple estimation of the V_{TFL} for a trap density of 10^{18} cm^{-3} yields a value of $\sim 1.4 \text{ kV}$ - rendering the above assumption highly improbable. On the other hand it is known that in practice, the value of V_{TFL} depends strongly on the behavior at the interfaces, for example, due to the presence of a thick oxide layer on LTG-GaAs material [90].

2.4.3. Optical characterization of the LTG-GaAs material

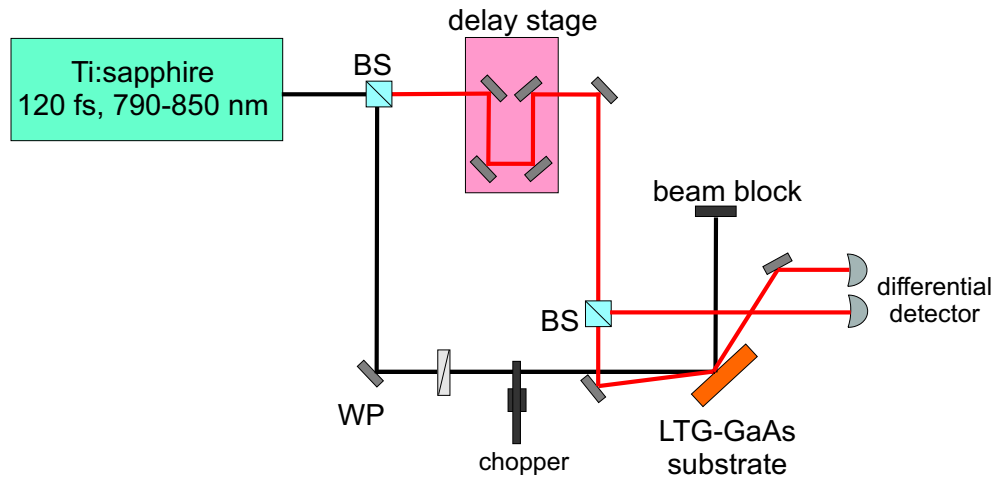


Figure 2.9.: Schematic of the experimental setup used for optical pump-and-probe transient reflectivity measurements.

Time-resolved reflectivity measurements were performed in order to determine the carrier trapping time for the LTG-GaAs materials. The experimental setup is schematically drawn in Figure 2.9. The laser system used was a mode-locked Ti:sapphire laser which was operated in the range 790 -850 nm. Typical pulse widths of 120 fs were delivered at a repetition rate of about 82 MHz. A beam-splitter (BS) divides the output laser beam into the pump and probe components, which are orthogonally polarized using a $\lambda/2$ wave-plate (WP) in order to minimize interference effects. A variable time delay is introduced between the pump and probe pulses with a computer controlled Newport delay stage. The pump beam was chopped at around 1 kHz while the probe beam was split in two components, one component being used as a reference while the other one was overlapped with the pump beam on the sample's surface. Both components of the probe beam were then focused on a calibrated differential detector (using two silicon photodiodes). The signal from the differential detector was fed to a lock-in amplifier which was locked to the chopping frequency. The pump beam power of around 30 mW for the G420 material and 50 mW for the TP983 was focused down to $\sim 40 \mu\text{m}$, generating a density of electron-hole pairs of 1.4, respectively $2.3 \times 10^{18} \text{ cm}^{-3}$.

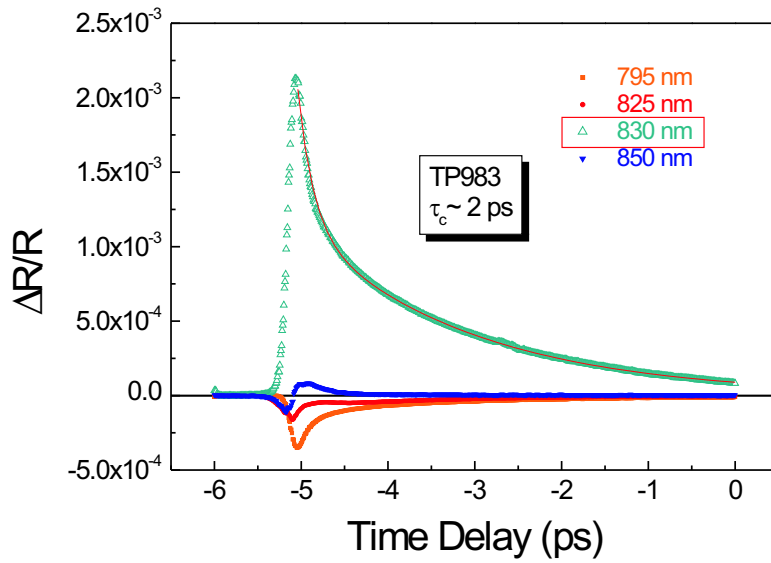


Figure 2.10.: Transient reflectivity signals measured at different wavelengths for the TP983 sample grown at University of Erlangen.

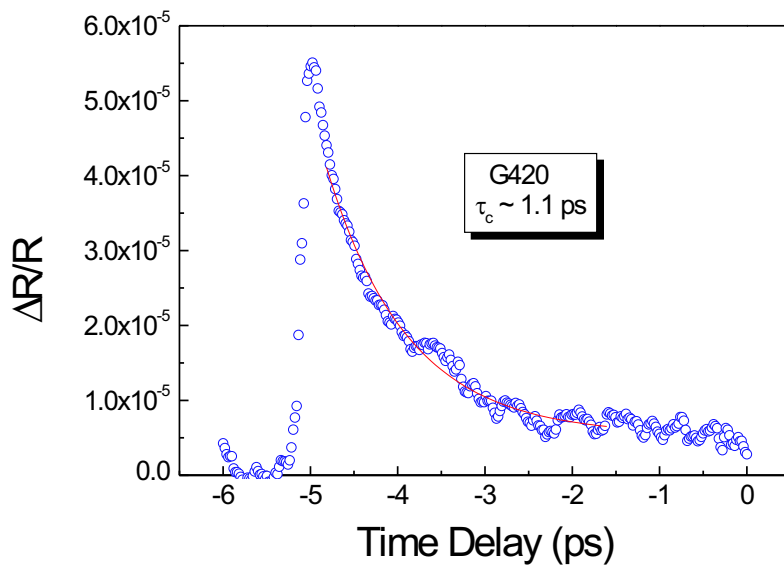


Figure 2.11.: Transient reflectivity signal for the G420 sample grown at University of Vienna.

Figure 2.10 shows the normalized transient reflectivity data for the TP983 sample grown at the University of Erlangen. One can see that, when changing the pump beam wavelength the sign of the reflectance changes as well, except for the signal measured at 830 nm. We interpret the change in the sign of the relative reflectivity as being an indication of several competing processes taking place in the sample, like band-filling, bandgap renormalization and free carrier absorption. Also, the magnitude of the reflectance change is more than two orders of magnitude higher than what is usually reported in the literature for good quality LTG material, typically in the order of 1×10^{-4} . All of this points to a non-optimal LTG-GaAs material. A double exponential fit yields two time constants, $\tau_1=0.2$ ps and $\tau_2=2$ ps; since we excited carriers with 830 nm, the photogenerated carriers possess an excess energy of around 80 meV with respect to the bandgap. Therefore, we assign the fast time decay as being related to intraband carrier dynamics, that is, relaxation of the carriers to the bottom of the conduction band (thermalisation). The second decay time can be interpreted to a good approximation as being the decay of the concentration of free electrons, that is, the carrier trapping time (τ_c). It was suggested by Ortiz et al. [98], that the presence of negative transients and sign changes as observed for the trace measured at 850 nm can be related to the existence of a high number of acceptors (V_{Ga} defects in the present case), that is, a slowly decaying hole population. As for the case reported there, the large concentration of V_{Ga} defects in our case could be due to the long annealing time (15 min).

Even if grown at higher temperatures, the G420 material seems to be of superior quality exhibiting a change of reflectivity of only 5×10^{-5} : a value very close to that reported in literature [63]. For the trace shown in Figure 2.11 an excitation wavelength of around 850 nm was used. Ignoring the first ultrafast decay due to the carrier thermalisation process, when fitted with a single exponential, the decay time which is believed to correspond to the electron trapping time amounts to 1.1 ± 0.1 ps.

3. Continuous wave THz generation by photomixing in LTG GaAs

In this chapter we deal with the theoretical as well as experimental aspects of continuous-wave (CW) THz generation in LTG-GaAs-based photomixers. At the outset we give an introduction of the physics underlying the photomixing process. Most of the work on the experimental setup presented in Section 3.2 represents the solution to our search for a compact, fast and reliable way to characterize the THz emission characteristics of photomixers - the probe station. Besides calibrated detectors for absolute power measurements, one of the most important features of the CW-THz setup we implemented, is the possibility to record the emitted THz power and the DC photocurrent simultaneously, as a function of the applied bias. As it will be shown here, this option facilitated us to gain some meaningful insight into the carrier transport properties of LTG-GaAs under high electrical fields, as presented in Section 3.5.

3.1. Fundamentals of photomixing

Photomixing can be very generally defined as the optical heterodyne down-conversion of two laser beams with detuned frequencies (here in the THz range). The “photoconductive mixer” or photomixer consists therefore of a current source, able to deliver a current modulated at high frequencies, connected to a planar distributed circuit such as a planar antenna or a coplanar waveguide. The active element, i.e. the photoconductive switch (sometimes erroneously called “photomixer” by some authors) is essentially a photoconductor. The photoconductance of the switch is modulated by the optical beating of the two cw laser sources (each assumed to be single mode), producing a THz current which when feed into a planar antenna generates electromagnetic radiation in the THz frequency range. The advantages and novelty introduced by the usage of LTG-GaAs as the photoconductive material resides in the extremely short carrier trapping time (suitable for modulation of the photocurrent at very high frequencies) and also the high dark resistivity and the relatively high mobility.

If two laser lines, oscillating at the frequencies ν_1 and ν_2 have a small frequency off-set with respect to each other, they can generate an optical beat if spatially overlapped, as shown in Figure 3.1. The superimposed optical fields of the two

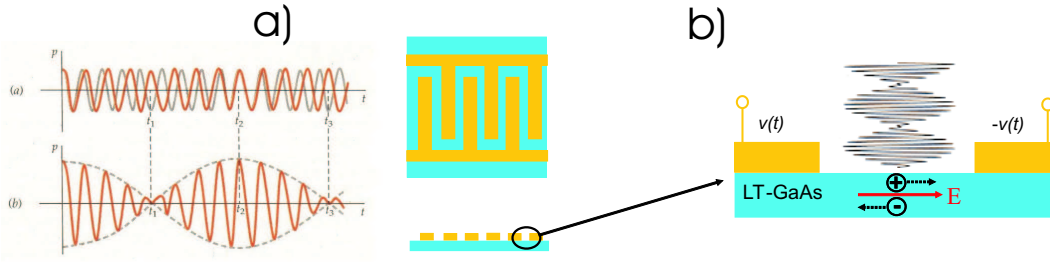


Figure 3.1.: Photomixing principles: a) the optical beats produced by two slightly detuned optical beams and b) interdigitated electrode geometry of the active element of a photomixer together with a cross-sectional view.

beams produce an instantaneous field:

$$E(t) = E_1 \cos(2\pi\nu_1 t) + E_1 \cos(2\pi\nu_2 t). \quad (3.1)$$

With the optical intensity defined as $I_{opt}(t) = E^2(t)$, and the optical power proportional to the intensity, the instantaneous optical power incident on the photomixer can be written:

$$P(t) = P_1 + P_2 + 2\sqrt{mP_1P_2} [\cos 2\pi(\nu_1 - \nu_2)t + \cos 2\pi(\nu_1 + \nu_2)t], \quad (3.2)$$

where P_1 and P_2 are the average power level of the two laser beams and m is the mixing efficiency that ranges from 0 to 1 depending on the spatial overlap of the beams and relative polarization (if, for instance the overlapped beams have perpendicular polarization than the mixing efficiency is 0).

The current source is usually a photoconductor, consisting either of a simple photogap (two planar electrodes) or a set of metallic electrodes (interdigitated fingers) as depicted in Figure 3.1 b), deposited on the top of a highly photoconductive material, LTG GaAs in the present case. Such structures are usually referred to as metal/semiconductor/metal (MSM) junctions, being widely employed as fast photodetectors when deposited on doped GaAs [99], forming Schottky contacts.

In a photoconductor the electrons and holes that are generated through the internal photoelectric effect (absorption of a photon with energy equal or greater than the bandgap of the photoconductive material) separate in the external field created by applying a bias voltage between the electrodes, producing a current flow in the external circuit. Here, one assumes that due to the relatively high number of photogenerated carriers the band-bending at the MSM junction is relatively small and the whole process is photoconductive rather than photovoltaic. In the following, for simplification purposes, one assumes that only electrons are contributing to the photocurrent flowing in the contacts. To maximize the optical coupling, the size of the active element should match that of the focused laser spot. The instantaneous

photoconductance $G(t)$ can be related to the density of excess carriers produced by incident light $N(t)$:

$$G(t) = eN(t)\mu, \quad (3.3)$$

where e is the electron charge and μ is the carrier mobility. Several assumptions have been made here. First, an ohmic transport regime of the photogenerated carriers was assumed, second, the drift velocity has a linear dependence on the applied bias. On the other hand, $N(t)$ could also be assumed as the instantaneous photocarrier *pair* density in case one does not discard the hole contribution to the photocurrent. Details of the photocurrent response to the CW illumination will be discussed in Section 3.5.

The photogenerated carrier density is found by solving the current continuity equation:

$$\frac{dN(t)}{dt} = \frac{\eta P_{opt}(t)}{h\nu} - \frac{N(t)}{\tau_e}, \quad (3.4)$$

where $h\nu$ is the photon energy, η is the total quantum efficiency (to be discussed in detail later) and τ_e is the free-carrier (mobility) lifetime. Substituting the solution of Eq. 3.4 in 3.3 yields the time-dependent photoconductance:

$$G(t) = G_0 \left(1 + \frac{2\sqrt{mP_1P_2} \sin(2\pi\nu_{THz}t + \phi)}{P_0\sqrt{1 + (\omega\tau_e)^2}} \right), \quad (3.5)$$

where G_0 is the time averaged photoconductance corresponding to the total incident power $P_0 = P_1 + P_2$ and $\phi = \tan^{-1}\left(\frac{1}{\omega\tau_e}\right)$ is the phase shift depending on the carrier lifetime and $\nu_{THz} = \nu_1 - \nu_2$ (where $\nu_{THz} = \frac{\omega}{2\pi}$). Looking back at Eq. 3.2 one can see that is the first cosine term that is responsible for modulation of the photoconductance, while the second term, approximately twice as the optical frequency, varies on a time scale much shorter than the free-carrier lifetime τ_e and thus does not modulate the photoconductance significantly.

As a general remark it is worthwhile mentioning that the quadratic dependence of the generation rate, hence of the photogenerated carriers density on the optical electric field is what makes the ultra-fast photoconductors “self-rectifying”. Thus, in response to a mode-locked laser, the photocarrier density can be computed in terms of the “envelope” of the optical pulse rather than the instantaneous electric field. Also, as already seen in response to two frequency-offset CW lasers, the photocarrier density shows a time-varying term at the difference frequency, the same effect as in microwave mixers in which the current has a *quadratic* dependence on voltage.

The equivalent circuit of a photomixer, as presented in Figure 3.2, consists of a time-varying photoconductance $G(t)$ depending on the driving optical power. One could also consider a resistance due to the contacts, connected in series but this

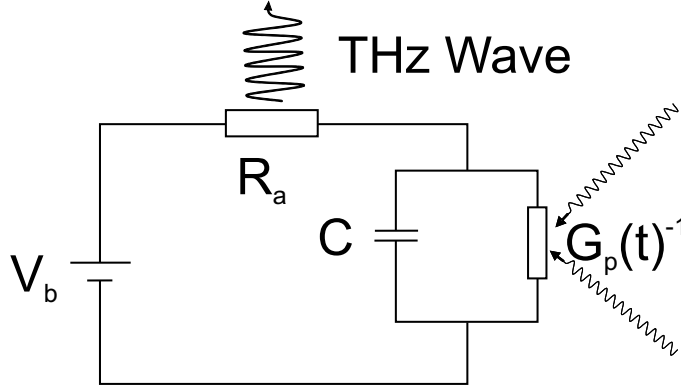


Figure 3.2.: Equivalent circuit of a lumped-element photomixer.

is usually very low and therefore discarded here¹. The conductance is in parallel with a capacitance C due to the electrodes, being also a function of the dielectric constant of the photoconductive material. The antenna is represented by a radiating resistance R_a , the whole circuit being biased with a DC bias voltage V_b . In order to calculate the radiated power one must first determine the time-varying voltage across the photogap $V(t)$. According to Kirchoff's circuital law, the current which is flowing across the antenna resistance can be expressed as:

$$i(t) = C \frac{dV(t)}{dt} + G(t)V(t) = \frac{V_b - V(t)}{R_a}. \quad (3.6)$$

This equation which cannot be solved in a closed form. An approximate solution is found if $V(t)$ is assumed to be of a harmonic form and neglecting the phase shift in the photoconductance. The radiated THz power is given by:

$$P_{THz}(\omega) = \frac{\frac{1}{2} (V_b G_0 \beta)^2 R_a [(1 + G_0 R_a)^2 + (\omega R_a C)^2]}{(1 + G_0 R_a)^2 [(1 + G_0 R_a)^2 + (\omega R_a C)^2 - \frac{1}{2} (G_0 R_a \beta)^2]}, \quad (3.7)$$

with $\beta = \frac{2\sqrt{mP_1P_2}}{P_0\sqrt{1+(\omega\tau_e)^2}}$. Using the small-signal theory, applicable for the limit $G_0 R_a \ll 1$, the above equation reduces to [100, 101]:

$$P_{THz}(\omega) = \frac{\frac{1}{2} I_{DC}^2 R_a}{[1 + (\omega\tau_e)^2] [1 + (\omega R_a C)^2]}, \quad (3.8)$$

where $I_{DC} = G_0 V_b$ is the DC photocurrent. Based on Eq. 3.8, one can obtain a fairly good prediction of the emitted THz power as well as of the main features concerning the efficiency of the THz photomixers. For example, it is obvious from the above expression that the radiated THz power depends strongly on the antenna resistance R_a , following a quadratic dependence on the applied bias V_b and the optical driving power (through the quadratic dependence on the DC conductance

¹The series resistance R_S can be neglected here as long as $G_0 R_S \ll 1$ and $R_L/R_S \ll 1$.

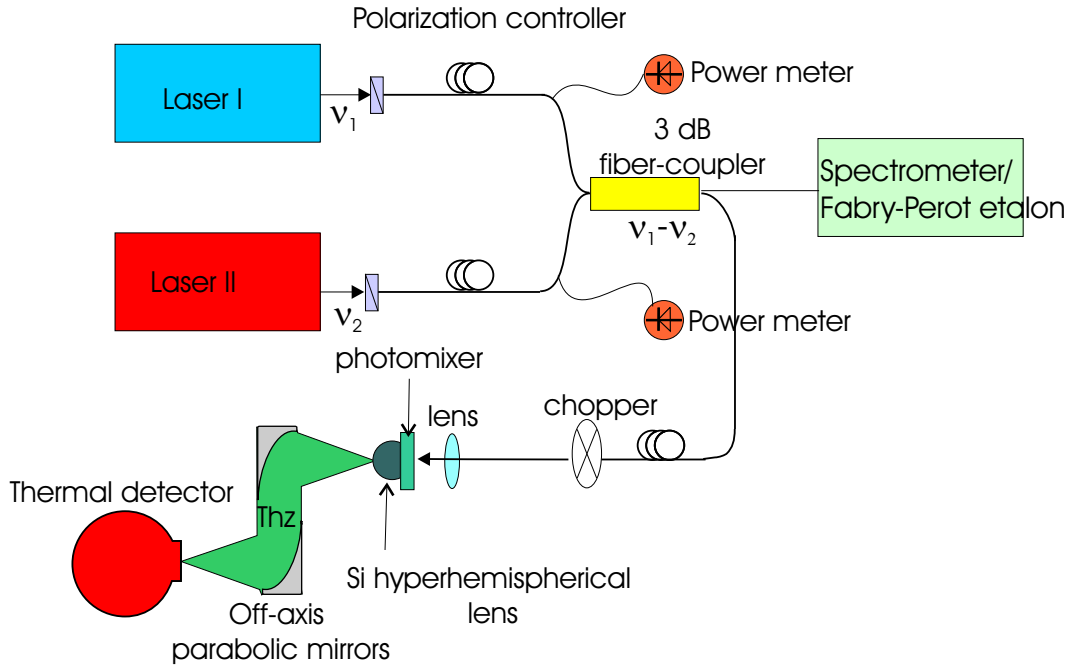


Figure 3.3.: Experimental setup for the generation and detection of CW THz radiation.

G_0 , which, for moderate optical power levels scales linearly with the incident optical power). For a broad-band antenna (i.e., where R_a is frequency independent), the spectral bandwidth of the photomixer is limited by the free-carrier lifetime τ_e and the RC time constant of the device, each contributing a 6 dB/octave roll-off in the frequency spectrum in the limiting case $\omega\tau_e \gg 1$, respectively $\omega R_a C \gg 1$.

3.2. Experimental setup for generation and detection of CW THz

For the measurements presented within the current chapter, a typical experimental system for generation and detection of coherent CW THz radiation was implemented as schematically depicted in Figure 3.3. Such a system usually has the following subsystems:

- a **laser system** containing two single-mode lasers or a single laser operating in two-color mode². The most frequently used systems are based on either solid-state Ti:Sapphire lasers or external-cavity diode lasers (ECDL). There are also other approaches like those described in Ref. [102]. The laser system used for the measurements presented in this work will be described in greater

²In this case, the laser output beam contains two modes (lines) with a very small separation between them.

detail in the following.

- a **beam combining system**, which could be just a non-polarizing beam splitter or an optical fiber network, as depicted in Figure 3.3. The linearly polarized output from each laser is delivered to the fiber network using a fiber coupler which contains a convex lens for focusing the divergent laser beam into the single-mode fiber (which has a core diameter of $\sim 5 \mu\text{m}$). An efficient coupling necessitates a good alignment of the beam to the coupler. Each input and output arm of the fiber network is passed through a polarization controller aimed to match the E-fields for maximum interference. The introduction of the polarization controllers is meant to counteract the polarization distortions that occur along the optical fiber. The input arms contain also an optical power meter (i.e., a calibrated photodiode with a linear response within the optical power range of interest). The photodiode was calibrated against a Newport power meter and its output connected to an electronic display. Due to the high sensitivity only 1 % of the input power is necessary as input for the photodiode. A small amount of light is also coupled to a Fabry-Perot etalon for checking the single mode output of each laser and to a spectrometer for reading the laser output wavelength and to check for mode-hopping and continuous tunability. The output of the CCD camera of the spectrometer is connected to a computer such that by reading the two laser wavelengths, the THz frequency is computed and displayed automatically, according to the formula:

$$\nu_{THz} \cong \frac{c}{\lambda^2} |\lambda_1 - \lambda_2|. \quad (3.9)$$

The advantage of the fiber network over the free-space beam overlapping resides in the easy-to-align configuration, an almost 100 % modulation depth (checked by visualizing the output of a fast photodiode on an oscilloscope when the two laser beams were detuned by only a couple of MHz), and compactness³ Also, the fiber beam combining is insensitive to misalignments and dust. Last but not least, combining the beams in the fiber network confers a high degree of mobility as well as flexibility since one could very easily switch between different applications⁴. After combining, the THz modulated output beam is transformed back into free space and focused on the photomixer's active region using a short focal length achromat lens (f=15 mm, producing an estimated spot size in the focus $\sim 7 \mu\text{m}$) or a microscope objective.

³For a reliable and therefore efficient overlapping of the laser beams in free-space one necessitates two apertures with a distance between them of at least 2 meters.

⁴The fourth output arm (not shown here) made it possible to run a CW electro-optical or a photoconductive detection system almost in parallel with the standard system based on a square-law detector.

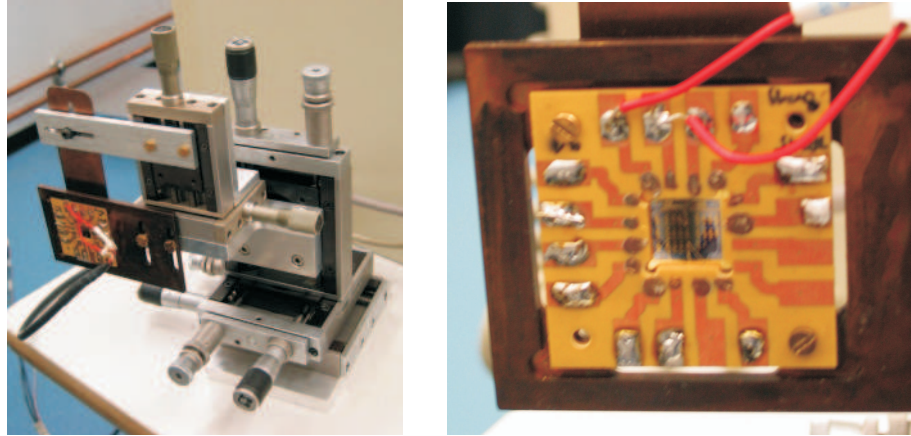


Figure 3.4.: A standard photomixer mount based on a x-y-z translation stage (left) together with a pertinax plate onto which the chip with the photomixers is attached (right).

- a **photomixer mount**, which also includes the biasing scheme. In an early stage of our photomixer characterization work we used a classical x-y-z translation-stage-based mount, as depicted in Figure 3.4. The chip containing the photomixers to be investigated were attached to a pertinax plate. The voltage was applied to the photomixer by wire-bonding each device and attaching the gold wires to the cooper pads on the pertinax plate using silver paste. The active pads (devices) were soldered to an coaxial cable which was then connected to an external circuit containing a voltage source (Keithley) and a nanoamp-resolution ammeter, connected in series. The voltage source and the ammeter were linked to a computer via GPIB connection that enabled the automatic recording of the DC dark-current/photocurrent versus the applied bias.
- the **THz optics** which collects the THz radiation and delivers it to the detection system. Due to the large difference in the dielectric constant, most of the THz radiation is emitted into the SI GaAs substrate. In order to couple the radiation out of the substrate, a high-resistivity silicon hemi-spherical lens is used [103]. The radiation coupled to free space is then guided to the detector's input aperture using a 90° off-axis parabolic mirror (one or two, depending on the detection system used). The silicon lens design impact on collection efficiency will be discussed at some length in this section.

The silicon lens mount which enabled a precise alignment to the device under test (DUT) was integrated into the photomixer mount. It should be emphasized that for each photomixer to be investigated, a very tedious alignment procedure was employed. Moreover, switching to another device caused

a breakdown in the alignment, rendering the entire photomixer characterization process into a very strenuous and time-consuming procedure. The large throughput of samples forced us into designing a stable and compact *Probe Station* which combines the end part of the fiber network with a sample holder system which was permanently aligned to the THz beam path. Details are to follow in Subsection 3.2.2.

- a **detection system** including usually a thermal detector (a square-law detector) due to the direct interest in the absolute values of the emitted THz power. The principal detectors used here were a Golay cell and a magnetic-field enhanced He-cooled InSb bolometer (both commercially available at QMC Instruments⁵). The characteristics of the two detectors will be discussed at some length later. To enable lock-in detection of the difference frequency, an optical chopper (set at a modulation frequency of ~ 1 kHz) was inserted in the output laser beam, right before this was delivered to the photomixer. The reading of the lock-in amplifier was again connected to a computer which converted the measured voltage into effective THz power units, according to the system optical response (SOR) of the detector in use. The linkage of the biasing scheme with the photocurrent and power reading facilitated the acquisition of precious information on the emission characteristics of the photomixers since the DC photocurrent can be recorded simultaneously with the emitted THz power.

3.2.1. Laser system

The first photomixing experiments, as well as the THz pulsed experiment with CW background (described in the next chapters) were performed using two in-house built Ti:Sapphire lasers, as shown in Figure 3.5. The use of two independent ring-shaped laser cavities [104] was the outcome of an extensive search for a laser system that meets all the requirements of CW THz generation: enough power at a single frequency (that is, single mode operation), continuous tunability, and mode-stability (avoiding mode-hopping). The ring cavity was preferred over the linear (Z-shaped) one because, as opposed to the linear (Fabry-Perot) cavity where a standing wave is formed, in a ring cavity there are two traveling waves circulating in opposite directions. Therefore, in a ring cavity, the spatial hole-burning effect [105] taking place in the gain medium (Ti:Sapphire crystal) responsible for multi-mode operation is prevented. As can be seen in Figure 3.5, the system was pumped by a 5.5 W Verdi V-5 system (manufactured by Coherent Inc.) which delivers single-mode radiation at 532 nm. The Brewster-angle-cut surface of the crystal was oriented such that the pump beam was collinear with the laser beam.

⁵QMC Instruments is based within the Physics Department of Cardiff University.

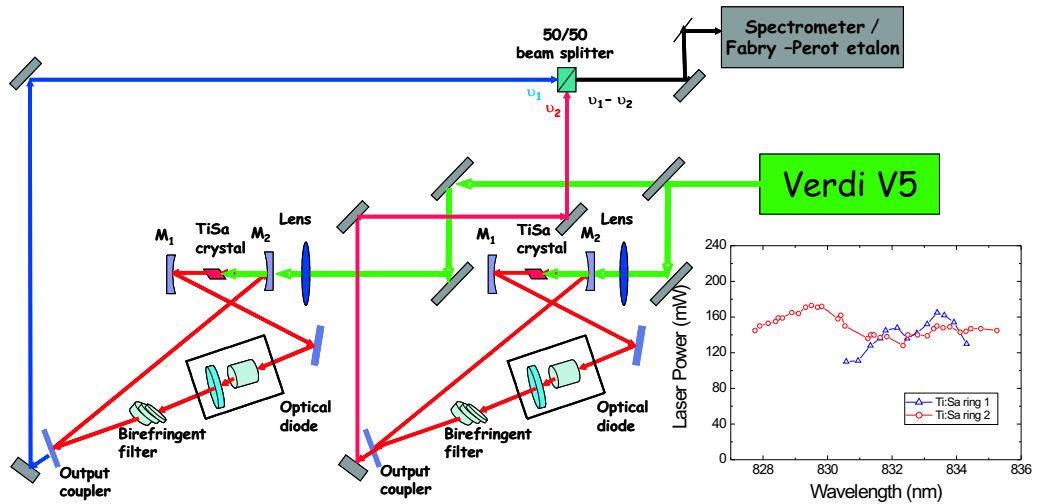


Figure 3.5.: In-house built continuously tunable single mode Ti:Sapphire ring laser system.

A careful alignment of the Ti:Sapphire crystal was necessary in order to avoid birefringence interplay effects between the different components of the laser cavity. For example, the c -axis of the crystal was aligned in the plane of incidence, while the crystal's surface was maintained perpendicular to the plane of incidence such that the polarization of the laser beam inside the cavity is in the same plane with the c -axis of the crystal. In order to enforce uni-directional operation with only one beam circulating in a cavity, we introduced a *non-reciprocal optical diode* consisting of a Faraday polarization rotator and a $\lambda/2$ plate. For bandwidth control and wavelength tuning, a 3-plate Lyot filter was used. It consists of a three quartz plates placed in the beam at Brewster's angle, with a thickness ratio of 1:4:16, the thinnest plate having a thickness of 0.013 in. To provide continuous tunability, a very tedious procedure was developed [106]. The system was able to deliver an average of ~ 150 mW output power per color around 830 nm, as showed in the inset of Figure 3.5. For certain wavelength ranges, the cavity could be tuned in steps of 0.1 nm (corresponding to ~ 25 GHz steps), the accessible frequency difference spanning from 50 GHz to 30 THz, while when checked with a Fabry-Perot etalon it displayed single-mode operation. The linewidth, imposed by the thinnest Lyot filter plate was estimated to be > 100 MHz. However, the system could not fully meet the requirements on stability: very sensitive to air and temperature fluctuations, while necessitating continuous maintenance and re-adjusting of the laser cavities, with skips and gaps in the tuning range and last but not least an insufficient tuning range which ended around 830 nm. Ultimately, the system had to be replaced by a diode laser system, as depicted in Figure 3.6.

The custom-made system, purchased and implemented from Sacher Laser (Mar-

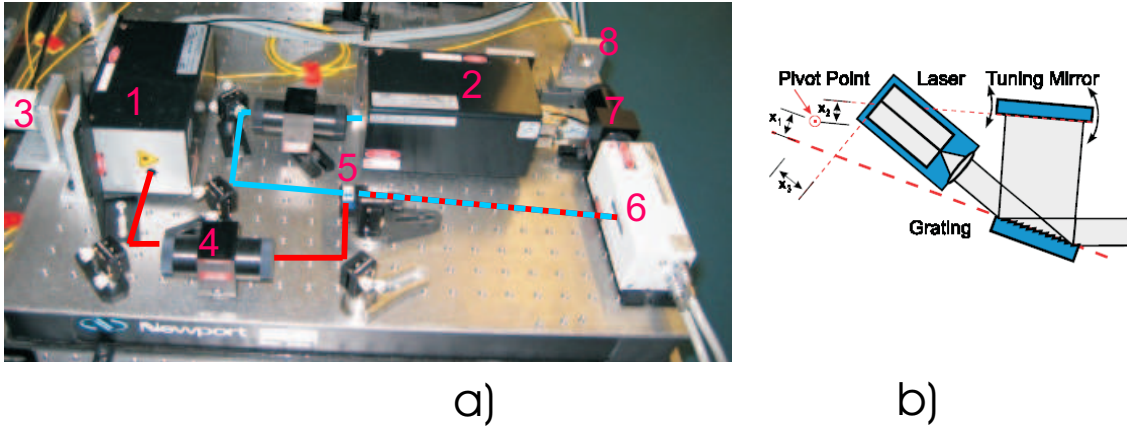


Figure 3.6.: ECDL system: (1) Diode Laser I, (2) Diode Laser II, (3) piezoelectric motor, (4,7) Fabry-Perot isolator, (5) polarizing beam splitter cube, (6) tapered amplifier, 8- Fiber coupler.

burg, Germany) consists of two external cavity diode lasers (TEC 500) in a Littman/Metcalf configuration, delivering each a 20 mW single-mode laser beam which is then combined with a polarizing beam-splitter cube and fed into a tapered amplifier. The output beam of each laser is passed through an optical (Faraday) isolator which prevents feed-back into the laser cavities. The result is a stable, narrow linewidth (< 5 MHz) laser system, best suited for CW THz generation.

Output power	> 500 mW @ 850 nm
Center wavelength	850 nm
Linewidth (20 s)	< 5 MHz
Beam Divergence	< 2 mrad
Beam quality M_2	< 1.7
Fine tuning / Mode- hop free	250 GHz / 30 GHz ..100 GHz
Polarization	Linearly $> 1000:1$

Table 3.1.: The key parameters of the Sacher diode laser system.

The external cavity of each laser is defined by a reflecting element (mirror or prism) and a diffraction grating, as can be seen in Figure 3.6 b). The zeroth diffraction order serves as the output beam, while the wavelength selectivity of the grating forces the laser to oscillate in one single longitudinal mode. Wavelength tuning is realized by a simultaneous translation and rotation of the reflective element, either by tuning the adjustment screw of the laser or electrically, with a low-voltage piezo-actuator. One of the cavities possesses a computer controlled dc servo-motor, thus enabling fully automatic frequency scans. The system is continuously tunable with an operation wavelength centered around 850 nm, having a large coarse-tuning

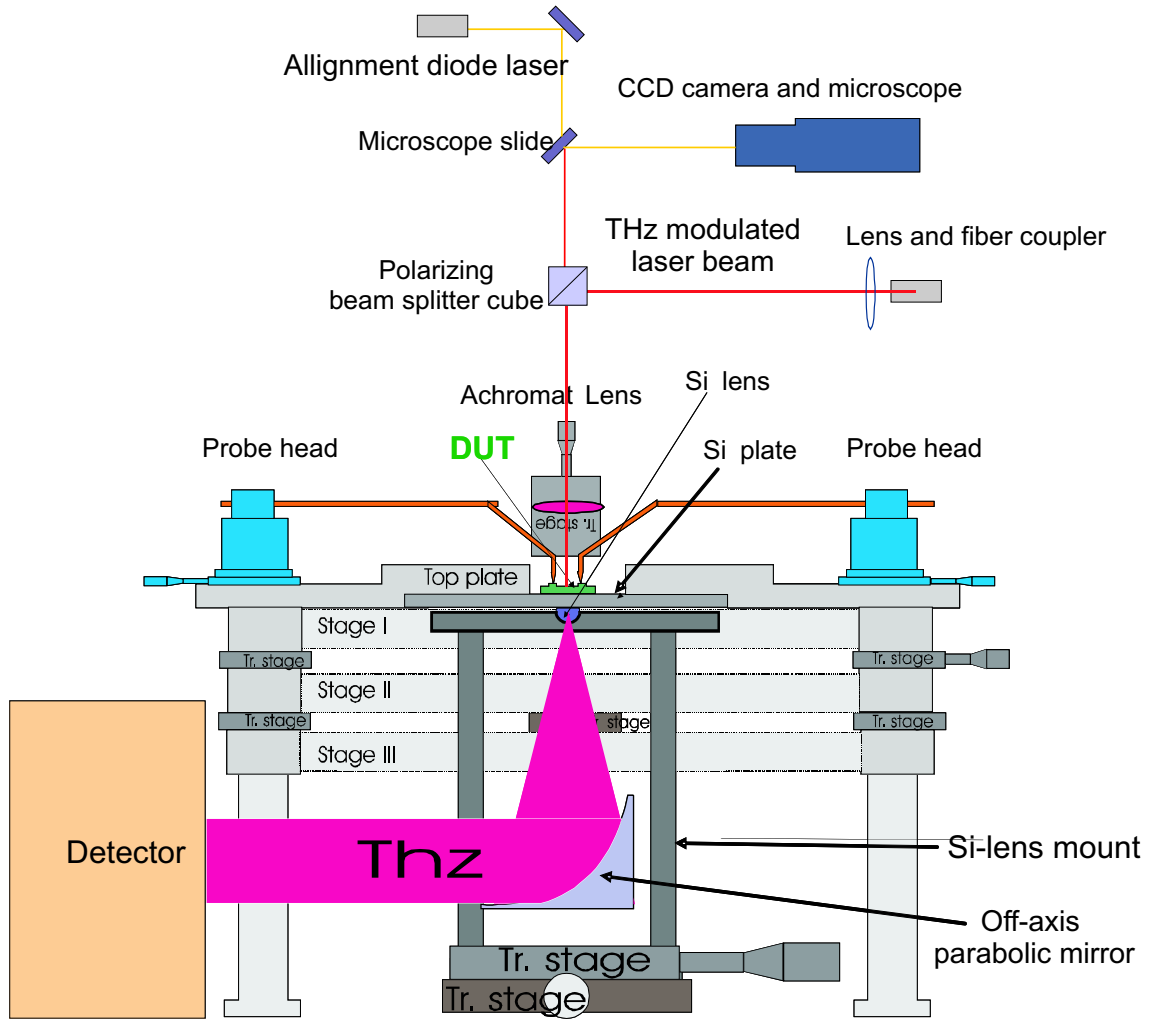


Figure 3.7.: Schematic of the in-house designed and built probe station.

range ($10 < \Delta\lambda < 90$ nm) together with a large mode-hop-free piezoelectric fine tuning range ($0.1 \text{ nm} < \Delta\lambda < 0.8$ nm). The key specifications of the system are listed in Table 3.1.

3.2.2. Probe station

As already mentioned, an in-house designed and built probe station was implemented. A sketch of it is shown in Figure 3.7. The guiding principle in the designing process was a fast and reliable characterization of photomixers. It consists of three main parts:

- The top part contains the VIS/NIR optics; here, the output from the laser system is delivered through a fiber coupler. The divergence of the fiber output is compensated with a short focal length convex lens and the beam is passed through a polarizing beam-splitter being then focused with an aspheric lens on the active area of the photomixer. The focusing lens is mounted on a rail that

can be moved in the z-direction (vertical) coarsely with a mechanical actuator or in very small steps (sub-micron) with an electrically-driven piezo-actuator. Due to the very small size of the active area, the device is very sensitive to the precise focusing of the laser beam. The top part also contains a system conceived to enable the visualization of the photomixer structure on a monitor, its main purpose being to ease the alignment of the laser beam onto the active area of the photomixer. It consists of a CCD camera, a microscope (2 lenses of very short focal length), a microscope-slide and is also sharing the aspheric lens used to focus the two-color laser beam. Additionally, a small-power diode laser was attached to the system, for illuminating the sample, serving also as rough guidance in the alignment procedure. The strong magnification and the relatively high resolution of the photomixer image on the control monitor helps in identifying possible damage of the metalization.

- The second part is the probe table, on the top of which a high resistivity (THz transparent) silicon wafer is mounted for sustaining the DUT. For ensuring mechanical stability, two massive steel-made plates are sliding parallel to each other in the x and y-direction. They can be moved in large steps using mechanical actuators, as well as in very fine steps with the help of electrically-driven piezo-actuators. This part comprises also the electrical contacting part which is made using two probe heads (Karl Suss) fixed with magnetic posts on the upper plate. Hence, the DUT can be aligned in the laser beam while the electrical contacts remain in position.
- The last part contains the THz beam path. A hemi-spherical Si lens is placed underneath the Si wafer (the non-polished side), making intimate contact with the wafer by applying silicon (vacuum) grease. The Si lens is mounted on a holder which can operate independently of the probe table, such that Si lens can slide along the x and y-directions, against the backside of the Si wafer. The way the Si lens is mounted ensures a match of the VIS/NIR beam focus with that of the THz beam such that an optimal THz beam path is realized when the active element of the photomixer is placed in the focus of the VIS/NIR beam. Underneath the silicon lens, a 2-inch 90° off-axis parabolic lens fixed on a x-y translation stage collects the THz radiation which is then focused on the Golay-Cell using a second parabolic mirror.

Alignment procedure: The probe stage was conceived such that the alignment of the VIS/NIR and THz beam is done only once, before getting the station in operation. Therefore, a reliable characterization and comparison of photomixer's performance is achieved. Before starting the alignment procedure, the Si wafer, the Si lens as well as the optical lens holder should be removed due the quasi-optical

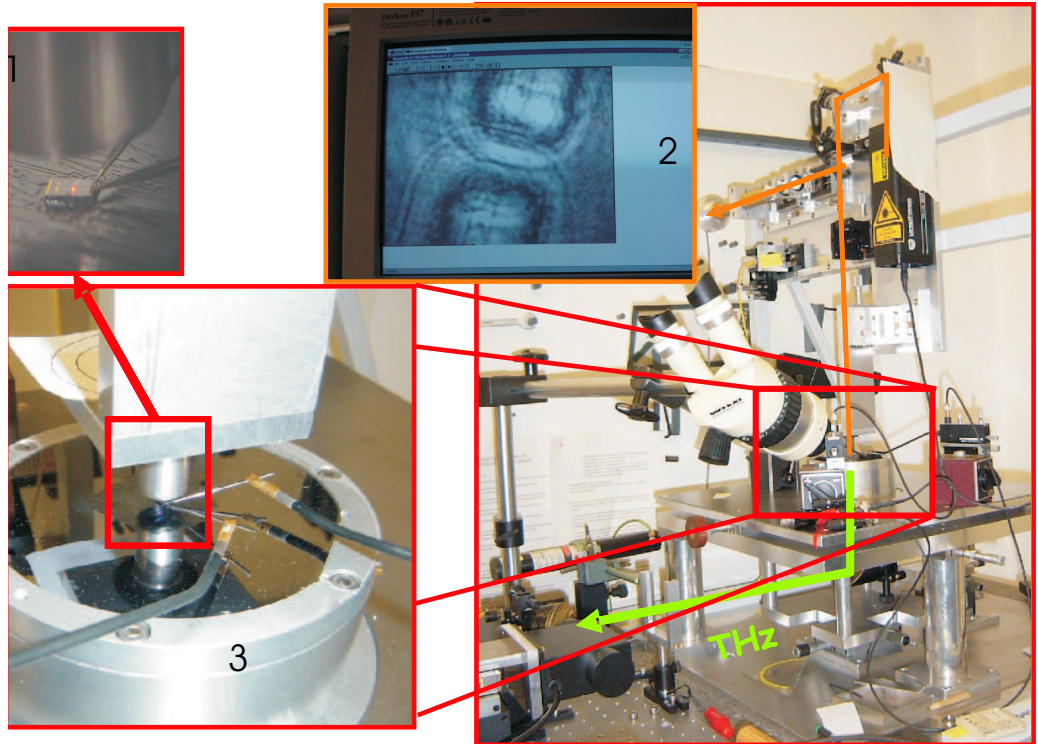


Figure 3.8.: Pictures of the probe station. The close-ups show: (1) an image of the chip with photomixers (2) an image of the photogap ($5 \times 10 \mu\text{m}$) as visualized on the control monitor; and (3) the silicon wafer together with the probe-needles.

alignment procedure involved (that is, VIS/NIR radiation is used in aligning the THz beam path for which Si is opaque).

◆ The VIS/NIR laser beam (around 850 nm) is aligned parallel with the arm of the lens holder, perpendicular to the optical/probe table. If one positions an iris right after the collimating lens, the alignment can be easily done by placing a metal mirror on the table surface and tracing back the reflection such that it is centered on the iris' aperture. In the same time, by moving the orientation of the microscope slide, one should obtain a clear reflection of the VIS/NIR beam on the CCD camera. If the beam is properly aligned, when moving the aspheric focusing lens in the z-direction the beam position on the control monitor should not change.

◆ The second step is aligning the laser pointer beam (operating around 670 nm) collinear with the VIS/NIR beam. The foci of the two beams should match on the CCD screen (an exact match is however difficult to be achieved due to the different wavelength and beam diameter).

◆ After completing this steps, one proceeds to the alignment of the off-axis parabolic mirrors (OAPM); with a scatterer placed on the silicon lens mount (6), at the same height with the sample, the focusing lens is placed back in position. If

the OAPM is correctly aligned, the scattered NIR/VIS beam should form a 2-inch, round shaped image on a panel positioned around 1 m away from the scatterer. One has to make sure that the shape and size of the scattered beam propagates parallel to the optical bench - this can be checked by placing two identical cross-hair reticulars, aligned in the beam and making sure that their projections overlap even after more than 3 m.

◆ The next step is the alignment of the Golay-Cell; using the second OAPM (placed at the same height with the first one) one should obtain a round focus (astigmatism-free) of the scattered VIS/NIR beam in the centre of the detector window. Any astigmatism should be corrected by tweaking the OAMP (for a good visualization of the scattered light a piece of paper can be placed on the detector window). After the above steps are completed, the Si wafer together with the Si lens are put back in position.

◆ The last step is the alignment of the silicon lens. For this purpose one uses a He-Ne laser beam which was previously aligned to the two cross-hairs, by reflecting the He-Ne beam on two mirrors. If the He-Ne beam is shone on the back-side of the Si-lens, a good indication of the right alignment is a clear, bright and round reflected image on a paper screen placed in front of the He-Ne laser output aperture.

3.2.3. Detector characterization

The detectors used within this work belong to the wide class of thermal detectors: (1) a magnetic field-enhanced InSb bolometer (QMC Inc.), operating at liquid Helium temperature (4.2 K) and (2) an opto-acoustic detector, the Golay cell (also known as the Golay pneumatic detector).

Generally, thermal radiation detectors include an absorbing element with heat capacity \mathcal{C} which converts the incident electromagnetic radiation into heat, and which is attached to a heat sink at temperature T_S via thermal conductance θ . When the incident radiation power P is turned on, the temperature of the absorbing element initially increases with time at a rate $\frac{dT_B}{dt} = \frac{P}{\theta}$ and approaches the limiting value $T_B = T_S + \frac{P}{\theta}$ with the thermal time constant $\tau = \frac{\mathcal{C}}{\theta}$. After the radiation is switched off, it relaxes back to T_S with the same τ . Thermal detectors are frequently used to give a periodic response to a signal which is modulated at a frequency $\omega = \frac{1}{\tau}$.

In the Golay detector (invented by M.J.E Golay in 1947 [107]), which operates at room temperature, the heat absorbed in a thin metal film is transferred to a small volume of gas. The resulting pressure increase changes the angle of a mirror in an optical amplifier. It is designed such that it can detect radiation at wavelengths in the range from 1 μm up to few millimeters.

The bolometer, invented by Langley [108], is a thermal infrared detector which employs an electrical resistance thermometer (thermistor) to measure the temperature

of the radiation absorber. In order to achieve very high sensitivity under conditions of low background power loading, bolometers are usually operated around liquid He temperatures. Bolometers are square law transducers, that is, they give an output voltage which is proportional to the square of the signal amplitude. In such devices, the responsivity falls-off for modulation frequencies above the relaxation frequency $\frac{1}{\tau}$. The InSb bolometer used here is a *hot-electron bolometer* (developed by Kinch and Rollin [109]). In this device, the electrons in degenerately doped n -type InSb are both the absorber and the thermometer. They absorb millimeter and sub-millimeter wavelengths close to the plasma frequency and reach internal thermal equilibrium at a temperature above that of the lattice. The electrical resistance decreases with increasing electron temperature due to the fact that Rutherford scattering of electrons from ionized impurities decreases with increased electron velocity. The relaxation rate set by the electron-phonon interaction and the electronic heat capacity is $\frac{1}{\tau} \approx 10^7 \text{ s}^{-1}$. In the absence of a magnetic field (Rollin mode), the utility of this device is limited by the roll-off in the electronic inverse-Bremsstrahlung absorption (free-electron absorption). If the InSb detector is operated in moderate magnetic fields ($\sim 5 \text{ kG}$), an enhanced NEP⁶ and responsivity in the 20-100 cm^{-1} range results. In this case, also referred to as magnetic field enhanced, the detector absorption and spectral response is dominated by the cyclotron resonance processes.

The phenomenological equation for a thermal detector can be written as:

$$V_{out} = \mathcal{M}rP_{ch}, \quad (3.10)$$

where V_{out} is the output voltage of the detection system, \mathcal{M} is the gain of the preamplifier, r is the responsivity of the detection system, and P_{ch} is the chopped incident power. For our InSb bolometer \mathcal{M} can be 100 or 1000, but for the measurements presented here it was 100. It should be outlined that actually the chopped incident power P_{ch} , can be related to the incident THz power with the relation: $P_{inc} = \frac{\pi}{\sqrt{2}}P_{ch} = 2.22 \cdot P_{ch}$. The 2.2 factor is derived by assuming that the lock-in signal is scaled such that it returns the *rms* level for a sinusoidal input and by calculating the cycle-averaged Fourier transform amplitude of the input signal at the primitive (chopping) frequency for a square-wave modulated signal.

The factory calibration⁷ of the B-field InSb bolometer was checked against a simple InSb bolometer whose calibration was well known (at low frequencies) and against a composite Si-bolometer (Infrared Ltd.), while the Golay cell is factory calibrated. The key specifications for each detector are presented in Table 3.2. It should be mentioned that each detector system has its pros and cons: the InSb bolometer offers a far better signal-to-noise behavior but requires cryogenic cooling,

⁶NEP=noise equivalent power, a figure of merit for thermal detectors, which is defined as the incident signal power required to obtain a signal equal to the noise in a one Hz bandwidth.

⁷The system optical responsivity.

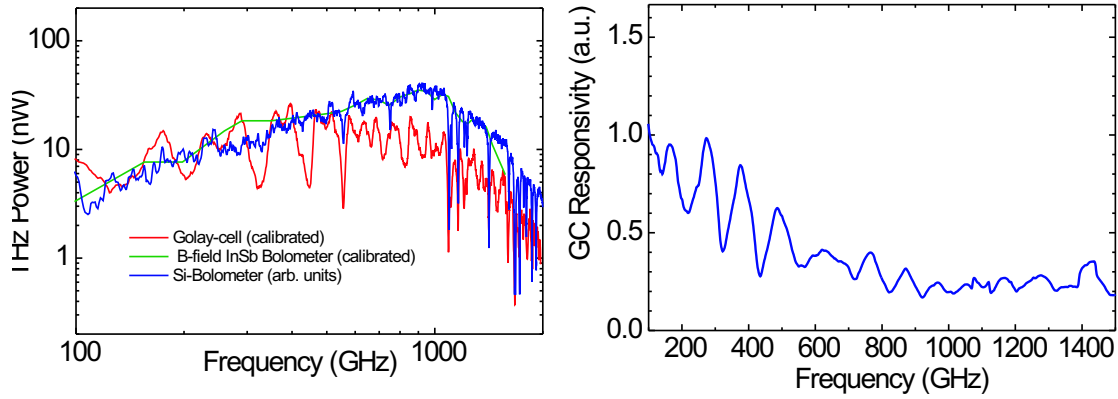


Figure 3.9.: Comparative frequency scans of a reference photomixer taken with different detectors (left) and the correction curve for the Golay cell (right).

Detector	B-field enhanced bolometer	Golay Cell
Optimum chopping frequency	1 KHz	20 Hz
System Optical Responsivity	0.85 kV/W	19.5 kV/W
Detector Optical N.E.P	$< 1 \text{ pW}/(\text{Hz})^{1/2}$	$< 246 \text{ pW}/(\text{Hz})^{1/2}$
Aperture diameter	15 mm	6 mm

Table 3.2.: The key specification of the detector systems used.

whereas the robust Golay-cell operates at room temperature but with a poorer signal-to-noise behavior. In Figure 3.9, a comparative plot of the THz emission spectra from a LT-GaAs based photomixer integrated with a resonant H-dipole antenna measured with 3 different detectors is displayed. The ripples in the Golay-cell response are associated with Fabry-Perot effects produced by a polystyrene plate mounted in front of the detector in order to filter out the thermal contribution from the lasers and the environment. To alleviate this effect, a correction curve based on numerical extrapolation algorithm was developed (Figure 3.9, right). Also, the small deviations (decreased sensitivity) are very likely due to aperture effects at the entrance window.

3.2.4. Silicon substrate lens

The efficient coupling of the THz radiation out of the SI GaAs substrate, as well as forming the subsequent quasi-Gaussian free-space beam, is done with a high resistivity ($>10 \text{ k}\Omega\text{cm}$) silicon lens [110, 111, 112]. The free-space approach is preferred around 1 THz due to the low losses, but also due to the fact that efficient waveguides

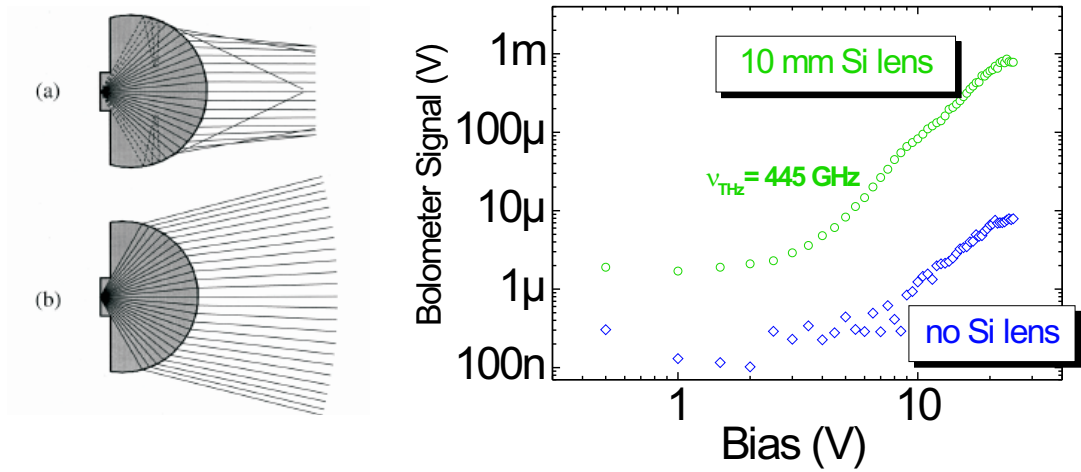


Figure 3.10.: The two lens designs (left): a) collimating and b) aplanatic hyper-hemisphere and (right) the effect of using a silicon lens upon detection efficiency.

at the corresponding wavelength are very difficult to manufacture. Due to the large difference between the dielectric constant of the air and SI GaAs substrate, around 96% of the total radiated THz power is directed into the substrate [113]. Also, one should keep in mind that due to the strong reflection at the air-dielectric interface, the substrate acts as a 3-dimensional resonator. Hence, depending on the thickness and the frequency of the emitted THz wave, a standing wave can occur, giving rise to the so called “substrate modes”, responsible for the trapping of the radiated power inside the substrate. This issue becomes particularly critical if the dimensions of the photomixers’ chip is small ($\sim 2 \text{ mm}$) [114]. The importance of using a silicon lens is illustrated in Figure 3.10 (right), here one can see that when using a substrate lens the signal is increased by a factor of ~ 100 .

The silicon lens can be either of an elliptical or an hyper-hemispherical shape. In all the THz systems implemented so far, two main designs have been considered, as presented in Figure 3.10 (left). In the collimating lens (a), the emitter is located at the focus of the substrate lens, so the THz rays emerge from the lens as a nearly collimated beam. The main drawback of this design is that at large angles the internal-incidence angle approaches the critical angle for total internal reflection [103], producing a strongly refracted ray and an aberrated wave front. Moreover, at still larger angles the radiation is trapped inside the lens. The design parameters are given by the formula:

$$d_{\text{coll}} = R \left(\frac{n}{n-1} \right), \quad (3.11)$$

where R is the radius of the hemisphere and n is the refractive index of silicon (~ 3.43). Here, d_{coll} is the distance from the emitter (microstructured antenna) to the tip of the lens and it also includes the thickness of the substrate t , such that the effective height of the hemisphere is given by: $h_{eff} = d_{coll} - t$. The other design, which was adopted for the THz system described here is based on the aplanatic hyperhemisphere, in which the emitter is positioned such that no rays are trapped by internal reflection, the radiation emerging with a $\sim 30^\circ$ cone angles (design (b) in Figure 3.10-left) and no wavefront aberration. The distance from the emitter to the tip of the lens is given by:

$$d_{hyper} = R \left(\frac{n+1}{n} \right). \quad (3.12)$$

For a substrate thickness of $\sim 400 \mu\text{m}$, and a lens diameter $2R=10.1 \text{ mm}$ the above formula yields an effective height $\sim 6.72 \text{ mm}$ for the design (a) and $\sim 6.12 \text{ mm}$ for the design (b). In order to check for the best design, we measured the emitted THz power around 500 GHz for lenses with the effective height of 5.72, 5.92, 6.12, 6.32 and 6.72 mm. Indeed, the best results were obtained for the 6.12 mm lens. For the other heights we observed a reduction up to 20 % of the radiated power [115]. The 10.1 mm diameter lens was also checked against a 2 mm lens which also gave only one tenth of the measured power.

3.3. State of affairs in photomixing

The first LTG-based photomixers were demonstrated by Brown et al. [101] at MIT. They consist of interdigitated MSM electrodes with $\sim 1 \mu\text{m}$ spacing and were coupled to broad-band self-complementary spiral antennas, thus generating CW THz radiation up to 3.8 THz [116]. In the last decade such photomixers have become one of the most versatile all-solid-state sources for CW THz generation. However, their main drawback is the relatively low power they can deliver. As far as the fundamental limitations of the energy-conversion efficiency in the photomixing process is concerned, one should clearly state that in contrast to difference-frequency generation (DFG) in a nonlinear optical crystal (which is limited by the Manley-Rowe relation⁸), the ultimate THz power available is limited only by the electrostatic energy stored in the photoconductive gap region, that is, $\frac{1}{2} \int_{gap} \varepsilon E_b dr$, where E_b is the bias field in the photogap. Hence, the photomixing process could in principle exceed the efficiency of nonlinear DFG.

Besides the fundamental limitations (i.e. very low quantum efficiency), there have been a series of issues addressed by numerous researches which sought various

⁸The energy conversion efficiency in converting a VIS or IR photon to a THz photon cannot exceed the frequency ratio of incident photons.

schemes to improve the performance of photomixers. On the shortlist: i) material properties (LTG-GaAs), ii) thermal effects, iii) device and circuit configurations, and last but not least iv) bias field effects. We discuss these four issues here in turn.

i) Early attempts to improve the output power were focused on reducing the carrier lifetime-dependent high-frequency roll-off term in Eq. 3.8 by shortening the carrier lifetime. Even though LTG-GaAs is one of the few materials to meet the requirements for a good ultrafast photoconductor, that is, a short carrier lifetime, a large breakdown field (in order to be able to apply a bias as large as possible for obtaining a large photocurrent) and a large mobility, the simultaneous achievement of a high quantum efficiency (i.e. high photocurrent) and a carrier lifetime roll-off-free device is not straightforward, imposing a compromise and a careful choice of the substrate growth parameters, as discussed in the previous chapter. For instance, two photomixers having different carrier lifetimes τ_e but the same illumination conditions, would generate the same THz power as long as $\omega\tau_e \gg 1$ but the DC photocurrent will be higher for the material with the longer τ_e . This causes a higher thermal load resulting in device failure. Also, as will be discussed later on, for a large photoconductive gain, a large mobility is required.

ii) As derived from Eq. 3.7, the THz power should increase quadratically with the pump laser power which is proportional to G_0 . It is believed that the limited photomixer lifetime is caused by a combination of optical power and ohmic heating, mainly due to the low thermal conductivity of the LTG-GaAs ($\sim 0.15 \text{ Wcm}^{-1}\text{K}^{-1}$), which limits the usable amount of incident optical power. For this reason, in an attempt to improve the thermal management of devices, Verghese et al. [117] doubled the output THz power by using a silicon substrate (thermal conductivity $\sim 1.1 \text{ Wcm}^{-1}\text{K}^{-1}$ compared with $\sim 0.44 \text{ Wcm}^{-1}\text{K}^{-1}$ for SI GaAs), while the work of Jackson at UCLA quantified the importance of thermal considerations [31], resulting in the implementation of a $2.5 \mu\text{m}$ AlAs buffer layer having twice the thermal conductivity of SI GaAs.

iii) Following the theoretical considerations of Brown [118], the carrier collection efficiency and hence the responsivity of photomixers was improved by using Bragg reflectors beneath the LTG-GaAs, creating a multiple-pass (asymmetrical Fabry-Perot) cavity while the reflection losses were alleviated by coating the active area with antireflection (AR) coating, usually SiO_2 .

Also, as derived from Eq. 3.8, the output power from a photomixer is proportional to the antenna impedance. Most of the early work on photomixers employed broad-band self-complementary antennas like bowtie, log-spiral and log-periodic, partly due to the frequency-independent characteristics [116, 117, 119]. However, the broad-band antennas present a rather low impedance (radiation resistance), around $70\text{-}80 \Omega$, hence lower THz power. An alternative to this would be the use of resonant structures like dipole and slot antennas which have a high impedance

at the resonance frequency. In Ref. [120], due to the high driving point impedances ($\sim 300 \Omega$) the radiated THz power was more than 3 times higher (at the resonant frequency) than that from broad-band structures. The reason lies in the fact that at the resonance frequency the impedance becomes a real quantity, thus yielding a high radiation resistance [121]. Very good results, standing for the state-of-the-art output power levels ($\sim 2 \mu\text{W}$ at 1 THz) with LTG-based photomixers were reported by Duffy et al. [27, 122], using resonant double (twin) dipole and slot antennas. There are a series of advantages derived from the use of the double resonant structures: firstly, a highly symmetric near-Gaussian beam pattern (while a single-dipole antenna showed large side-lobes) which ensures high directive gain, thus the reflection loss at the silicon substrate lens is avoided; secondly, the flexibility of inductance tuning by adjusting the length of the transmission line which connects the photogap and the antenna, way in which the capacitance of the photogap is canceled, and therefore offers the possibility of attaining higher frequencies (0.8 up to 2.7 THz). The power levels reported in Ref. [27] are 3-10 times higher than those obtained from single-dipole antennas. One could also see in Eq. 3.8 that from the standpoint of the metal structure deposited on the LTG-GaAs layer, the high-frequency operation of the photomixer could be improved by minimizing the photomixer's capacitance C as well as maximizing G_0 . Unfortunately, for a lumped-element photomixer (such as that presented at the beginning of this chapter), these are competing goals, since both are proportional to the device area. A compromise has been found in reducing the electrode width and the distance between the electrodes but present technological limitations set the electrode width at $\sim 0.2 \mu\text{m}$ [118]. A very promising approach that circumvents the problem of fixed-frequency operation imposed by the use of resonant structures, is the development of a photomixer with a distributed active area where the generated THz wave propagates along a microwave transmission line. Hence, the RC-time roll-off can be eliminated from the picture since the distributed inductance of a traveling wave structure resonates out the distributed capacitance (a transmission line has a frequency independent impedance). The straightforward advantage, besides eliminating the effect of the capacitance, a traveling-wave design allows for more optical power, hence a larger G_0 , also distributing the optical and ohmic thermal load over a large area (volume). Using this approach, Matsuura et al. [28], obtained 200 nW at 2.5 THz. Similar structures have been developed by Duerr et al. [113] and E. Michael et al. [123] which reported 1 μW at 1 THz.

iv) Eq. 3.8 predicts that the emitted THz power depends quadratically on the applied bias field. Even if this might be the case at low bias fields (10 kV/cm), in general the THz power dependence on the applied bias is complicated by material properties and the inhomogeneous distribution of the field in the active region. Brown [118], from calculations of the field distribution, pointed out that for 0.2- μm -wide electrodes and a 0.8- μm -wide gap, the electric field strength decays by one

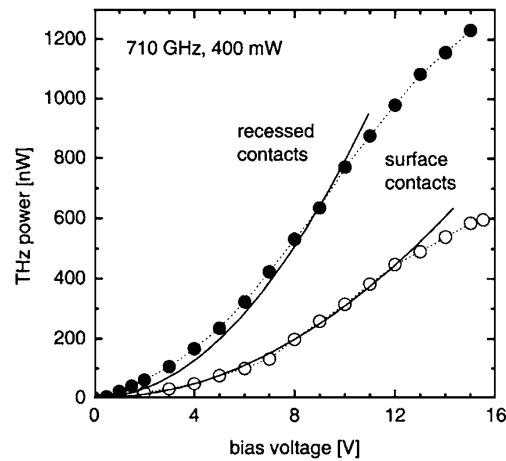


Figure 3.11.: THz power versus applied bias for a recessed contacts structure as described in Ref. [29].

order of magnitude within $1 \mu\text{m}$ of substrate. Another problem, as described by Zamdmer et al. [32], is the elongation of the carrier lifetime at high fields. Other aspects which will receive greater attention in the following sections are effects like the velocity overshoot (field-dependent mobility) and space charge effects. Several attempts to alleviate the bias field effects were concretized in new designs like the vertical photomixer structure developed by the group of D. Lippens [124, 30], in which the active LTG-GaAs layer was sandwiched between two vertical contacts with no contact to the SI GaAs substrate. As opposed to the planar structure, the vertical one should be freed of the two-dimensional effects described by Brown, also the photocurrent should be distributed in a greater volume hence better thermal management. Unfortunately, the reported power levels are rather low, around $0.1 \mu\text{W}$ at 700 GHz. Very recently, Mikulic et al. [29] reported increased power levels ($\sim 1 \mu\text{W}$ around 800 GHz) for a traveling-wave photomixer with recessed (buried) contacts, which should account for an improved electric field distribution inside the active layer, thus accounting for a more effective carrier collection. The two-fold increase in output power for the recessed contacts is a good proof-of-principle.

In almost all of the above mentioned works on photomixers, there are two salient features which could not be explained satisfactory or could not be explained at all. First, the deviation from linearity in the photocurrent versus bias, and secondly, the deviation from the quadratic behavior of the THz power versus bias at higher applied field followed by saturation or even a decrease, as most recently seen in Ref. [29] and depicted in Figure 3.11.

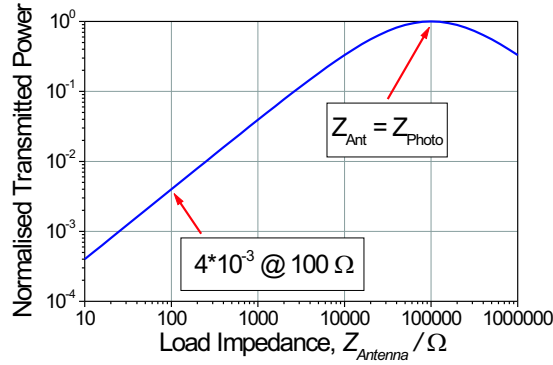


Figure 3.12.: Normalized transmitted power versus antenna impedance.

3.4. Design and fabrication of photomixers

As discussed in the previous section, several schemes to improve the conversion efficiency of photomixers (currently, on the order of 10^{-4} - 10^{-5}) have been sought, but with limited success. Since photocurrent measurements with planar gaps (no interdigitated fingers) showed that the high resistivity of LTG-GaAs material leads to a high *source impedance* (with typical values of about 100 k Ω) one viable approach is to use an interdigitated finger structure, thus reducing the impedance of the photogap. The necessity of a low source impedance can be understood if one considers that the THz power is radiated by a planar antenna with typical feedpoint impedances in the range of 70-200 Ω , and the normalized transmitted power is given by:

$$P_T = 1 - |r|^2,$$

with

$$r = (Z_a - Z_g)/(Z_a + Z_g),$$

where Z_a and Z_g are the antenna and photogap impedance.

Thus, as illustrated in Figure 3.12, for a photogap impedance of 100 k Ω , the transmitted power to an antenna with a feedpoint impedance of 100 Ω drops down to 4×10^{-3} , the enormous impedance mismatch accounting for the observed low emitted power in LTG-GaAs based photomixers. The use of bias lines without filter structures, together with the high permittivity of the GaAs substrate ($\epsilon_r = 12.9$) make the matters worse. However, since the main purpose of the present work is not to report on record power levels but to explore the fundamental shortcomings derived from the usage of LTG-GaAs material, we are not concerned with further improving the photomixer's circuitry. In addition to the higher impedance, the usage of interdigitated fingers provide better homogeneity of the electric field in the photogap, together with a higher photocurrent. The drawback lies in an additional

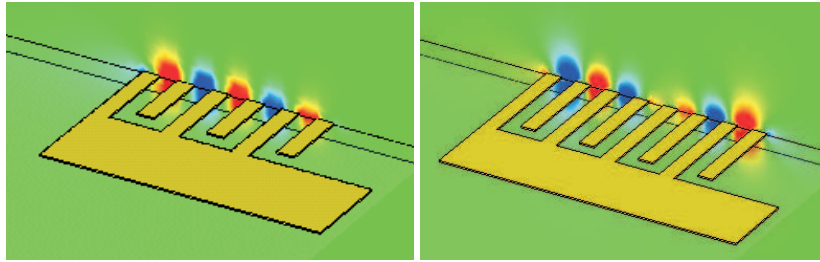


Figure 3.13.: Electric field distribution (at 1 THz) across the 6-(left) and 8-(right) finger photogap.

parasitic capacitance which reduces the device bandwidth.

We chose the smallest finger size to be $1 \mu\text{m}$ in order to ensure the technical feasibility in a standard photolithography process. The geometry and number of fingers were chosen following a theoretical simulation of electrical field distribution at 1 THz. As can be seen in Figure 3.13, the 6-finger structure shows a regular field pattern between the fingers while the field distribution for the 8-finger structure is too large for this frequency causing a large phase shift between the fingers and therefore the photocurrents at 1 THz are canceling each other. The above investigations resulted in a 6-interdigitated-finger photogap with an active area of $10 \times 10 \mu\text{m}$, as depicted in Figure 3.16 (right), with a resistance that should be 45 times less than for a finger-free gap. The small spacing between the fingers also allowed us to look at the high-field characteristics of photomixers.

In order to investigate the impact of material and charge transport properties on the frequency characteristics of photomixers we chose a relatively frequency-independent antenna. The family of frequency-independent antennas comprises antennas that maintain the same impedance and radiation pattern over a wide frequency range. There are several criteria when designing a broad-band antenna. Of the two main characteristics - radiation pattern and impedance - the former poses serious challenges if a clean Gaussian beam is required (in THz emission spectroscopy, for instance). Fortunately, in the measurements presented here the shape of the THz beam is not playing an important role. The first design criteria, due to Rumsey [125], refers to an antenna shape that is only defined by angles, its most simple illustration being the infinite bow-tie antenna, consisting of two triangles connected by the feed. The second principle (or Mushiake's principle [126]) is derived from Babinet's principle in electromagnetics and allows for calculation of the input impedance in

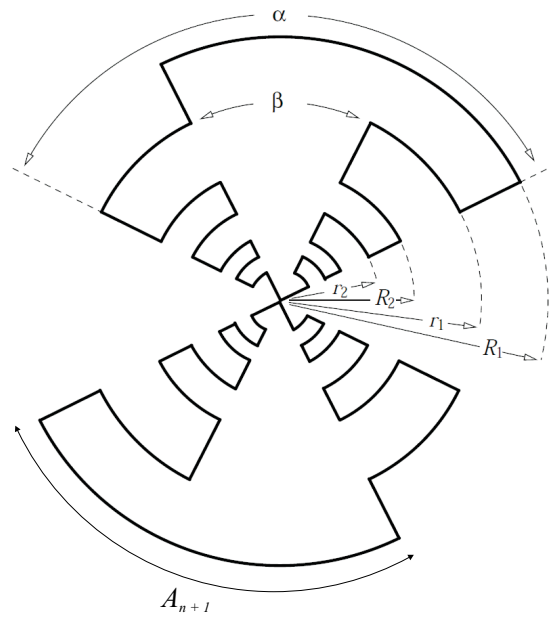


Figure 3.14.: Schematic view of a log-periodic toothed planar antenna with the design parameters.

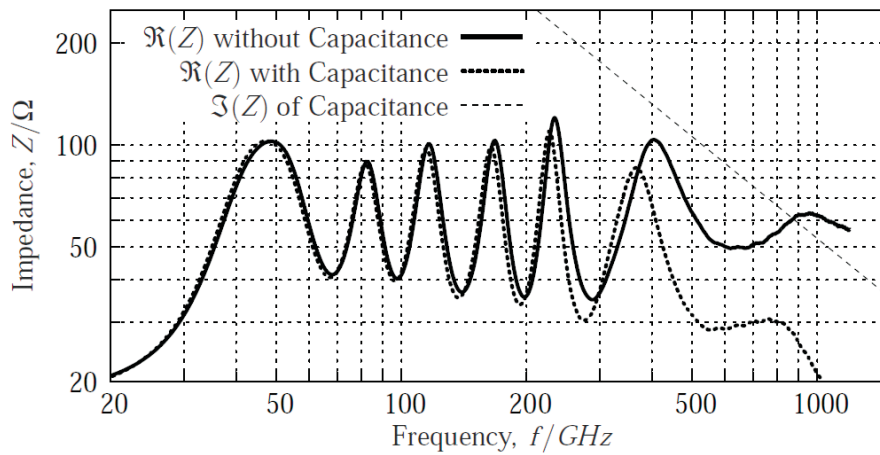


Figure 3.15.: Calculated impedance of the log-periodic antenna, with and without electrode capacitance.

the case of a self-complementary (SC) antenna⁹: $Z_{air}Z_{metal} = (\eta^2/4)$ where $\eta = \sqrt{\frac{\mu}{\epsilon}}$ is the characteristic impedance of the medium surrounding the antenna. Since the impedance of the antenna equals that of its complementary structure, the input impedance of the SC antenna for the free space is given by $Z_A^{air} = (60\pi)$ (Mushlake's relation). For GaAs, taking the relative permittivity $\epsilon_r=12.9$, the antenna impedance becomes $Z_A^{substrate} = (60\pi/\sqrt{\epsilon_{eff}})$ where $\epsilon_{eff} = [(1 + \epsilon_r)/2]$ is the effective dielectric constant, yielding a value of $\sim 72 \Omega$ for any planar broad-band self-complementary antenna on a LTG-GaAs substrate. In principle, the antennas mentioned so far should extend to an infinite radius as they are defined only by angles, and a thorny problem was to determine the physical dimensions for an antenna such that it could acceptably approximate an infinite radius, such that the current distribution remains constant regardless of the wavelength over the finite geometry. Thus a third criteria was introduced by DuHamel in 1957 [127] by inserting logarithmic repeated features in the antenna pattern. For the antenna used in our experiments, *the log-periodic toothed antenna*, the introduction of periodically positioned teeth shorts out the current distribution along the antenna by transforming the open end of the tooth into a short when its length corresponds to a quarter wavelength ($\lambda/4$). Therefore, the antenna characteristics (impedance) repeat periodically with the logarithm of frequency. For the log-periodic toothed planar antenna shown in Figure 3.14 the ratio of edge distances is constant and is given by the following scale factor: $\tau = \frac{R_{n+1}}{R_n}$, where parameter τ gives the period of the structure, therefore a periodic pattern and impedance behaviour with the same period would be expected. The antenna is resonant when the length of any of the arcs A_n is equal to $\lambda_{eff}/2$, the arc length can be calculated as: $A_n = \left(\frac{\pi}{2}\right) \left(\frac{R_n+r_n}{2}\right)$. The corresponding resonant frequencies are:

$$f_n = \frac{2c}{\pi (R_n + r_n) \sqrt{\epsilon_{eff}}}. \quad (3.13)$$

The calculated impedance for the antenna used in our experiments presents indeed 6 resonances, corresponding to the number of teeth, as indicated in Figure 3.15. Also, the antenna impedance was calculated including the capacitance of the interdigitated fingers. For the antenna shown in Figure 3.16, the design parameters are $\alpha=50^\circ$, $\beta=100^\circ$, $\tau=0.5$, $R_1=640 \mu\text{m}$ and $n=3$. Our log periodic antenna was designed to have a frequency coverage of 50-1100 GHz. The self-complementarity criteria ($\alpha+\beta = 90^\circ$) was not fulfilled, and thus the impedance of our antenna is somewhat lower $\sim 65 \Omega$. The emitted radiation is linearly polarized with the polarization angle changing with

⁹A self-complementary antenna is an arbitrarily shaped antenna which constitutes a half of an infinitely extended planar-sheet conductor such that the shape of its complementary structure is identical with the original structure with two terminals for the simplest case. The self-complementary antenna has a constant input impedance independent of the source frequency and the shape of the structure.

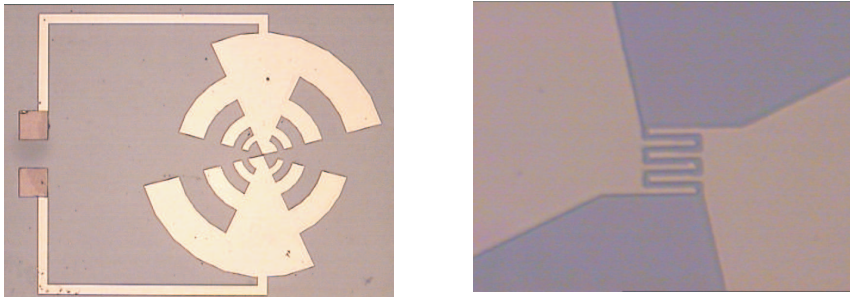


Figure 3.16.: Log-periodic toothed planar antenna (left) and a close-up of the 6 finger active area (right).

the operation frequency.

The fabricated photomixers consisted of a $1.5\text{-}\mu\text{m}$ -thick LTG-GaAs without (TP983) and with (TP984) a Bragg reflector, on a $500\text{-}\mu\text{m}$ SI GaAs. The $1\text{-}\mu\text{m}$ wide and $9\text{-}\mu\text{m}$ long fingers together with the log-periodic antennas were defined photolithographically and metallized in a high-vacuum (HV) chamber at TU Darmstadt using 100 nm of platinum. There was no post-deposition anneal, but a thin layer of SiO_2 was deposited as an AR coating. This series of devices was denominated CW1a-d and CW2a-d (4 identical devices on each chip), as listed in Appendix B.



Figure 3.17.: Oxidation (black islands) of LTG-GaAs photomixers with Bragg reflectors exposed to air.

A series of devices was processed on substrates with embedded Bragg mirrors, as described in the previous chapter. Due to the limited absorption depth ($\sim 1\text{ }\mu\text{m}$ at 850 nm) and the relatively thick LTG-GaAs layers ($1.5\text{ }\mu\text{m}$) we did not expect an increased carrier generation and collection, hence enhanced photocurrent and THz power, but want to exclude the possibility of photocarriers generated in the substrate. For the samples with Bragg reflectors a violent oxidation process could be observed, probably due to the presence of Al in the AlAs layers which form the

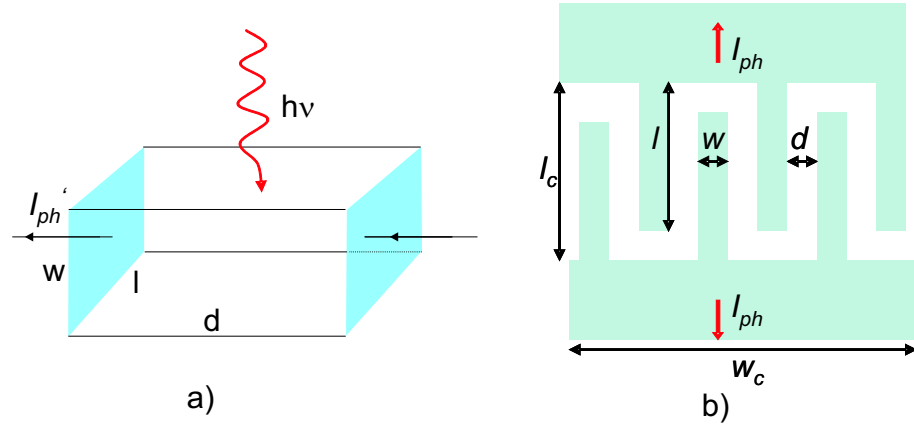


Figure 3.18.: Schematic view of a MSM interdigitated fingers photogap used in deriving the photocurrent.

Bragg mirror (Figure 3.17). The oxidation pits are increasing with time, in our case approaching dimensions of ~ 1 mm, destroying the photomixer patterns. Similar effects were reported by Jackson [31] and a possible remedy would be coating the LTG-GaAs layer with SiN.

3.5. Analysis of photocurrent and THz emission characteristics

3.5.1. DC photocurrent vs. applied bias voltage

To illustrate the way one calculates the DC photocurrent in a photomixer structure, we assume the elementary structure sketched in Figure 3.18 (a), representing a bulk of photoconductive material between two metal electrodes under a constant bias V and illuminated with radiation at an energy $h\nu$ (which is larger than the bandgap of the photoconductor). The spacing between electrodes is denoted by d , while the width and length of contacts are denoted by w and l , respectively. Although the real structure used in our experiments is an interdigitated MSM finger structure, as shown in Figure 3.18 (b), for the sake of clarity, we assume that the elementary photocurrent which flows between two neighboring electrodes I'_{ph} of the MSM structure can be derived by using the simplified structure in Figure 3.18 (a). The total current flowing in the external circuit (to the antenna) is given by the number of gaps multiplied with the elementary current $N_g I'_{ph}$ (in an equivalent circuit picture one can imagine N_g current sources in parallel). At this point, we consider the LTG-GaAs a simple photoconducting material, in which, under constant illumination, a certain density of electron-hole pairs (EHP) is generated. We define the optical generation rate g'_0 as the number of absorbed incident photons per second, i.e. photon flux $(P'_0/h\nu)$ per unit volume (lwd) , multiplied by the optical quantum efficiency η_{opt} ,

which accounts for reflections at the air-LTG-GaAs interface, as well as for the finite thickness of the photoconductive layer. Accordingly, we define the optical quantum efficiency as $\eta_{opt} = \mathcal{T}(1 - e^{-\alpha t_{LT}})$, where \mathcal{T} is the transmission coefficient at the air-semiconductor interface and t_{LT} is the thickness of the LTG layer. Hence, the generation rate becomes:

$$g_0' = \eta_{opt} \frac{P_0'}{h\nu} \frac{1}{\mathcal{V}'}, \quad (3.14)$$

where $\mathcal{V}' = ldw$ is the elementary volume associated with the elementary photocurrent I_{ph}' .

For the real structure, the total incident optical power P_0 is distributed over a total contact area $A_c = l_c w_c$ and the corresponding volume given by $\mathcal{V} = A_c t_{LT}$, yielding a total generation rate g_0 . Also, as discussed later in this section, to account for the reflection of the incident light by the metal fingers, one must introduce a *shadowing factor*, S_f .

If we consider n and p the densities of free photogenerated electrons and holes (assumed spatially homogeneous), we can write the current continuity equation:

$$\frac{dn}{dt} = g_0 - R = g_0 - \frac{n}{\tau_e}, \quad (3.15)$$

where $R = \frac{n}{\tau_e}$ is the electron recombination rate. In fact, in case of LTG-GaAs photoconductor one should replace the recombination rate with the trapping rate. The same equation holds for holes. For an uniformly illuminated photoconductor, the electron and hole current densities are given only by the drift components, since there is no diffusion due to the lack of spatial dependence ($\partial/\partial x \equiv 0$):

$$\begin{aligned} J_n &= env_e(E) \\ J_p &= epv_h(E) \end{aligned} \quad (3.16)$$

where $v_{e,h}$ is the field-dependent electron (hole) drift velocity. The total current density is $J = J_n + J_p$, where, at this point the holes contribution to the photocurrent is discarded due to their low mobility in LTG-GaAs. Moreover, the low mobility of holes produces a small displacement of the hole population in the external applied field, whereas due to their much higher mobility a significant number of electrons are displaced into the cathode (+); hence, for maintaining the space-charge neutrality in the illuminated gap and current continuity at the electrodes¹⁰, a replenishment of electrons at the anode is necessary (i.e. electron injection). The DC photocurrent flowing into the external circuit is given by:

$$I_{ph}^{DC} = Aenv_e(E), \quad (3.17)$$

where A is the total contact area. With G_0 independent of time, that is $\partial/\partial t \equiv 0$ at steady state, from Eq. 3.15, the density of photogenerated electrons becomes:

¹⁰The total current flowing into the external circuit must be equal at anode and cathode.

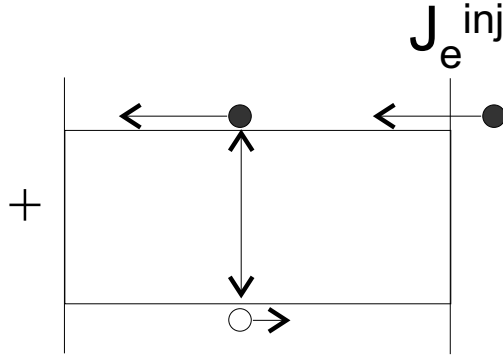


Figure 3.19.: Schematic energy-level representation of electron injection at the anode (-).

$$n = \frac{\eta_{opt}}{\mathcal{V}} \left(\frac{P_0}{h\nu} \right) \tau_e, \quad (3.18)$$

and by substituting it into Eq. 3.17 we obtain:

$$I_{ph}^{DC} = e \frac{\eta_{opt}}{d} \left(\frac{P_0}{h\nu} \right) \tau_e v_e(E). \quad (3.19)$$

We can regroup the terms in Equation 3.19, by denoting the primary photocurrent $I_{ph}^p = e\eta_{opt} \left(\frac{P_0}{h\nu} \right)$ and introducing the *photoconductive gain* $g = \frac{\tau_e}{t_{tr}(E)}$ where $t_{tr}(E) = \frac{d}{v_e(E)}$ is the photocarrier transit time. In other words, the photoconductive gain is determined by how fast the electrons can transit across the electrodes and contribute to the photocurrent in the circuit before they recombine with the holes, or as in the case of LTG-GaAs material, they become trapped. In most of the existing designs of LTG-GaAs photomixers, the carrier transit time is neglected since the transit time for an electrode spacing of $\sim 1 \mu\text{m}$ is much larger than the carrier lifetime. For example, assuming a trapping time of $\sim 1 \text{ ps}$ and a drift velocity of $\sim 4.4 \times 10^6 \text{ cm/s}$, this yields a transit time of $\sim 25 \text{ ps}$ and a gain of about 0.04 ($\ll 1$), hence the low quantum efficiency of photoswitches. This large difference between the carrier transit and lifetime means that the LTG-GaAs photomixer is a *carrier lifetime dominated device*.

In Eq. 3.19, the electron drift velocity is affected by the saturation effects and has the general form:

$$v_e(E) = \frac{\mu_e E}{1 + \frac{\mu_e E}{v_{sat}}}, \quad (3.20)$$

where μ_e is the carrier mobility and v_{sat} the saturation velocity. At low electric fields one can assume a field-independent mobility, such that $v_e(E) \simeq \mu_e E \simeq \mu_e \frac{V}{d}$. Replacing in Eq. 3.19, we obtain:

$$I_{ph}^{DC} \cong e\eta_{opt} \left(\frac{P_0}{h\nu} \right) \tau_e \mu_e \frac{V}{d^2}. \quad (3.21)$$

3.5.2. THz photocurrent

If we now consider the photocurrent modulated at a THz frequency, following the analysis in Section 3.1, we can write:

$$I_{ph}^{THz} = \frac{I_{ph}^{DC}}{\sqrt{1 + (\omega\tau_e)^2}} = e \frac{\eta_{opt}}{d} \left(\frac{P_0}{h\nu} \right) \frac{v_e(E)\tau_e}{\sqrt{1 + (\omega\tau_e)^2}}. \quad (3.22)$$

In essence, the reduction of the current contributing to the THz signal at high frequencies is a result of the response time of the electrons τ_e compared with the modulation frequency ω . Since the response of the photogenerated carriers is decreasing with increasing modulation frequency, the THz photocurrent (feeding the antenna) decreases. Also, if $\omega\tau_e \ll 1$, the AC (THz modulated) photocurrent is *exactly* equal to the DC photocurrent, hence the DC responsivity is a good indication of the THz photomixer performance.

3.5.3. THz power dependence on the applied bias

The amount of generated THz power can be found following the small-signal analysis presented in Section 3.1. If we replace the THz photocurrent and solve the dynamic current equation, we can write, with the appropriate approximations:

$$P_{THz} \propto \frac{(I_{ph}^{DC})^2}{(1 + (\omega\tau_e)^2) (1 + (\omega R_a C)^2)} \propto \left(e \frac{\eta_{opt}}{d} \left(\frac{P_0}{h\nu} \right) \right)^2 \frac{v_e^2(E)\tau_e^2}{(1 + (\omega\tau_e)^2) (1 + (\omega R_a C)^2)}. \quad (3.23)$$

Having a closer look at Eq. 3.23, one notices that by approximating $v_e(E) \simeq \mu_e E \simeq \mu_e \frac{V}{d}$, the emitted THz power should follow a quadratic dependence on the applied bias. In the same manner, the THz power should increase quadratically with the incident optical power.

From Eq. 3.21, one can see that the expected DC photocurrent dependence on the applied bias should be linear for low applied fields, and then saturate at higher fields. However, as shown in Figure 3.20, the measured $I_{ph} - V$ characteristics for both series of photomixers, CW1 (non-Bragg) and CW2 (Bragg), display a sub-linear relation to the applied bias (up to 3-5 V) approaching a linear behavior, to become super-linear for biases higher than ~ 8 V (80 kV/cm applied bias field). Both characteristics were measured under CW illumination conditions, with an incident optical power of 20 mW, while the bias was varied from 0 to 20 V (0-200 kV/cm applied bias field). Identical characteristics were obtained when measuring the output THz power dependence on the applied bias (in the latter case, the recorded photocurrent value had to be multiplied with 2 due to the optical chopping of the laser beams). Even if we can invoke carrier velocity saturation for explaining the sublinear dependence at

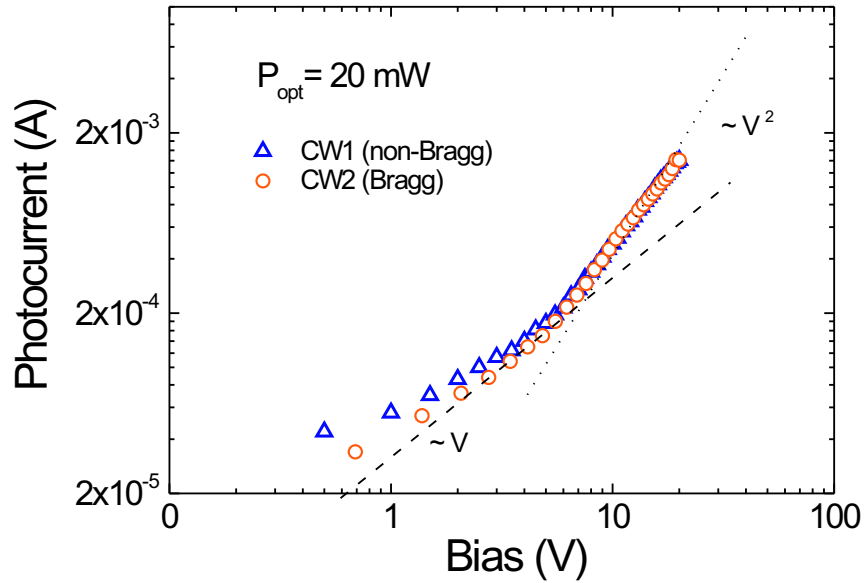


Figure 3.20.: DC photocurrent vs. applied voltage characteristics for the Bragg (circles) and non-Bragg (triangle) devices.

low fields (10-50 kV/cm), the almost quadratic dependence of photocurrent on bias for high fields inspired many researchers in the field to ascribe it to various effects, to be discussed in the remainder of this chapter.

Another set of data is presented in Figure 3.21 where the emitted THz power was recorded against the applied bias. The frequency offset of the two laser beams was set to ~ 400 GHz, while the total laser power was 20 mW. Although slightly different at low applied bias values (perhaps due to the measurement noise offset at low power levels), the $P_{THz} - V$ characteristics become almost identical at higher bias values. Here too, one can observe the deviation from the photomixing theory: while at low voltages the THz power follows an almost quadratic behavior, at higher voltages the relation becomes quartic ($P_{THz} \sim V^4$), and the crossover voltage is the same as for the $I_{ph} - V$ characteristics. Another interesting feature is that the quartic relation is preserved at higher frequency (800 GHz), as can be seen in Figure 3.21 for the CW2 emitter. At all frequencies, the quartic dependence is followed by saturation and an ultimate decrease of the emitted power.

Brown et al. [128] were the first to report this kind of behavior for LTG-GaAs photomixers was , performing photomixing experiments at 200 MHz. The authors tried to explain the data by assuming a “recombination-limited transport”, based on the different electron and hole lifetimes, which leads to the formation of non-neutral

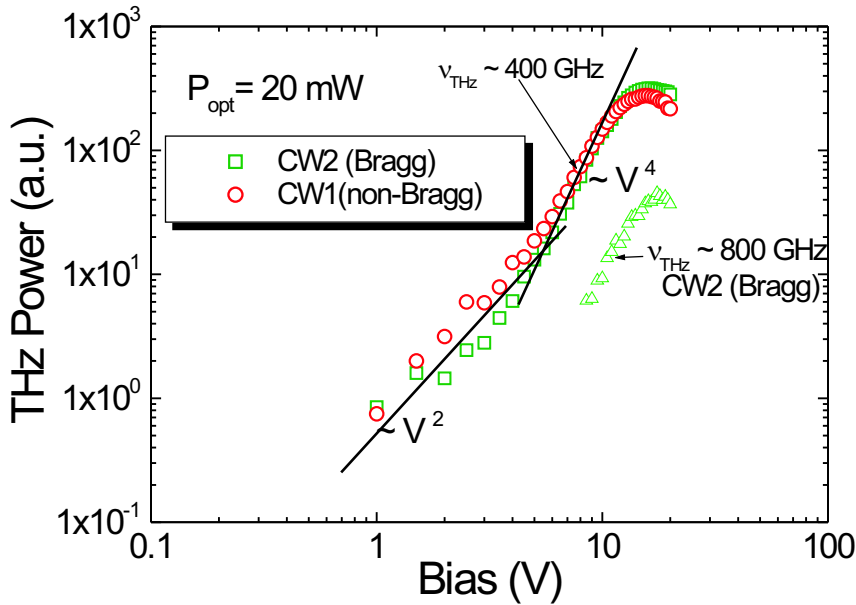


Figure 3.21.: Output THz power vs. applied bias characteristics recorded at 400 and 800 GHz.

space charge domains at high biases, resulting in a behavior similar to the space-charge limited current (SCLC), $J_{SCLC} \sim V^n$, with $n > 1$, and hence $P_{THz} \sim V^m$, with $m > 2$. Satisfactory at a first glance, the model was built on the argument that at very high fields the holes are swept out of the collection region before they can recombine with the trapped electrons, that is $t_{tr}^h < \tau_h - \tau_e$, where t_{tr}^h is the transit time for holes. However, should this be the case, the drift velocity of holes must take an unphysical value; for instance, for the parameters used $d=0.6 \mu\text{m}$, $\mu_e=400 \text{ cm}^2/\text{Vs}$, $\mu_h=100 \text{ cm}^2/\text{Vs}$, $\tau_e=0.2 \text{ ps}$ and $\tau_h=5 \text{ ps}$, in order to satisfy the above condition $t_{tr}^h < 5 \text{ ps}$, the holes must have a drift velocity $v_h > 1.2 \times 10^7 \text{ cm/s}$, whereas the reported saturation velocity in SI GaAs is less than 10^7 cm/s [129]. The authors also predict that this behavior should disappear at THz frequencies, since the model prediction (and the implicit quartic dependence of the THz power) should only be observed as long as the hole transit time is much less than a half-period of the illumination cycle, that is $t_{tr}^h \ll (\nu_{THz})^{-1}$, but it was reported at frequencies as high as 910 GHz [123].

Another hypothesis which was put forward in trying to explain the non-ohmic behavior of the illuminated I-V characteristics was motivated by the results obtained by Marso et al. [130]. They fabricated free-standing LTG-based photomixers in which the native SI-GaAs substrate was removed and the photomixer was transferred to

either silicon or even plastic. A first striking observation was that the dark I-V curves showed an ohmic behavior over the entire bias range, with much lower values of the dark current for the free-standing devices, while the device processed on the SI-GaAs substrate was affected by strong nonlinearities in current-voltage relationship. This suggested that the non-linear behavior in the illuminated I-V might be caused by the carriers (electrons) generated in the SI-GaAs substrate and which, for very intense fields, could be collected thus contributing to the DC photocurrent. However, since we observed the same behavior also for devices with a Bragg reflector this hypothesis should be discarded. Besides, the carriers generated in the SI-substrate would have a much longer lifetime, not contributing to all at the THz signal, contrary to what we observed.

In trying to explain the super-linear behavior of the photocurrent, Zamdmer et al. [32] proposed a mechanism based on electron heating and Coulomb-barrier lowering of the deep ionized states (As_{Ga}^+ in the case of LTG-GaAs). Thus, the electron capture time, and therefore the electron lifetime does not remain constant for different applied electric fields, but instead, it increases with the field because the effective cross-section of Coulomb-attractive electrons traps decreases with increasing electric field due to the electron heating and Coulomb-barrier lowering. Since the electron capture time is inversely proportional to the capture cross-section of the ionized defect, the proposed field dependence has the form:

$$\tau_e(E_0) = \tau_{e0} \left(1 + \frac{\lambda e E_0}{k_B T} \right)^{\frac{3}{2}} \left(\frac{r(E=0)}{r(E_0)} \right)^3, \quad (3.24)$$

where T is the lattice temperature, r is the radius of the Coulomb potential well in the direction of the applied field, k_B is Boltzmann's constant, λ the optical-phonon mean free path, while τ_{e0} is the field-independent carrier trapping time which is usually obtained from time-resolved reflectance measurements. The value of λ (~ 2 nm) is smaller than the value of the optical phonon mean free path in normal GaAs with low defect density, which is 5.8 nm. In Eq. 3.24, the second term is due to electron heating while the third one is due to Coulomb-barrier lowering. It should be emphasized that the model proposed by Zamdmer fully discards the contribution of holes to the photocurrent, assumes a very short hole trapping time (~ 0.7 ps) and also the fact that electrons and holes are captured at the same defect (As precipitates). An approximation to Eq. 3.24, which reproduces the sharp transition from a bias-independent lifetime to the functional dependence of $E^{\frac{3}{2}}$, used with success in fitting the photocurrent characteristics, is:

$$\tau_e(E_0) = \tau_{e0} \left(1 + \left(\frac{E_0}{\chi S} \right)^3 \right)^{\frac{1}{2}}, \quad (3.25)$$

where E_0 is the electric field in V/m, χ is a factor that accounts for the non-uniformity of the electric field given by $\chi = \frac{2}{\ln[(2d+w)/w]}$ where, as depicted in Fig-

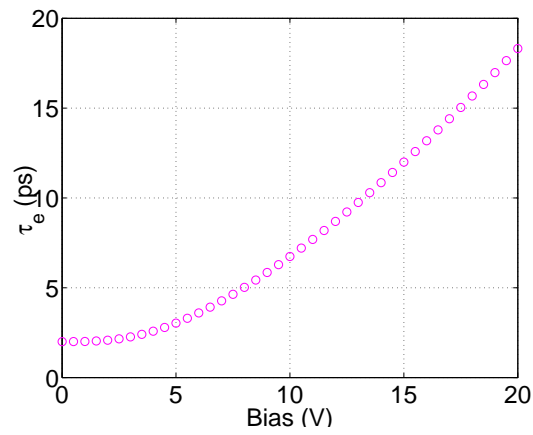


Figure 3.22.: Calculated electron lifetime increase with the applied field (bias) using Equation 3.25.

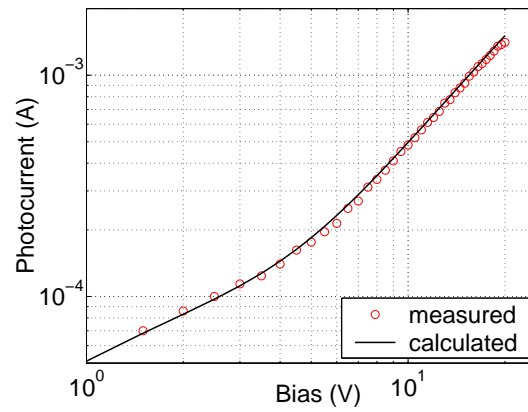


Figure 3.23.: Measured and calculated DC photocurrent data for the **CW1** (non-Bragg) photomixer.

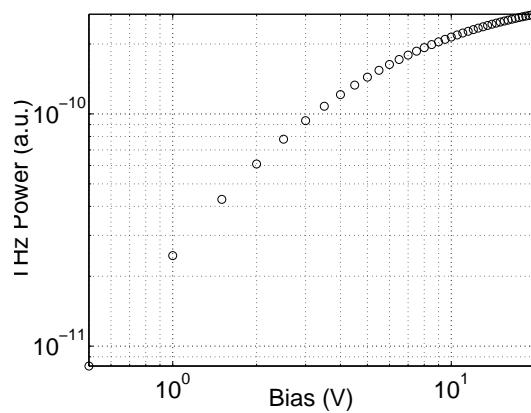


Figure 3.24.: Calculated THz output power using the model of field-dependent electron lifetime.

ure 3.18, d and w are the width of the gap and fingers, respectively. S is a scaling factor which is on the order of 10^6 .

By replacing the field-dependent lifetime in the expression for the photocurrent, as given by Eq. 3.19, with the drift velocity given by Eq. 3.20, taking $\mu_e=164 \text{ cm}^2/\text{Vs}$ and assuming an electron saturation velocity of $4.4 \times 10^6 \text{ cm/s}$, we produced an excellent fit of the measured data for the CW1 (non-Bragg) device, as shown in Figure 3.23. The value for the scaling factor used in our fit is $S=2.52 \times 10^6$ and χ calculated for the configuration and dimensions of our photogap amounts to 1.82. Here, the field-independent carrier lifetime was taken as 2 ps.

We also calculated the carrier lifetime dependence with the applied field, as shown in Figure 3.22. As it can be seen, the carrier lifetime increases up to $\sim 18 \text{ ps}$ for 20 V applied bias, with catastrophic consequences for the THz performance. As plotted in Figure 3.24, at higher bias, the produced THz power strongly saturates, rendering the use of interdigitated fingers ineffective. However, the THz power dependence on the applied bias does not reproduce the one observed in our data (Figure 3.21). Therefore, we tried to extend the analysis of the experimental data, considering the dependence of carrier lifetime with the applied field as a starting point.

3.5.4. Determination of carrier lifetime vs. electric field dependence

In Figure 3.25 we plot the DC photocurrent together with the square root of the emitted THz power as a function of the applied bias, measured for the CW1-type photomixer. The $\sqrt{P_{THz}}$ curve was scaled such that it could be overlapped with the DC photocurrent. As one can see, the DC photocurrent and the $\sqrt{P_{THz}}$ curves follow the same dependence with the applied bias up to $\sim 11 \text{ V}$, after this point, the $\sqrt{P_{THz}}$ saturates and decreases. Remembering that $P_{THz} \propto (I_{ph}^{THz})^2 / (1 + (\omega R_a C)^2)$ and since $\tau_{R_a C} \sim 0.2 \text{ ps} \ll \tau_{THz} \sim 4 \text{ ps}$ at $\nu_{THz} = 385 \text{ GHz}$ (that is, at the measurement frequency) the photomixer is RC roll-off free ($\omega R_a C \ll 1$), and therefore to a good approximation one can consider the square-root of the THz power as the THz photocurrent. Looking at the Eq. 3.22 it becomes clear that the only parameter which could cause the departure of the THz from the DC photocurrent is the carrier lifetime changing with the applied bias field.

We also checked the DC photocurrent behavior vs. THz current as a function of the applied bias for the photoconductive switch PC1 (G420) when operated as a photomixer, as displayed in Figure 3.26. The incident optical power was 50 mW in this case and the THz frequency was set to $\sim 500 \text{ GHz}$. Although the $I - V$ characteristic displays some non-linearity for the intermediate bias range, one can see that here the DC and the THz photocurrent follow the same dependence on the applied bias. This could be explained by the relatively low values of the applied electric field due to the larger dimensions of the photoswitch. The $5\text{-}\mu\text{m}$ -long pho-

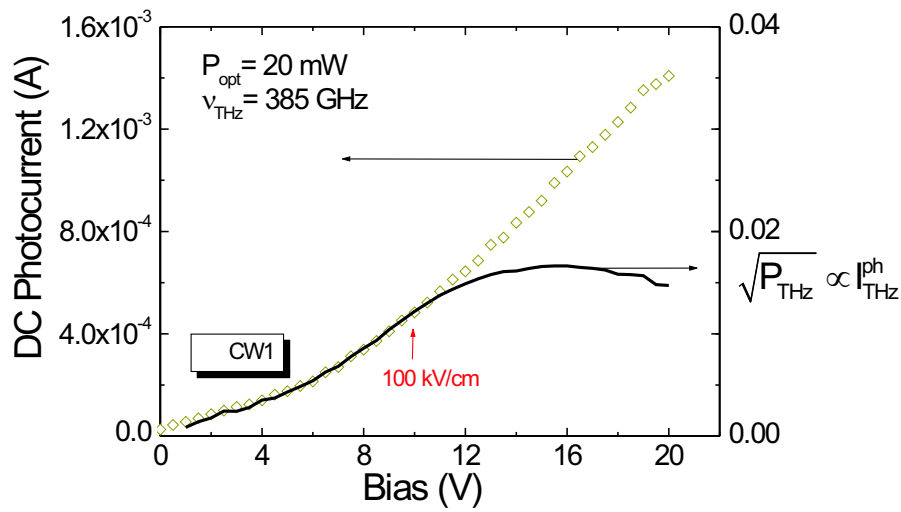


Figure 3.25.: Linear plot of the DC photocurrent vs. applied bias together with the square-root of the THz power for the **CW1** (non-Bragg photomixer).

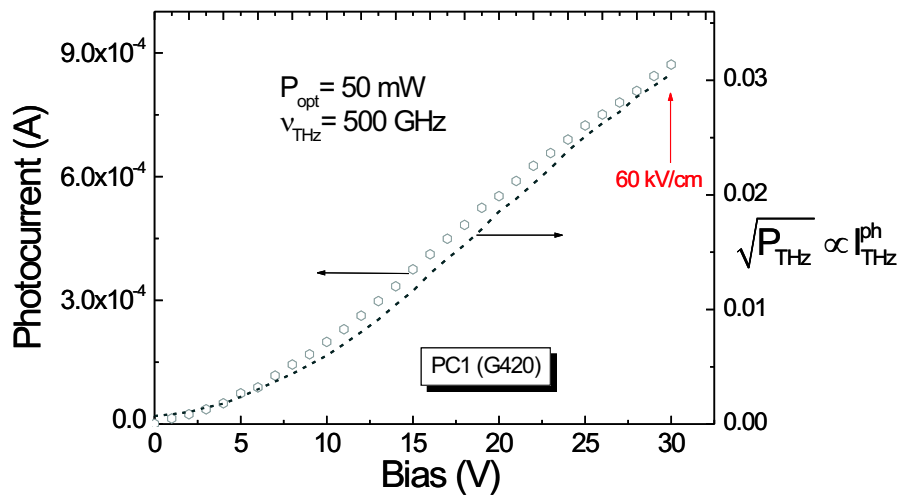


Figure 3.26.: Linear plot of the DC photocurrent vs. applied bias together with the square-root of the THz power for the **PC1** (G420).

togap produces only a 60 kV/cm field at an applied bias of 30 V. We believe that the slight departure from linearity for the observed characteristics may be ascribed to the 2-D effects caused by the non-uniform distribution of photogenerated carriers and applied field, mainly due to the large size of the photogap. Also, the lower DC photocurrent value measured for the PC1-type photomixer (although the applied optical power was considerably higher) can be accounted for by the lower mobility of the G420 LTG-GaAs layer, together with the shorter trapping time.

On the other hand, it seems possible by using Eq. 3.23 to extract the values of the electron lifetime as a function of the applied bias, by using the experimentally determined values of DC photocurrent and THz power for the CW1 device. From Equation 3.23 it follows:

$$\tau_e(E) = \frac{1}{\omega} \sqrt{\frac{R_a (I_{ph}^{DC})^2}{2P_{THz} (1 + (\omega R_a C)^2)} - 1}, \quad (3.26)$$

where, in the above equation, for an accurate determination of the field-dependent electron lifetime, the term P_{THz} should be replaced with the detected THz power P_{THz}^{det} corrected with a factor θ_c , which accounts for THz radiation coupling losses, reflection and diffraction phenomena. The θ_c is defined as:

$$\theta_c = \frac{P_{THz}^{emit}(I_{DC}(U_b = 5V))}{P_{THz}^{det}(U_b = 5V)}, \quad (3.27)$$

where $P_{THz}^{emit}(I_{DC}(U_b = 5V))$ is the calculated THz power given by Eq. 3.23 using the measured DC photocurrent value corresponding to a bias of 5 V, a field-independent carrier lifetime $\tau_e = 2.3$ ps, the measurement frequency $\nu_{THz} = 385$ GHz, the photomixer capacitance $C = 3$ fF and an antenna resistance $R_a = 65 \Omega$. The factor θ_c should be calculated at low voltages (applied fields) where the electron lifetime is supposed to be field-independent, and so the THz power dependence is not affected by the increase of the carrier lifetime, that is, the range within the THz power follows a quadratic relation to the applied bias. Loading the experimental data in a Matlab routine which also calculates the emitted and detected power (in W), the outcome is plotted in Figure 3.27. One can see that even assuming a large field-independent carrier lifetime (2.3 ps) the increase is not as severe as determined from the theoretical model of Zamdmer. However, by plotting the data in a log-log scale (see the inset of Figure 3.27) we observed that the increase in lifetime shows agreement with the $(E)^{\frac{3}{2}}$ dependence as given by the theory.

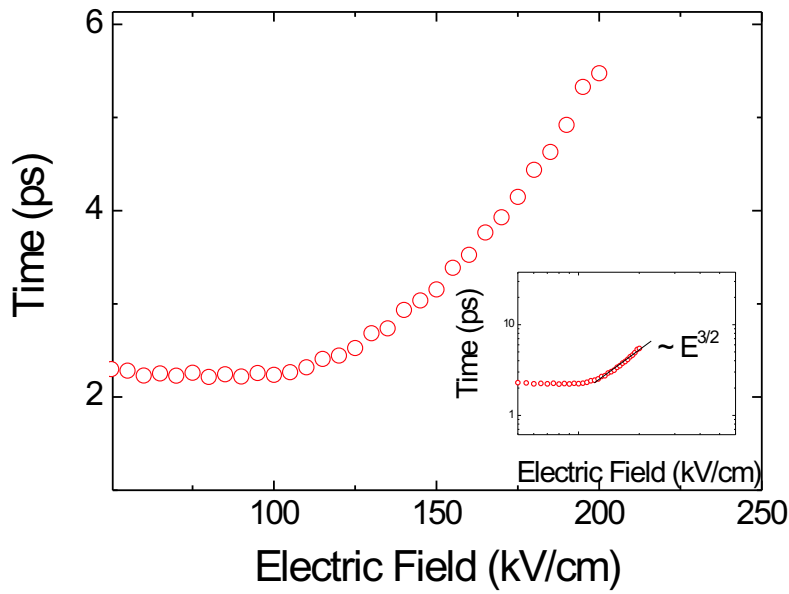


Figure 3.27.: Experimentally determined values for the field-dependent electron lifetime.

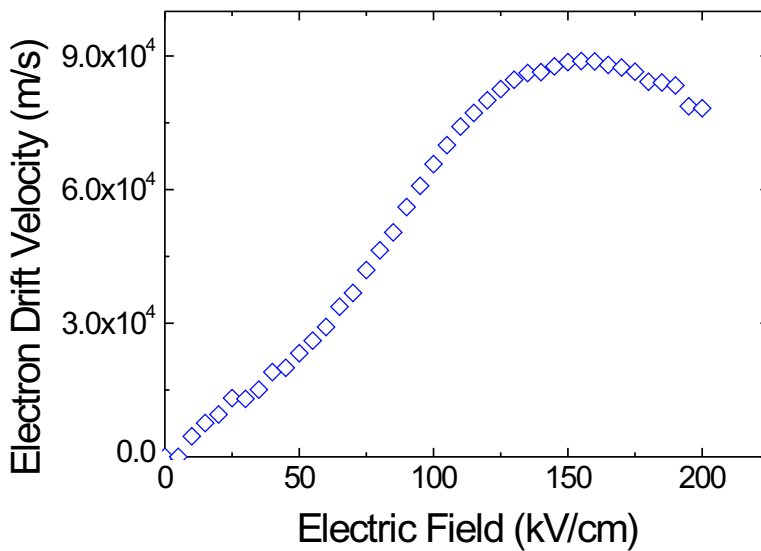


Figure 3.28.: Electron drift velocity vs. applied field as determined from the experimental data.

3.5.5. Determination of electron drift velocity vs. electrical field. Velocity overshoot in LTG-GaAs.

Having the experimental values for the field-dependent carrier lifetime and for the DC photocurrent, from Equation 3.19 it is now possible to determine the electron drift velocity dependence with the applied field:

$$v_e(E) = \frac{I_{ph}^{DC}}{P_0 \frac{\eta_{opt}}{d} \left(\frac{e}{h\nu}\right) \tau_e(E)}, \quad (3.28)$$

where, as for the case of the carrier lifetime, to obtain an accurate estimation of the carrier drift velocity, a precise estimation of η_{opt} (photon collection efficiency) is necessary. The accurate expression for η_{opt} reads:

$$\eta_{opt} = S_f \mathcal{T} (1 - e^{-\alpha_{LTG} t}),$$

where S_f is a shadowing factor accounting for the incident light reflected by the metal electrodes. It can be expressed as:

$$S_f = (l_c w_c - N_e(lw)) / l_c w_c,$$

with the l_c , w_c , l , w , explained in Figure 3.18 and N_e the number of electrodes. \mathcal{T} is given by $\mathcal{T} = 4n_{LTG} / (n_{LTG} + 1)^2$, assuming $n_{LTG}=3.62$. The value for the absorption coefficient α_{LTG} was taken to be 15000 cm^{-1} at 850 nm, although the values published in literature are scattered from 10000 to 20000 cm^{-1} . For the DC photocurrent data of the non-Bragg photomixer plotted in Figure 3.20, with $P_0=20 \text{ mW}$ and the experimentally determined $\tau_e(E)$ (Figure 3.27) we obtain the velocity versus field dependence depicted in Figure 3.28. The shape of the $v - E$ curve strongly suggests the existence of a “velocity overshoot phenomenon” in our samples.

Of crucial importance for the operation of modern semiconductor devices, the *velocity overshoot phenomenon* (VOP) manifests itself in the fact that the drift velocity has a maximum above the saturation velocity (as depicted in curve i) of Figure 3.30). The conditions under which VOP occurs are [131]: i) a carrier relaxation rate that is larger than the carrier energy relaxation rate and which is an increasing function of energy or, ii) heavier mass satellite conduction valleys at low enough energy to have a significant electron population in the steady state. While the first criteria explains VOP in non-polar semiconductors like Si, the second criteria applies for GaAs. As depicted in Figure 3.29, while the conduction band minimum in GaAs occurs at the Brillouin zone center, there are also conduction band minima at the L points, which lie about 0.3 eV higher in energy. The effective mass of electrons in these L valleys is not isotropic (for motion along the axis of the valleys the longitudinal mass is $1.9m_0$ while the transverse mass is $0.075m_0$) and also much larger than the effective mass

of $0.067m_0$ for electrons in the Γ valley. The mobility of the carriers and thus the drift velocity varies accordingly with the effective masses as described above. For a highly-crystalline material and for low excitation densities, the electrons which are generated just above the bandgap (close to the bottom of the Γ valley) accelerate very efficiently due to their small effective mass, the main scattering processes being carrier-phonon interactions (mainly acoustic phonons, hence elastic scattering) leading to momentum relaxation of carriers: the drift velocity increasing linearly with the field. At medium fields, the dominant coupling mechanism of the electrons to the crystal lattice is polar-optical (inelastic) scattering with longitudinal-optical (LO) phonons (a Froehlich-type interaction), causing a sub-linear increase of the drift velocity with the field. The carriers are still in thermal equilibrium with the lattice, the thermalisation process being very effective through momentum relaxation via polar scattering with LO phonons. Up to a threshold field (Gunn-field [132]) the carriers are still kept within the Γ -valley, this field value (~ 5 kV/cm) corresponding to the maximum electron drift velocity in thermal equilibrium¹¹ ($\sim 10^7$ cm/s in GaAs). If the field is further increased, the electrons can gain an amount of energy that is comparable to the energetic distance between the bottom of the Γ minimum and the side valleys in the L direction of the Brillouin zone (~ 330 meV for GaAs), and a very efficient momentum relaxation sets in due to *intervalley scattering*¹², with scattering times less than 20 fs [133] (at very high electric field a certain fraction of electrons might even reach the X valleys). Now, the intervalley scattering is competing with the LO phonon scattering which happens on a time interval of ~ 200 fs. On the other hand, due to the much lower density of states (DOS) of the Γ valley compared to that of the L valley, the time it takes the electron to return to the Γ valley is of the order of ps. Hence, a nonstationary situation is created, with the majority of electrons being excited into the L (or X) valley which present a lower mobility, and thus a transient velocity overshoot occurs before a steady-state drift velocity is established in the L and X valleys.

If one assumes that the band structure of LTG-GaAs is the same as that of GaAs (except that LTG-GaAs has an additional deep donor midgap band), then one can expect the occurrence of VOP. Unfortunately, compared to the numerous experimental evidence for VOP in high crystallinity GaAs, the evidence for the same phenomenon in LTG-GaAs is scarce. For example, based on THz emission data, Ludwig et al. [134], claim that VOP is responsible for THz pulse shortening

¹¹When the rates at which the carriers gain energy under the high electric field are larger than those for energy loss to the lattice, the carriers are not longer at thermal equilibrium with the lattice, becoming *hot carriers*.

¹²This process occurs via deformation potential coupling to various phonons at the zone boundary, i.e. a zone-edge phonon can scatter an electron from a band minimum at the zone center to a band minimum at the zone edge [129].

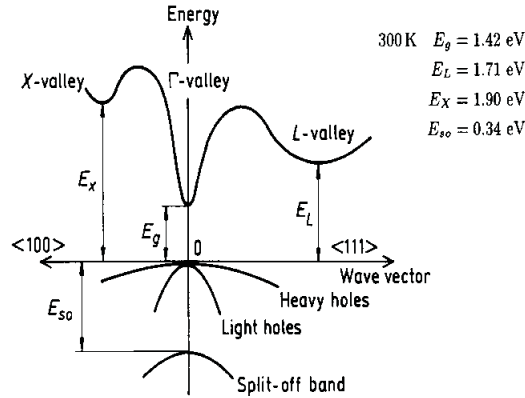


Figure 3.29.: Schematic of the valance and conduction band structure for normal GaAs. The band structure of LTG-GaAs is assumed similar to this one with an additional deep donor band at the midgap.

in the time domain. Lippens et al. [30] ascertain the nonlinear dependence of the photocurrent on the non-steady-state velocity dependence with the applied field. The possibility of VOP in LTG-GaAs was explored at some length with the help of Monte Carlo (MC) simulations by Arifin et al. [96] and latter by Reklaitis et al. [95]. In Ref. [96], the buried Schottky barrier model is used, the main parameters being the concentration and the size distribution of As precipitates, as well as the compensation ratio. Here, the electron motion in LTG-GaAs is due to the acceleration in the uniform external field on one side, as well as a non-uniform, spatially inhomogeneous internal electric field in the depletion regions surrounding the precipitates, while the electrons are simultaneously experiencing scattering events. The electric field surrounding the precipitate is repulsive and so the electron can move towards the precipitate only as long as it has enough kinetic energy. Besides the already mentioned scattering mechanisms, additional scattering due to the ionized impurities and As precipitates was accounted for. The consequence is a shift of the threshold field at which the intervalley transfer takes over to much higher field values with increasing precipitate concentration. For example, due to the additional precipitate scattering, for a precipitate concentration of $1 \times 10^{17} \text{ cm}^{-3}$, at 15 kV/cm the electron population in the L valley is reduced from 70 % to about 5 %. As can be seen in Figure 3.30, the presence of precipitates also changes the field dependence of the drift velocity. As the precipitate concentration increases (from (ii) to (vi)), the probability that an electron is reflected by the precipitate also increases, reducing the electron mean free path, and therefore a higher electric field for VOP is required at higher precipitate concentration, in order that electrons gain enough energy to reach the satellite valleys (curve (v) in Figure 3.30). This is to some extent similar to our findings (Figure 3.28), while the extremely high field ($\sim 150 \text{ kV/cm}$) at which

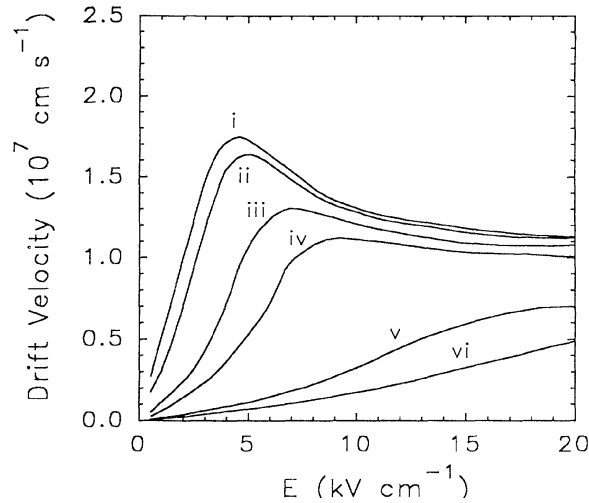


Figure 3.30.: Monte Carlo simulation of electron drift velocity as a function of electric field for different As precipitate concentrations: (i) 0, (ii) $1 \times 10^{15} \text{cm}^{-3}$, (iii) $5 \times 10^{15} \text{cm}^{-3}$, (iv) $1 \times 10^{16} \text{cm}^{-3}$, (v) $5 \times 10^{16} \text{cm}^{-3}$ and (vi) $1 \times 10^{17} \text{cm}^{-3}$ (from Ref. [96]).

the overshoot occurs can in fact be only the external field, with the effective field inside the LTG-GaAs material being much lower due to the very probable screening due to the photogenerated carriers at the contacts [135]. A very interesting result of MC simulations of electron dynamics in LTG-GaAs-type materials is presented in Ref. [95], where, on the account of the short trapping time, the authors show that both the electron excess energy of the photogenerated electrons as well as the drift velocity exceed the steady-state values. The reason lies in the fact that due to the short carrier lifetime (~ 1 ps) the photoelectron energy does not reach its stationary value at a given electric field and the drift velocity remains overshoot as long as the photogenerated electrons are present in the LTG material.

For the sake of correctness, one should also mention that one strong argument against the VOP occurrence in LTG-GaAs is the extremely short scattering times measured from THz spectroscopy [34, 75] yielding values ranging from 10-50 fs, that is, on the same time scale as the intervalley transfer.

The low-field mobility estimated from the slope of the $v - E$ curve in Figure 3.28 amounts to 160-180 cm^2/Vs , being situated at the lower end of the mobility values reported on LTG-GaAs material.

It should be emphasized that in view of the findings from Chapter 6, one should be cautious when referring to the values of the applied field as absolute field values. There we show that the long-term effect of the space-charge created after the photogeneration and transport of carriers causes a drop of the internal field in the photoswitch to only $\sim 60\%$ of the applied field. Therefore, the use of these values

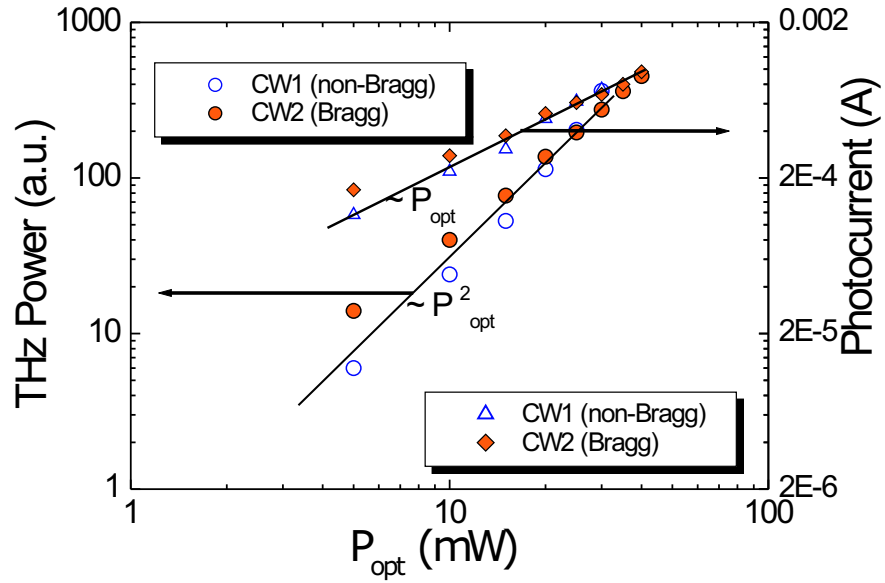


Figure 3.31.: Output THz power (left axis) and DC photocurrent (right axis) vs. optical pump power recorded at a constant bias of 10 V.

seems inappropriate for calculating parameters like mobility. Indeed, if we make the necessary corrections for the data presented in Figures 3.27 and 3.28, the resulting values for the onset of velocity shifts to only 50 kV/cm, much closer to the values predicted in Ref. [96]. Also, the value for electron mobility is situated now between 400 and 500 cm²/Vs, which is again, much closer to the values reported in literature.

3.5.6. Optical power dependence of the emitted THz power and DC photocurrent

Since we assumed LTG-GaAs a photoconductor, as derived from Eq. 3.21, linearity of photocurrent response with the optical power is expected. In Figure 3.31 we plot the THz output power and DC photocurrent versus laser pump power recorded at a constant applied bias of 10 V. In case of the Bragg-photomixers one can see a small deviation from the expected dependence, for both the THz power and DC photocurrent.

The slower increase of the THz power with the optical pump power was also reported in the literature [123] and the explanations for these observations are the photogenerated carrier-screening effect (at higher generation rates the external applied bias field is screened by the spatial separation of photogenerated carriers) or the effect of the long-lived states in LTG-GaAs material. At lower power levels, carriers with a long lifetime can affect the photocurrent and hence the THz power, even if

there are relatively few states, because the $v_e\tau_e$ product makes a dominant contribution to the photocurrent. However, at higher optical power levels, the photocurrent is dominated by electrons with a very short lifetime, since the number of short-lived traps is much larger than that of the long-lived ones. A detailed discussion of this phenomena can be found in Chapter 6.

3.5.7. Frequency response from two types of antenna and the influence of LTG-GaAs material parameters

Last, but not least, the ways in which the carrier dynamics affects the photomixer operation can also be identified by checking the THz frequency spectra. The occurrence of the effects discussed previously has an obvious deleterious impact upon the bandwidth of the photomixer. In order to characterize the performance of the photomixer, we define a figure of merit, the *efficiency*, as the ratio of the emitted THz power to the corresponding photocurrent:

$$Eff = \frac{P_{THz}}{(I_{ph}^{DC})^2} \propto \frac{1}{(1 + \omega^2\tau_e^2)}, \quad (3.29)$$

depending almost entirely on the lifetime of the carriers. As already discussed, due to the ohmic heating and the risk of burn out, a good photomixer should deliver a high THz power level for a low photocurrent.

In order to evaluate the performance of our photomixers, we recorded the frequency spectra at three different operation voltages: 6, 11, and 17 V, as presented in Figure 3.32 for the CW1 device, using the twin-diode system in the sweep mode. The 3 dB bandwidth given by the low-field carrier lifetime (assumed here ~ 2 ps) is approximately 80 GHz which is consistent with the observed 6 dB/octave roll-off for the low frequency regime. The onset of the RC time constant roll-off is given by:

$$f_{3dB}^{RC} = \frac{1}{2\pi R_a C}, \quad (3.30)$$

where by taking $R_a=65 \Omega$ and $C= 3$ fF yields ≈ 820 GHz. However, as can be seen in Figure 3.32, the frequency response of the emitted THz power for a bias of 17 V decreases above ~ 500 GHz with 12 dB/octave due to the increased carrier lifetime. Also, consistent with the saturation and decrease of THz power at high bias, we report the lowest efficiency for the 17-V-trace. Despite the quadratic increase of the THz power with applied bias, operating the photomixer at high voltage levels not only increases the burnout hazard but also yields lower efficiencies. The calculated efficiency curves, by using the field-dependent carrier lifetimes corresponding to each measurement voltage (also shown in Figure 3.32) predict quite well the frequency roll-off as well as the scaling of the experimental traces. The measured DC photocurrents corresponding to 6, 11 and 17 V were respectively 214, 566 and 1130 μA , and the carrier lifetimes 2.23, 2.32 and 3.93 ps.

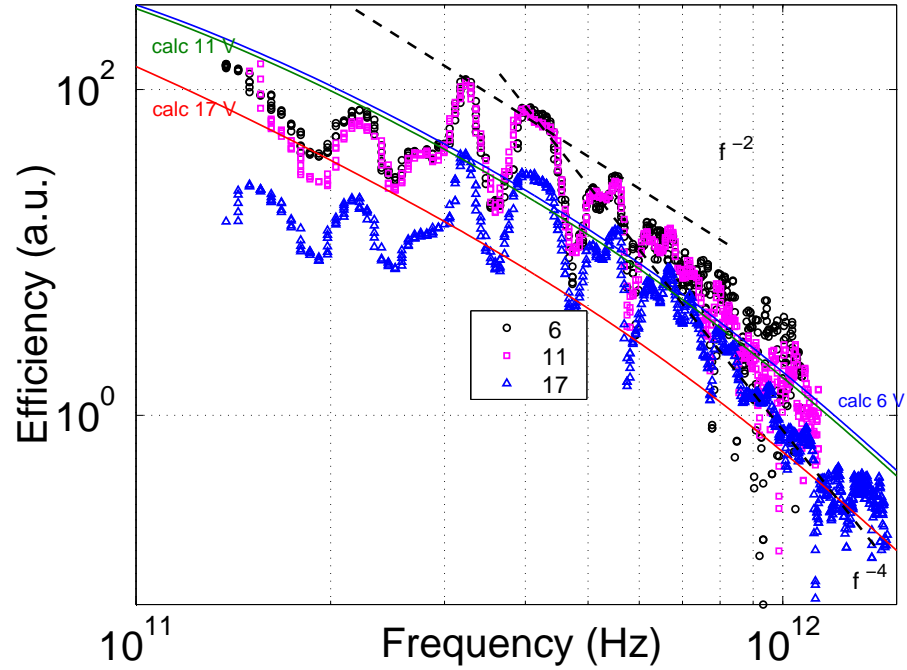


Figure 3.32.: Measured and calculated THz emission efficiency at three different applied biases for the **CW1** device. The 6 dB/octave (f^{-2}) and 12 dB/octave (f^{-4}) roll-off is indicated with a dashed line.

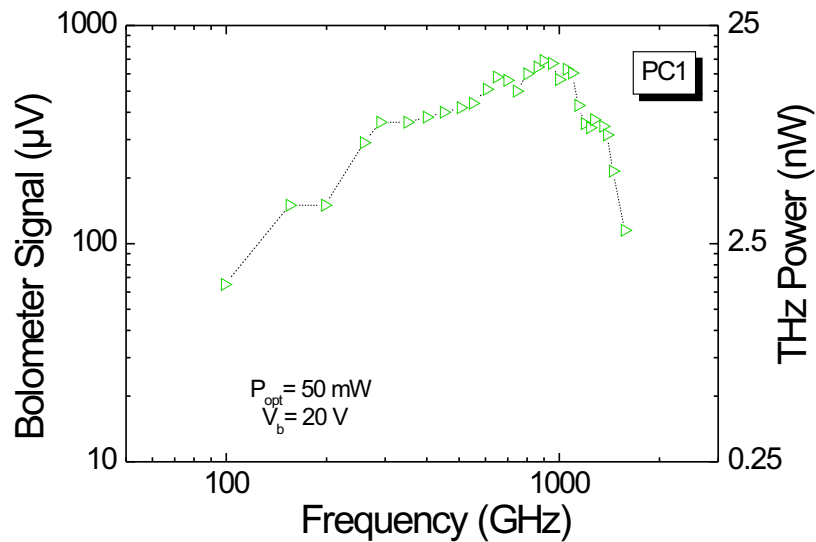


Figure 3.33.: THz power spectra of PC1 (H-dipole) emitter (G420 material).

We also recorded the CW-THz power spectra from the photoconductive antenna (PC1) grown on G420 material. The photoswitch was integrated with a H-dipole planar antenna, each dipole being 50 μm long. As already discussed in detail in Section

3.4, for a planar antenna on a dielectric half-space, the free-space resonant frequencies are modified by factoring in the effective dielectric constant for the antenna: $f_{\text{eff}} = f_0 / \sqrt{(\varepsilon_{\text{eff}})}$. Thus, the half-wave resonance frequency is given by [136]:

$$\nu_r = \frac{c}{\lambda_r} = \frac{c}{2l_e \sqrt{(1 + \varepsilon_r)}/2}, \quad (3.31)$$

where l_e and ε_r are the dipole length and the dielectric constant of the substrate. In our case, the calculated resonance is centered around 1.1 THz. On the other hand, as discussed previously, the emission bandwidth is limited by the carrier lifetime. The 1.2-ps-long trapping time determined for the G420 material yields a 3-dB cutoff frequency of ~ 132 GHz, which can partially account for the relatively low emitted THz power, on the order of tens of nanowatts. The frequency spectra presents a rather broad resonance around 1 THz, spanning a range of 200-300 GHz. Although the radiation impedance of the dipole antenna around the resonant frequency is relatively high, according to Ref. [137] the broadening of the spectral bandwidth can be due to the low Q-factor of the antenna itself, that is, a significant contribution of the off-axis components and the localization of the current distribution due to the antenna geometry.

However, the reduced efficiency of the emitters presented in this chapter can only partly be ascribed to high-field effects or impedance mismatching. As it will be discussed in the next chapters, there are others effects like long-lived screening fields with a severe impact upon the THz emission efficiency.

4. Pulsed THz radiation generated with photoconductive antennas

The present chapter contains an extensive study of THz-pulse emission from a LTG-GaAs-based photoconductive (PC) emitter¹, representing the cornerstone on which the Chapters 5 and 6 are built. After describing the principles of THz-pulse generation using a small-size photoconductive antenna, with an emphasis on the most relevant theoretical approaches in modeling the emitter response, the experimental section opens with the description of an hybrid optoelectronic generation and electro-optic (EO) detection experimental set-up used for the characterization of emitters. A thorough investigation of the emitter response as a function of the applied bias and optical power is discussed and compared against the relevant literature in the field. The observed nonlinearities (saturation behavior) in the emitter response to incident optical power is modeled through the implementation of an equivalent circuit for the PC antenna, showing that the “radiation field screening” effect induced by the presence of the dipole antenna has a dominant impact on the emitter response.

4.1. Principles of THz pulse generation with photoconductive antennas

Among the first and the simplest photoconductive (PC) antennas used to generate electromagnetic transients on a pico-second time scale was the Auston switch (also known as the photoconductive switch) [8]. It consisted of a gap in a uniform transmission line defined by thin-film metal fabrication on the top surface of an ultra-fast photoconductor (rd-SOS), acting as a Hertzian dipole. The first to report on PC antennas patterned on LTG-GaAs (or GaAs:As epilayer) were Warren et al. [138], who measured an integrated pulse width of ~ 0.71 ps and an ultrafast turn-on time due to the much higher mobility, compared to rd-SOS.

The antenna used in this work is a dipolar antenna structure, depicted in Figure 4.1, and was previously employed for pulsed THz radiation by van Exter et. al [11] due its superior characteristics: extended frequency response and increased beam power. The dipole antenna structure with a small photoconductive gap is located at the center of a coplanar transmission line, defined photo-lithographically on a LTG-

¹A planar dipole antenna integrated with a photogap on LTG-GaAs material.

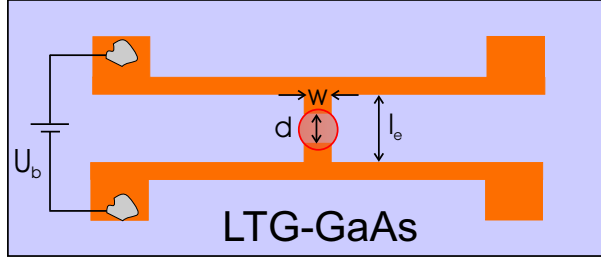


Figure 4.1.: Representation of an ultrafast photoconductive switch integrated with an dipolar antenna and terminated by the charged coplanar transmission line. The laser spot is represented by the red circle.

GaAs layer grown on a SI GaAs substrate. The emitter can be biased at any of the two ends of the transmission line through the bias pads (see Figure 4.1). The principle of operation is as follows: initially, the gap at the centre of the transmission line creates an open-circuit condition. When the small photoconductive gap is irradiated by a femtosecond laser pulse with energy greater than the band gap of the semiconductor (LTG-GaAs in our case, $E_g=1.43$ eV), electrons and holes are generated in the conduction and valence band, respectively. The instantaneous concentration of the electron and hole pairs is high enough to “short-out” the gap. The carriers are then accelerated by the bias field and decay with a time constant determined in principle by the free-carrier lifetime, resulting in a pulsed photocurrent (or a step-function-like photocurrent in long-carrier-lifetime photoconductors) flowing into the arms of the photoconductive antenna. Due to the fact the photocurrent varies on a time scale with the trapping time in LTG GaAs material (i.e. subpicosecond regime) the radiated electromagnetic (EM) transient is in the THz domain. Assuming an Hertzian dipole in an isotropic media with a refractive index $n = \sqrt{\varepsilon/\varepsilon_0}$, the electric field radiated from a time-dependent dipole moment $p(t)$ (the photogenerated carriers moving in the external bias field) is [8]:

$$E(r, \theta, t) = \frac{1}{4\pi\varepsilon} \left(\frac{1}{r^3} p(t) + \frac{n}{cr^2} \dot{p}(t) + \frac{n^2}{c^2 r} \ddot{p}(t) \right) \sin \theta, \quad (4.1)$$

where r is the distance from the dipole, θ is the angle relative to the dipole axis, and c is the speed of light in vacuum. The three terms in the Eq. are: the quasi-static field, the near field and the far field, each with different spatial and temporal variations. Due to its $1/r$ dependence, the far-field will dominate as we move away from the emitter. Hence, the magnitude of the radiated field can be estimated from the fact that the first derivative of the dipole moment is equal to the product of photocurrent $i_{pc}(t)$ in the photogap and the length of the dipole l_e . Therefore, the detected far-field radiation amplitude is proportional to the time derivative of the

transient photocurrent $\partial i_{pc}(t)/\partial t$ and the effective antenna length l_e :

$$E_{THz}(r, \theta, t) = \frac{l_e}{4\pi\epsilon c^2 r} \frac{\partial i_{pc}(t)}{\partial t} \sin \theta. \quad (4.2)$$

The photocurrent has a rapid rise time due to the excitation of free carriers by the femtosecond laser pulse, and decays rapidly due to their capture at traps. Hence the radiated optical field will have a bipolar shape with a positive component having an amplitude proportional to the photocurrent rise time followed by a negative component due to the decay time.

The photocarrier generation rate $g(\vec{r}, t)$ is the number of electron-hole pairs created per unit volume per unit time, depending on the incident pump beam intensity:

$$g(\vec{r}, t) = \frac{\alpha I_{opt}(\vec{r}, t)}{h\nu} = \frac{\alpha E_{opt}^2(t)}{Z_0 h\nu}, \quad (4.3)$$

where α is the absorption coefficient, $E_{opt}(t)$ is the time-dependent optical electric field, Z_0 is the intrinsic impedance of the medium, and $h\nu$ is the photon energy. One can see that due to its quadratic dependence on the optical electric field, the photocarrier density in response to a mode-locked laser can be computed in terms of the ‘‘envelope’’ of the optical pulse rather than the instantaneous field. In terms of the incident optical power, one can write the photocarrier generation rate as:

$$g(\vec{r}, t) = \eta \frac{P_{pulse}(t)}{h\nu}. \quad (4.4)$$

The quantum efficiency in this case is given by:

$$\eta = \frac{P_{abs}}{P_{inc}} = (1 - \mathcal{R})(1 - e^{-\alpha t_{LT}}),$$

where \mathcal{R} is the reflectivity of the photoconductor-air interface ($\mathcal{R} \simeq 0.3$ for LTG-GaAs-air interface), and t_{LT} the thickness of the photoconducting layer.

The hyperbolic secant time-dependence of ultrashort pulses from a mode-locked laser can be approximated to a very good extent by assuming a Gaussian pulse shape:

$$P_{pulse}(t) = P_{pulse}^0 \frac{1}{T_0} \sqrt{\frac{2}{\pi}} \exp\left(-\frac{t^2}{T_0^2}\right), \quad (4.5)$$

with $T_0 = \frac{T_{FWHM}}{\sqrt{4 \ln 2}}$, where T_{FWHM} is the pulse duration at full width half maximum.

The time evolution of photogenerated carriers density is given by the following rate equation:

$$\frac{dn}{dt} = \eta \frac{P_{pulse}(t)}{h\nu} - \frac{n}{\tau_c}, \quad (4.6)$$

where τ_c is the electron trapping time, and n is the electron density, and the same equation holds for holes. Here, we made a series of simplifying assumptions: the carrier recombination is *bimolecular*, meaning that the excess electrons and holes

annihilate in pairs, the number of empty traps is not significantly changed throughout the pump duration, uniform illumination and neglecting any diffusion current. The solution to Eq. 4.6 including both the homogeneous and inhomogeneous solutions, can be found from the signal processing theory, calculating the convolution between the impulse response function $h(t, t')$ and the optical pulse. Considering the free-carrier relaxation governed by a single exponential, the impulse response function is of the form $h(t, t') = e^{-\frac{(t-t')}{\tau_c}}$, and the solution of Eq. 4.6 becomes:

$$\begin{aligned} n(t) &= \frac{\eta}{h\nu} \int_{-\infty}^t h(t, t') P_{pump}(t') dt' \\ &= \eta \left(\frac{P_{pulse}^0}{h\nu} \right) \frac{1}{T_0} \sqrt{\frac{2}{\pi}} \int_{-\infty}^t \exp\left(-\frac{(t-t')}{\tau_c}\right) \exp\left(-\frac{t'^2}{T_0^2}\right) dt' \quad , \quad (4.7) \\ &= \eta \left(\frac{P_{pulse}^0}{h\nu} \right) \frac{1}{\sqrt{2}} \exp\left(-\frac{t}{\tau_c}\right) \exp\left(\frac{T_0^2}{4\tau_c^2}\right) \left[1 - \operatorname{erf}\left(\frac{T_0^2}{2\tau_c} - \frac{t}{T_0}\right) \right] \end{aligned}$$

where erf is the *error function* with the integral representation $\operatorname{erf}(x) \equiv \frac{2}{\sqrt{\pi}} \int_0^x \exp(-t^2) dt$.

The dynamics of the photogenerated carrier density is a critical part of the analysis and also a subtle issue in ultrafast photoconductors since it is a sensitive function of the trapping and recombination mechanisms.

In fact, for a LTG-GaAs based PC antenna, the rise and decay of the photocurrent is a very sensitive function of the optical pulse duration, the laser photon energy, the device capacitance, the spatial distribution of the electric field in the photogap as well as the photogenerated carrier mobility and lifetime in the LTG-GaAs material. For example, the emitted THz radiation cannot contain frequency components varying more rapidly than the derivative of the pulse envelope, which limits the bandwidth to ~ 5 THz. The optical excitation energy plays an important role since exciting carriers with an excess energy above the bandgap results in the complication of the carrier dynamics through intraband carrier relaxation mechanisms [139].

If we include the effect of a transient velocity $v_e(t)$, the instantaneous photocurrent density flowing in to the antenna can be described as [140]:

$$j_{pc}(t) = P_{pulse}(t) \otimes (en(t)v_e(t)) \quad , \quad (4.8)$$

where \otimes denotes the convolution product and the $en(t)v_e(t)$ product represents the impulse current of the photoswitch. The time-dependent average velocity, assuming a one-dimensional Drude-Lorentz model², can be expressed as:

$$\frac{dv(t)}{dt} = -\frac{v_e}{\tau_s} + \frac{e}{m^*} E \quad , \quad (4.9)$$

²The applicability of the Drude-Lorentz model for the PC emitter is supported by the generated high carrier density 10^{17} - 10^{19} cm^{-3} , since at these densities scattering acts very efficiently on restoring thermal equilibrium among the carriers in less than 100 fs [141].

where τ_s is the momentum relaxation time, m^* is the carrier effective mass and E is the local electric field (i.e., the local electric field “sensed” by the carriers). Based on the above equations, numerous authors like Jepsen et al. [141], Piao et al. [142] and Duvillaret et al. [140] calculated and predicted the emission characteristics of the PC antennas. The same authors outlined the considerable importance of the electron-hole interaction on the picosecond time scale (i.e., the ultrafast dynamics of the screening field produced by the polarization of the electrons and holes moving in the external field). Nemeč et al. [65] developed a model that allows for extracting the parameters of ultrafast carrier dynamics in LTG-GaAs from the shape of the generated THz waveform, in a THz pump–probe experiment, also taking into account the spectral response of the detector. They add an extra term on the right-hand-side of Eq. 4.9 as a correction for the mean velocity v of the free carriers during the generation process, accounting for the density of newly generated carriers with zero average speed: $-\frac{v_{eg}(t)}{n}$.

To attain the highest frequencies, the temporal parameters (pulse duration, carrier lifetime, carrier scattering time) should be as short as possible. Also, according to simulation results [140], the increase of the carrier lifetime (trapping time) and of the scattering time enhances the signal in the low-frequency part of the spectrum, as well as the total THz power integrated over the hole spectrum. The increase in the amplitude of the THz radiation is due to the increase of the saturation velocity proportional to the carrier scattering time τ_s [142]. More recently, Castro-Camus et al. [143], performed a semi-classical Monte Carlo simulation of THz emission from PC switches as a function of bias voltage, pump-pulse duration and pump-pulse position on the photogap, confirming some of the experimental observations. The simulations shows that, for example, for pulses longer than 40 ps, the bias field screening due to the long injection time of the carriers affects the overall performance of the emitters. It was also found that the field screening is mainly controlled by the carrier dynamics and not by the injection time for pulses shorter than 100 fs.

In this chapter we are looking at some of the basic characteristics of the LTG-GaAs based PC antennas, trying to understand certain features of the THz emission which develop when the operation conditions (bias and pump power) change, while the more intricate aspects of carrier dynamics (trapping and recombination processes and field screening effects) will be dealt with in the next chapters.

4.2. Experimental setup for pulsed THz generation and detection

The experimental set-up used for the generation and detection of THz-pulsed radiation consists of a femtosecond laser source, a LTG-GaAs-based photoconductive antenna, an optical delay line, THz optics and a detection system, as illustrated in Figure 4.2.

A mode-locked Ti:Sapphire laser (Tsunami, Spectra Physics) was pumped with 5 W CW radiation at 532 nm derived from a diode-pumped solid-state (intracavity-doubled Nd:YAG) laser system (Millenia, Spectra Physics), delivering pulses as short as 100 fs at a wavelength centered around 800 nm at an average power of ~ 1 W. The pulse repetition rate (given by the duration of one pulse round trip inside the resonator) was 82 MHz.

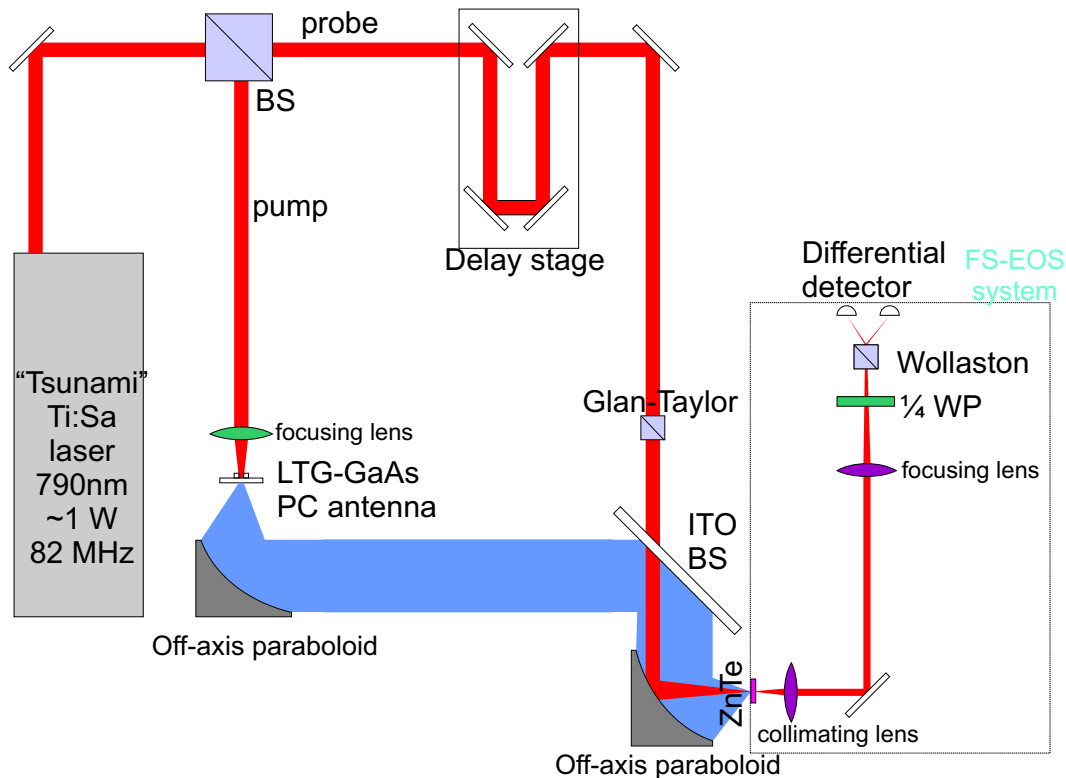


Figure 4.2.: Schematic of the experimental setup for THz-pulse generation and detection.

In order to allow for free-space electro-optic sampling (FS-EOS), the output beam of the Ti:Sapphire laser was split with a beam-splitter into two beams: a pump beam (high power) and a probe beam (low power). The probe beam, arriving at the THz detector crystal, was synchronized with the THz pulse using a scanning optical delay line consisting of a corner cube mounted on a computer-controlled delay stage (Newport). To ensure a linear polarization, necessary for the detection scheme, a

Glan-Taylor polarizer was inserted in the probe beam after passing through the optical delay line.

The pump beam illuminates the photoconductive antenna emitter after passing through a short focal length lens ($f=20$ mm) which focuses the ~ 5 mm laser beam down to a $\sim 7 \times 7 \mu\text{m}^2$ area in the photogap. The level of optical power incident on the emitter was varied by inserting a circular neutral-density (ND) filter in the pump beam. A voltage bias was applied to the emitter by connecting the coaxial cable from the PC antenna in series with a variable ($0\text{-}\pm 30$ V) voltage source connected in series with an ampere-meter (Keithley), enabling also the monitoring of the DC photocurrent flowing in the photogap. To allow for lock-in detection, the pump beam was optically chopped at a frequency of ~ 1.5 kHz. The lock-in time constant and sensitivity were set to around 100 ms and 1 mV, respectively. For an enhanced signal-to-noise ratio (SNR), the emitter was biased with a 25 kHz square-wave signal between ± 12.5 V from a function generator. Unfortunately, this biasing scheme prevents us from monitoring the DC photocurrent. As a word of caution, one should be careful with the size and the isolation of the wires between the PC antenna chip and the coaxial cable since, if not properly isolated, those could in principle emit RF transients that are then picked-up by the EO detection scheme (giving rise to THz signal artifact).

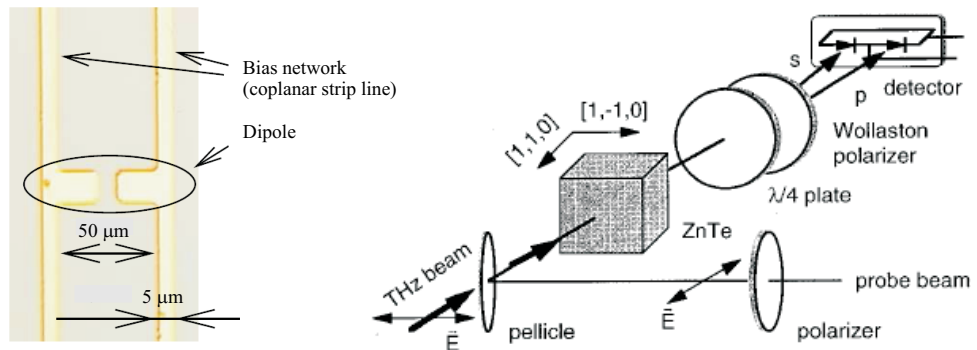


Figure 4.3.: Picture of the THz emitter used (left) and details of the EO detection system (right).

For all the experiments described in this work involving THz-pulse generation, the PC antenna employed was an H-shaped dipole antenna [11] with a $50\text{-}\mu\text{m}$ long dipole and a $5 \times 10 \mu\text{m}^2$ photoconductive gap, embedded in a $50\text{-}\mu\text{m}$ spaced coplanar transmission line, as shown in Figure 4.3 (left). The manufacturing of devices was done by photolithography. The metalization consisted of 200 nm of Ti/Au for the emitter fabricated on the LTG-GaAs material grown at TU Wien (for an accurate description of the LTG-material used see Chapter 2), from hereon denominated as PC1, and 100 nm of Pt for the emitters processed on the LTG-GaAs material grown

at the University of Erlangen, denominated as PC2 for the LTG-GaAs substrate without Bragg reflector (“non-Bragg”) and PC3 for the emitter with an embedded Bragg reflector (“Bragg”). An inventory of the PC emitters used in the present work is presented in Appendix B.

The generated THz beam was collected and collimated by an off-axis paraboloidal mirror with an effective focal length (off-axis distance) of $f=50.4$ mm. A pellicle beam splitter (a thin ITO film) which acts as a reflector for THz but transmits the optical radiation is used to combine and overlap the THz and the probe beam so that they copropagate. The collimated THz beam together with the probe beam were then focused onto a 1-mm-thick $\langle 110 \rangle$ -cut ZnTe crystal for electro-optic detection with a second paraboloidal mirror of the same focal length as the first one.

Figure 4.3 (right) shows the detailed FS-EOS system used for coherent detection of the THz-pulse beam [144, 145, 146, 147, 148, 149]. The detection principle is based on the linear electro-optic (EO) effect (Pockels effect): the incident electric THz field strength alters the refractive index ellipsoid of the EO crystal (ZnTe, in this case) producing a phase retardation (PR) of the linearly polarized optical probe beam. By monitoring the PR, the field strength of the THz pulse is detected. The polarization of both the THz and optical beams are aligned parallel to the $[1,-1,0]$ direction of a $\langle 110 \rangle$ oriented ZnTe crystal for optimal electro-optic phase modulation, as illustrated in Figure 4.3 (right). Since ZnTe has no intrinsic birefringence, a quarter-wave ($\lambda/4$) plate is used to impinge a $\pi/4$ retardation (optical bias), allowing the system to be operated in the linear range. The THz-radiation-field-induced PR of the probe beam is converted to an intensity modulation between two mutually orthogonal linearly polarized beams using a Wollaston prism. The optical intensity modulation is detected using two balanced silicon photodiodes. We can write the probe intensities in the s and p polarizations:

$$\begin{aligned} I_s &= \frac{I_0}{2} (1 - \Gamma) \\ I_p &= \frac{I_0}{2} (1 + \Gamma) \end{aligned} \quad (4.10)$$

where Γ is the phase difference between the two beams and I_0 is the input intensity. In the two beams, the signals have the same magnitudes but opposite signs. For balanced detection, the difference between I_s and I_p is recorded, yielding the signal:

$$I_{signal} = I_p - I_s = I_0 \Gamma, \quad (4.11)$$

where Γ is the THz-induced phase change which is given by:

$$\Gamma = \frac{\pi d n^3 \gamma_{41}}{\lambda} E, \quad (4.12)$$

where d is the thickness of the crystal, n is the refractive index of the ZnTe crystal at the wavelength of the probe beam, λ is the probe wavelength, γ_{41} is the EO coefficient, and E is the electric field of the THz pulse. The optical delay line changes

the time delay between the THz pulse and the (much shorter) probe pulse and the THz electric field-waveform can be obtained by scanning this time delay and performing a repetitive sampling³ measurement. Note that due to the shorter relative wavelength, the optical probe beam focuses more tightly in the ZnTe crystal than the THz beam, therefore only the on-axis THz electric field is effectively sampled in the detector crystal. The balanced detectors suppress the laser noise (fluctuations). The probe power used in the FS-EOS detection was about 5 mW (around 2.5 mW on each photodiode). In order to maximize the SNR, the photocurrent in each photodiode has to be maximized but be kept below saturation. In achieving a good sensitivity of the EO detection setup, a good electrical and optical balancing of the two photodiodes forming the differential detector is crucial. First, one must check if a constant bias of 12 V is present at the terminals of each photodiode. The optical balancing is done by optically chopping the probe beam and monitoring the signal from the differential detector on the lock-in amplifier: by rotating the $\lambda/4$ -wave-plate the signal on the lock-in should be extinguished for a well balanced detector (the sensitivity of the lock-in can be as high as 300 μV).

Due to the fact that one has to detect very small changes in polarization, typically on the order of 10^{-4} – 10^{-5} , the FS-EOS detection scheme is very sensitive to low-frequency mechanical and acoustical disturbances.

4.3. Emission characteristics of LTG-GaAs-based photoconductive antennas

Under the assumption that the transient photocurrent is the primary THz-pulse generation mechanism, it is believed that the pulse waveform reflects the non-equilibrium transport dynamics of the photogenerated carries in the emitter [150]. In an attempt to elucidate at least some of the properties/features of carrier dynamics in LTG-GaAs-based devices, this section deals with some of the emission properties of the PC antennas obtained for different operating conditions (i.e., different bias and optical power).

4.3.1. Voltage bias dependence of the emitted THz field

First we performed an investigation of the waveform, amplitude and spectral width of the THz-pulse for different values of applied bias. We measured PC antennas on three different substrates (PC1, PC2 and PC3, see Appendix B) but since all emitters displayed essentially identical features, we choose to display only data from PC1. The bias was varied between 2 and 30 V (4-60 kV/cm) while the optical pump

³Because the EO (Pockels) effect is almost instantaneous on the THz time scale, FS-EOS gives a signal directly proportional to the THz electric field - acting as a sampling detector.

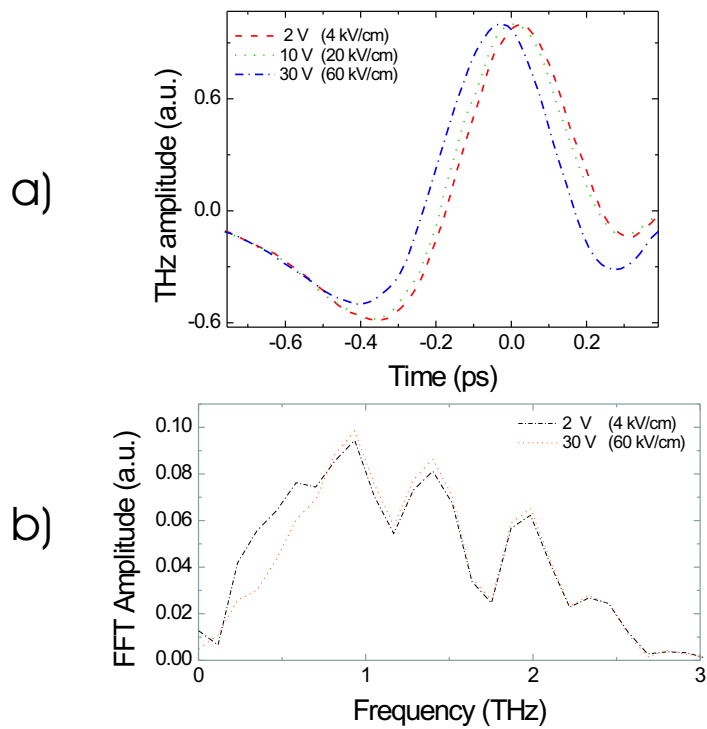


Figure 4.4.: Normalized THz pulse shape at three different biases (a) and Fourier spectra of the THz pulses for two different biases (b) for the **PC1** emitter.

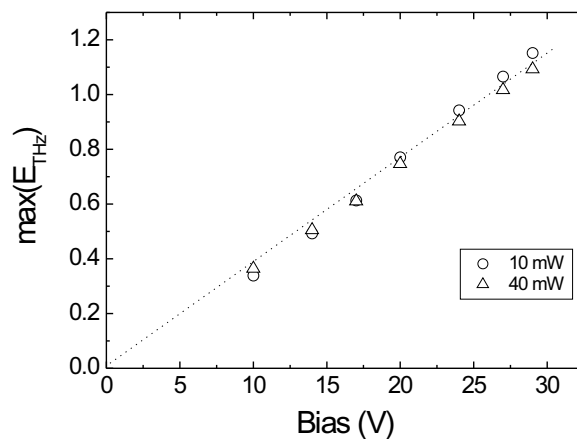


Figure 4.5.: Dependence of the THz peak amplitude with the applied bias for 10 and 40 mW optical power measured from the **PC1** emitter.

power was kept constant around ~ 20 mW, corresponding to an excitation density of $\sim 6.7 \times 10^{18} \text{ cm}^{-3}$. To be able to compare the changes in THz waveform with bias, we normalized each temporal profile to unity. As one can see in Figure 4.4 (a), at higher external bias fields, the THz-pulse shape displays a stepper increase together with the shift of the peak to earlier time delays and also an earlier decay. We estimate around 90 fs difference between the arrival of the peaks between the 4- and 60-kV/cm bias condition. By taking the FFT of the normalized waveforms, we obtain the frequency spectra of the THz wave, as plotted in Figure 4.4 (b). Unfortunately, since the THz generation and detection experiments were not performed under purged N_2 atmosphere, one can notice the "fingerprints" of water-absorption lines [151]. In accordance with the shortening and shifting of waveform at earlier times, the maximum of the THz spectra shifts to higher frequencies.

The same behavior was reported by Ludwig et al. in [134] for the same type of emitter under somewhat slightly different experimental conditions, namely higher applied biases (up to 100 kV/cm) and lower excitations density ($\sim 3 \times 10^{16} \text{ cm}^{-3}$). Inspired by the work of Son et al. [150] and Iverson et al. [152], the authors associate the observed features with the occurrence of velocity overshoot in the LTG-GaAs material. As previously discussed in Section A.1, the positive peak of the THz waveform is associated with the acceleration of photogenerated carriers in the external bias field. Also, the negative peak corresponds to the photocurrent decay through trapping or deceleration. Hence, the above experimental observations are associated with a faster carrier acceleration followed by the earlier transfer from the high-mobility Γ -valley to the low-mobility L -valley and hence a stronger deceleration which results in a photocurrent overshoot. Indeed, as can be seen in Figure 4.4 (a), at 60 kV/cm the negative peak is more pronounced than the one at 4 kV/cm. However, we excite a rather high density of carriers, which according to Ref. [132] should prevent the occurrence of velocity overshoot due to the very effective carrier-carrier scattering. Contrary to what is reported in Ref.s [134] and [150], where the peak amplitude of the THz pulse saturates and then decreases for fields > 40 kV/cm, we measured a linear dependence of the maximum amplitude of the THz pulse with applied bias for two different excitation densities as illustrated in Figure 4.5, similar to what Sakai et al. reported [153]. The data measured for 10 and 40 mW are normalized. The slightly steeper slope for the 10 mW-curve might be due to photogenerated carrier field-screening effects, as discussed in the next chapters.

4.3.2. Optical power dependence of the emitted THz field

Next, we checked the influence of the photocarrier density upon the waveform and the peak electric field of the radiated THz pulse. We measured both the DC photocurrent and the THz-pulse peak amplitude as a function of optical pump power.

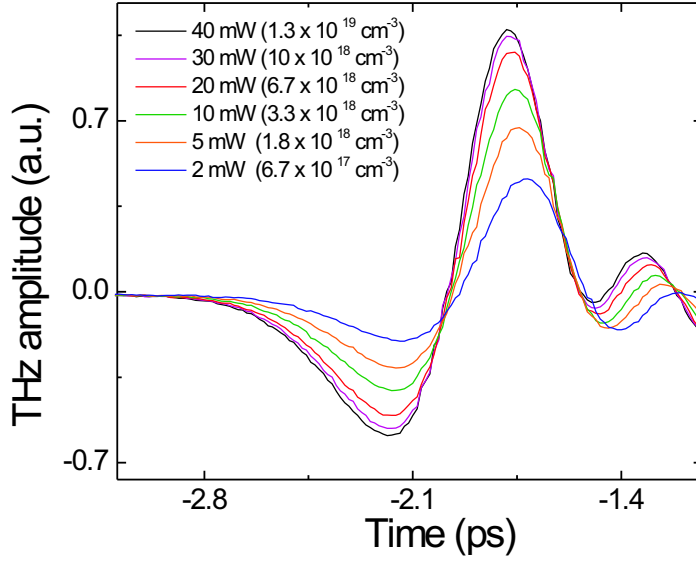


Figure 4.6.: THz temporal waveforms for PC2 emitter recorded at different optical power levels and a constant applied bias of 5 V (10 kV/cm).

We performed these measurements at two different biases (5 and 10 V) for all three types of PC antenna available, observing for each emitter similar features. In Figure 4.6 we plot the recorded THz waveforms from PC2 at a constant applied bias of 5 V (10 kV/cm) while the incident optical power was varied from 2 to 40 mW. Care must be taken here when assessing the shift of the THz-pulse peak towards earlier times since in varying the optical power, the neutral density filter might have changed its optical path length and therefore the zero-time delay of the experiment shift slightly. However, one can observe a slight broadening of the THz waveform at higher excitation densities. But the most interesting feature is the saturation of the THz-pulse peak with increasing optical fluence.

The first to report on this phenomenon in small-size PC antennas was Tani et al. [136], measuring different types of antenna on LTG-GaAs. The same author also reports the saturation of the peak current signal in PC detectors fabricated on SI-InP, LTG-GaAs and SI-GaAs, similar to the saturation of the DC photocurrent observed by us. Recently, Liu et al. [154] using H-dipole PC antenna fabricated on arsenic-ion-implanted GaAs observed the same saturation behavior, while recently, Chimot et al. [155] reported it for heavy-ion-irradiated InGaAs PC antennas illuminated at 1.55 μm , where the saturation level is increased with increasing the irradiation dose (lower mobility).

In early attempts to explain the observed saturation behavior, Tani and other

authors cited above attributed the observed saturation behavior for both the photocurrent and the radiated THz field to the screening of the applied bias field by the photogenerated electrons and holes [136, 156]. The saturation behavior was analyzed following the model of Darrow et al. [157, 158] and Benicewicz et. al [159] derived for large aperture PC emitters, hence neglecting the limitations imposed by the non-uniform boundary conditions imposed by the micrometer-sized PC antenna. First of all, one should mention that the work of Darrow et al. is concerned with the screening of the applied bias field by the generated THz radiation field (hence the name “radiation field-screening”) and not with the screening produced by the spatial separation of electrons and holes, which, as latter shown by Rodriguez et al. [160] plays an insignificant role in large-area PC emitters. As described in detail in Ref.s [157] and [159], in large-aperture photoconductive antenna⁴ a screening of the applied bias field occurs due to the radiated THz near-field. This phenomenon is caused by the boundary condition on the electric and magnetic fields at the surface of the emitting region. The radiated near-field $E_r(t)$ is given by [157]:

$$E_r(t) = -E_b \frac{\sigma_s \eta_0}{\sigma_s \eta_0 + (1 + \sqrt{\varepsilon})}, \quad (4.13)$$

where E_b is the bias field, σ_s is the surface conductivity, η_0 is the characteristic impedance of the free space (377Ω) and ε is the dielectric constant of the photoconductor. The surface current can also be expressed as a function of the radiated field (into the substrate):

$$J_s = -\frac{E_b \sigma_s}{1 + \frac{\sigma_s \eta_0}{(1 + \sqrt{\varepsilon})}}. \quad (4.14)$$

Thus, when the surface photoconductivity of the emitter is on the same order of magnitude to the radiation admittance, the radiated near field will saturate at a value compared to that of the applied bias. If the detection is performed in the far-field, than the term at the numerator becomes squared, the saturation behavior being more accentuated.

For the large-area PC emitters this radiation field screening effect is valid only for emitters with dimensions much larger than the emitted THz wavelength. Even if it is very tempting to apply this model to the small PC antenna, one should take care, because, as early mentioned by Darrow et al., there are a sum of assumptions made for the large-area emitters: firstly, due to its much smaller center wavelength compared to the current distribution dimensions, the radiated field can be best approximated with plane waves and, secondly, the inward and outward radiated field are equal - which is not true in case of a Hertzian dipole antenna on a dielectric [8]. The dipole antennas also produce highly divergent radiation due to the fact

⁴A large aperture photoconducting antenna consists of a planar photoconductor (GaAs or InP) onto which parallel conducting electrodes with the spacing varying from $500 \mu\text{m}$ to 30.0 mm are defined.

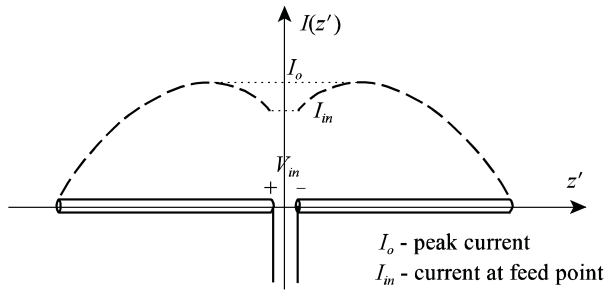


Figure 4.7.: Schematic representation of the current distribution across a center-fed dipole antenna illustrating the concept of input impedance by designating the input current and voltage.

that their dimensions are comparable to the emitted wavelength, hence the field uniformity condition can not be fulfilled.

However, as discussed in the next section, we ascribe part of the saturation behavior to a similar effect, that is, a screening of the applied bias field in the photogap due to the near-field THz radiation of the antenna as a whole.

4.4. Saturation behavior and radiation field screening in small-size LTG-GaAs photoconductive antennas

As already mentioned in Section A.1, the two metallic antenna arms situated halfway along the coplanar strip-lines of the PC emitter are fed with the time-varying photocurrent produced by the incoming laser pulse and the electrical field across the photogap, constituting a center-fed half-wavelength dipole. Without getting to much into the details of antenna theory, we outline in the following some basic parameters that can explain in a simple equivalent circuit picture the mechanism of radiation field screening.

4.4.1. Antenna impedance and radiation resistance

The *input impedance* of an antenna can be defined as “the impedance presented by an antenna at its terminals or the ratio of the voltage to current at a pair of terminals, or, the ratio of the appropriate components of the electric to magnetic fields at a point”[121]. If we consider a dipole antenna as illustrated in Figure 4.7 being driven with the input voltage V_{in} and current I_{in} , the antenna impedance (or driving point impedance) can be expressed as:

$$Z_{in} = \frac{V_{in}}{I_{in}} = R_{in} + jX_{in}, \quad (4.15)$$

where R_{in} and X_{in} are the antenna resistance and reactance, respectively at the input terminals (for a given frequency). Usually, the resistive part R_{in} is the sum of the loss resistance (power dissipated through the ohmic heating of metalization) and the *radiation resistance*. The reactive part represents energy stored in the static field near the antenna.

According to Ref. [161], the radiation resistance of an antenna is that equivalent resistance which would dissipate the same amount of power as the antenna radiates when the current in that resistance equals the input current at the antenna terminals. To refer the radiation resistance to the input terminals of the antenna, the antenna itself is assumed to be lossless.

In order to find the input resistance for a lossless antenna, one can form the Poynting vector in terms of the complex \mathbf{E} - and \mathbf{H} -fields radiated by the antenna:

$$\mathcal{P} = \frac{1}{2} \mathbf{E} \times \mathbf{H}^*. \quad (4.16)$$

The total power radiated by the source (antenna) is obtained by integrating the Poynting vector over a closed surface (usually a sphere) while relating the real part of it to the radiated power and the radiation resistance:

$$\begin{aligned} P &= \oiint_S \mathcal{P} ds \\ &= \frac{1}{2} \iint_S \mathbf{E} \times \mathbf{H}^* ds \quad , \\ &= P_{\text{rad}} + j2\omega(\tilde{W}_m - \tilde{W}_e) \end{aligned} \quad (4.17)$$

where P is the power in the radial direction, P_{rad} is the time-average radiated power while:

$$\begin{aligned} \tilde{W}_m &= \frac{1}{2} \iiint_V \frac{1}{2} \mu |\mathbf{H}|^2 d\mathbf{v} \\ \tilde{W}_e &= \frac{1}{2} \iiint_V \frac{1}{2} \varepsilon |\mathbf{E}|^2 d\mathbf{v} \end{aligned} \quad (4.18)$$

are the time-average electric and magnetic energy density (in radial direction), respectively.

In terms of the incident current and voltage defined in Figure 4.7, a statement of power flow can be written as:

$$P = \frac{1}{2} V_{\text{in}} I_{\text{in}}^* = \frac{1}{2} Z_{\text{in}} I_{\text{in}} I_{\text{in}}^* = \frac{1}{2} Z_{\text{in}} |I_{\text{in}}|^2. \quad (4.19)$$

By equating the right-hand-side of Eq. 4.17 and 4.19 one obtains:

$$Z_{\text{in}} = \frac{P_{\text{rad}} + 2j\omega(\tilde{W}_m - \tilde{W}_e)}{\frac{1}{2} I_{\text{in}} I_{\text{in}}^*}. \quad (4.20)$$

Through separation of the real and imaginary parts in Eq. 4.20, the radiation resistance at input (feed) terminals becomes:

$$R_{\text{in}} = \frac{P_{\text{rad}}}{\frac{1}{2} |I_{\text{in}}|^2}. \quad (4.21)$$

For the situation depicted in Figure 4.7, the radiation resistance is referred to the maximum current I_0 , which for some lengths of the dipole does not occur at the input terminals of the antenna. To obtain the radiation resistance, one must equate the power at the input terminals to the power at current maximum:

$$\frac{1}{2} |I_{\text{in}}|^2 R_{\text{in}} = \frac{1}{2} |I_0|^2 R_{\text{rad}}, \quad (4.22)$$

and thereby:

$$R_{\text{rad}} = \frac{|I_{\text{in}}|^2}{|I_0|^2} R_{\text{in}}. \quad (4.23)$$

For example, for the type of dipole antenna we use in the present work it can be shown [162] by extensive mathematical calculus using the above equations that the radiation resistance takes the following form:

$$R_{\text{rad}} = 10\pi^2 \left(\frac{l}{\lambda} \right)^2, \quad (4.24)$$

where l and λ are the dipole length and the wavelength, respectively. One can see that the radiation resistance is different from the free-space impedance $\eta = 120\pi \Omega$ and instead depends on the antenna geometry and dimensions.

When the stored magnetic and electric energy are equal in Eq. 4.20, a condition of resonance exists, and the reactive part of Z_{in} vanishes. For a thin dipole antenna this occurs when l is close to a multiple or a half-wavelength, in this case one has $I_{\text{in}} = I_0$ and $R_{\text{rad}} = R_{\text{in}}$.

However, in the practical case of a real antenna the calculation of input (driving-point) impedance is a very tedious procedure, involving knowing the current distribution and involving numerical solutions. There are several computational methods which can be used to determine the antenna impedance such as "induced emf method" or "integral-equation moment-method" [121]. For example, in the "induced emf method" the reactive near-fields (which contribute to the imaginary power) are calculated, in order to determine the input reactance. Such methods are beyond the scope of the present work, the sole purpose of the present section is to introduce the concept of antenna impedance and radiation resistance. Moreover, as expressed by the Eq. 4.15, one can see that by driving a time-varying current into an antenna, the radiation process through the antenna impedance is responsible for a voltage drop at its input terminals.

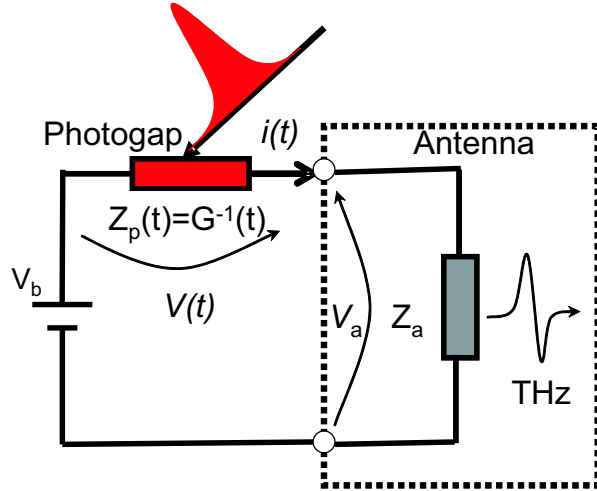


Figure 4.8.: Schematic of the equivalent circuit of a LTG-GaAs-based PC antenna.

4.4.2. Equivalent circuit of a small-size photoconductive antenna

To illustrate the effect of the radiated THz field upon the photogap as well as upon the overall performance of the emitter, one can envision the photoconductive antenna and the external circuit as being formed by a voltage generator containing a DC bias source and a time-varying conductance (resistance) supplying a time-varying current $i(t)$ to the antenna terminals, as schematically represented by the equivalent circuit in Figure 4.8. The planar antenna can be represented as a load with an impedance Z_a , having a resistive part only⁵, causing, as mentioned in the previous section, a voltage drop V_a at the antenna terminals, due to the emitted THz radiation. The photoconductive gap is represented by a time varying photoconductance $G(t)$ modulated by the optical power incident on the gap. In the equivalent circuit picture we can neglect the capacitance presented by the photogap, since it was shown that for the dimensions of our devices it is on the order of ~ 100 aF [163]. The two elements in series are biased with a DC voltage V_b , which together with the time-varying optical intensity and voltage drop due to the emitted THz wave induces a voltage modulation $V(t)$ across the photogap.

To be able to calculate the emitted THz field/waveform and the DC photocurrent, we proceed to calculate the current flowing across the photogap and into the antenna, by expressing the photoconductance in terms of conductivity:

$$G(t) = \frac{A}{d}\sigma(t), \quad (4.25)$$

where A and d are the active area of the photogap and the distance between the two metal electrodes (see Figure 4.1), respectively. The change in conductivity can

⁵The H-dipole used for the PC emitter in this work is assumed to be a resonant structure.

be related to the free-carrier density $n(t)$ and $p(t)$ produced by an optical pulse:

$$\sigma(t) = e(\mu_e n(t) + \mu_h p(t)), \quad (4.26)$$

Here, μ_e is the electron mobility and $n(t)$ is the photogenerated electron density in response to a Gaussian femtosecond pulse as given by Eq. 4.7. In writing Eq. 4.26 we assumed an ohmic transport regime across the photoconductive gap; moreover, the electron drift velocity is considered to have a linear dependence on the applied bias $v_e \simeq \mu_e E$ (accurate at low applied electrical fields). If we discard the hole contribution based on their low mobility, the photoinduced current density flowing in the photogap is given by:

$$\begin{aligned} j_{pc}(t) &\cong en(t)\mu_e E_g(t) \\ &\cong en(t)\mu_e \frac{V(t)}{d}, \end{aligned} \quad (4.27)$$

with $E_g(t) = \frac{V(t)}{d}$ being the time-dependent field across the gap. As discussed in the previous section, most of the voltage drop at the antenna terminals is caused by the THz emission process and thus the total voltage across the photogap becomes:

$$\begin{aligned} V(t) &= V_b - V_a \\ &= V_b - i_{pc}(t)Z_a, \end{aligned} \quad (4.28)$$

with the corresponding local electrical field in the gap given by:

$$\begin{aligned} E_g(t) &= \frac{V_b - i_{pc}(t)Z_a}{d}, \\ &= E_b - E_{rad}(t) \end{aligned} \quad (4.29)$$

where

$$E_{rad}(t) = \frac{i_{pc}(t)Z_a}{d} \quad (4.30)$$

represents the field generated across the gap due to the radiative process. One can see that the applied bias field is “screened” by the flow of photocurrent into the antenna resulting in the THz radiation, hence the name “radiation field screening”.

In terms of the equivalent circuit presented in Figure 4.8, instantaneously, the sending-end voltage source sees a voltage divider composed of the antenna impedance Z_a and the photoconductance $G(t) = Z_g^{-1}(t)$ where, by applying the circuit laws, the time varying voltage across the photogap can be written:

$$V(t) = V_b \frac{Z_g(t)}{Z_g(t) + Z_a} = V_b \frac{1}{1 + G(t)Z_a}. \quad (4.31)$$

Inserting Eq. 4.31 in 4.27 and multiplying with the area of the photogap A yields the time-varying photocurrent as a function of optically induced conductivity $\sigma(t)$:

$$i_{pc}(t) = V_b \frac{\frac{A}{d}\sigma(t)}{1 + Z_a \frac{A}{d}\sigma(t)}, \quad (4.32)$$

which in view of Eq. 4.25 can be put into a simpler form:

$$i_{pc}(t) = V_b \frac{1}{Z_a + G^{-1}(t)}. \quad (4.33)$$

By comparing the form of Eq. 4.14 in Section 4.3 and Eq. 4.32, one can notice the similarity between the expression of the surface current density in case of large-area emitters and the photocurrent flowing in the gap for a small-size photoconductive antenna, where for the latter case the antenna impedance Z_a has replaced the free space impedance η_0 . This similarity strongly suggest that the effects encountered in both type of photoconductive emitters are fundamentally the same, i.e. radiation field screening and that the different type of impedance used accounts for the way the radiation process occurs.

The second form for the photocurrent as given by Eq. 4.33, has been widely employed to describe the behavior of the high frequency-photocurrent which propagates down a coplanar transmission line when a photogap is embedded in it, for example as usually is the case in photoconductive sampling experiments [164]. The nonlinearity of the photocurrent response to intense optical illumination predicted by Eq. 4.33 has also been exploited in autocorrelation experiments in order to determine the ultrafast dynamics in photoconductors [165, 166].

The radiated THz far field can be obtained according to Eq. 4.2, by taking the time derivative of the photocurrent:

$$E_{\text{THz}}(t) \propto \frac{di_{pc}(t)}{dt} = V_b \frac{\frac{A}{d} \frac{d\sigma(t)}{dt}}{\left(1 + Z_a \frac{A}{d} \sigma(t)\right)^2}. \quad (4.34)$$

Thus, one can see that in Eq. 4.32 and 4.34, the denominator is responsible for the saturation of the photocurrent and THz output with the optical power, respectively, through the photoinduced conductivity $\sigma(t)$.

4.4.3. DC photocurrent

The DC photocurrent flowing through a photoconductive antenna under pulsed illumination can be expressed as the time average of the instantaneous photocurrent $i_{pc}(t)$:

$$I_{DC} = \frac{1}{T_{rep}} \int_0^{T_{rep}} i_{pc}(t) dt, \quad (4.35)$$

where T_{rep} is the repetition period of the femtosecond laser. By taking the expression for time-dependent carrier density as given in Eq. 4.7, the integration of Eq. 4.35 does not produce a closed form solution. However, a useful simplification is obtained within the "impulse limit" (i.e., when the rise- and fall-time of the laser pulse is assumed much less than the carrier lifetime). In this case, the *erf* function very

rapidly approaches unity and the density of the photogenerated carriers takes the simple form:

$$n(t) \simeq n_0 \exp\left(-\frac{t}{\tau_c}\right), \quad (4.36)$$

where n_0 represents the carrier density at $t = 0$ ps. Within this approximation, the DC photocurrent is given by:

$$\begin{aligned} I_{DC} &\simeq \nu_{rep} V_b \int_0^\infty \frac{\frac{A}{d} \sigma_0 \exp\left(-\frac{t}{\tau_c}\right)}{1 + Z_a \frac{A}{d} \sigma_0 \exp\left(-\frac{t}{\tau_c}\right)} dt \\ &\simeq \nu_{rep} \frac{V_b \tau_c}{Z_a} \ln\left(1 + \frac{AZ_a \sigma_0}{d}\right) \end{aligned} \quad (4.37)$$

with

$$\sigma_0 = e\mu_e n_0 \quad (4.38)$$

and

$$n_0 = \eta \frac{1}{\nu_{rep}} \left(\frac{P_0}{h\nu}\right) \frac{1}{\mathcal{V}}, \quad (4.39)$$

where ν_{rep} and P_0 are the laser repetition rate and average optical power, respectively. By making the appropriate substitutions, the DC photocurrent can be expressed as a function of the average incident optical power P_0 :

$$I_{DC} \simeq A(V_b, Z_a, \tau_c, \mu_e) \ln(1 + B(\mu_e) Z_a P_0), \quad (4.40)$$

where A and B which combine a set of parameters. From Eq. 4.40 one can see that the DC photocurrent tends to saturate as the optical pump power is increased. The same behavior is expected for the peak of the THz waveform described by Eq. 4.34. The $B(\mu_e)$ term in the above equation can explain for example, the variation of the saturation level with the irradiation dose for photoconductive antenna on ion-bombarded InGaAs [155].

4.4.4. Calculated THz waveforms and transient photocurrent

Using Eq. 4.32 and 4.34, the temporal evolution of the photocurrent and the emitted THz waveform for different optical power levels at a fixed applied bias of 10 V are calculated and displayed in Figure 4.9 and 4.10, respectively. We used a Gaussian pulse with a duration $T_{FWHM}=120$ fs, a carrier lifetime of 1.2 ps, $Z_a=100 \Omega$ and $\mu_e=600 \text{ cm}^{-2}/\text{Vs}$. The time-dependent form of the free-carrier density used in defining the time-dependent photoconductance was that given by Eq. 4.7. One can notice that, consistent with the experimental evidence in Figure 4.6, the negative peak of the THz waveform is always smaller than the positive peak due to the finite carrier lifetime, therefore the amplitude and spectral bandwidth are primarily dependent on the photocurrent rise time (i.e. laser pulse width). It can also be seen that the amplitude of the photocurrent as well as THz field tends to saturate at higher optical power levels, as already observed for the experimental data in Figure 4.6.

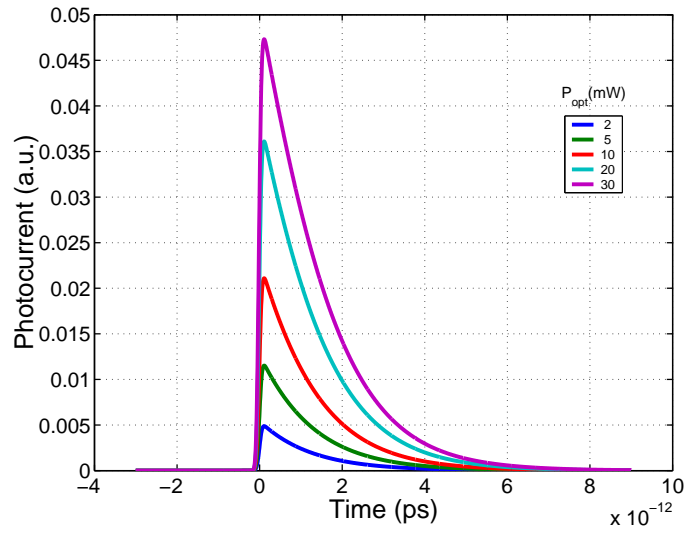


Figure 4.9.: Rise and decay of photocurrent calculated for different optical power levels according to Eq. 4.32.

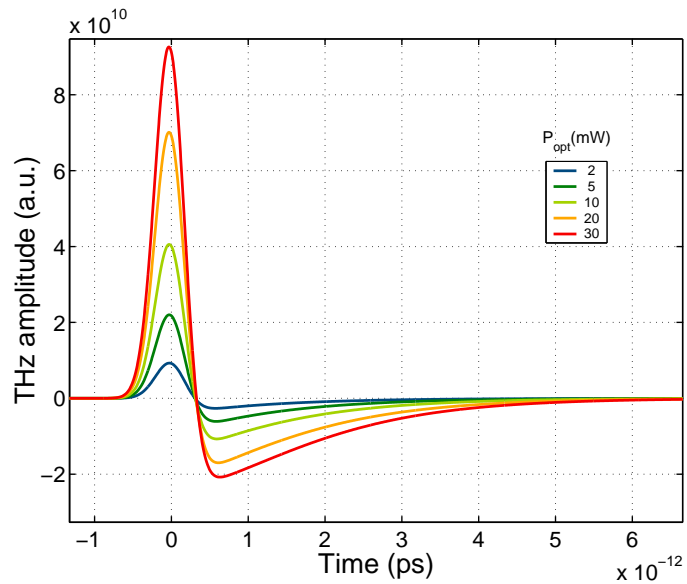


Figure 4.10.: THz waveforms calculated for different optical power levels according to Eq. 4.34.

4.4.5. Experimental saturation data and agreement with the equivalent circuit model of radiation field screening

In Figure 4.11 and 4.12 we compare the measured and calculated saturation curves for the DC photocurrent as well as for the maximum field amplitude of the THz waveform as they were recorded from the PC1 and PC2 emitters. For both photoconductive antennas investigated here, the measured values plotted in the lower panels of Figure 4.11 and 4.12 correspond to the peak of the time-dependent THz field displayed in Figure 4.6 for various optical power levels, as obtained from the PC2 antenna. The data was obtained under an applied bias of 10 V and by varying the optical power from 2 to 40 mW. The DC photocurrent was recorded by monitoring the display of an ammeter connected in series with the voltage source and the PC antenna, while also recording the maximum amplitude of the THz field at a given optical power.

In full accordance with the predictions of Eq.s 4.37 and 4.34, and consistent with the saturation of the THz maximum field already observed in Section 4.3.2 for the PC2 antenna, we observe a strong saturation of the measured DC photocurrent as well as for the peak THz field with increasing optical power. Note that at low optical intensities the values of DC photocurrent scale linearly with the optical power, whereas above 10 mW they display a sub-linear dependence. The same observation holds for $E_{\text{THz}}^{\text{peak}}(t)$ with the additional remark that the peak of the THz field starts to saturate at lower optical power levels and the saturation is much more stronger, in accordance with the quadratic dependence of the denominator in Eq. 4.34. This can be easily understood in terms of the equivalent circuit depicted in Figure 4.8, together with Eq. 4.31. Thus, one can easily see that if the photoconductive antenna is driven with a low optical intensity, the photocurrent $i_{\text{pc}}(t)$ is linear in P_0 since $G(t)^{-1} \gg Z_a$ and the photocurrent is approximately voltage biased (i.e. the voltage drop across the gap is approximately equal to the voltage delivered by the voltage source). Using $\ln(1+x) \approx x$ for $x \ll 1$, in the low optical intensity case Eq. 4.40 becomes:

$$I_{DC} \simeq \nu_{\text{rep}} V_b \tau_c \frac{A \sigma_0}{d} \simeq S(V_b) P_0, \quad (4.41)$$

being linear in P_0 , where $S(V_b)$ is the responsivity of the photogap. However, at larger optical intensities, the photogap is not longer voltage biased but now becomes biased through a load impedance Z_a , responding nonlinearly in P_0 when $G(t)^{-1} \approx Z_a$. The same reasoning applies for understanding the different response of the photocurrent and emitted THz in the case of continuous-wave versus pulsed illumination, the PC antenna being successfully employed as both, photomixer and THz-pulse emitter, and so the equivalent circuit is the same in both cases. As shown in Chapter 3, for the continuous-wave case, the photocurrent responds linearly to the incident optical power. This can be easily understood if we make a simple evalu-

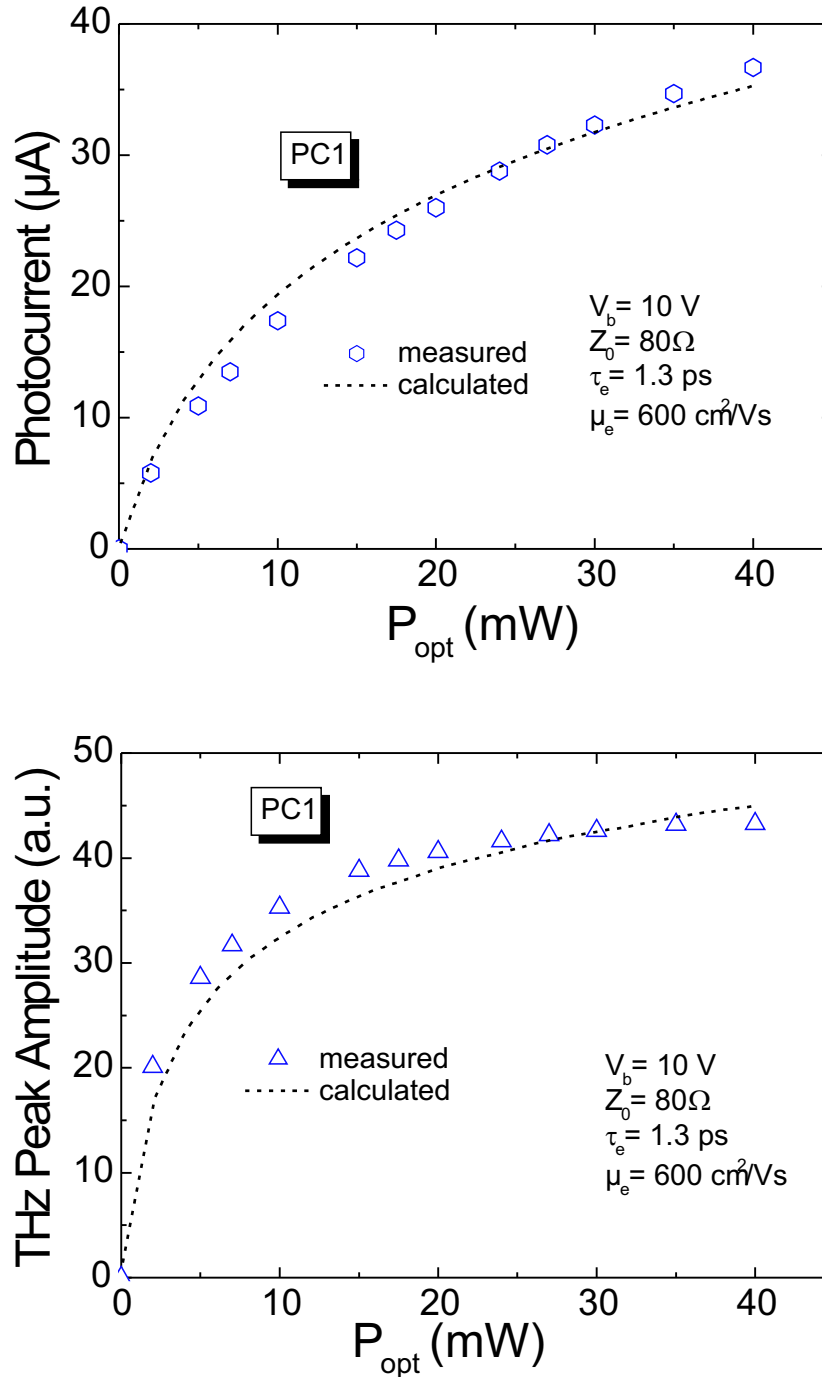


Figure 4.11.: Fit of the DC photocurrent (upper panel) and THz pulse amplitude (lower panel) vs. optical power for the PC1 photoconductive antenna.

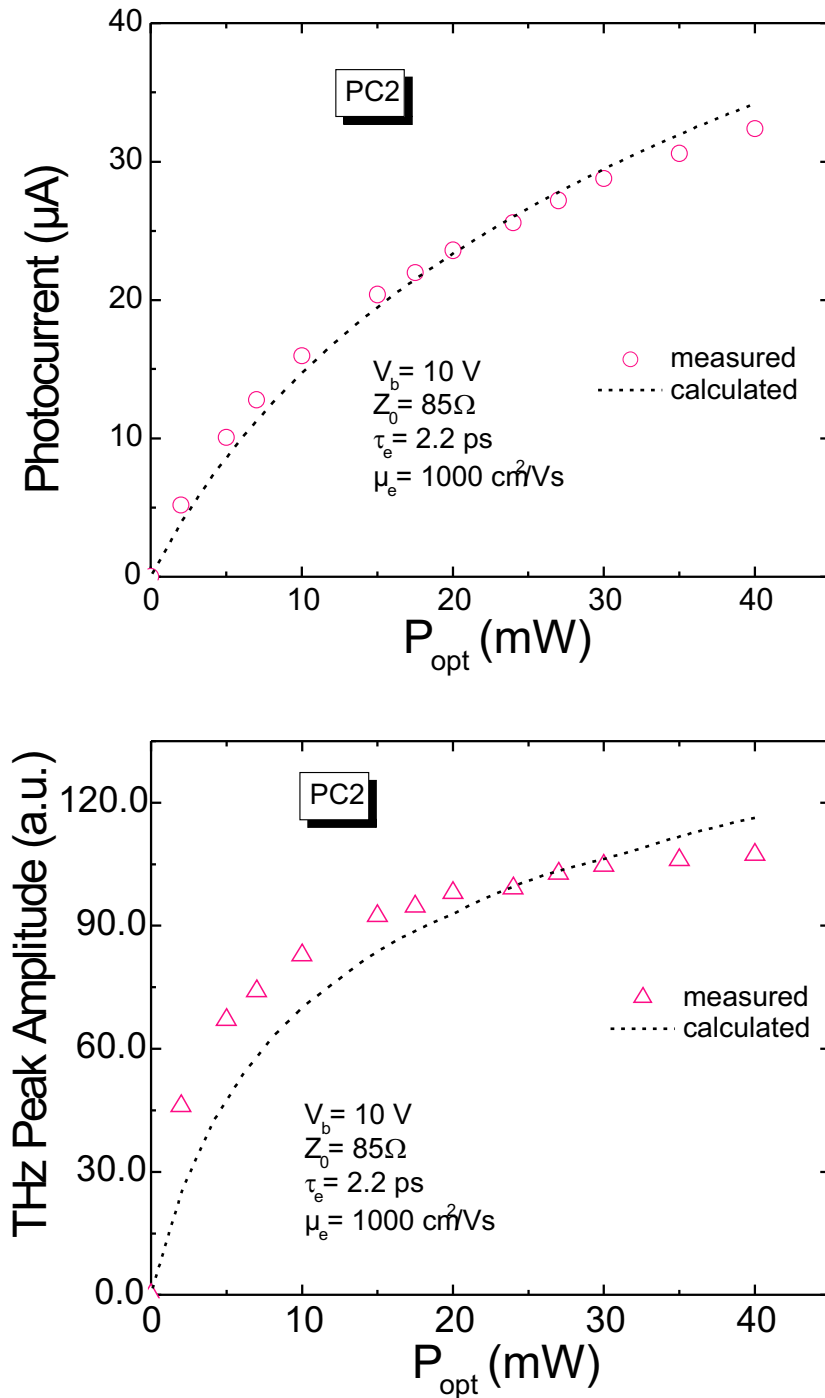


Figure 4.12.: Fit of the DC photocurrent (upper panel) and THz pulse amplitude (lower panel) vs. optical power for the PC2 photoconductive antenna.

ation of the excitation density and hence of the instantaneous conductance for both operation regimes. For instance, assuming an CW incident power of 30 mW in an LTG-GaAs based photoconductor with a carrier lifetime of ~ 10 ps, the generated photocarrier density is $\sim 3.6 \times 10^{14} \text{ cm}^{-3}$, which according to Eq.s 4.25 and 4.38 yields a conductance $G_0 = 3 \times 10^{-5} \text{ S}$, whilst for the same average optical power level under pulsed operation the excitation density becomes $\sim 1 \times 10^{19} \text{ cm}^{-3}$ and the peak conductance $G_0 = 9 \times 10^{-2} \text{ S}$, that is $G_0^{-1} \sim 11 \Omega$. To conclude, the effect of the "voltage divider" in the equivalent circuit depicted in Figure 4.8 is synonymous to the effect of "THz radiation field screening"; *the existence of a load impedance due to the THz antenna connected in series with the photogap impedance determines a saturation of the bias across the photogap $V(t)$ when the optically induced conductance is on the same order of magnitude with the antenna admittance.*

We performed a fit of measured data based on the equivalent circuit model implemented in Sections 4.4.2 and 4.4.3 as shown in Figure 4.11 and 4.12. It is important to mention that both dependencies were fitted with a single/common set of parameters, as listed bellow:

Device	V_b (V)	Z_a (Ω)	$\mu_e \text{ cm}^{-2}/\text{Vs}$	τ_c (ps)	A (μm^2)	d (μm)
PC1	10	80	600	1.3	10×5	5
PC2	10	85	1000	2.2	10×5	5

Table 4.1.: List of parameters used to calculate the saturation characteristics displayed in Figure 4.11 and 4.12.

It can be seen from Figure 4.11 that the calculated DC photocurrent is in very good agreement with the measured data. For the THz field emitted by the PC2 antenna, we note that the experimental data saturates faster than the theoretical estimation. However, the saturation of the peak THz field for the PC2 emitter could be fitted very well individually, by taking larger values of the antenna impedance $Z_0 \sim 250 \Omega$.

Looking at Eq. 4.34 one notes that the radiated THz field in the near field (as for the case of large-area photoconductive antenna) is proportional to the instantaneous photocurrent and hence the THz near-field can be approximated with the expression given by Eq. 4.31. Here again, one can notice a striking similarity between the radiated field given by Eq. (18) in Ref. [158] and the radiated near-field given by Eq. 4.31, if the free space impedance is replaced with the antenna impedance Z_a .

The inclusion of a transient velocity was required in Ref.s [158, 167] due to the excitation of carriers higher up in the conduction band, hence intraband relaxation and hot electron effects as well as electron-hole collision can play an important role

in carrier dynamics. In our case, the linear dependence of the THz peak amplitude with bias is a good indication that Ohm's law holds well; however, at higher biases it may be necessary to include a more accurate description of the transport, as presented in Ref. [167].

A very important note is that we do not exclude the possibility of an interplay between different screening mechanisms (i.e., radiation field screening and photogenerated space-charge screening) as discussed in the next chapters, but the outcome of our study on saturation shows that the effect of the radiation field screening is to be considered as the main reason for the saturation of both the DC photocurrent and emitted THz peak amplitude versus optical power.

5. Double-pump pulse THz spectroscopy on LTG-GaAs-based PC antenna

The current chapter offers an insight into the ultrafast dynamics of the local electrical field in LTG-GaAs-based photoconductive antennas excited with femtosecond laser pulses. This was done by employing a THz-pump–probe spectroscopy technique, the so-called “double-pulse technique”, which consists of exciting the photoconductive antenna with two temporally distinct laser pulses. The qualitative and quantitative evaluation of experimental findings is carried out by extending the equivalent circuit model presented in Chapter 4, such that besides the effect of the radiation field screening discussed already, it accommodates the space-charge field screening effects produced by photogenerated carriers moving in the external bias field, an effect which is present in photoconductors at high excitation densities. Initially, a simulation of the PC antenna response to a single-pulse excitation allows us to clearly identify the temporal evolution, as well as the magnitude of each of the field screening mechanisms co-existing in the photoswitch in the first picoseconds subsequent to excitation. The same model is then used for modeling the double-pulse results, by considering the solution of the carrier density response to the double-pulse excitation. The observed incomplete recovery of the double-pulse signal at negative time delays suggests long-living screening effects, which will be addressed in greater detail in Chapter 6.

5.1. Why double-pump pulse experiments?

The excitation of photoconductive antennas with femtosecond laser pulses has become one of the most widely used sources for broadband THz radiation, in part also due to its relatively high bandwidth and efficiency. While the use of femtosecond laser pulses is responsible for the generation of ultrafast electrical transients, the trapping time of the photoconducting material (semiconductor) ensures the subpicosecond duration of the electrical pulse. At the same time, photoconductive switching has also been employed in the generation of CW THz radiation through optical heterodyning of two slightly detuned laser beams, as presented in Chapter 3. Therefore, the material characteristics of the photoconductor, such as the dark and illuminated resistivity, carrier mobility and carrier lifetime are of utmost importance in designing PC emitters with a satisfactory gain-bandwidth product. As already discussed in Chapter 2, among the most assiduously studied ultrafast photoconduc-

tors, LTG-GaAs exhibits unique properties, like a very short free carrier lifetime, high dark resistivity and a relatively high carrier mobility. Given the complex and so far not fully understood, carrier trapping and recombination mechanisms (in part due to the controversy over the trapping centers, defects vs. As-clusters), the carrier dynamics in LTG-GaAs has been the subject of extensive research. For instance, information on the carrier lifetime as well as the carrier relaxation processes was obtained from optical pump–probe (transient reflectivity) measurements [67]. However, the interpretation of the measured signals is hampered due to the multitude of relaxation processes taking place at once in the LTG-GaAs material. The mobility of photogenerated electrons was extracted from optical-pump THz-probe experiments [34, 75] which are sensitive to the temporal evolution of the conductivity, assumed to be dominated only by electrons. Other authors developed models in which material parameters were obtained from the emitted THz waveform [65]; however, the model employed proved to be inefficient at high excitation densities due to trap-saturation and carrier screening effects. The reason lies in the fact that the magnitude and the waveform of the electrical pulse generated in a PC emitter does not only depend on the lifetime, mobility and density of free carriers but also on the displacement current [94] caused by the bias field screening and its subsequent redistribution in the gap. There has been substantial evidence, sustained by both theory and experiment, that space-charge effects occurring in photoconductors, following to the optical injection of carriers, have a deleterious impact upon device performance [99]. Furthermore, based on the discussion in the previous chapter, one should account for the effect of radiation field screening which also affects the magnitude of the electric field in the photogap. Hence, it appears of great importance to trace and understand the transport and recombination properties of photogenerated carriers together with the electric field dynamics in the device, as opposed to the mere observation of photoconductivity decay as in the “contactless” methods enumerated above. In view of the facts at hand, for most of the THz generation applications it is important to characterize the properties of the photoconductive material when already integrated into the device, that is, under operating conditions. This allows one to probe the overall device performance instead of the LTG-GaAs layer alone, resulting in a more direct path to optimization of photomixer performance.

One type of experiment that would allow us to acquire this kind of information is the double-pump pulse (DPP) experiment, also referred to as a THz-pump–probe experiment. First implemented by Pedersen et. al [168], the DPP experiment was successfully used in investigating the carrier and field dynamics in SI GaAs [141, 168, 169], GaAs on Si [169], radiation-damaged silicon on sapphire [170]. Also, small size photoconductive dipole antennas [171, 172, 173] as well as large area emitters [174, 175, 176] based on LTG-GaAs and GaAs were investigated.

We also believe that this kind of experiment should provide us with information

on the recombination time, and thereby the duration of the field-screening processes, a parameter of typically underrated importance in designing ultrafast switches.

5.2. Principle and experimental realization of the double-pulse experiment

The principle behind the double-pump pulse experiment is to excite a PC antenna with two laser pulses: the first pulse, from hereon referred to as the THz-pump, unmodulated, should generate free carriers in the photogap (and an initial THz-pulse), while the second pulse, from hereon named THz-probe, modulated by an optical chopper, is used to generate a second THz pulse which is detected. Since the radiated THz field strength is proportional to the electric field in the photogap, the measurement of the peak value of the THz signal as a function of the delay between the THz-pump and -probe will give the time-resolved behavior of the changes in the local field in the photoswitch. By chopping only the THz-probe beam and using the phase sensitive (lock-in) detection, we detect only the THz waveform produced by the THz-probe beam. A third beam (the THz-detection beam) is also passed over a delay stage and utilized in the detection scheme. The time delay between the THz-detection (TD) beam and the THz-probe beam is kept fixed at the value of maximum amplitude of the THz pulse generated by the THz-probe beam, with the amplitude of the THz signal being recorded, while varying the time delay between the THz-pump and -probe pulses.

The experimental setup is shown in Figure 5.1, being a modified version of a standard THz generation-electrooptic (EO) detection setup described in Chapter 4, now having three synchronized pulses for the THz pump-THz probe measurement. A pump beam derived from the femtosecond laser was split into two beams at a polarizing beam splitter (PBS1): a THz-pump beam (TP) and a THz-probe (Tp) beam. The splitting ratio of the two beams can be controlled by rotating a half-wave plate (WP1/2). To be able to recombine the beams without losses, each of the two beams were passed again through a half-wave plate (WP1/2), which rotated the plane of polarization by 90° , and then combined in a second polarizing beam-splitter (PBS2). The polarization of the two beams at the emitter is perpendicular, thus avoiding undesired interference effects when hitting the PC antenna simultaneously (coherent artifacts).

The synchronization of the three optical beams was realized by using two delay stages: the time delay (τ) between the optical pump (THz-probe) and probe (THz-detection beam) was changed using a first translation stage (DS1), while the time delay between the THz-pump and the THz-probe pulse was adjusted by passing the THz-pump through a second translation stage (DS2).

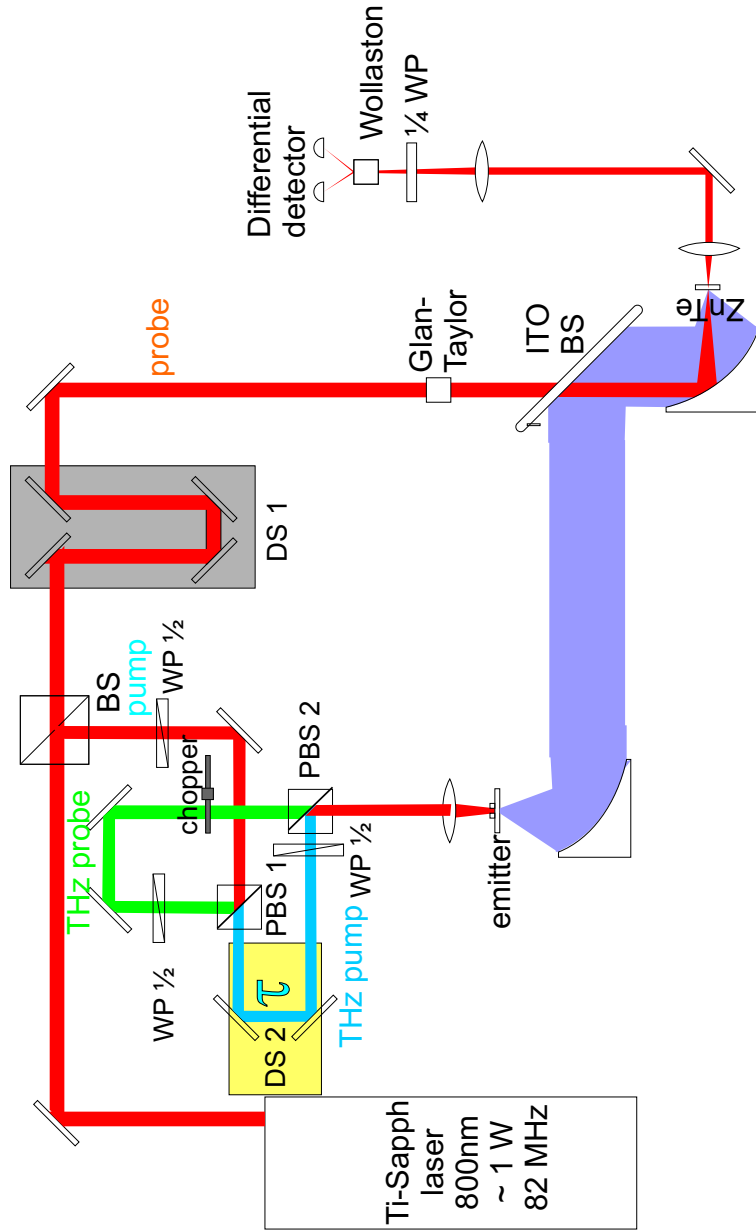


Figure 5.1.: Schematic representation of the double-pulse experimental setup. The pump beam derived from the Tsunami femtosecond laser is split into a THz-pump and a THz-probe beam. The optical probe pulse is kept fixed at the maximum of the THz-waveform generated by the THz-probe pulse.

A very challenging part in setting up the experiment was the alignment of the THz-pump and THz-probe beam, since they must propagate collinearly and their focus must perfectly overlap in the photogap. The reliability and reproducibility of data is only ensured when the THz-pump does not change its lateral focus position; given the tight focusing ($\sim 10 \mu\text{m}$), a slight walk-off of the THz-pump beam while the delay stage DS2 is moved might result in injecting carriers at different positions in the photogap, in this way the THz-probe beam would probe the effect of inhomogeneous illumination at different moments in time. Therefore, a strenuous alignment procedure was employed, including the overlapping of the two beams over large distances ($> 4 \text{ m}$) on two different spots, using the reflection from PBS1, whilst the final alignment was checked by moving the DS2 over its whole travel range and monitoring the DC photocurrent from the THz-pump beam. A good alignment was assumed if the DC photocurrent drift was less than 5% over the entire travel range (~ 50 times greater than the delay range used in the experiments). For the same reasons as explained above, we chose to pass the third (THz-detection) beam and not the initial pump beam over the first translation stage.

To illustrate the effect of the THz-pump pulse on the THz-probe pulse and by that, the principle of the double-pump pulse experiment, we recorded individual THz waveforms from the THz-pump and -probe beam using the setup described above, only with a different modulation scheme. Thus, with a fixed delay time between the THz-pump and THz-probe, we took a reference scan for each of the incident pulses, plotted with a distinct color in Figure 5.2. The optical power was the same $\sim 15 \text{ mW}$ in both beams and the applied bias was 10 V (20 kV/cm). The next step, by chopping both the THz-pump and THz-probe beams, we recorded the waveform produced by both pulses arriving at the emitter at different moments in time. As one can see, the THz-pump pulse here arrives $\sim 4 \text{ ps}$ earlier than the THz-probe. Although the THz-pump and -probe beams had the same power, one can notice that the maximum amplitude from the THz-probe pulse drops by more than 30% due to the presence of the THz-pump pulse. This observation suggests that the THz emission efficiency of the THz-probe pulse is seriously affected when the THz-pump pulse precedes it, indicating that the external voltage bias is still "screened" $\sim 4 \text{ ps}$ after the THz-pump illumination.

Next, to generate the double-pulse traces, the time delay between the THz-detection and THz-probe pulses was fixed at the maximum amplitude of the waveform produced by the THz-probe pulse (as indicated by the red circle in Figure 5.2) which was monitored by chopping the THz-probe only at a frequency of $\sim 2.5 \text{ kHz}$, while the THz-pump beam was blocked. Unblocking the THz-pump beam caused a strong decrease of the lock-in signal when the time delay between the THz-pump and THz-probe pulse was set to zero. The lock-in time constant and sensitivity were set to 100 ms and 1 mV , respectively, over the whole range of the investigated THz-

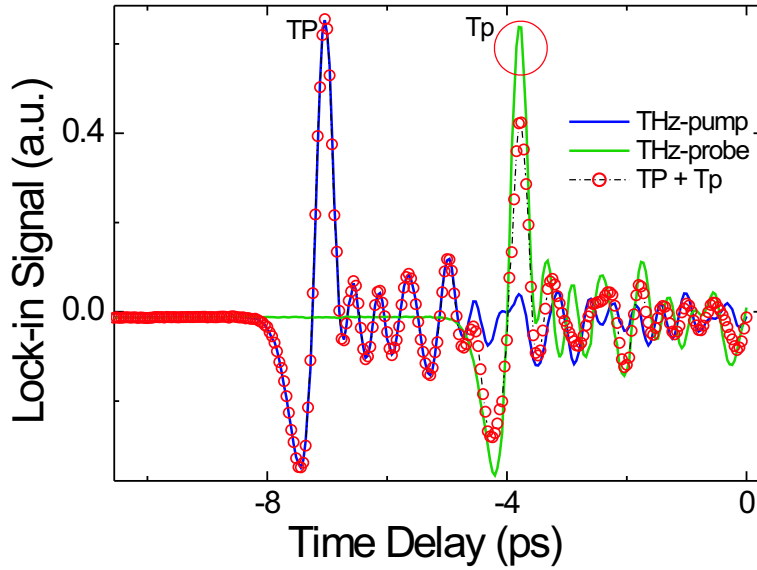


Figure 5.2.: THz waveforms generated by the THz-pump and THz-probe pulses, recorded individually (distinct color) and simultaneously (red circles), showing the reduction of the THz-probe signal when preceded by the THz-pump pulse.

pump power levels. For double-pulse traces recorded at high applied bias fields the sensitivity of the lock-in amplifier was switched to 3 mV but the data acquisition program recorded the absolute value of the THz signal, allowing for comparison of traces obtained at different sensitivities of the lock-in amplifier.

To avoid any artifacts caused by the shifting of the zero-time delay between the THz- pump and -probe, instead of using a neutral density filter, the optical intensity of the two beams was changed only by rotating the $\lambda/2$ plates. As opposed to other authors who performed such double-pulse experiments [171], the choice of EO detection in our approach was strongly motivated by the instantaneous response of the EO crystal, as opposed to the PC antenna detection, where the carrier lifetime of the photoconductive material sets the time resolution of the experiment.

It is also important that the THz-probe beam intensity is kept well below the threshold at which the saturation of the THz-field occurs such that the double-pulse measurement reveals the ultrafast dynamics of the bias field, following the photoexcitation by the THz-pump pulse. According to the saturation data presented in Chapter 4, the saturation of the emitted THz field occurs at pump power levels above 5 mW, that is, an excitation density of $\sim 1 \times 10^{18} \text{ cm}^{-3}$. Given that, we set the

average optical power of the THz-probe to 2 mW¹. One should also keep in mind that there is a trade-off between sensitivity and reliability: a too low power level of the THz-probe reduces the signal-to-noise ratio (SNR) of the signal and degrades the quality of the analysis.

5.3. Double-pump pulse experimental results and their preliminary interpretation

5.3.1. Double-pulse characteristics from the PC1 antenna

Figure 5.3 displays the raw data from the double-pulse measurements recorded at different power levels of the THz-pump beam on the PC1 antenna (G420 material) and under an applied bias of 10 V (20 kV/cm applied field). The THz-probe beam used in this case was 2 mW. This probe level corresponds to an excitation density of $\sim 3.5 \times 10^{17} \text{ cm}^{-3}$ by assuming a laser beam diameter of approx. 10 μm , a reflectance of 0.3 at the air-LTG-GaAs interface and a photon energy of 1.55 eV. The highest THz-pump power (28 mW) corresponds to a photogenerated carrier density of $\sim 1 \times 10^{19} \text{ cm}^{-3}$. Here, as described in the previous section, the time axis denotes the time delay between the THz-pump and THz-probe pulses (τ introduced by DS2 in Figure 5.1).

One can notice that as the THz-pump power increases, the magnitude of the relative signal change at $\tau = 0$ becomes higher, whilst at the highest excitation density the detected THz signal decreases to almost zero. Assuming that the generated THz signal is proportional with the local field in the photogap, this means that the emitter and the field are completely "switched-off" around $\tau = 0$ for a THz-pump power of 28 mW. Note that the recovery of the THz signal takes place on a longer time scale when the excitation density increases. Also, we notice a change in the shape of the measured signal: at low excitation densities the fast recovery of the THz signal follows an exponential dependence, whilst, for higher generated carrier densities the initial recovery becomes almost linear-like, deviating from the mono-exponential behavior. Note that for high THz-pump levels the negative pedestal created by the incomplete signal recovery becomes more prominent.

A striking feature of the unprocessed data presented in Figure 5.3 is represented by the different THz signal levels measured at negative time when varying the THz-pump power. Although initially we believed we are confronted with an experimental artifact, by carefully checking the experimental conditions (i.e. monitoring the laser fluctuations/drift, sample heating effects) we ensured the reproducibility of the measured data. According to the principle of the double-pulse measurements exposed

¹For a better SNR and to monitor the changes in the DPP traces when the THz-probe power is altered, we have also measured DPP data at a THz-probe power level of 4 mW.

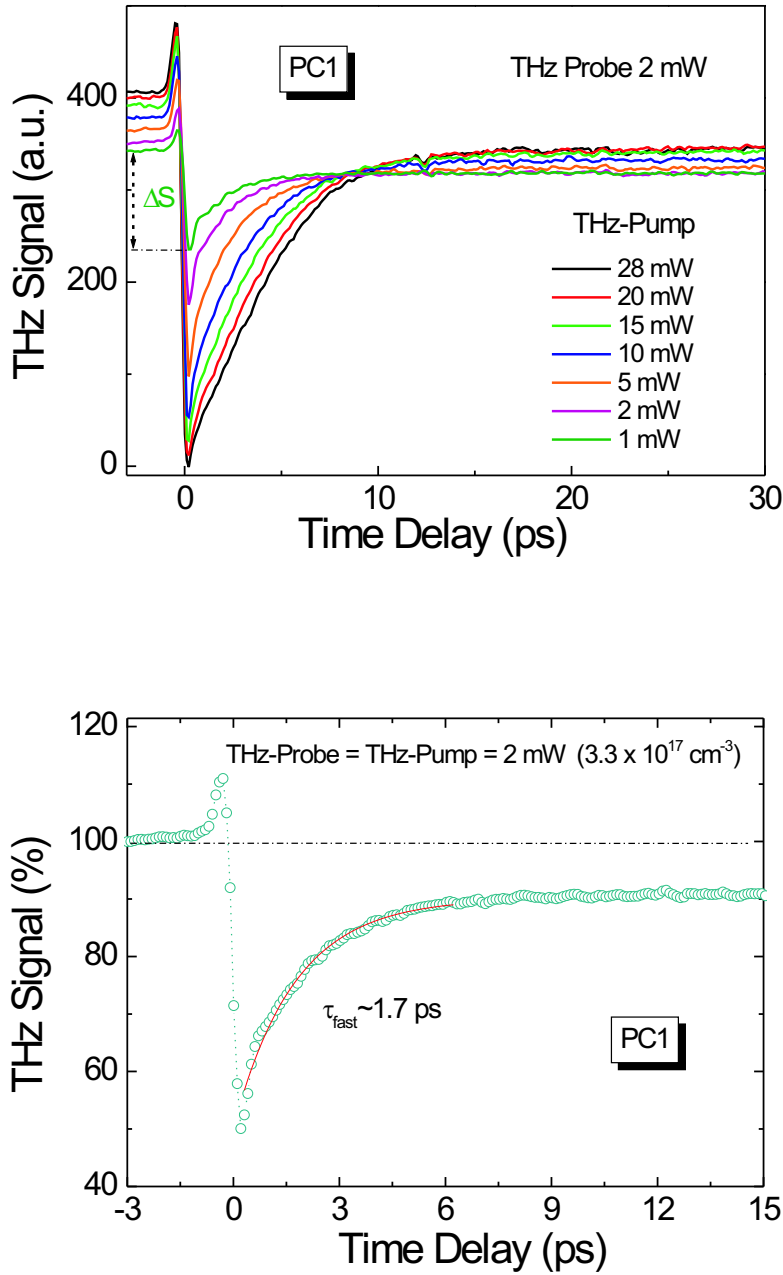


Figure 5.3.: **Upper panel:** THz double-pulse signals from the **PC1** emitter obtained at various optical power levels of THz-pump measured at an applied bias (field) of 10 V (20 kV/cm); **Lower panel:** Normalized THz double-pulse signal trace obtained at a equal power level of 2 mW for the THz-pump and THz-probe beam. The fast decay of the THz signal after $\tau = 0$ was fitted with a single exponential.

in the previous section, one would expect the amplitude of THz signal for negative time delay to be totally independent to the level of THz-pump power, since for $\tau = 0$ the THz-probe pulse arrives first at the emitter. However, as discussed in great detail in Chapter 6, one should keep in mind that the output of the mode-locked laser consists of femtosecond pulses spaced by ~ 12 ns and thus, the different levels of THz signal at negative time delays are an indication that we are observing remnant effects from the THz-pump pulse that arrived ~ 12 ns earlier and therefore the influence of trapped carriers that outlive the repetition rate of the laser system. In this chapter, however, we are mainly investigating the ultrafast effects (electric field dynamics) occurring on the same time scale as the trapping of carriers as well as the nature of the field screening. A detailed discussion of the effects observed at $\tau < 0$ can be found in Chapter 6.

The lower panel of Figure 5.3 displays a single trace measured at a THz-pump power of ~ 2 mW, equal to the THz-probe power. Here, the THz signal is normalized to 100 % at the level of essentially constant signal measured for negative time delays. We can clearly identify three distinct temporal regimes for the amplitude of the THz radiation: at negative time delays, the THz-probe pulse is incident in advance of the THz-pump pulse and a constant² THz signal amplitude is recorded. In less than 1 ps following the zero-time delay (where the THz-pump and THz-probe are arriving at the same time at the emitter) a sudden decrease of the signal corresponding to carrier injection by the THz-pump beam can be observed. The positive peak observed at small negative time delays is attributed to the cross-talk between the THz-pump and -probe beams, i.e., the weak saturation caused by the THz-probe pulse modulates the local field in the PC antenna at the chopping frequency and, as a consequence, some of the THz radiation emitted from the THz-pump pulse is detected. Around $\tau = 0$, the drop of the THz signal amounts to approximately 50 % of the full THz amplitude measured at negative time delays for 2 mW. At small, positive values of the time delay, where the THz-pump clearly precedes the THz-probe pulse, the THz signal recovers to a value larger than that measured at $\tau = 0$ but smaller than that measured for $\tau < 0$, giving rise to a negative pedestal which was proved to persist for more than 50 ps.

We applied an exponential fit to the fast recovery component of the 2 mW double-pulse trace, as shown in Figure 5.3 (lower panel), obtaining a recovery time constant of ~ 1.7 ps. In comparison to the free carrier relaxation time (trapping time $\tau_c \cong 1.1$ ps) yield by transient reflectivity measurements on the LTG-GaAs material used for this emitter (see Chapter 2), the recovery of the THz signal takes place on a slightly longer time scale.

²The signal is only constant in that effects from previous pulses are on slow time scales.

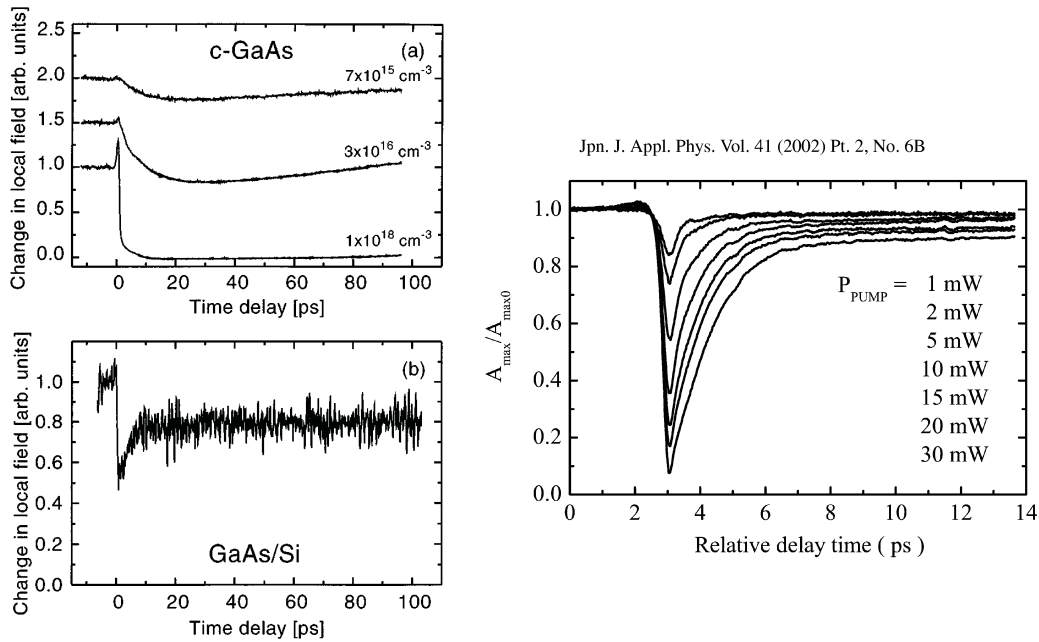


Figure 5.4.: Typical double-pulse traces from PC emitters on c-GaAs and GaAs/Si, from Ref. [169] (left panel) and from LTG-GaAs-based PC antennas [171] (right panel)

5.3.2. A review of the literature on double-pulse measurements

Although THz double-pulse experiments have been performed for over a decade now, the main features of the double-pulse traces are not fully explained nor understood. The fast drop of the THz signal around $\tau = 0$ was ascribed to various effects:

- In Ref. [169, 171], to the screening of the applied bias field due to the space-charge induced by the separation of electrons and holes;
- Ref. [172] suggests the screening of the applied bias field by the THz radiation as the main cause;
- Ref. [173] attributes the effect to the carrier-carrier scattering mechanisms.

In the following, we will briefly discuss each of these possible contributions.

The first reports using THz-pump and -probe experiments on an ultrafast photoconductor are due to Jacobsen et al. [169], who investigated screening in ultrafast photoconductive switches based on GaAs and GaAs/Si. In comparison to the highly crystalline GaAs, the GaAs grown on Si possesses a high density of dislocations and cracks due to the relatively large lattice mismatch (4%) between GaAs and Si. These defects act as trapping and recombination centers, leading to a very short free carrier lifetime (~ 1 ps), thus very similar in nature to the LTG-GaAs used in

our investigations. This assumption is confirmed in Figure 5.4 (left panel), where double-pulse traces from both investigated materials are presented. One can notice the temporal evolution of the THz signal amplitude from the GaAs/Si sample (Figure 5.4 (b)) as being very similar to the one presented in Figure 5.3 (lower panel) for LTG-GaAs. The authors associated the fast recovery of the THz signal (assumed to be the decay of screening produced by the photogenerated carriers at $\tau = 0$) with the carrier recombination time. A negative plateau is also encountered here, its presence being attributed to the generation of free carriers in the Si substrate. Although apparently of only limited relevance for our investigations, the strongly contrasting features of the double-pulse traces from the GaAs sample indeed reveal precious information. One can see that for low excitation densities the sudden drop of the THz signal is absent but instead, at $\tau = 0$, it starts to decrease slowly for more than 20 ps, a time interval associated with the retardation time³ across the 80 μm gap. One should keep in mind that for GaAs there is no fast trapping, the photogenerated carriers recombining at the electrodes or in the bulk. A long recovery of the THz amplitude is observed to last for more than 100 ps. The origin of the slow decrease and the long recovery can be understood through the work of Hu et al. [177] who studied the ultrafast carrier transport in bulk GaAs with the double-pulse technique, using a large aperture Schottky diode. They shown that the slow decrease of the signal around zero time-delay is due to the increasing electron-hole displacement and hence of the polarization induced by the photogenerated carrier pairs which screens the internal electric field. Therefore, based on the above observations, for our PC antenna we expect that the increase of the space-charge screening will happen on a time scale where the carriers are still mobile, that is, within the trapping time of 1-2 ps. This, however, is in strong conflict with the supposition that the sudden drop in the THz signal is due to the space-charge screening.

In the same manner, Tonouchi and coworkers [171], performing double-pulse experiments with PC antennas manufactured on LTG-GaAs (see Figure 5.4 (right panel)), assign the rapid drop of the THz peak amplitude at zero time-delay to the field-screening (polarization) induced by the separation of carriers in the external bias field, while the fast recovery of the signal is ascribed to the decay of polarization through a series of scattering and relaxation processes, followed by the trapping of carriers. Each experimental trace was fitted with four decay times, suggesting that there are at least three carrier relaxation processes occurring during the fast polarization decay process. Among them, the most important ones at early times are the hot-electron relaxation at the Γ -valley and electron recombination at the ionized As precipitates.

³Retardation time = the time needed to build up an uncompensated space-charge distribution through the spatial displacement of carriers in the external field, resulting in a screening field.

As pointed out in Ref. [172], the decay of polarization due to the uncompensated space-charge and by that, of the field screening, can only be caused by the decrease of carrier density which produced it. Therefore, processes like those enumerated above, including intraband relaxation and carrier trapping can not be responsible for the decrease of the carrier density since they do not result in the annihilation of an electron-hole pair (i.e., carrier recombination). Carriers scattered into the side-valley might reduce their drift velocity but remain mobile and electrically active. The same applies for the trapped carriers which continue to statically screen the applied field. Also, the fast regeneration of the electric field on a time scale of ~ 1 ps contradicts the experimentally determined recombination times in LTG-GaAs material, which are believed to range from tens (optimistic) to hundreds of picoseconds [71].

Inspired by the results of Darrow et al. [158] on large-area PC antennas (with dimensions on the mm scale), Siebert et al. [172] attribute the rapid drop of the THz signal at $\tau = 0$ to the screening produced by the generated THz field. Indeed, from experimental findings sustained by simulations of the double-pulse experiments on large area photoconductive emitters [174, 175], it was shown that at high excitation densities (well into the THz output saturation regime) the sudden drop of the signal observable at $\tau = 0$ is due to the emitted THz near-field. Since the radiated electrical field is proportional to the current in the photoconductor, it contributes to the screening of the applied field until it disappears either because of recombination or trapping of carriers [158]. Here too, different features are observed from emitters on SI-GaAs and LTG-GaAs, similar to the SI-GaAs and GaAs/Si presented in Figure 5.4 (left panel). A fast recovery of the THz signal is reported only in the case of LTG-GaAs; the difference is explained in terms of the free carrier lifetime, since for SI-GaAs the very long recombination times (hundreds of ps) is responsible for a long-lived current generating a THz field which screens the applied over a long time. It is believed that space charge screening does not play an important role in this devices, given the large interspacing between electrodes (~ 5 mm) [178].

Recently, Yano et al. [173] performed a systematic study of the THz waveforms and double-pulse signals from a PC antenna on LTG-GaAs. The authors investigated the change that occurs in the THz waveform and the frequency spectra (FFT transform) as a function of the delay between the THz-pump and -probe pulse. Here, the fast recovery time at low optical pump levels matched with the trapping time from transient reflectivity measurements. Similar to the data presented in Figure 5.3, at higher excitation densities the authors also report a dependence of the fast recovery time constant with the THz-pump power level, attributed to the saturation of traps. The sudden drop and the fast recovery of the THz signal are explained in terms of the carrier-carrier scattering processes taking place between the THz-pump and -probe generated carriers, and trapping of carriers, respectively, using the simple

equation:

$$E_{\text{THz}}(t) \propto \frac{\partial(nev_e)}{\partial t} = ev_e \frac{\partial n}{\partial t} + en \frac{\partial v_e}{\partial t}. \quad (5.1)$$

Thus, the carriers injected by the THz-pump pulse at $\tau = 0$ increase the carrier-carrier scattering rates (due to the enhanced Coulomb repulsion) reducing the momentum relaxation time τ_s . Accordingly, the mobility of the electrons decreases and by that the carrier drift velocity, resulting in a lower value of the last term on the right-hand-side of Eq. 5.1, when the THz-pump beam precedes the THz-probe beam. The recovery is attributed to the trapping of electrons at ionized As_{Ga}^+ defects which screen the Coulomb field of each carrier, increasing the momentum relaxation time of the THz-probe carriers. However, we do not expect a significant contribution from the carrier-carrier interactions since (i) they become important only in degenerate systems (at very high carrier densities $> 10^{18} \text{ cm}^{-3}$) and (ii) the sudden drop is observed at densities where the number of injected carriers is lower or equal to the number of defects, therefore one would expect the electron mean free path to be on the same order of magnitude as the distance between As antisite defects, and thus no significant scattering should occur.

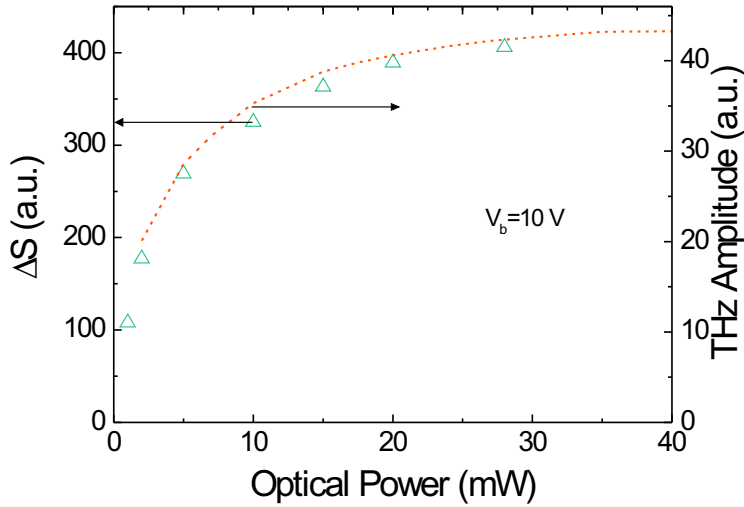


Figure 5.5.: Comparative plot of the THz signal drop at $t = 0$ (ΔS) for the **PC1** emitter, corresponding to the double-pulse data in Figure 5.3 together with the maximum amplitude of the THz-waveform measured with single-pulse excitation.

5.3.3. Experimental evidence for the radiation field screening effects

In preparation for the modeling of the double-pulse experiment (Section 5.4), we go one step further in analyzing some of the experimental facts. In Figure 5.5 we plot the relative change in signal ΔS at $\tau = 0$ as a function of the THz-pump power (measured with an applied bias of 10 V) corresponding to the data displayed in Figure 5.3. We also plot the THz-signal amplitude measured from *single-pulse excitation* for different optical power levels, at the same applied bias. The two plots are scaled with respect to each other, such that they overlap. One can clearly see that the magnitude of ΔS from the double-pulse measurements displays the same dependence on the THz-pump power as the peak of the THz-signal from the single-pulse measurements. The saturating behavior is consistent with the effect of the voltage divider in the equivalent circuit of the photoconductive switch, as discussed in the previous chapter. This piece of experimental evidence leads us to consider the effect of the equivalent circuit when modeling and interpreting the double-pulse data.

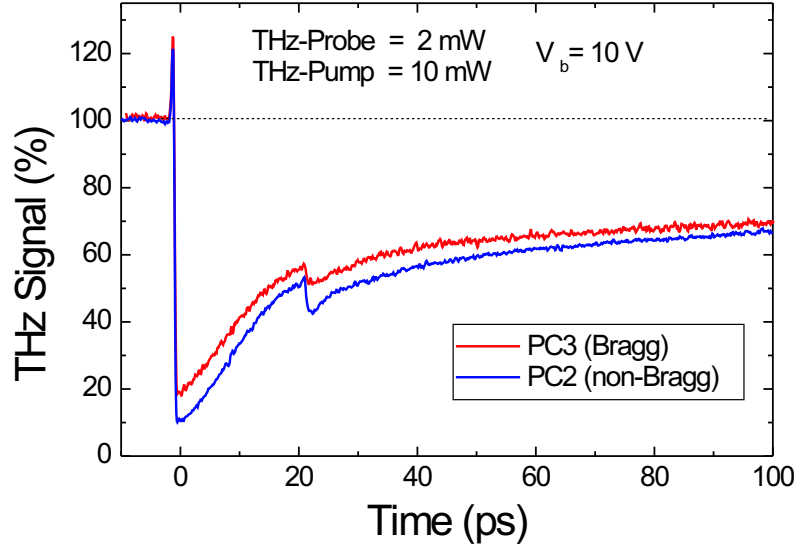


Figure 5.6.: Results of the double-pulse measurements on emitters with identically grown and annealed LTG-GaAs material with (**PC2**) and without Bragg reflector(**PC3**) embedded between the LTG- and SI-GaAs substrates.

5.3.4. Double-pulse traces on PC emitters with Bragg reflectors: no evidence for carriers generated in the GaAs substrate

As a concluding note for this section, we should mention that in almost all the above cited studies, the incomplete recovery of the THz signal (long-living pedestal) was explained through the absorption of light in the semi-insulating GaAs substrate, thereby generating carriers with a very long lifetime which would act to screen the internal field over many nanoseconds. With regard to this possibility, we manufactured two different PC emitters (PC2 and PC3) whose active LTG-layers (TP983 and 984) were grown and annealed in identical conditions (see Chapter 2), with the only difference that for the PC3 emitter a Bragg reflector was inserted between the $1.5\text{-}\mu\text{m}$ -thick LTG-GaAs layer and the $\sim 400\text{-}\mu\text{m}$ thick SI-GaAs substrate. The Bragg reflector consists of 20 sequences of $\text{Al}_{0.15}\text{Ga}_{0.85}\text{As}/\text{AlAs}$ alternating layers, each pair of the Bragg reflectors being $\sim 61\text{ nm}$, respectively $\sim 72\text{ nm}$ thick, the total thickness of the Bragg mirror being $\sim 2.6\text{ }\mu\text{m}$, and thus the penetration of a significant amount of laser light into the SI-GaAs substrate can be totally ruled out. Moreover, the Bragg reflector also acts as a diffusion barrier, confining the photo-generated carriers to the LTG-GaAs layer only, thus impeding the carrier diffusion into the low-electric field regions of the SI-GaAs substrate.

The results of the double-pulse measurements on the PC emitters with and without Bragg reflector are shown in Figure 5.6. Here again, the THz-signal amplitude was normalized to the THz signal measured at negative time delays, such that the relative change of signal at $\tau = 0$ can be expressed in percentage. The THz-pump and -probe power were set to 10 and 2 mW respectively, while the applied bias was 10 V. Besides the much slower recovery of the signal compared to the PC1 device (G420 material) (related to the different growth conditions of the active layer for the PC2 and PC3 devices, as discussed later), one can clearly see that the double-pulse traces are almost identical. The small ridge-like structure observed around 20 ps is most probably due to a small amount of optical-probe (TD) beam suffering a back-reflection at one of the EO-setup components, thus re-exciting the emitter. The comparison of the two traces reveals that for both emitters the signal recovers only to about 50 % of the THz signal measured at negative time delays, with the negative plateau persisting for longer than the time window of the measurement (> 100 ps). Therefore, we relate the existence of the long-living plateau exclusively to the intrinsic properties of the LTG-GaAs layer under illumination.

5.4. Modeling the double-pump pulse experiment

To understand the double-pulse experiments we implement a theoretical model in two steps: first, we extend the equivalent circuit model (which already takes radiation field screening into account as discussed in the previous chapter) such that it includes the space-charge screening effects due to the displacement of photogenerated carriers. The photoconductive antenna is excited with one pulse (assumed to be the THz-pump pulse) and the outcome of the model is the temporal evolution of the electrical field in the photogap, subsequent to the carrier photogeneration. According to the principle of the double-pulse experiment, it is this temporal field evolution that is “probed” by the THz-probe pulse.

In a second step, we modeled the response of the photoconductive antenna to a double-pulse excitation, including the detection of the THz-probe beam only, thus obtaining double-pulse traces that can be compared to the experimental ones.

5.4.1. Extended equivalent circuit model and the response to single-pulse excitation

The equivalent circuit model of a photoconductive antenna implemented in Chapter 4 was modified accordingly, as shown by the schematic in Figure 5.7. Here too, the photogap is modeled as a time-varying impedance Z_p , while the voltage drop due to the THz radiation emission process is accounted for through the antenna impedance Z_a , producing the “voltage divider” effect discussed in Chapter 4. Additionally, the

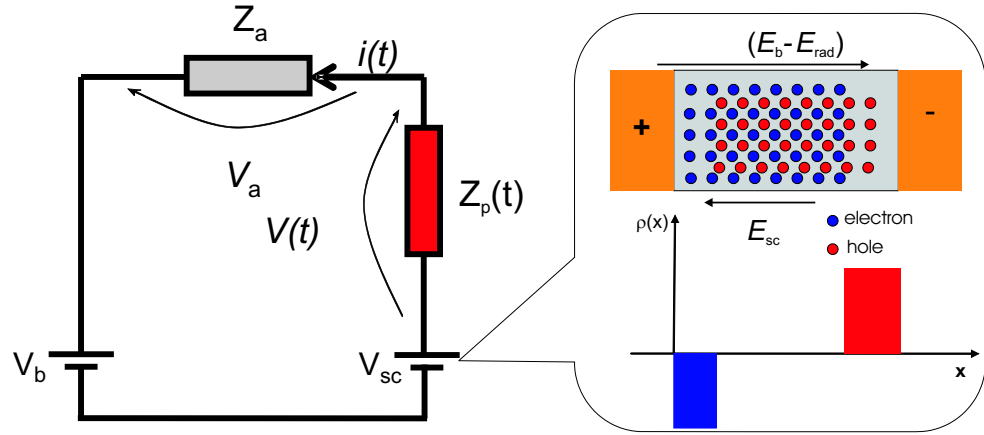


Figure 5.7.: Schematic representing the equivalent circuit of the PC emitter (left) and the microscopic representation of the space-charge effects in the illuminated photogap (right).

polarization induced by the charge carriers separating in the external field is symbolized by a voltage source V_{sc} . The total voltage drop across the photogap can be written:

$$V(t) = V_b - V_a(t) - V_{sc}(t), \quad (5.2)$$

with the corresponding electrical field given by:

$$E(t) = E_b - E_{rad}(t) - E_{sc}(t), \quad (5.3)$$

where $E_b = \frac{V_b}{d}$ is the applied bias field and d is the effective gap length, $E_{rad}(t)$ is the radiation field screening term:

$$E_{rad}(t) = \frac{j(t)A}{d} Z_a \quad (5.4)$$

and $E_{sc}(t)$ is the space-charge field screening.

The field screening E_{sc} arises from the space-charge created by the spatial separation of the photogenerated electrons and holes drifting in the external bias field, as illustrated in Figure 5.7 (right panel), that is, when the electrons and holes move to the electrode of opposite polarity, regions of net (uncompensated) positive and negative space-charge $\rho(x)$ develop. The electric field induced by the space-charge is oriented into the opposite direction to the external field, and therefore it screens the external applied bias.

Within a simplified point-dipole model, the screening field can be expressed in terms of the polarization $P(t)$ created by the separating carriers [170]:

$$E_{sc}(t) = \frac{1}{\mathcal{D}\kappa\epsilon} P(t), \quad (5.5)$$

where \mathcal{D} is a factor accounting for the geometry of the field in the active region, κ is a *screening factor* and ε is the permittivity of the photoconductive material. We assume the geometrical factor \mathcal{D} to be equal to 1 for the remainder of this work. The time dependence of the polarization can be obtained solving the rate equation:

$$\frac{dP}{dt} = j(t) - \frac{P}{\tau_R} = en_f(t)v(t) - \frac{P}{\tau_R}. \quad (5.6)$$

In writing the above equation we implicitly assumed that both free and trapped carriers can recombine with a time constant τ_R . As one can see from Eq. 5.6, the generation of the polarization is due to the displacement of carriers moving into the contacts, yielding a current flow in the external circuit, while the decay of polarization is caused by the recombination of carriers.

The different contributions to the photocurrent made by both types of free-carriers (electrons and holes), due to different mobilities and trapping times are accounted for by the screening parameter χ . Although it is mainly electrons contributing to the ultrafast photocurrent transient, the process and dynamics of the field screening involves also the holes.

The current density flowing in the gap is given by:

$$j(t) = \frac{i(t)}{A} = en_f(t)v(t), \quad (5.7)$$

with A the effective contact area of the photoconductive gap and $i(t)$ the time-dependent current flowing in the external circuit. The measure of the photocurrent in the data presented here is a measure of the time average of the above current density. The equivalence between the internal gap current and external circuit current assumes that no trapping takes place at the electrode boundaries. In Equation 5.7 $n_f(t)$ is the instantaneous density of free-carriers:

$$\frac{dn_f}{dt} = -\frac{n_f(t)}{\tau_c} + g(t), \quad (5.8)$$

with τ_c the carrier trapping time and $g(t)$ the photocarrier generation rate. A complete derivation of the solution of the rate equation for carrier density in response to a single Gaussian pulse excitation can be found in Appendix A.1.

The solution to Eq. 5.6 can be found using the Green's function method:

$$\begin{aligned} P(t) &= e \int_{-\infty}^t dt' n_f(t') v(t') e^{-(t-t')/\tau_R} \\ &= ee^{-t/\tau_R} \int_{-\infty}^t dt' n_f(t') v(t') e^{t'/\tau_R}. \end{aligned} \quad (5.9)$$

Here, the physical meaning of the convolution integral is that the photogenerated carriers move in the external field with a velocity $v(t)$ until they are captured at

the defects [170]; once they are trapped, the screening of the external field stops increasing, but the trapped carriers still continue to statically screen the external applied field. The screening due to the free and trapped carriers decays over a time determined by the recombination τ_R .

The motion of carriers in the time dependent electrical field is governed by:

$$\frac{dv(t)}{dt} = -\frac{v(t)}{\tau_s} + \frac{e}{m^*}E(t), \quad (5.10)$$

where $1/\tau_s$ is the carrier scattering rate. If we assume a very efficient scattering mechanism at low electric fields (like for instance, scattering with acoustic phonons), in the approximation $\tau_s \rightarrow 0$, the drift velocity becomes:

$$v(t) = \mu_e E(t), \quad (5.11)$$

where μ_e is the carrier mobility. Making the appropriate substitutions, the polarization and current density takes the form:

$$P(t) = e\mu_e e^{-t/\tau_R} \int_{-\infty}^t dt' n_f(t') E(t') e^{t'/\tau_R}, \quad (5.12)$$

and respectively:

$$j(t) = e\mu_e n_f(t) E(t). \quad (5.13)$$

Substituting Eq. 5.13 into Eq. 5.7 and Eq. 5.12 into Eq. 5.5, the time dependent electric field in the photogap can be written:

$$E(t) = E_b - \frac{e\mu_e Z_a A}{d} n_f(t) E(t) - \frac{e\mu_e}{\kappa \varepsilon} e^{-t/\tau_R} \int_{-\infty}^t dt' n_f(t') E(t') e^{t'/\tau_R}. \quad (5.14)$$

The above integral equation can be transformed into a differential equation, via differentiation and back-substitution (see Appendix A.2):

$$\left[1 + \frac{e\mu_e Z_a A}{d} n_f(t) \right] \frac{dE}{dt} = - \left[\frac{1}{\tau_R} + \left(\frac{e\mu_e Z_a A}{\tau_R d} + \frac{e\mu_e}{\kappa \varepsilon} \right) n_f(t) + \frac{e\mu_e Z_a A}{d} \frac{dn_f}{dt} \right] E(t) + \frac{E_b}{\tau_R}. \quad (5.15)$$

Eq. 5.15 self-consistently describes the temporal evolution of the electric field in the gap and can be solved numerically [179]. One possibility to implement the computational algorithm is to form a system of differential equations containing the equation for $n_f(t)$ together with the equation for $E(t)$, or alternatively, one can use the solution of $n_f(t)$ in response to a single Gaussian pulse excitation as given in Appendix A.1 and solve numerically only for $E(t)$.

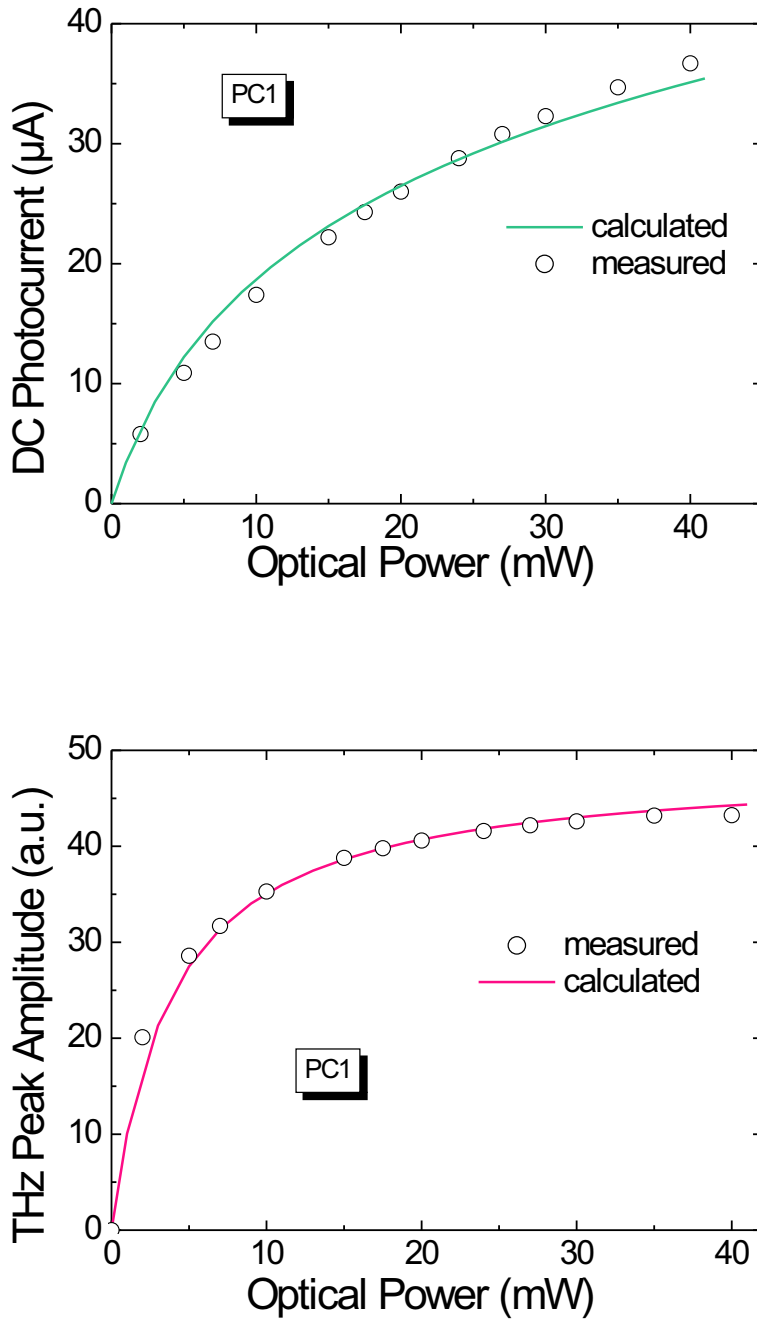


Figure 5.8.: Calculated and experimental data for the saturation of the DC photocurrent (upper panel) and THz-field peak (lower panel) with optical power for the **PC1** emitter. The applied bias field was 20 kV/cm (10 V).

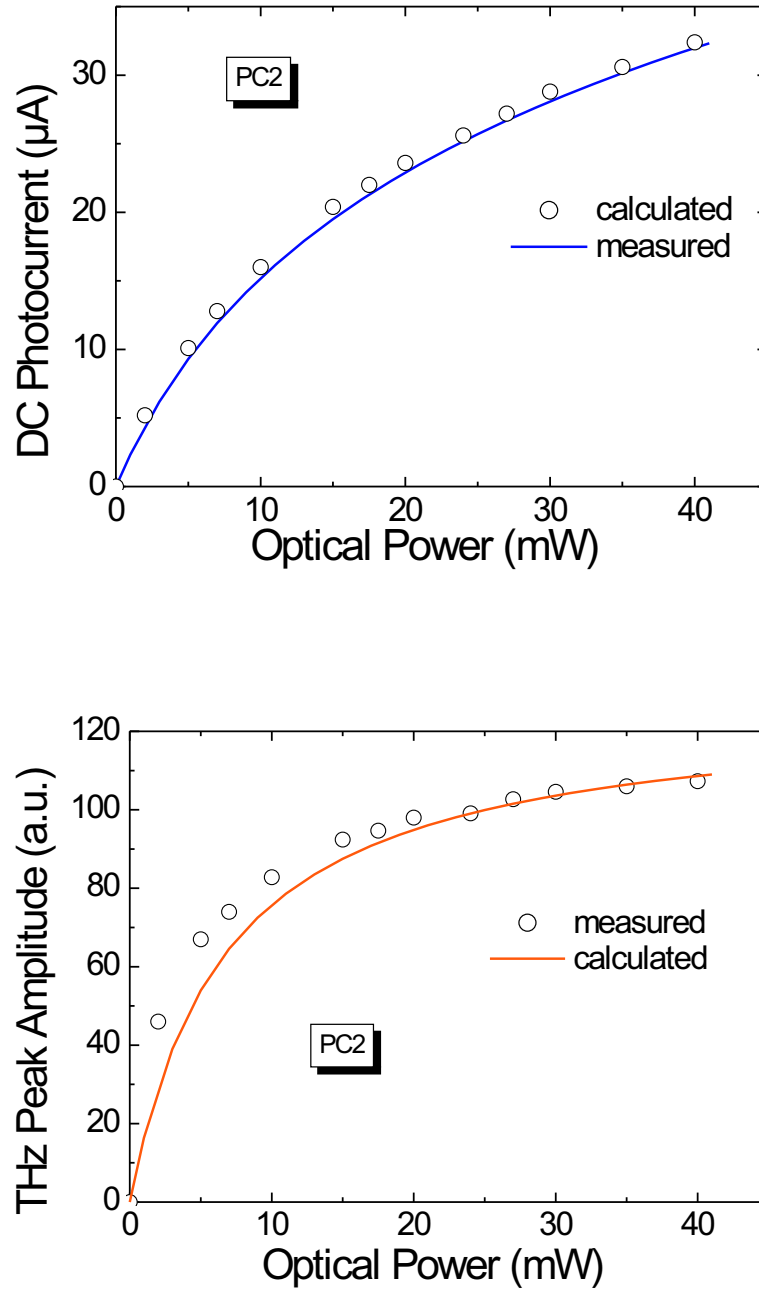


Figure 5.9.: Calculated and experimental data for the saturation of the DC photocurrent (upper panel) and THz-field peak (lower panel) with optical power for the **PC2** emitter. The applied bias field was 20 kV/cm (10 V).

5.4.2. Validation of the equivalent circuit model for single-pulse excitation

To check the applicability of our model and to obtain some preliminary information on the parameters we can use in modeling of the double-pulse experiment, first we compared the model against the experimental single-pulse excitation data for saturation data presented in Chapter 4 (Figure 4.11).

First, we calculated the temporal evolution of the electrical field in the photogap and the photocurrent flowing in the external circuit, as given by the solution of Eq. 5.15 and 5.13, respectively. The density of free carriers was simplified to $n_f \propto n_0 e^{-\frac{t}{\tau_c}}$ (i.e. assuming an infinitely short optical pulse). By taking the time-derivative of the photocurrent, we calculated the THz waveform and thereby the maximum amplitude of the THz field, as well as the DC photocurrent, by taking the time average of the instantaneous photocurrent over the repetition rate⁴. The procedure was repeated for several optical intensities, ranging from 2 to 40 mW. The results of the simulation were compared against experimental data measured for the emitter PC1 (G420) at an applied bias of 10 V. A few of simulation parameters, i.e. antenna geometry d , antenna impedance Z_a and applied bias V_b , were kept constant while other parameters, i.e. carrier trapping time τ_c , the screening factor κ and electron mobility μ_e were varied, such that the calculated values best matched the experimental data. The calculated curves did not seem to depend in a sensitive manner on the recombination time for values above 100 ps, hence τ_R was set to 1 ns. The best results, obtained for the parameters listed in Table 5.4.2, are plotted in Figure 5.8. Following the same procedure we also fitted the DC photocurrent and THz peak signal of the PC2 emitter as shown in Figure 5.9. As can be seen, the modeled data agrees very well with the experimental data for both emitters. The significance of the higher values for mobility (μ_e) and trapping time (τ_c) used in calculating the data for the PC2 antenna will be addressed in Section 5.5.

Emitter	κ	μ_e	τ_c	τ_R	V_b	Z_a
PC1	800	900 cm ⁻² /Vs	1.1 ps	>100 ps	10 V	75 Ω
PC2	700	1600 cm ⁻² /Vs	3.8 ps	>100 ps	10 V	75 Ω

Table 5.1.: Parameters used to fit the experimental saturation curves in Figures 5.8 and 5.9.

It is important to mention that we also tried to reproduce the saturation of the DC photocurrent and THz peak amplitude with optical power for PC1 emitter (as depicted in Figure 5.8), by only taking into account the effect of space-charge

⁴A similar procedure was used in Chapter 4.

screening and discarding the effect of the equivalent circuit (by setting the antenna impedance Z_a to zero). Although we observed a small non-linearity in the calculated time-averaged photocurrent, the magnitude of the saturation behavior could not be reproduced.

5.4.3. Temporal evolution of the field in the photogap

With the fitting parameters listed in Table 5.4.2, we proceeded to calculate and plot the solution for $E(t)$ of Eq. 5.15, which gives the temporal evolution of the electric field in the gap, subsequent to the excitation with a single pulse. Knowing the field in the gap, one can now calculate the instantaneous photocurrent flowing into the circuit $i(t)$ and hence, the voltage drop across the load impedance Z_a represented by the antenna, thus yielding the radiation field screening as given by Eq. 5.4. The temporal evolution of the space-charge screening field can be obtained by subtracting the field in the gap together with the field due to radiation field screening from the applied bias field.

In Figure 5.10 we plot the numerical solution for $E(t)$, $E_{vd}(t)$ and $E_{sc}(t)$ (upper panel) and for $j(t)$ (lower panel) at two different optical pump intensities, 2 and 28 mW, respectively. Here (Figure 5.10), the moment $t = 0$ denotes the time at which the laser pulse intensity reaches its maximum, as does the density of the photogenerated carriers. At 2 mW (excitation density $\sim 6 \times 10^{17} \text{ cm}^{-3}$) one can clearly see that there is a sudden drop of the field in the gap at $t = 0$, followed by an almost complete exponential recovery on the same time scale as the trapping time. For the higher optical intensity, the field in the gap drops to almost 20 % of the value before the pulse arrival, while recovering only partially on a much longer time scale (> 4 ps) with a non-exponential behavior. The contrary is observed for the voltage drop across the antenna impedance, which takes the same shape as the temporal dependence of the photocurrent (lower panel), having its maximum at $t = 0$. The contribution of screening to the decrease of the field in the gap is far higher for the higher excitation density.

The physics of the whole electric field dynamics in the first picoseconds following the single-pulse excitation of the photogap can be well understood within the frame of the radiation field and space-charge screening model presented here. Thus, at $t = 0$, the photogenerated current flowing into the dipole arms determines an instantaneous response through the antenna impedance, caused by the radiation emission process, which materializes in a voltage drop across the dipole arms (i.e. at the boundaries of the photogap), hence building up an electrical field $E_{rad}(t)$ which screens the applied bias field across the photogap. Since the magnitude of the radiation screening field is proportional to the current flowing into the antenna, it contributes to screening of the bias field until the current disappears either because

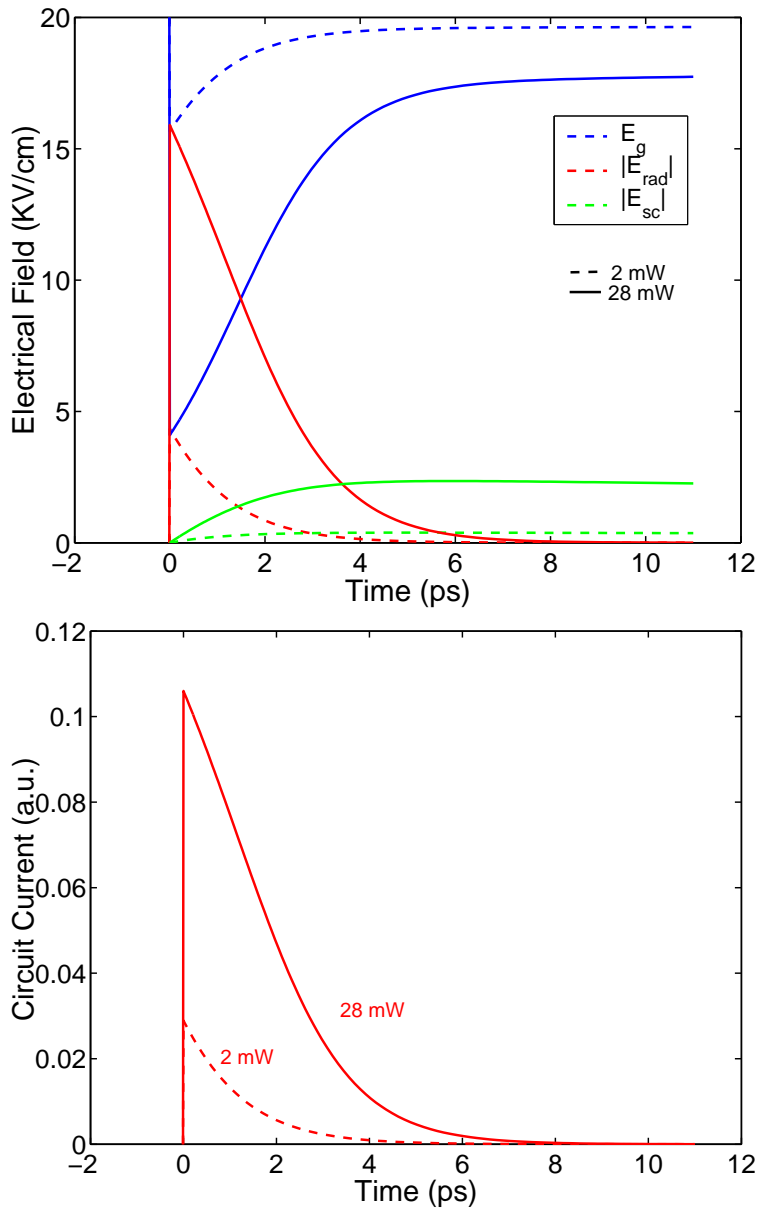


Figure 5.10.: **Upper panel:** temporal evolution of the electrical field in the gap $E(t)$, the field screening $E_{vd}(t)$ caused by radiation field-screening and space-charge field screening $E_{sc}(t)$; **Lower panel:** the photocurrent flowing into the external circuit.

of the recombination at electrodes or trapping of carriers.

On the other hand, the *building up* of the space-charge screening field $E_{sc}(t)$ is concomitant with the photocurrent flow, therefore approaching its maximum on the time scale of the carrier trapping time. Due to the fact that the trapped carriers continue to statically screen the electrical field until they recombine, the drop in the field at the gap caused by the screening persists on a long time scale (here, we assumed $\tau_r > 100$ ps).

For an alternative way to understand the dynamics, we focus again on the equivalent circuit sketched in Figure 5.7. At $t = 0$ the influx of photogenerated carriers decreases the impedance of the photogap $Z_p(t)$, thus leading to a drop of the applied voltage $V(t)$, and hence of bias field at the gap. In the same time, at high excitation densities, the photogap is basically short-circuited and most of the bias voltage drops on the load impedance Z_a presented by the planar antenna. In this THz-saturation regime, the relationship between the time-dependent local impedance $Z_p(t)$ induced by the laser pulse and optical power P_{opt} becomes non-linear [165], as reflected in the saturation curve displayed in Figure 5.5. Here, as discussed in the previous chapter, for $Z_a \approx Z_p$, the photogap becomes biased through the load impedance Z_a ⁵, as opposed to the case of low optical intensities ($Z_p(t) \gg Z_a$), where the photogap and hence the photocurrent is approximately voltage biased (i.e. the bias applied across the photogap is approximately the bias delivered by the voltage source). As the photogenerated carriers are captured by the defects, the impedance of the photogap rises to its dark value and hence the voltage across the gap recovers on almost the same time scale as the trapping of free carriers. Also, the voltage drop due to the space-charge screening “turns on” on a time scale equal with that of the carrier capture time and it “turns off” after a time which equals the recombination time.

Note that the model we propose here does not differentiate between the conduction current and displacement current. The particle current is given by the carriers recombining at the electrodes, while, according to Maxwell’s equations, the displacement current is caused by the change of the internal electric field (due to field-screening in the present case):

$$J_d = \varepsilon_0 \varepsilon_r \frac{dE(t)}{dt}.$$

This could be understood as follows: due to the boundary conditions at the electrodes, that is, the external field should match the field inside the photogap at any instant of time, every moving charge species causes a readjusting of the electrical field between the electrodes by inducing on each electrode a certain amount of op-

⁵The impedances in series presented by the antenna and the photogap form a *voltage divider*, that is, it supplies a voltage lower than that from the voltage source, that is the photocurrent in the gap is no longer voltage biased.

posite charge (Gauss' law) which amounts for the displacement current that flows into the external circuit.

The displacement current makes an important contribution to the total transient current response for pulsed illumination, especially at early times and high illumination intensities, as pointed out by Dunn et al. [135] from Monte Carlo simulations on MSM photodetectors. The preponderance of displacement current in the total current measured on LTG-GaAs-based MSM photoconductors was demonstrated by Klingenstein et al. [94].

The key point of investigating the response of the photoconductive antenna to a single-pulse excitation within the demonstrated present model lies in a better understanding of the double-pulse experiment: the THz-probe “senses” the changes in the local field induced by the THz-pump beam arriving at $\tau = 0$ under the condition that the THz-probe beam intensity is low enough below the saturation level. According to our understanding of the phenomenon, the double-pulse trace (obtained by chopping the THz-probe only) directly reflects E_g displayed in Figure 5.10. Therefore, we can conclude that the reason for the sudden drop in the signal observed at $\tau = 0$ in the double-pulse traces is due to radiation field screening; also, the fast recovery component is related to the carrier trapping process while at long times space-charge field screening prevails.

The viability of our theoretical approach in understanding the double-pulse experiments is also supported by the results published recently by Eusebe et al. [164]. The authors investigated the dynamics of the electric field in Be-doped LTG-GaAs by means of photoconductive sampling, using a photoconductive switch embedded in a coplanar waveguide. In contrast to our approach, the pump and probe beams were localized at different places on the device, the pump beam alters the biasing scheme of the photoswitch which is then probed with a second laser beam. The difference here consists in that the antenna was replaced with a transmission line whose characteristic impedance determines a voltage drop across the photogap when a ultrafast current pulse propagates along the line. Here too, as in the case of our double-pulse experiments, the change in the local electric field in the photogap is monitored, revealing the ultrafast carrier dynamics. From modeling the photoswitch as a time-varying impedance and considering two species of carriers (electrons and holes) the authors determine some of the carrier recombination parameters (i.e., a slow recovery of the signal is attributed to holes being trapped after 12 ps). However, in this approach the screening present at high intensities used is not taken into consideration.

5.4.4. Photoswitch response to double-pulse excitation

In calculating the response of a PC antenna to double-pulse excitation, the procedure described in Section 5.4 yields an extremely long computation time. A solution to this was found by substituting Eq. 5.13 and Eq. 5.5 in Eq. 5.3 and solving for $E(t)$. After recasting the terms (see Appendix A.3), we obtain:

$$E(t) = \left[1 + \frac{e\mu_e Z_a A}{d} n_f(t) \right]^{-1} \left[\frac{V_b}{d} - \frac{P(t)}{\kappa\varepsilon} \right], \quad (5.16)$$

which if inserted in Eq. 5.11 and finally in Eq. 5.6, after a number of extensive algebraic manipulations yields an inhomogeneous differential equation with time-dependent coefficients:

$$\frac{dP}{dt} = -a(t)P(t) + b(t),$$

with

$$a(t) = \frac{1}{\tau_R} + \frac{e\mu_e}{\kappa\varepsilon} \frac{1}{1 + \frac{e\mu_e Z_a A}{d} n_f(t)} n_f(t)$$

and

$$b(t) = \frac{e\mu_e n_f(t)}{1 + \frac{e\mu_e Z_a A}{d} n_f(t)} \frac{V_b}{d}, \quad (5.17)$$

with the general solution of the form:

$$P(t) = \left[\int_{-\infty}^t dt' b(t') \exp \left\{ \int_{-\infty}^{t'} dt'' a(t'') \right\} \right] \exp \left\{ - \int_{-\infty}^t dt'' a(t'') \right\}. \quad (5.18)$$

If we assume that the carrier density can be found analytically (see below), one needs to solve for $P(t)$ and to substitute this back into Eq. 5.16 to obtain the current density. Since $E_{\text{THz}}(t) \propto \frac{dj}{dt}$, we can then calculate the THz waveform. Eq. 5.18 can be calculated by numerical integration much faster than an iterative solution to the differential equation (Eq. 5.15).

Since the solution to the rate equation of the free-carrier density generated with a single Gaussian pulse is linear⁶ (Appendix A.1), the solution for the double-pulse excitation can be obtained by adding the solutions for each pulse and introducing an arbitrary time delay between the pulses. Assuming a Gaussian time-dependence for the double-pulse excitation, where the THz-pump pulse arrives a time $\Delta\tau$ before the THz-probe, we can describe the temporal profile of the optical power as:

$$P_{\text{opt}}(t) = \frac{1}{T_0\sqrt{\pi}} \left[J_{\text{pump}} \exp \left(-\frac{(t + \Delta\tau)^2}{T_0^2} \right) + J_{\text{probe}} \exp \left(-\frac{t^2}{T_0^2} \right) \right], \quad (5.19)$$

⁶The depletion of electrons in the valence band (i.e. photobleaching) is neglected here as is reasonable for the excitation densities used.

where $J = \frac{\bar{P}}{\nu_p}$ is the optical pulse energy, \bar{P} and ν_p are the average optical power and laser repetition rate, respectively, while $T_0 = \frac{T_{FWHM}}{\sqrt{4 \ln 2}}$ is a measure of the pulse width.

According to Eq. A.8 in Appendix A.1, the solution for the carrier density in this case becomes:

$$n_f(t) = \frac{1}{2} \frac{\eta}{h\nu\mathcal{V}} \exp\left(\frac{T_0^2}{4\tau_c^2}\right) e^{-\frac{t}{\tau_c}} \left\{ J_{\text{pump}} \left[\text{erf}\left(\frac{t+\tau}{T_0} - \frac{T_0}{2\tau_c}\right) + 1 \right] e^{-\frac{\Delta\tau}{\tau_c}} + J_{\text{probe}} \left[\text{erf}\left(\frac{t}{T_0} - \frac{T_0}{2\tau_c}\right) + 1 \right] \right\}, \quad (5.20)$$

where η and \mathcal{V} are the quantum efficiency and the active volume, respectively.

5.4.5. Validation of the equivalent circuit model for double-pulse excitation

Based on the theoretical considerations described above, we implemented a numerical procedure that allowed us to calculate the detected THz (lock-in) signal for a typical double-pulse experiment. The simulation procedure for the double-pulse excitation differs to that used for a single-pulse excitation, given the different nature of the pump-pulses and detection scheme, that is, only one of the two pump pulses was chopped (i.e. the THz-probe pulse). Therefore, the simulation should reproduce the detection of the THz signal from the second excitation pulse (THz-probe) only, but including the effect of the first pulse (THz-pump). To accomplish this, at first we computed the reference THz waveform from a single-pulse excitation for both THz-pump and -probe separately, identifying the best probe detection time by looking for the maximum of the THz-field amplitude for the THz-probe pulse alone. Then, we repeated the calculations with double-pulse excitation, as given by Eq. 5.20, and the corresponding traces were obtained by subtracting the amplitude of the reference THz waveform (THz-pump only) from the amplitude of the calculated double-pulse THz waveform. This procedure is then repeated for different values of the time-delay τ between the two pulses.

In Figure 5.11 we compare the experimental data (upper panel) from the PC1 antenna against the results of the calculated (lower panel) double-pulse traces following the algorithm described above. Consistent with the discussion in Section 5.4, we simulated the double-pulse response using the same parameters as for the single-pulse response, that is, the same parameters (see Table 5.4.2) which fit the saturation curves measured for the PC1 (G420) emitter in Figure 5.8. The applied bias was 10 V and the THz-probe beam power in this case was taken as 2 mW, while the THz-pump power was varied between 2 and 28 mW, as for the set of experimental data. Since the model we used in approaching the double-pulse response of a PC emitter does not include the cumulative effects of the long-lived screening which would result in the level of the THz signal at negative time delay being dependent on

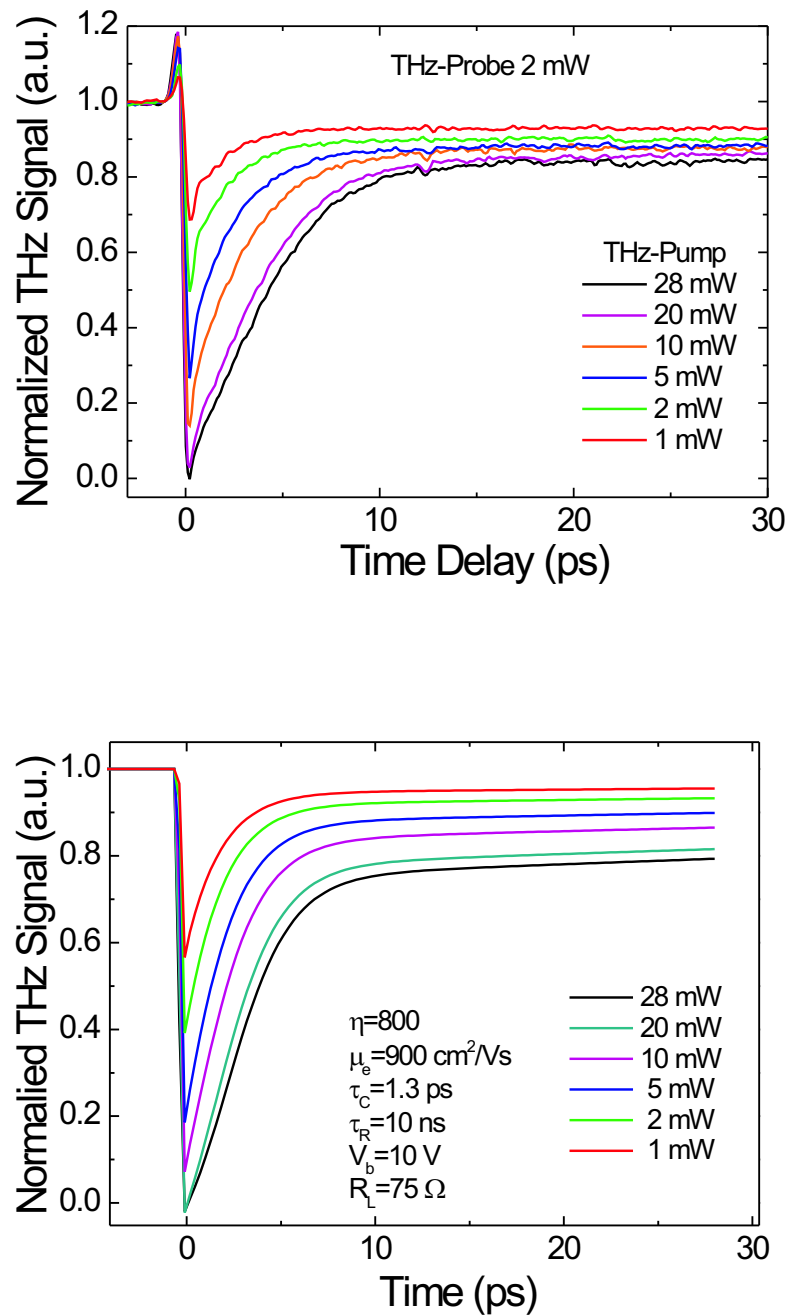


Figure 5.11.: **Upper panel:** Normalized THz signal for the double-pulse measurements from the **PC1** compared against **Lower panel:** simulation results of the double-pulse traces, obtained with the parameters displayed in the inset.

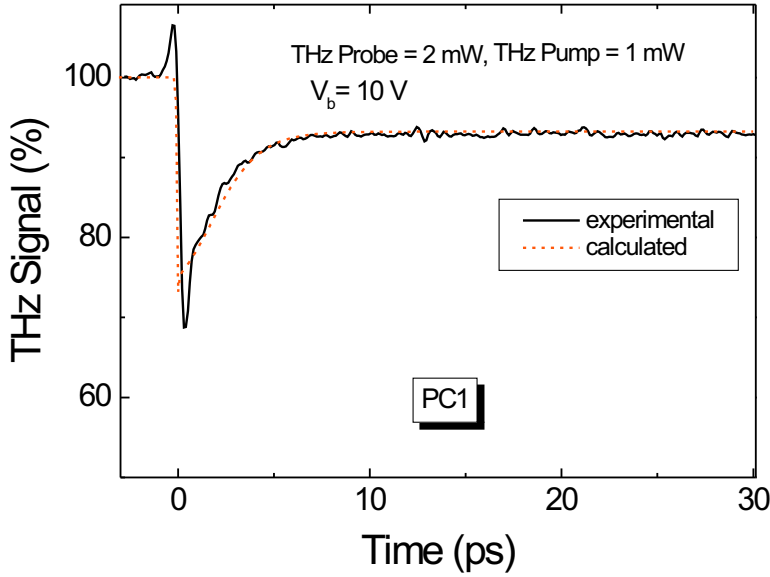


Figure 5.12.: Comparison between the calculated and experimental double-pulse data as obtained from the **PC1** emitter for a THz-pump power of 1 mW (lower panel).

the THz-pump intensity, we normalize the experimental data to unity on the negative time delay in order to compare it with the results of our calculations. We observe a fairly good qualitative agreement between the corresponding curves in the upper and lower panels of Figure 5.11, especially at low excitation densities. However, the simulated data does not accurately reproduce the variation of the long-living pedestal with the THz-pump power (i.e. for $\tau \geq 10$ ps), as observed for the experimental data, but all main trends observed in the whole set of experimental data are reproduced well by the calculated double-pulse curves. These are the maximal level of screening, the time scale of the THz signal relaxation and the approximate magnitude of the long-persisting pedestal. The slight disagreement between the measured and calculated double-pulse traces can be attributed, as mentioned earlier, to not accounting for effects like the long-living trapped carriers from previous pulses (see discussion in Chapter 6), as well as limitations due to the relatively simple model (i.e. neglecting effects like 2-D space-charge effects and inhomogeneous illumination across the photogap).

We tried to fit each of the measured double-pulse traces individually with the parameters listed in Table 5.4.2, and one can see that the trace measured at the lowest THz-pump power (1 mW) is reproduced accurately by the model, as illustrated in Figure 5.12. From the normalized experimental data (Figure 5.11 (upper

panel)), one can see that the signal level of the long-living pedestal tends to saturate for high excitation densities. Also, the partial recovery of the experimental data takes place on a slightly longer time scale than the simulated data. The discrepancy between the measured and simulated data may be due to the fact that in our approach we implemented a trapping time τ_c that does not depend on the density of the free carriers generated by the optical pulse. Several groups have investigated the lifetime of free-carriers at high excitation densities by means of optical-pump and -probe [70, 180] or optical pump-THz-probe techniques [34, 75] reporting a considerable slowing down of the conductivity-decay and hence an increased trapping time with increasing density. The estimated density of traps (assuming deep ionized As_{Ga}^+ antisite defects as electron traps) for the material used for the PC1 emitter can be extrapolated from the growth and annealing temperatures [54], yielding a trap density of approximately $\sim 10^{18} \text{ cm}^{-3}$. This implies that for THz-pump power levels higher than 5 mW (excitation density $\sim 1.5 \times 10^{18} \text{ cm}^{-3}$) we expect the trap saturation phenomena to occur. In this case, both free-carrier decay as well as the trapped-carrier decay rates are interrelated and become a function of optical intensity. The removal of carriers from the conduction band in this case is not determined solely by a constant carrier trapping time anymore, but also by the trap emptying time (i.e. recombination, which also comprises the hole capture time) creating a "bottleneck" effect.

The same issues arises for the screening E_{sc} generated by each THz-pump pulse; assuming that the amount of screening is given by the number of trapped carriers, when the density of traps is outnumbered by the photogenerated carriers, the screening level and hence the magnitude of the long-living pedestal saturates with increasing the optical intensity, consistent with the trend observed in the experimental data.

Last but not least, one has to take into consideration the effect of the high excitation density on the carrier mobility, since, at high carrier densities the carrier-carrier scattering becomes quite efficient [181], causing the mobility to drop. For an accurate description of the screening process one needs to model the photoswitch response by considering a time-dependent mobility, as used for example in Ref. [178]:

$$\mu(t, t') = \frac{\mu_f - (\mu_f - \mu_i) \exp[-(t - t')/\tau_\mu]}{1 + B \int_{-\infty}^t P_{\text{opt}} \exp[-(t - x)/\tau_c] dx}. \quad (5.21)$$

The above equation describes a mobility that decreases with carrier density, as well as an exponential increase of mobility from its initial value μ_i to a final value μ_f within a time τ_μ .

5.5. Double-pulse measurements on emitters with different LTG-GaAs materials

To illustrate the usefulness of the double-pulse measurements in characterizing and optimizing the LTG-GaAs-based photoswitches, in Figure 5.13 we display the double-pulse signal from two emitters (PC1 and PC2) with identical antennas processed on different LTG-GaAs material (G420 and TP983). The measurement conditions in this case were identical, the emitters were biased with 10 V and the THz-pump and -probe power were both 2 mW. Although we performed measurements where the THz-pump intensity was varied over a wide range, we choose to compare the curves obtained for a low excitation density ($\sim 3 \times 10^{17} \text{ cm}^{-3}$), in order to avoid trap saturation effects. The signals were normalized to 100 % at the negative time delay, such that the relative drop of the THz signal at $\tau > 0$ could be easily quantified. It would appear that the signal from the PC2 emitter is stronger; a possible explanation could be the higher mobility assumed for the TP983 material (discussed latter) or the slightly different beam-focusing conditions.

Two features are striking at a first glance: first, in spite of the fact that the TP983 material was grown at a much lower temperature (200 °C) than the G420 (270 °C) it shows a much slower recovery of the THz signal, which reaches the long-living pedestal only after ~ 20 ps, whereas in the case of G420 this occurs within ~ 5 ps. A second feature is the magnitude of the recovery: the G420-based PC emitter recovers to more than 80 % of the negative delay signal, while the TP983-based device only to about 50 %.

The parameters used in calculating the double-pulse response for the PC1 and PC2 emitters (as displayed in Figure 5.13) are listed in Table 5.5. We could fit the measured double-pulse curve from the PC2 emitter only by setting the carrier trapping time to ~ 3.8 ps and the mobility to $1800 \text{ cm}^2/\text{Vs}$, while the data for the PC1 emitter was reproduced using a lower mobility and carrier trapping time. This observation could be correlated with the information obtained from the optical-pump-probe measurements performed on the TP983 and G420 materials, as discussed in Chapter 2. For the TP983 (PC2) substrate, the free-carrier decay dropped to its $1/e$ -value with a 2 ps time-constant, while the strong signal (unexpected for

Emitter	κ	μ_e	τ_c	τ_R	V_b	Z_a
PC1	700	$900 \text{ cm}^{-2}/\text{Vs}$	1.3 ps	> 100 ps	10 V	75Ω
PC2	700	$1800 \text{ cm}^{-2}/\text{Vs}$	3.8 ps	> 100 ps	10 V	75Ω

Table 5.2.: Model parameters for the PC1 and PC2 emitters.

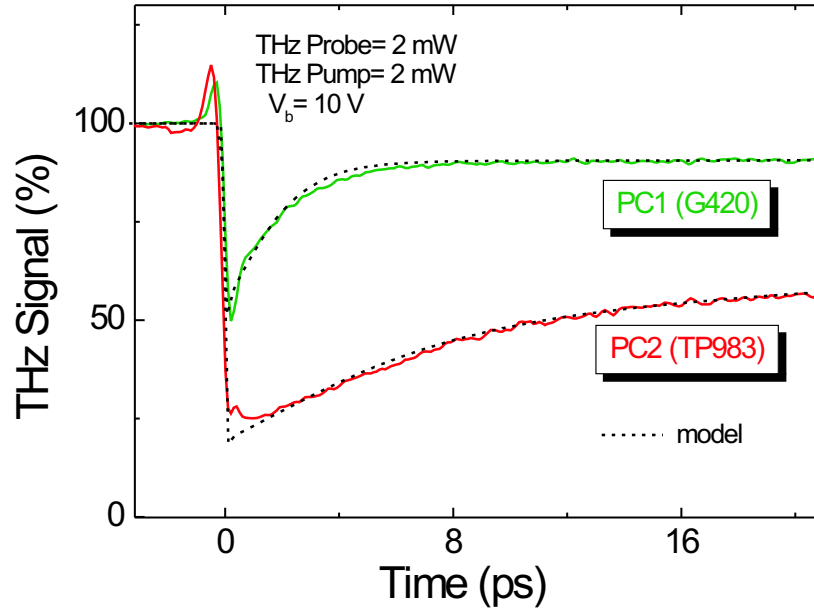


Figure 5.13.: Comparison of the double-pulse traces measured under similar experimental conditions for two PC emitters manufactured on different materials; the measured data from the PC1 and PC2 emitters was fitted with the parameters displayed in Table 5.5.

a good-quality LTG-GaAs material) suggests a high-degree of crystallinity in the LTG-GaAs material. This could also explain the larger mobility which fits the data, and by that the stronger negative time-delay signal observed for the PC2 emitter. In the same manner, the weak signal observed in the optical pump-probe measurements performed on the G420 (PC1) corresponds to a much shorter carrier lifetime and mobility. Also, the increased magnitude of the THz signal change at $\tau = 0$ for the PC2 emitter can be explained through this higher mobility, due to the stronger radiation field screening effect.

Formally, the only difference in the post-growth treatment of these samples was the different annealing times (5 min for G420 and 15 min for TP983). As pointed out in Ref. [75], during the annealing process, the excess As atoms form clusters/precipitates, reducing the lattice strain. Therefore, increasing the annealing time results in larger clusters with greater separation. This could explain the longer carrier trapping times, while the decrease in the lattice strain could be responsible for the increased mobility. Another fact that could explain the anomalous behavior of the TP983 material might lie in the different origin of the sample, that is, the calibration of the thermocouple used in controlling the growth temperature can

severely differ from one MBE reactor to another. Thus, the real growth temperature difference between the two materials is unknown. In spite of this uncertainty, the double-pulse measurement technique reveals the less optimal character of the TP983 material for ultrafast device applications.

In any case, a delicate issue that remains is the ability to capture carriers and by that, the field-screening properties of the As precipitates/clusters. If we consider only the As_{Ga}^+ defects as trapping centers, the decreased density of ionized As antisite defects due to the high growth temperature or annealing would result in a reduced level of screening (long-lived pedestal) for the samples grown at lower temperatures. This is in contradiction with the results of Kawasaki et. al [182], where the level of screening (the magnitude of the long-living pedestal) increased with the growth temperature. Recently, Gregory et al. [183] proposed a two-trap model for LTG-GaAs where the point defects and precipitates are described independently, representing two different types of recombination centers with different recombination time constants. It is suggested that the carriers trapped at the precipitates recombine with a time constant close to the carrier life-time in SI-GaAs (50 ps to 1 ns, depending upon purity).

5.6. Bias dependence of the double-pulse traces

We have also investigated the double-pulse response of the PC1 emitter under different bias conditions, as shown in Figure 5.14. To be able to identify the effect of altering the bias we kept the THz-pump and -probe power at the same level (both ~ 5 mW), while the bias was varied. A constant THz-pump level implies that the same amount of charge per pulse (here, $\sim 1.5 \times 10^{18} \text{ cm}^{-3}$ EHP) was generated in the photogap.

One can notice that at negative time delay the amplitude of the THz-signal scales linearly with the applied bias, as expected from the linear dependence of the THz-field amplitude with the applied bias (see Chapter 4). Note that also the magnitude of the signal change at zero time delay scales linearly with the applied bias field. After the fast drop at $\tau = 0$, the signal recovers with almost the same time constant, although to a slightly different level. To emphasize this effect, we choose to plot the absolute value of the double-pulse THz signal, since in this case, the normalization of data to unity at $\tau < 0$ can lead to erroneous conclusions (see Ref. [184]). In conformity with the interpretation of the double-pulse signal, as discussed in Section 5.4, by comparing the absolute magnitude of the long-living pedestal, one can obtain quantitative information on the field screening occurring in the PC emitter, for a given pulse intensity and applied bias. Therefore, in the inset of Figure 5.14 we plot the magnitude of the pedestal, denoted as ΔE_{sc} . Indeed, as predicted by our model, the level of field screening increases as the bias field increases. This can

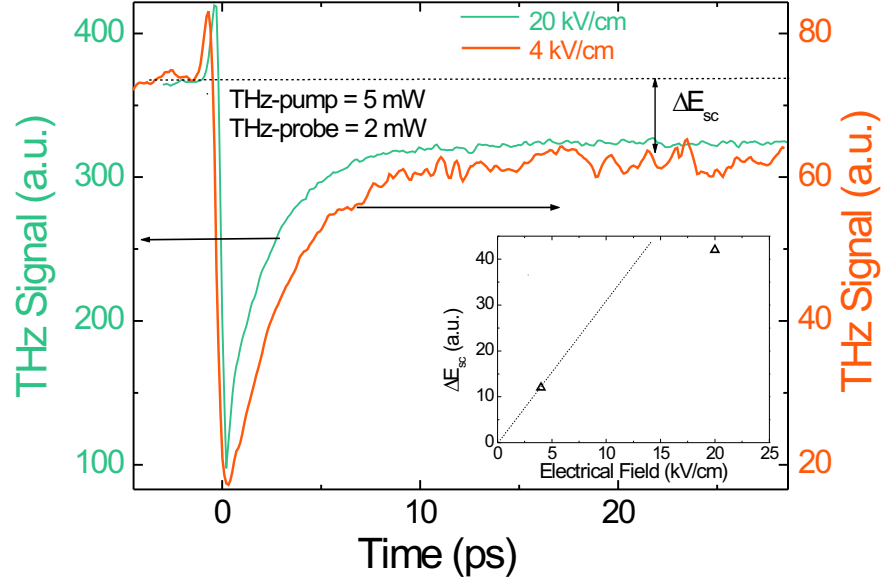


Figure 5.14.: Double-pulse traces measured for the PC1 emitter with the same value of THz-pump power (5 mW) and different bias field values.

be understood as follows: when the photogenerated electrons and holes are drifting in the external field, they recede from the region close to their respective injection electrodes. After they become trapped, regions of uncompensated trapped charge forms at the contacts, similar to the situation sketched in Figure 5.15. The amount of uncompensated charge and hence the screening field can be determined from the amount of charge that flows into the contacts, and is therefore related to the measured DC photocurrent, as will be discussed in the next chapter. Knowing the carrier trapping time τ_c and mobility μ for each of the carrier species, the charge collected at the electrodes is given by:

$$Q^{\text{cont}} = Q^{\text{gen}} \frac{v\tau_c}{d}, \quad (5.22)$$

where Q^{gen} is the amount of generated charge per pulse and $\frac{v\tau_c}{d}$ is also known as the photoconductive gain. From Eq. 5.22, one sees that by assuming a linear dependence of the carrier drift velocity v with the electric field, an increased field and hence a higher drift velocity results in wider regions of uncompensated trapped charge, hence stronger screening, as observed in Figure 5.14. For our LTG-GaAs material, by taking $\tau_c = 1.2$ ps and $\mu_e = 900$ cm²/Vs for electrons and $\tau_c = 10$ -12 ps and $\mu_e = 50$ -100 cm²/Vs for holes (as reported in literature), the drift length $l_{e,h} = v_{e,h}\tau_c$ for

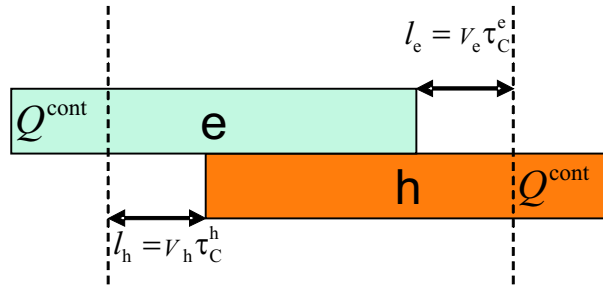


Figure 5.15.: Schematic representation of the photogenerated charge distribution under an applied bias field; at each electrode a region of uncompensated trapped charge equal to the carrier drift length is formed, screening the field in the photogap.

electrons and holes (and hence the length of the space charge regions) is almost equal, being estimated to be $\sim 0.3 \mu\text{m}$.

However, the deviation from linearity of the ΔE_{sc} values suggests that the above considerations might be imprecise. One possible reason for the observed sub-linear dependence could be electron velocity saturation (field-dependent mobility) but, as mentioned previously, this would be also reflected in the amplitude of the signal at $\tau < 0$. A plausible explanation could also be different electron injection contributions for different values of the applied bias, as assumed in Chapter 3.

At this point, in the view of the space-charge effects discussed above, it seems that the short trapping time, as well as the existence of the traps in LTG-GaAs pose a serious shortcoming to the usage of LTG-GaAs in ultrafast optoelectronic applications. Moreover, as will be discussed in Chapter 6 the screening of the applied field in the photoswitch persists over a nanosecond time scale, with cumulative and therefore deleterious impact upon the device's performance. An alternative to employing photoconductive material with traps/defects (also responsible for space-charge effects) where the device response is limited by the trapping time, would be a transient-time-limited device, where the response is given by the carrier collection time. Due to the fact that in these devices the carriers are entirely recombining at the electrodes (leaving no space-charge behind) they are a viable alternative to LTG-based photoswitches. The drawback lies in the large capacitance and hence the higher RC time-constant, produced by the narrow photogap necessary for a short transit time.

In conclusion, from the results and discussions presented in this chapter, one can conclude the double-pulse measurements are a very versatile and useful tool when quantifying the screening phenomenon in LTG-GaAs-based PC emitters.

6. Evidence of long-living screening fields in LTG-GaAs-based photoconductive switches

In the previous chapter, we employed double-pulse measurements and a corresponding model to study the ultrafast carrier dynamics and the electric field temporal evolution following the photogeneration of electrons and holes. The interpretation of the experimental observations indicate that simultaneously with the trapping of free carriers on a picosecond time-scale, the formation of uncompensated space-charge domains near the contacts causes the screening of the applied bias field inside the photogap. We could identify the presence of the screening field over a time interval longer than the time-measurement window (>100 ps in our case). According to the simple model we present to interpret the double-pulse signal, the screening produced by the trapped carriers should decay when the electrons and holes recombine. Although, as often reported in literature, the carrier recombination time in LTG-GaAs is assumed to be on the order of tens of picoseconds, most of our experimental data could only be fitted by assuming a very long recombination time (on the order of nanoseconds).

It should be emphasized that almost all the studies reporting picosecond recombination times are based either on optical pump-probe measurements of reflectivity or on “contactless” optical-pump-THz-probe measurements, and therefore not reproducing the actual operating conditions of a PC emitter (i.e., under applied bias field). Accordingly, the information available on carrier recombination times and field screening in LTG-GaAs under bias is rather scarce; for example, based on photoconductivity measurements under moderate illumination and bias conditions, Stellmacher et al. [80] showed that the carriers lifetime spans over a wide range of values, ranging from tens of picoseconds to a couple of nanoseconds, being dependent on the density of photogenerated carriers, consistent with the results we report in the present work.

In this chapter, we extend the analysis of the double-pulse experimental data, taking into account the impact of the THz-pump pulse on the THz signal emitted by the THz-probe pulse at both positive as well as negative time delay. There is evidence that the screening effects last longer than the repetition rate of the femtosecond laser system employed (>12 ns), thus suggesting that the carrier dynamics extends on the time scale of the repetition period.

In order to quantify the impact of field screening upon the efficiency of the CW-THz generation process in LTG-GaAs-based photoconductive switches, we per-

formed additional experiments where we monitor the changes that the waveform and the amplitude of a THz-pulse undergo when a CW background illumination (as used in photomixing experiments) is applied to the PC emitter.

6.1. Long-living transients observed in the double-pulse measurements

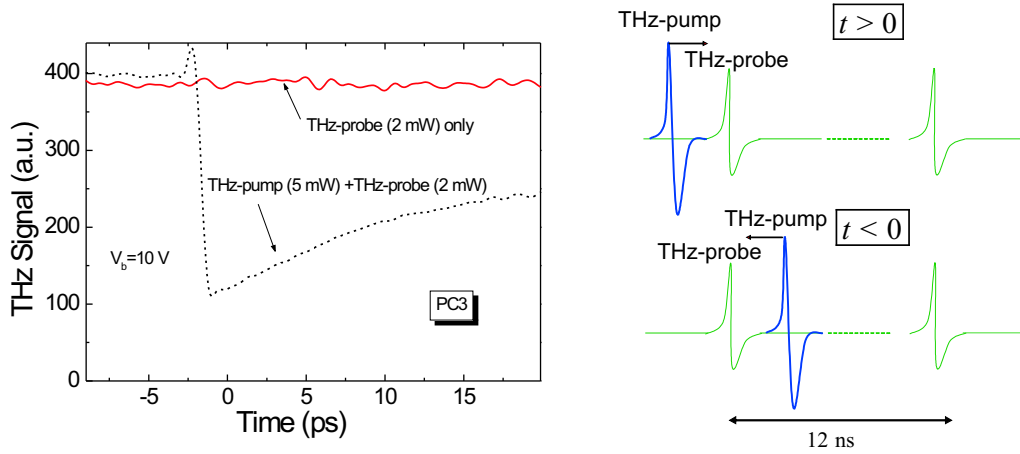


Figure 6.1.: **Left:** Experimental THz signals corresponding to the THz-probe-only condition together with the signal measured with double-pulse excitation; **Right:** Temporal representation of the double-pulse excitation.

Figure 6.1 (left) displays double-pulse data from the PC3 emitter (for a complete listing of the devices see Appendix A) at a THz-pump power of 5 mW together with the THz signal recorded for the case when the THz-pump beam was blocked. In both cases the THz-probe power was 2 mW and the applied bias was 10 V. As already discussed in Chapter 5, contrary to what is expected from the principle of the double-pulse technique, the signal level at $\tau < 0$ for the case when both the THz-pump and THz-probe (this is arriving first) are present at the emitter does not coincide with the signal recorded with the THz-probe only, the former showing a larger amplitude. This behavior appears to be anomalous since at negative time delays the THz-pump arrives at the emitter *after* the THz-probe pulse (see Figure 6.1 (right)), that is, the causality principle would imply that the THz-probe should not “sense” an event (the THz-pump pulse) which has not happened yet! However, based on the fact that the mode-locked femtosecond laser emits a train of pulses (which are spaced by ~ 12 ns in our case) the enhanced signal from the THz-probe pulse can be accounted for only by considering the effect of the THz-pump upon the THz-probe pulse which arrives at the emitter ~ 12 ns *later*, as illustrated in Figure

6.1 (right). An immediate conclusion is that the effect of the THz-pump&probe pulses outlive the repetition time of the laser system (~ 12 ns), being responsible for an incomplete signal recovery after 12 ns. If this were not the case, the amplitude of the THz signal obtained by chopping the THz-probe beam only should stay constant independent of the presence and intensity of the THz-pump pulse at negative time delays.

In view of the discussion in Section 5.6, the incomplete signal recovery at negative time delay can be understood by assuming the existence of the long-lived space-charge (and hence of field screening) produced by the THz-probe pulse which lasts longer than 12 ns. Since the THz signal at $\tau < 0$ increases with increasing the THz-pump power, the presence of the higher-intensity THz-pump pulse seems to alleviate to a certain degree the effect of screening, thus enhancing the emission efficiency of the THz-probe pulses. Although this may seem paradoxical at a first glance, since one would expect the magnitude of the screening to increase with increasing the optical intensity, the whole effect can be qualitatively explained by enhanced carrier recombination rates due to the carriers injected by the THz-pump pulse. Since we assume that the screening of the bias field is caused by uncompensated electrons and holes trapped in the vicinity of electrodes, their recombination rates and hence, the decrease of the screening depends on the availability of carriers from the opposite species. Therefore, every 12 ns a THz-pump pulse arriving before or after the THz-probe pulse provides new recombination partners, thus reducing the field screening and increasing the THz emission of the THz-probe pulses.

6.1.1. THz-pump power dependence of the incomplete THz-probe signal recovery

To be able to quantify the effects described above, in Figure 6.2 we plot the double-pulse traces from the PC1 and PC2 emitters, recorded over a wide range of THz-pump power levels. Here, complementary to the discussion in Chapter 5, we focus on the variation of the THz signal with the THz-pump power at negative time delays. The excitation density due to the THz-pump beam varied from $\sim 3 \times 10^{17} \text{ cm}^{-3}$ (1 mW) to $\sim 8 \times 10^{18} \text{ cm}^{-3}$ (28 mW) for the PC1 device while for the PC2 the highest excitation density was $\sim 1.2 \times 10^{19} \text{ cm}^{-3}$ (40 mW). For the data displayed in Figure 6.2 the THz-probe power was 2 and 4 mW for the PC1 and PC2 device, respectively. For the PC2 emitter we also plot the THz signal obtained from the THz-probe alone. For reasons to become clear later, we chose to plot the experimental data in Figure 6.2 expressed in percentage relative to the amplitude of the THz signal recorded at negative time delay corresponding to the highest intensity of the THz-pump beam. Hence the maximum observed signal corresponds to 100 % at 28 mW for PC1 and 40 mW for PC2. As one can see, the amplitude of the signal from

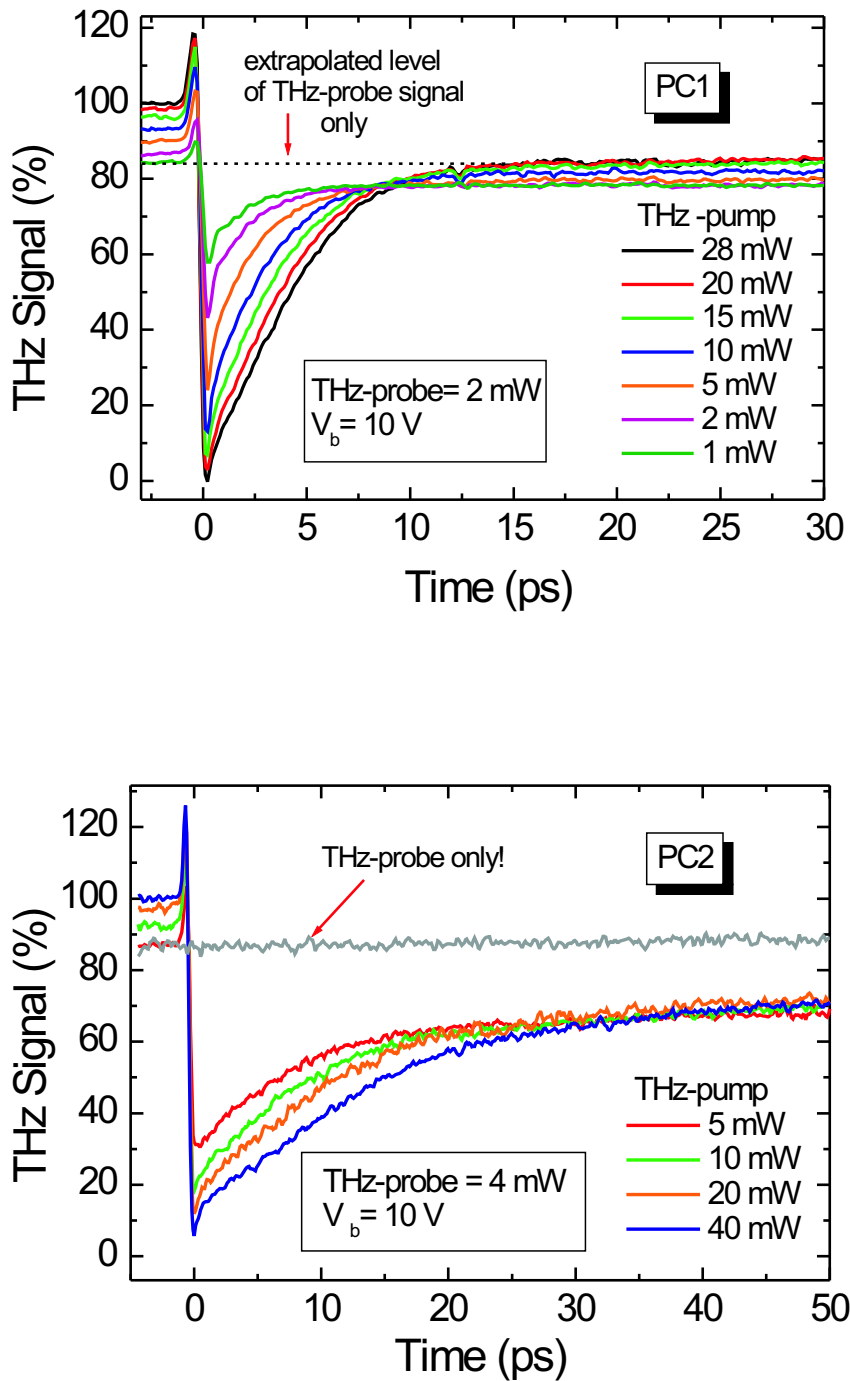


Figure 6.2.: Double-pulse traces measured from the PC1 (upper panel) and PC2 emitter (lower panel); the THz signal amplitude is expressed in percentage relative to the signal measured for the highest THz-pump power at $t < 0$; also shown (lower panel) is the THz signal measured from the THz-probe only (grey line).

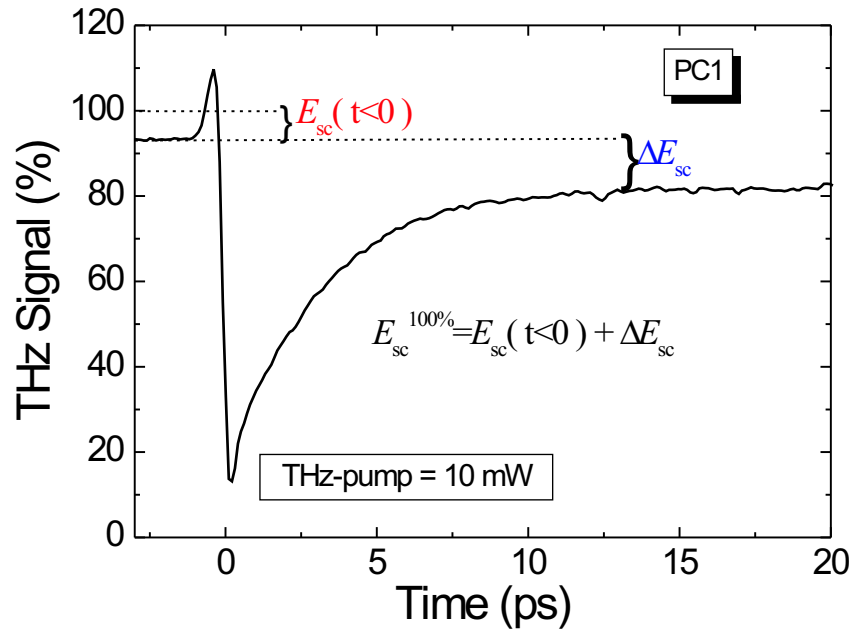


Figure 6.3.: Double-pulse experimental trace with the illustration of the field-screening parameters: the green line represents the maximum efficiency attained by the PC emitter, while the red line indicated the efficiency obtained from the 2 mW THz-probe beam only.

the THz-probe beam alone amounts to only $\sim 85\%$ of the signal recorded when THz-pump beam is incident on the emitter.

The most interesting trend in the data plotted in Figure 6.2 is the increase of the THz signal at $\tau < 0$ with increasing the THz-pump power, followed by saturation at highest power levels. As discussed earlier, the enhanced emission efficiency of the THz-probe pulse observed at higher THz-pump intensities suggests an enhancement in the recombination, that is, less space-charge screening. The saturation could be attributed to the onset of the trap-filling mechanism above $\sim 10^{18} \text{ cm}^{-3}$, since, as derived from Shockley-Read-Hall (SRH) theory, the efficiency of the carrier recombination process depends on the number of available recombination centers (deep traps, in the present case).

6.1.2. Evaluation of the de-screening time from double-pulse data

We proceed to a quantitative evaluation of the screening process by introducing three different parameters, which are explained with the help of Figure 6.3:

- $E_{sc}(t < 0)$ represents the level of screening which is still present after a time

interval equal to the pulse repetition period of the femtosecond laser. It can be obtained for each THz-pump power value by subtracting the values at $t < 0$ of the corresponding THz signal from the signal measured at the highest THz-pump power. Consequently, we assume that the long-lived screening is almost zero for the maximum THz-pump power.

- ΔE_{sc} gives the field screening induced by the THz-pump pulse only, being equal to the magnitude of the long living pedestal (when the data is not normalized to unity at $t < 0$).
- $E_{\text{sc}}^{100\%}$ sums up the remnant screening $E_{\text{sc}}(t < 0)$ from the previous pulse and the screening induced by each THz-pump pulse (ΔE_{sc}), expressing the total level of screening, induced by both THz-pump and -probe pulses.

For each double-pulse trace plotted in Figure 6.2 we extracted $E_{\text{sc}}(t < 0)$ and ΔE_{sc} as a function of the optical power incident on the photoswitch, as plotted in Figure 6.4. When plotting $E_{\text{sc}}(t < 0)$ the incident optical power comprised both the THz-pump and -probe power (according to the earlier definition), while for ΔE_{sc} only the THz-pump power was considered.

By replacing $P(t) = E_{\text{sc}}(t)\varepsilon\kappa$ in Eq. 5.6 of Chapter 5, and considering the particular case of $\tau_{\text{R}} \gg \tau_{\text{c}}$, which also implies that $j_{\text{pc}}(t) \rightarrow 0$, we obtain the rate equation for the screening field:

$$\frac{dE_{\text{sc}}}{dt} = -\frac{E_{\text{sc}}(t)}{\tau_{\text{R}}}, \quad (6.1)$$

with the solution:

$$E_{\text{sc}}(t) = E_{\text{sc}}^{100\%} e^{-\frac{t}{\tau_{\text{R}}}}, \quad (6.2)$$

where, as defined above:

$$E_{\text{sc}}^{100\%} = E_{\text{sc}}(t < 0) + \Delta E_{\text{sc}}. \quad (6.3)$$

By setting $t \rightarrow T_{\text{rep}}$, followed by the substitution of Eq. 6.3 in 6.2 and solving in terms of τ_{R} we obtain:

$$\tau_{\text{R}} \cong \frac{T_{\text{rep}}}{\ln\left(1 + \frac{\Delta E_{\text{sc}}}{E_{\text{sc}}(t < 0)}\right)}, \quad (6.4)$$

which allows us to calculate the value of recombination (de-screening)¹ time at different values of optical intensity.

¹Although the subscript "R" stands here for "recombination", we should be cautious when using the term "recombination" describing the decrease of the field screening (see also the discussion in the concluding part of this chapter).

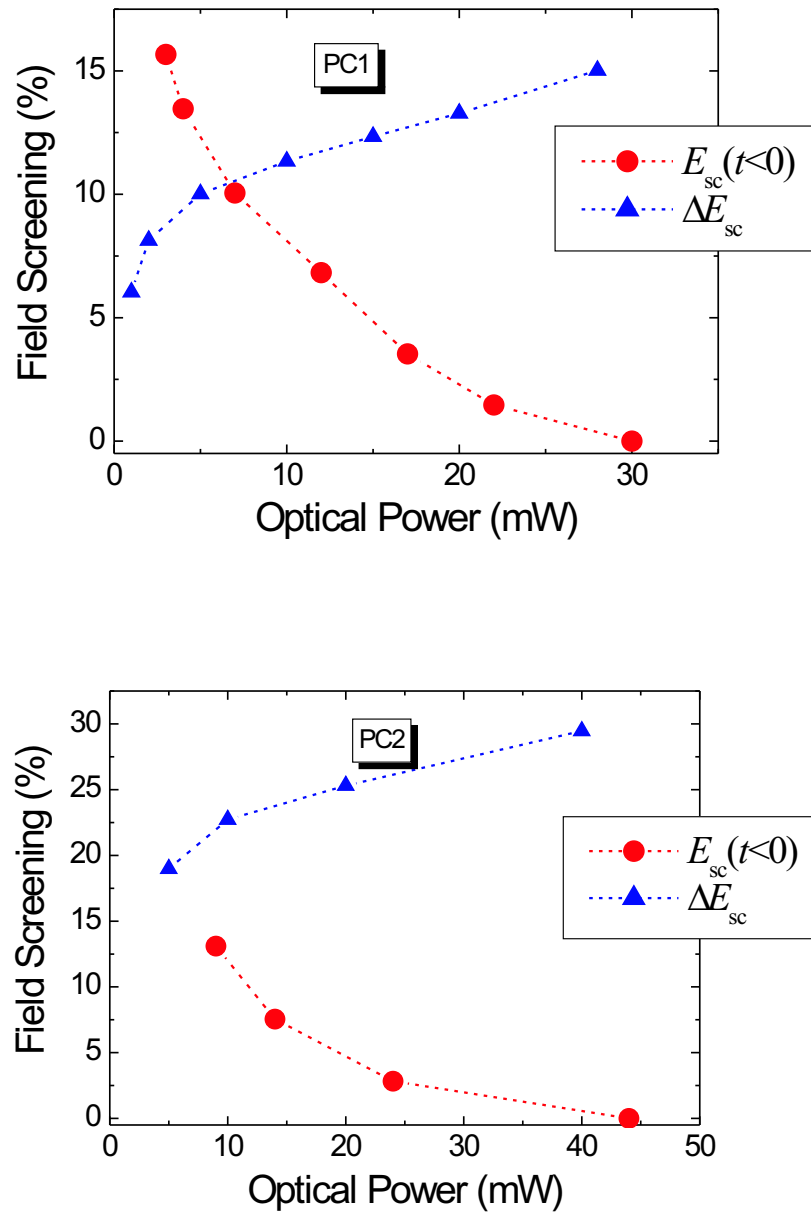


Figure 6.4.: The field-screening parameters $E_{sc}(t < 0)$ and ΔE_{sc} plotted against the incident optical power, as extracted from the raw data plotted in Figure 6.2.

6.2. THz-pulsed emission from a PC emitter with CW background illumination

In addition to the double-pulse experiments, we investigated the waveform of the THz-pulses obtained for the case when the photoswitch is excited with single optical pulses as well as different levels of background CW optical power. This type of measurement is believed to provide us with some qualitative insight upon the field-screening effects that might occur when the photoswitch is employed as photomixer in CW THz generation.

6.2.1. Experimental realization of the pulsed-THz with CW background experiment

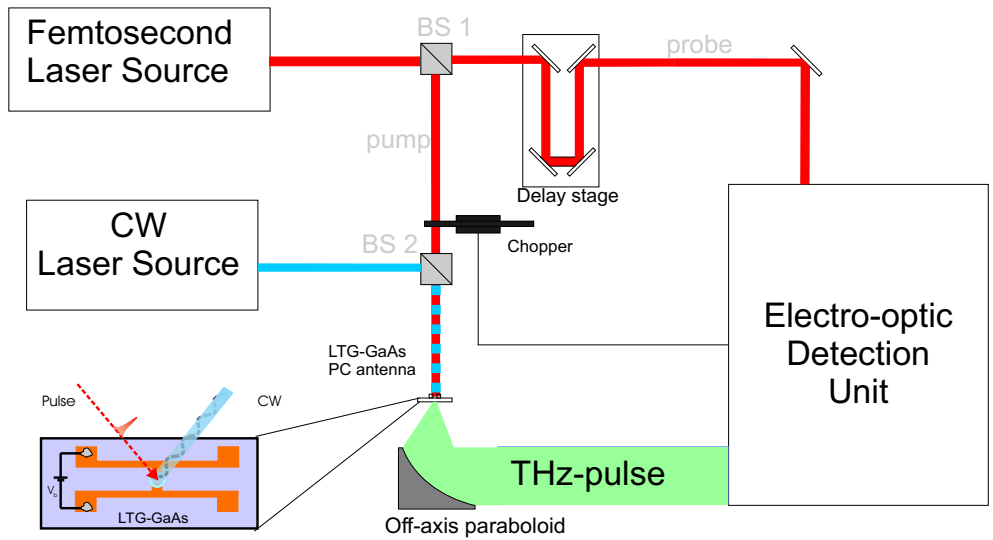


Figure 6.5.: Schematic representation of the experimental setup used for studying the effect of a CW background upon the THz-pulse emission efficiency.

The experimental setup we used is schematically illustrated in Figure 6.5, consisting of two distinct laser sources: a femtosecond laser for THz-pulse generation and a CW laser beam derived from two ring-cavity Ti:Sapphire lasers. The two laser beams are combined in a beam-splitter cube and aligned such that they travel collinearly, allowing for the simultaneous driving of the PC emitter when the focuses of the two beams are matched in the photogap. A small fraction of the femtosecond laser output was passed over a time delay stage and then delivered to an electro-optic detection setup, whose signal was then fed to a lock-in amplifier. To be able to identify the changes in the THz waveform induced by the presence of the CW background, we chose to mechanically chop the CW laser beam at a frequency of ~ 1.8 kHz, which was used to reference the lock-in amplifier. The CW optical power was varied from 2

to almost 40 mW, while the bias applied to the PC antenna was either 2 (4 kV/cm) or 10 V (20 kV/cm). For each THz waveform recorded under CW illumination we also recorded a waveform where the background CW light was switched off, such that any drift of the signal due to the femtosecond laser noise/instability or heating of the sample could be suppressed. For all the CW background measurements presented in this chapter we used the PC1 (G420 LTG-GaAs material) emitter.

6.2.2. Experimental observation of THz-field reduction due to CW background illumination

Figure 6.6 (upper panel) shows a THz-waveform recorded for applied biases of 2 (right y-axis) and 10 V (left y-axis) applied bias when the PC emitter was driven simultaneously with 2 mW average pulse power and 5 mW CW background illumination, together with the waveform measured when the CW light was switched off. One can notice that if a steady-state carrier photogeneration process is taking place in the background (CW light on), the amplitude of the emitted THz-field decreases substantially to approximately 70 % of the value without CW background. By plotting the data together we are able to compare the magnitude of the screening and found that the reduction of the THz field amplitude scales linearly with the applied bias.

For each value of applied bias we compared the shape of both waveforms and found no significant difference, suggesting that the carrier dynamics directly responsible for the surge and decay of the photocurrent is not directly influenced by the presence of the CW illumination. The photogeneration rate produced by the 10 mW CW beam amounts to $\sim 5 \times 10^{25} \text{ cm}^{-3} \text{ s}^{-1}$, which when multiplied with an assumed electron lifetime of 10 ps (at steady-state, the recombination rate equals the photogeneration rate), yields a free-carrier density of $\sim 3 \times 10^{14} \text{ cm}^{-3}$. The low excitation density in the CW case excludes a significant contribution from the radiation field screening effect for the CW beam alone.

The lower panel of Figure 6.6 displays the effective reduction of the THz-field measured at different levels of CW optical power and at the two different applied bias values. Here again, as for the case of double-pulse data, the effective reduction of the THz field was expressed in percentage as a function of the maximum amplitude of the THz waveform recorded without the CW light in the background. As can be observed, for CW illumination less than 10 mW, the THz-field amplitude decreases monotonically with increasing CW power, leveling off to about 60 % efficiency at 20-30 mW. Since the radiated THz power scales quadratically with the THz field, a 60 % efficiency of the THz-field implies that the THz power efficiency is reduced to 36 %, that is, a significant reduction in the generated THz power occurs if a CW background is applied to the PC emitter. All of the data indicate that

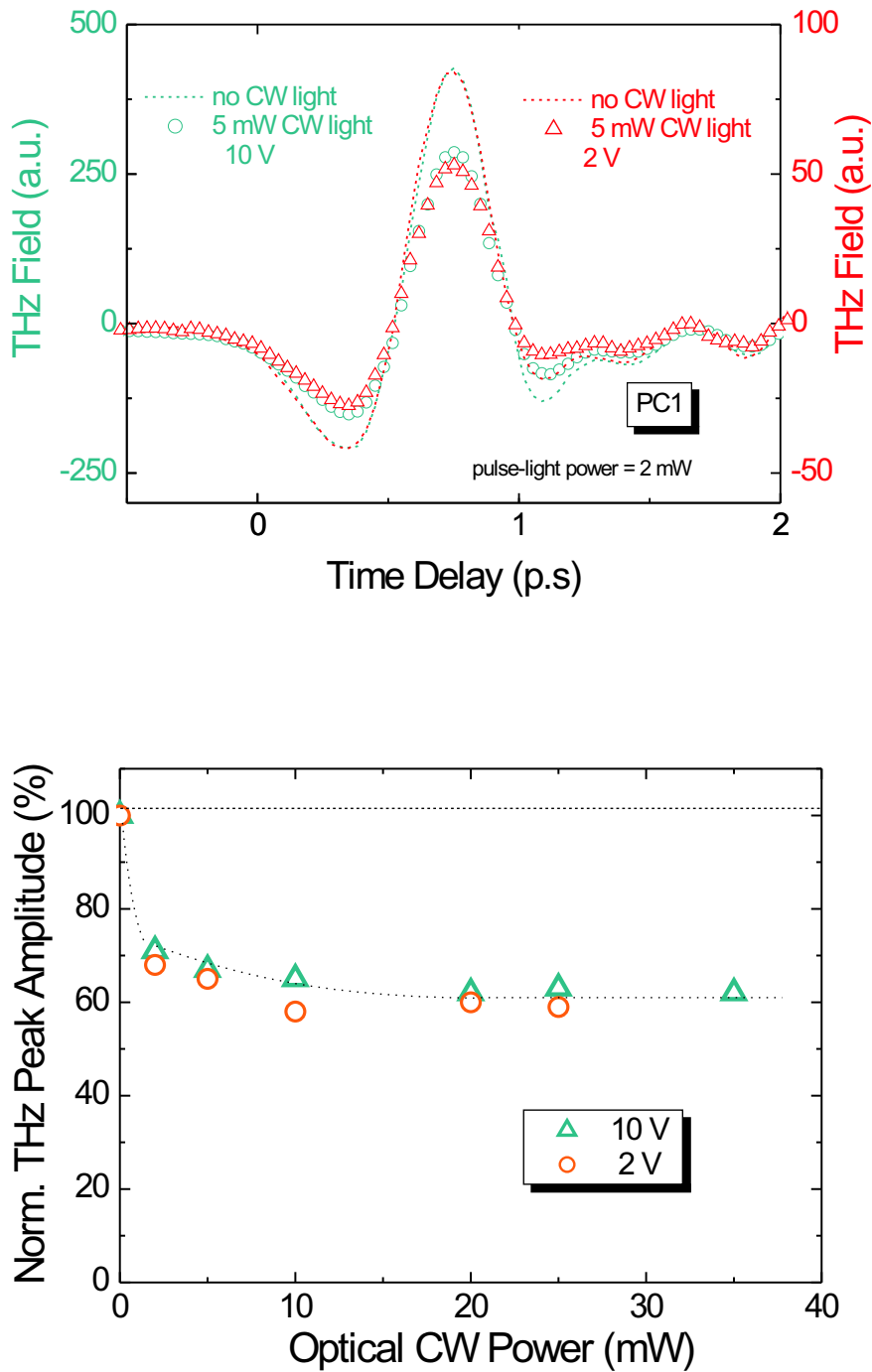


Figure 6.6.: **Upper panel:** THz waveforms illustrating the decrease of the emission efficiency when a 5 mW CW background is applied to the PC emitter, at two different voltages (2 V right y-axis, 10 V left y-axis); **Lower panel:** the variation of the peak amplitude of the THz waveform with the applied CW optical power, here expressed in percentage relative to the amplitude of the signal peak measured without CW background (the dotted line is a guide for the eye).

the peak amplitude with and without CW background illumination scale linearly with bias voltage (leading to a bias-independent relative reduction as shown in Figure 6.6 (lower panel)), suggesting that indeed, the field screening effect is due to the depletion regions near electrodes, their length scaling with the applied bias.

6.2.3. Evaluation of the de-screening time for the case of CW background illumination

Assuming that the main reason for the reduced emission efficiency of the PC emitter are the space-charge effects due to spatial displacement of CW photogenerated carriers, it is possible to exploit the information on the field-screening obtained from the double-pulse experiments in order to extract the recombination (de-screening or space-charge relaxation) time for the CW case.

We consider again the Eq. 5.6, describing the build-up and decay of polarization due to the carriers moving in the external bias field and recombining, respectively. By dividing it with $\kappa\varepsilon$ and assuming steady-state conditions, which imply $\frac{\partial}{\partial t} = 0$, one obtains the screening field produced by CW illumination:

$$\frac{E_{sc}}{\tau_R} \cong \frac{I_{DC}}{\kappa\varepsilon A}, \quad (6.5)$$

where I_{DC} is the measured DC photocurrent and we made the substitution $j_{pc} \rightarrow \frac{I_{DC}}{A}$.

The reduction of the emitted THz field efficiency due to the field screening can be expressed as:

$$\frac{E_{sc}}{E_b} = \Delta E_{sc}^{CW}, \quad (6.6)$$

where E_b is the applied bias field and ΔE_{scr} is graphically explained in Figure 6.6 (lower panel). Accordingly, Eq. 6.5 becomes:

$$\frac{\Delta E_{sc}^{CW}}{\tau_R} = s I_{DC}^{CW}, \quad (6.7)$$

with:

$$s = \frac{1}{\varepsilon\kappa A E_b}. \quad (6.8)$$

The parameter s can be obtained from the double-pulse data based on the argument that the amount of screening induced by each THz-pump pulse can be associated with an average induced space-charge. One can show that this space-charge can be derived from the DC photocurrent measured under pulsed illumination. As shown in Chapter 5, the build-up of space-charge screening is given by the free carriers moving toward the contacts, leaving trapped uncompensated charge behind; thus, based on the Eq. 5.6, the built-up field screening due to the THz-pump pulse

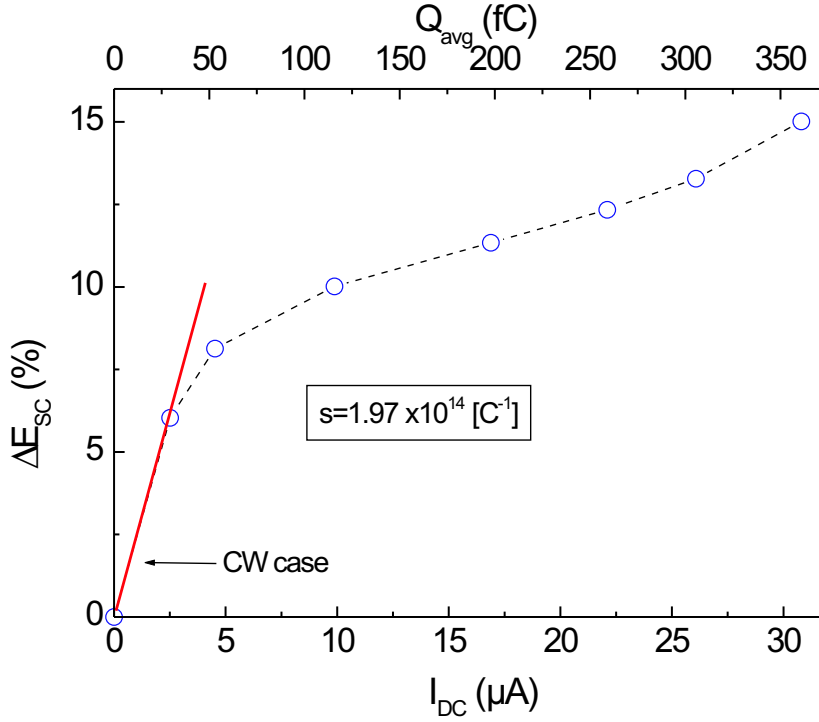


Figure 6.7.: The level of THz-pump induced screening plotted versus the DC photocurrent under pulsed operation (lower x axis) and the corresponding amount of induced uncompensated charge responsible for screening (upper x axis).

is described by:

$$\frac{dE_{sc}}{dt} = \frac{i_{pc}}{A\kappa\epsilon}. \quad (6.9)$$

By integrating Eq. 6.9 one obtains the amount of screening measured by the double-pulse experiment:

$$E_{sc} = \int_0^{E_{sc}} dE_{sc} = \frac{1}{A\epsilon\kappa} \int_0^\infty i_{pc}(t)dt. \quad (6.10)$$

The average space-charge induced by each laser pulse can be defined as:

$$Q_{avg}^{pulse} = \int_0^\infty i_{pc}(t)dt, \quad (6.11)$$

where by taking into consideration Eq. 6.6 we arrive at:

$$\Delta E_{sc} = \frac{Q_{avg}^{pulse}}{E_b A \epsilon \kappa} = s Q_{avg}^{pulse}. \quad (6.12)$$

The average uncompensated charge per pulse Q_{avg}^{pulse} can be calculated by knowing the DC photocurrent and the pulse repetition period T_{rep} :

$$Q_{avg}^{pulse} = I_{DC} T_{rep}. \quad (6.13)$$

In Figure 6.7 we plot ΔE_{sc} versus I_{DC} measured under pulsed illumination and the calculated values of Q_{avg}^{pulse} (upper axis). The flattening of the curve of ΔE_{sc} vs. photocurrent at 5 μA is attributed to an enhancement of the photocurrent which occurs when the available trap states in the LTG-GaAs material are filled after THz-pump excitation. This saturation does not occur in the case of CW excitation, which, as shown previously, generates a rather low free-carrier density. A linear fit of the first two data points (assumed to describe well the CW excitation regime in Figure 6.7) with Equation 6.13 yields a value of s equal to $\sim 2 \times 10^{14} C^{-1}$. By knowing the values of DC photocurrent recorded for a bias of 10 V under CW illumination (device responsivity at 10 V) corresponding to the optical intensities for which we measured the values of ΔE_{sc}^{CW} displayed in Figure 6.6, we can calculate the recombination time as a function of incident optical power from Eq. 6.7.

6.3. Discussion: long-lived screening in LTG-GaAs

In Figure 6.8 we plot the values of carrier recombination (de-screening) time for the PC1 and PC2 emitters, as they were obtained from Eq. 6.4 and Eq. 6.7, as a function of pulsed and CW illumination power. The recombination time decreases monotonically with the optical power for CW illumination, with values situated between 1 and 10 ns, whereas for the double-pulse measurements, the screening relaxation time decreased more abruptly beyond 10 mW. Note that, although the LTG-GaAs materials of the PC1 and PC2 emitters were grown and annealed under different conditions, they display field-screening relaxation times in the same range, varying from almost 40 ns at very low optical intensities, to values close to the laser repetition rates (12 ns) at the highest intensities used. Another important feature of the results displayed in Figure 6.8 is that even though the average optical power level on the x axis for both experimental conditions (pulse and CW illuminations) is of the same order of magnitude, the corresponding instantaneous density of photogenerated free-carriers differs substantially; for instance, a pulsed 10 mW average pump power generates $\sim 3 \times 10^{18} cm^{-3}$ free carriers, while the same amount of average CW power produces only $\sim 10^{13} cm^{-3}$. This observation, together with the different magnitude of screening obtained for the CW versus pulsed illumination points to a particularization of the screening process depending on the temporal distribution of the optical excitation. However, we shall assume that the core mechanism responsible for the observed decrease of THz emission efficiency of PC emitters under different illumination conditions is caused by the long-lived screening, hence, the long recombination times of the carriers trapped in the regions near the electrodes.

One should clearly differentiate between the recombination times reported in this work, which correspond to the decay of field screening, and the recombination times which are commonly reported in optical pump-probe experiments, where no external

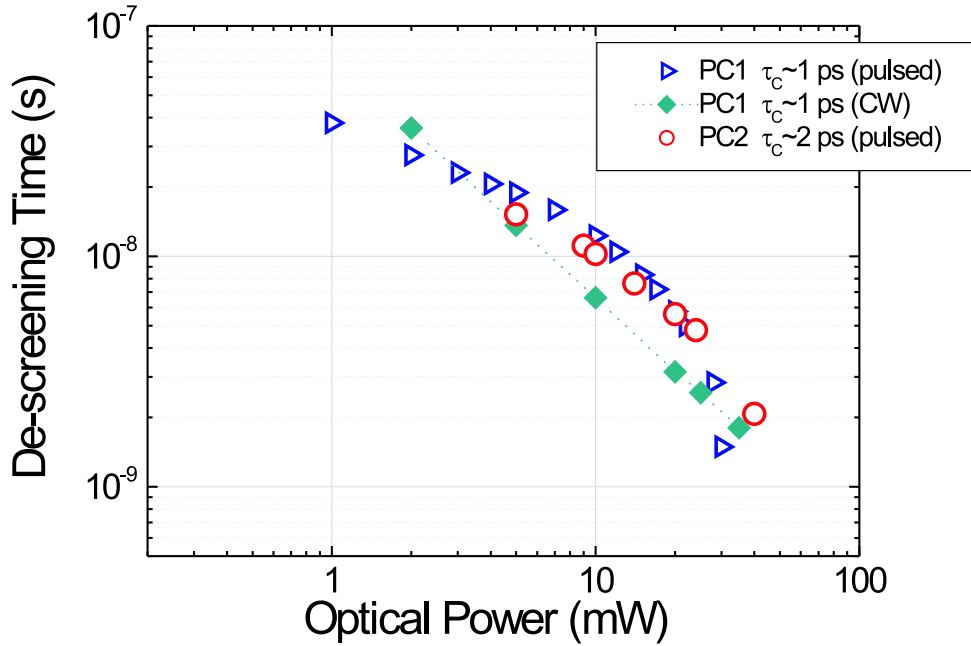


Figure 6.8.: The recombination (de-screening) time plotted as a function of the average incident power for the pulsed and CW illumination. The data was obtained at an applied bias of 10 V (the legend also displays the trapping times as measured from the transient reflectivity measurements).

bias is applied to the semiconductor. The reason lies in the particularity of the recombination process, as discussed below.

As we recall from Chapter 2, unannealed LTG-GaAs contains a large density of point defects (As_{Ga}) ($\sim 10^{17}$ - 10^{20}) [185] and gallium vacancies (V_{Ga}), due to the excess incorporation of arsenic (As) during the growth process. After annealing, the density of point defects drops by one order of magnitude. It has been commonly assumed that the subpicosecond trapping times in LTG-GaAs are caused by ionized arsenic antisite defects As_{Ga}^+ . On the other hand, due to the very limited experimental evidence, the hole trapping mechanisms are still very ambiguous: neutral As antisites defects (As_{Ga}^0) [71] and Ga vacancies (V_{Ga}) [70] were suggested as possible trapping centers for holes in LTG-GaAs.

If the deep-defect level created by the As_{Ga} point defects can capture both types of carriers, then it should act as a recombination level, and the whole carrier recombination process can be described by the Shockley-Read-Hall (SRH) theory of indirect (trap assisted) recombination [186]. In this case, the resulting carrier lifetime is somewhat more complicated than is the case for direct (bimolecular or band-to-band) recombination, since is necessary to account for unequal times required for capturing each type of carrier. Generally, as defined within the SRH model, the net

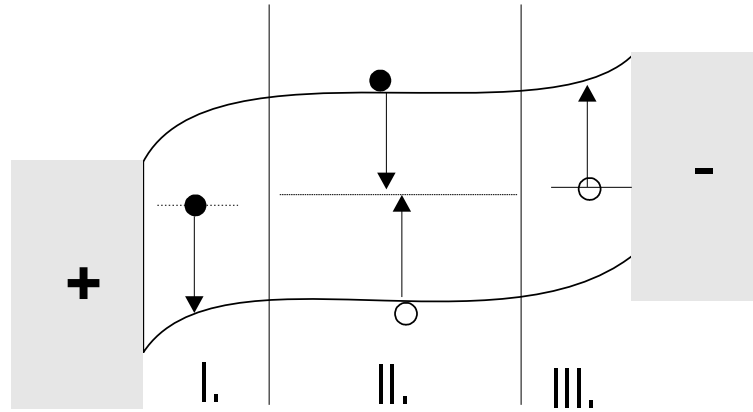


Figure 6.9.: A sketch of the energy band-diagram in the photogap, illustrating three distinct regions, each of which has a different recombination dynamics.

recombination rate is given by [90]:

$$U = \frac{np - n_i^2}{\tau_c [p + n + 2n_i \cosh((U_t - U_i)/k_B T)]}, \quad (6.14)$$

and the trapping time is given by:

$$\tau_c = \frac{1}{N_t v_{th} \sigma}, \quad (6.15)$$

where N_t is the trap density, σ is the carrier capture cross-section (the capture cross section for an unoccupied recombination center for a free-electron, and the capture cross section of an occupied recombination center for a free hole, respectively.), while v_{th} is the electron thermal velocity. In Eq. 6.14, $n = n_0 + \Delta n$ and $p = p_0 + \Delta p$, where Δp and Δn are the excess carrier density produced by the incident light, whereas U_t and U_i define the depth of the trap level and the mid band-gap, respectively. Thus, the rate of recombination through a defect state depends on the occupancy of the defect state which in turn is related to the free carrier densities through the two capture cross-section which characterize the particular recombination center. The carrier lifetime for each of the two carrier species is defined as:

$$\tau_{n,p} = \frac{\Delta n, p}{U}. \quad (6.16)$$

For the particular case of our study, due to the drift of carriers in the applied external field, the energy-band diagram of the photogap should adopt the configuration sketched in Figure 6.9, constituting three different regions according to their net charge distribution. In region (I) the net trapped charge at the anode is negative, causing the downward bending of the energy-band. The same situation occurs at the cathode, except here, due to the positive net charge the energy-band is bent

upwards (region III). The intermediate domain (region II) is neutral, due to the equal number of trapped electron and holes. Each of the three regions has a different carrier recombination dynamics, depending mainly on the density of carriers from the opposite species. Thus, within region II, as soon as an electron is captured, the carrier recombination time is defined by the time needed by the recombination center to capture a hole, that is, the hole trapping time. Its value may range from a couple of picoseconds [78] to several tens or even hundreds of picoseconds, if the holes, as suggested in Ref. [70] are usually trapped at a distinct defects (V_{Ga}) to the electron traps. It should also be pointed out that electron and hole capture at the As antisite defect does not lead to their immediate recombination, since the recombination process require a significant lattice relaxation at the defect site, thus the recombination time is longer than the hole capture time. The situation changes dramatically in regions I and III, since here the recombination partners are scarce or absent. The time spent by an electron (hole) in a trapped state may reach tens of nanoseconds, as illustrated by the results in Figure 6.8. However, if the photogap is illuminated by a new laser pulse, the presence of photogenerated electron-hole pairs in the regions I and III, enhance the recombination probability, thus shortening the recombination time. Based on Eq. 6.16 and Eq. 6.14, one can express the carrier lifetime as [90]:

$$\frac{1}{\tau_{n,p}} = \frac{1}{\tau_C} f_{n,p}, \tag{6.17}$$

where $f_{n,p}$ represents the probability that a recombination center be occupied (capture) by a hole (region III) or electron (region I) . We expect that $f_{n,p}$ increases with increasing optical excitation density consistent with the dependence of the de-screening time-constants upon the optical pump power.

A full explanation of the recombination dynamics requires consideration of the spatial carrier distribution and may involve trap saturation and other nonlinear aspects.

7. Conclusions and Overview

The present work contains results obtained from investigating the continuous-wave (CW) and pulsed THz emission characteristics of photoconductive switches based on LTG-GaAs. The study is aimed at evaluating the impact of material properties upon the THz generation efficiency, an important goal derived from the need to understand the relatively low THz power levels measured from LTG-GaAs-based photomixers.

The measurements were performed on two types of LTG-GaAs materials grown and annealed under different conditions. The first one (G420), was grown following recipes that are the result of a long optimization procedure towards optimum performance of the material in photoconductive switches. The second one (TP983), although grown at a lower nominal temperature, shows a longer trapping time and hence less optimal properties for ultrafast optoelectronic applications. Both materials were initially characterized in terms of free-carrier lifetime by using optical pump-and-probe transient reflectivity measurements. However, this kind of measurements are difficult to interpret, mostly due to the multitude of carrier relaxation phenomena taking place at once. Moreover, these measurements cannot offer clear information on the carrier recombination dynamics and on the field screening effects associated with carriers trapped at the As-antisite defects, and hence on the material growth parameters' impact on the overall emitter efficiency.

Two distinct types of planar antennas were processed on the above materials, each type was chosen accordingly to best suit a certain type of experiment. Thus, for investigating the CW THz performance of the photoswitches we employed a broadband (log-periodic) antenna and a photogap with interdigitated MSM fingers, in order to access emission characteristics at different frequencies and to be able to apply high bias fields, respectively. Both types of antenna were also processed on a LTG-GaAs material (TP984) grown under the same conditions as TP983 but with an additional Bragg reflector consisting of 20 sequences of AlGaAs/AlAs. The sole purpose of this active layer was to rule out the possibility of carriers being generated in the semi-insulating GaAs substrate.

We monitored and recorded simultaneously the DC photocurrent and the emitted THz power from the devices as a function of the applied bias at different optical power levels and operation frequencies. Several key trends could be identified, the most important one being the deviation of the illuminated I-V characteristic from the expected ohmic (linear) dependence for fields higher than 100 kV/cm, where the

$I - V$ dependence trends toward quadratic. Despite several effects made responsible in the literature for the observed non-linearity (space-charge-limited current, carriers generated in the GaAs substrate), we ascribed the observed non-linearity mainly to the elongation of electron trapping time at high bias fields due to Coulomb barrier-lowering and electron-heating effects. However, these effects alone could not explain the deviation from the expected quadratic dependence on the applied bias predicted by the photomixing theory, as well as the strong saturation and decrease of the THz power at higher applied bias voltages.

Consequently, we implemented a procedure that allowed us to extract the values of the carrier trapping time, with the measured DC photocurrent and THz power as the key input data. The obtained dependence showed at 200 kV/cm a 3-fold increase with respect to the low-field value derived from the optical measurements, consistent with the $E^{\frac{3}{2}}$ dependence predicted by the theory. A central assumption we used was electrons dominate the measured photocurrent and THz signal (such that the holes could be neglected). The fact that the observed saturation and decrease of the THz power was present at two different operation frequencies (~ 400 and ~ 800 GHz) suggests that the electron transport characteristics are altered at high bias fields. As a consequence, based on the experimentally derived values for electron trapping time, we extended the above procedure to yield the values of electron drift velocity as a function of the applied bias field. We obtained a velocity vs. electric field characteristic with a clear overshoot feature. Although without consistent experimental evidence in LTG-GaAs-based devices, previous Monte-Carlo simulations results of Arifin et al. [96] do not exclude the occurrence of velocity overshoot phenomenon at fields much higher than for normal GaAs. The magnitude of the fields at which we observed the overshoot phenomenon must be reconsidered in view of the screening effects reported in Chapter 6.

The central part of the work presented here opened with a chapter on THz transients emitted from photoconductive antennas on LTG-GaAs, excited with femtosecond laser pulses (Chapter 4). The antennas used here were resonant H-dipoles, integrated with a plain photoconductive gap. Based on the idea that the waveform and the amplitude of the emitted THz pulse can provide information on the carrier dynamics and "THz circuit" effects, we performed a systematic study of the emitted waveforms as a function of the applied bias and the driving optical power. We found a slight change in the shape of the THz pulse - the peak of the THz field shifted to earlier times, accompanied by an increase in the negative peak - at higher applied bias fields (60 kV/cm). Although this feature was associated in literature with velocity overshoot, according to the observations from the CW characteristics, we do not expect this phenomenon to occur at these relatively low field values. Moreover, the linear dependence of the THz peak amplitude with applied bias suggested a linear relationship between the carrier (electron) drift velocity and electric field.

As often reported in literature, we observed a saturation of the maximum amplitude of the THz field and of the DC photocurrent, with increasing the average optical intensity of the femtosecond pulses. The same feature was observed in large-area photoconductive emitters and was attributed to the screening of the applied bias field by the emitted THz near-field. In order to explore the possibility of a similar effect on the small-size photoconductive antenna under study here, we developed a equivalent circuit model where the photoconductive gap was modeled by a time-varying conductance, while the antenna was represented by a load impedance (with a resistive part only). We found that indeed, the presence of the integrated dipole antenna becomes responsible for a "radiation field-screening" effect. This can be explained in terms of the voltage drop at the antenna terminals due to the power dissipated through the THz radiation process (represented by the concept of *radiation resistance* of the antenna), thus reducing the magnitude of the external applied bias field across the photogap. In the equivalent circuit picture this phenomenon can be seen as a "voltage divider effect", being responsible for the observed nonlinearities in the photocurrent and THz amplitude dependence at higher optical power levels.

In order to obtain a clearer picture of the relationship between the ultrafast free-carrier relaxation process on one side, and photogenerated carrier screening effects on the other, both identifiable from the dynamics of the local electric field in the photoswitch, we employed a THz-emission spectroscopy method, the so-called "double-pulse THz technique". It consists of exciting the photoswitch with two consecutive femtosecond pulses with a variable time-delay between them. While the first pulse (THz-pump) generates free carriers in the photogap, by detecting and monitoring the peak amplitude of the THz signal generated by the second pulse (THz-probe), one obtains the time-resolved evolution of the local field in the photogap.

For every double-pulse trace we measured, we identified three distinct temporal regimes, each associated with a predominant effect. The constant signal measured at negative time-delay corresponds to the THz-probe pulse arriving in advance of the THz-pump pulse. At zero time-delay the signal shows a sudden drop, recovering almost exponentially on a time scale equivalent with the carrier trapping time. For long positive time-delay values the recovery of the signal is incomplete, displaying a negative pedestal.

The double-pulse experiment was modeled by extending the equivalent circuit model implemented for the single-pulse excitation case, such that, besides the radiation field screening effect, it accommodates space-charge field screening effects produced by the photogenerated carriers moving in the external bias field. This approach allowed us to clearly identify the temporal evolution as well as the magnitude of each of the field screening mechanisms co-existing in the photoswitch. By performing initial simulations of the response to single-pulse excitation, we identified that the effect of the radiation field screening dominates the initial response,

on a time interval corresponding to the carrier trapping time, in parallel with the onset space-charge effects due to trapped carriers which dominate the response at later times. The experimental double-pulse data were very well reproduced by the model at low excitation densities, where we used the carrier trapping time, a screening parameter and the electron mobility as the main adjustable parameters of the model.

When investigating the dependence of the double-pulse traces on the THz-pump pulse power we found further evidence in support of our theoretical approach, since the magnitude of the relative THz signal drop at zero time-delay follows the same dependence on the optical power as the peak amplitude of the emitted THz pulse in the single-pulse excitation case.

However, in an apparent conflict with the principle of the double-pulse experiment, we found the amplitude of the THz signal at negative time delay was constant, but increasing with the THz-pump power, suggesting an incomplete recovery of the signal at negative time delays.

As for the origin of the observed long-lasting negative pedestal, almost all the literature in the field suggested it might be due to the long-living carriers generated in the semi-insulating GaAs substrate. We invalidated this hypothesis by producing identical double-pulse traces from an emitter which had a Bragg reflector embedded between the active LTG-GaAs layer and the SI GaAs substrate. Thus, we attributed the negative pedestal to the space-charge effects due to the trapped carriers. This hypothesis was also confirmed by the measurements performed at two different bias voltages, which showed a scaling of the pedestal magnitude with the applied bias, providing further evidence that the long-lived screening is caused by the uncompensated trapped carrier distribution generated by the carrier transport into the contacts.

The double-pulse technique was also used in ascertaining the suitability of a specific material for ultrafast device applications. Thus, by comparing emitters with identical antennas grown on different LTG-GaAs materials (G420 and TP983), the traces measured from the TP983 reflect its less optimal character, showing a much longer recovery time (~ 4 ps compared with the transient reflectivity data - 2 ps) and a stronger screening due to space-charge effects.

The observed dependence of the THz signal at negative time-delay on the THz-pump pulse power for the double-pulse traces constitutes evidence of space-charge field screening effects outliving the pulse repetition period of the femtosecond laser system (~ 12 ps). The long-lived screening effects are ascribed to a subgroup of carriers - both electrons and holes - trapped in a narrow region near the electrodes, depleted of the opposite charge carrier species due to the charge density imbalance resulting from the transport of carriers into the electrodes. We extended the analysis of the space-charge screening on the nanosecond time-scale and derived the relax-

ation (de-screening) time of the space-charge. The experimental data suggest that at higher optical intensities the carrier recombination process is enhanced since more recombination partners are provided.

Additionally, by measuring the THz transients generated by a constant laser pulse with and without a CW laser background illumination, we noticed a strong reduction of the THz signal amplitude of 40 %, corresponding to a reduction in power with 64 % at a CW optical power of 10-20 mW. This phenomenon was also attributed to the existence of long-living space-charge effects and in a manner similar to the pulsed case we derived the de-screening time.

The principal conclusion of the present study is that, besides shortcomings imposed by the THz-circuitry, photomixers based on materials with traps (defects) exhibit great "affinity" for long-lived space-charge screening effects with cumulative and therefore deleterious impact upon the device's performance. An alternative would be the usage of a transit-time-limited device where the response time is given by the carrier collection time, possibly with only one type of carrier responsible for THz signal generation.

A. Auxiliary theoretical derivations

A.1. Analytic expression for the carrier density generated by a single Gaussian pulse excitation in a photoconductor with traps

Assume an optical pulse with a Gaussian temporal profile:

$$P_{opt}(t) = \frac{J}{T_0\sqrt{\pi}} \exp\left(-\frac{t^2}{T_0^2}\right) \quad (\text{A.1})$$

where $J = \frac{\bar{P}}{\nu_p}$ is the optical pulse energy, \bar{P} and ν_p are the average optical power and laser repetition rate, respectively. Here also $T_0 = \frac{T_{\text{FWHM}}}{\sqrt{4\ln 2}}$, where T_{FWHM} is the full-width-half-maximum (FWHM) pulse duration.

The rate equation for the carrier density under pulsed excitation is given by:

$$\frac{dn_f}{dt} = -\frac{n_f(t)}{\tau_c} + \frac{1}{\mathcal{V}}\eta \left(\frac{P(t)_{opt}}{h\nu} \right) \quad (\text{A.2})$$

with τ_c the carrier trapping time, η the quantum efficiency and \mathcal{V} the active volume.

The solution to Equation A.2 can be found using the standard Green's function method:

$$n_f(t) = \eta \frac{1}{h\nu\mathcal{V}} \int_{-\infty}^t dt' P_{opt}(t') e^{-(t-t')/\tau_c} \quad (\text{A.3})$$

Inserting Eq. A.1 in Eq. A.3 yields:

$$\begin{aligned} n_f(t) &= \eta \frac{J}{h\nu\mathcal{V}} e^{-t/\tau_c} \int_{-\infty}^t dt' e^{-(t')^2/T_0^2} e^{t'/\tau_c} \\ &= \eta \frac{J}{h\nu\mathcal{V}} e^{-t/\tau_c} \int_{-\infty}^t dt' \exp\left(-\frac{t'^2}{T_0^2} + \frac{t'}{\tau_c}\right) \\ &= \eta \frac{J}{h\nu\mathcal{V}} e^{-t/\tau_c} \int_{-\infty}^t dt' \exp\left[-\frac{1}{T_0^2} \left\{ \left(t' - \frac{T_0^2}{2\tau_c}\right)^2 - \left(\frac{T_0^2}{2\tau_c}\right)^2 \right\}\right] \\ &= \eta \frac{J}{h\nu\mathcal{V}} \exp\left(\frac{1}{T_0^2} \left(\frac{T_0^2}{2\tau_c}\right)^2 - \frac{t}{\tau_c}\right) \int_{-\infty}^t dt' \exp\left[-\frac{1}{T_0^2} \left(t' - \frac{T_0^2}{2\tau_c}\right)^2\right]. \end{aligned} \quad (\text{A.4})$$

By making the substitution:

$$\left[u = t' - \frac{T_0^2}{2\tau_c} \right], \quad (\text{A.5})$$

one obtains:

$$n_f(t) = \eta \frac{J}{h\nu\mathcal{V}} \exp\left(\frac{1}{T_0^2} \left(\frac{T_0^2}{2\tau_c}\right)^2 - \frac{t}{\tau_c}\right) \int_{-\infty}^{t-T_0^2/2\tau_c} du \exp\left(-\frac{u^2}{T_0^2}\right) \quad (\text{A.6})$$

where using:

$$\int_{-\infty}^a du \exp\left(-\frac{u^2}{T_0^2}\right) = \frac{\sqrt{\pi}}{2} T_0 \left(1 + \operatorname{erf}\left(\frac{a}{T_0}\right)\right) \quad (\text{A.7})$$

yields:

$$n_f(t) = \frac{\sqrt{\pi}}{2} \eta \frac{JT_0}{h\nu\mathcal{V}} \exp\left(\frac{1}{T_0^2} \left(\frac{T_0^2}{2\tau_c}\right)^2 - \frac{t}{\tau_c}\right) \left(1 + \operatorname{erf}\left(\frac{t - T_0^2/2\tau_c}{T_0}\right)\right) \quad (\text{A.8})$$

A.2. Derivation of the differential equation describing the temporal evolution of the electric field in the photogap

In Eq. 5.14 we reach the result:

$$E(t) = E_b - \frac{e\mu_e Z_a A}{d} n_f(t) E(t) - \frac{e\mu_e}{\kappa\varepsilon} e^{-t/\tau_R} \int_{-\infty}^t dt' n_f(t') E(t') e^{t'/\tau_R} \quad (\text{A.9})$$

The integral equation can be transformed into a differential equation, via differentiation and back-substitution:

$$\frac{dE}{dt} = -\frac{e\mu_e Z_a A}{d} \left[E(t) \frac{dn_f}{dt} + n_f(t) \frac{dE}{dt} \right] - \frac{e\mu_e}{\kappa\varepsilon} \left[-\frac{1}{\tau_R} e^{-t/\tau_R} \int_{-\infty}^t dt' n_f(t') E(t') e^{t'/\tau_R} + n_f(t) E(t) \right]. \quad (\text{A.10})$$

We recast thus the integral equation to yield:

$$e^{-t/\tau_R} \int_{-\infty}^t dt' n_f(t') E(t') e^{t'/\tau_R} = -\left(\frac{e\mu_e}{\kappa\varepsilon}\right)^{-1} \left\{ \left[1 + \frac{e\mu_e Z_a A}{d} n_f(t) \right] E(t) - E_b \right\} \quad (\text{A.11})$$

Substituting into the differential equation A.10 and factoring terms:

$$\frac{dE}{dt} = -\frac{e\mu_e Z_a A}{d} \left[E(t) \frac{dn_f}{dt} + n_f(t) \frac{dE}{dt} \right] - \frac{e\mu_e}{\kappa\varepsilon} \left[\frac{1}{\tau_R} \left(\frac{e\mu_e}{\kappa\varepsilon}\right)^{-1} \left\{ \left[1 + \frac{e\mu_e Z_a A}{d} n_f(t) \right] E(t) - E_b \right\} + n_f(t) E(t) \right] \quad (\text{A.12})$$

or,

$$\begin{aligned} \frac{dE}{dt} = & -\frac{e\mu_e Z_a A}{d} E(t) \frac{dn_f}{dt} - \frac{e\mu_e Z_a A}{d} n_f(t) \frac{dE}{dt} \\ & - \left(\frac{e\mu_e}{\kappa\varepsilon} \right) \frac{1}{\tau_R} \left(\frac{e\mu_e}{\kappa\varepsilon} \right)^{-1} \left\{ \left[1 + \frac{e\mu_e Z_a A}{d} n_f(t) \right] E(t) - E_b \right\} - \left(\frac{e\mu_e}{\kappa\varepsilon} \right) n_f(t) E(t) \end{aligned} \quad (\text{A.13})$$

which results in Eq. 5.15:

$$\left[1 + \frac{e\mu_e Z_a A}{d} n_f(t) \right] \frac{dE}{dt} = - \left[\frac{1}{\tau_R} + \left(\frac{e\mu_e Z_a A}{\tau_R d} + \frac{e\mu_e}{\kappa\varepsilon} \right) n_f(t) + \frac{e\mu_e Z_a A}{d} \frac{dn_f}{dt} \right] E(t) + \frac{E_b}{\tau_R} \quad (\text{A.14})$$

A.3. Derivation of the differential equation describing the temporal evolution of the polarization due to the separation of carriers

Starting from the time-dependent field in the photogap:

$$E(t) = \frac{V_b}{d} - \frac{e\mu_e Z_a A}{d} n_f(t) E(t) - \frac{P(t)}{\kappa\varepsilon} \quad (\text{A.15})$$

and solving for $E(t)$ gives:

$$E(t) = \left[1 + \frac{e\mu_e Z_a A}{d} n_f(t) \right]^{-1} \left[\frac{V_b}{d} - \frac{P(t)}{\kappa\varepsilon} \right] \quad (\text{A.16})$$

Considering the rate equation for polarization:

$$\begin{aligned} \frac{dP}{dt} = & -\frac{P(t)}{\tau_R} + j(t) \\ = & -\frac{P(t)}{\tau_R} + e\mu_e n_f(t) E(t) \end{aligned} \quad (\text{A.17})$$

after substituting Eq. A.16 in Eq. A.17 we get:

$$\begin{aligned} \frac{dP}{dt} = & -\frac{P(t)}{\tau_R} + \frac{e\mu_e n_f(t)}{1 + \frac{e\mu_e Z_a A}{d} n_f(t)} \left[\frac{V_b}{d} - \frac{P(t)}{\kappa\varepsilon} \right] \\ = & -\frac{P(t)}{\tau_R} + \frac{e\mu_e n_f(t)}{1 + \frac{e\mu_e Z_a A}{d} n_f(t)} \frac{V_b}{d} - \frac{e\mu_e n_f(t)}{1 + \frac{e\mu_e Z_a A}{d} n_f(t)} \frac{1}{\kappa\varepsilon} P(t) \\ = & - \left[\frac{1}{\tau_R} + \frac{e\mu_e}{\kappa\varepsilon} \frac{1}{1 + \frac{e\mu_e Z_a A}{d} n_f(t)} n_f(t) \right] P(t) + \frac{e\mu_e n_f(t)}{1 + \frac{e\mu_e Z_a A}{d} n_f(t)} \frac{V_b}{d} \\ = & -a(t) P(t) + b(t) \end{aligned} \quad (\text{A.18})$$

where,

$$a(t) = \frac{1}{\tau_R} + \frac{e\mu_e}{\kappa\varepsilon} \frac{1}{1 + \frac{e\mu_e Z_a A}{d} n_f(t)} n_f(t)$$

and

$$b(t) = \frac{e\mu_e n_f(t)}{1 + \frac{e\mu_e Z_a A}{d} n_f(t)} \frac{V_b}{d}.$$

The solution of Eq. A.18 can be obtained using the Green's function method:

$$\begin{aligned} P(t) &= \left[\int_{-\infty}^t dt' b(t') \exp \left\{ \int_{-\infty}^{t'} dt'' a(t'') \right\} + P(-\infty) \right] \exp \left\{ - \int_{-\infty}^t dt'' a(t'') \right\} \\ &\rightarrow \left[\int_{-\infty}^t dt' b(t') \exp \left\{ \int_{-\infty}^{t'} dt'' a(t'') \right\} \right] \exp \left\{ - \int_{-\infty}^t dt'' a(t'') \right\} \end{aligned} \quad (\text{A.19})$$

and implemented numerically using an integration procedure written for MATLAB.

B. Overview of the THz emitters used in the present work

A complete listing of the THz emitters used in the present work is given in Table B.

Emitter	Substrate	Antenna type	Metallization (nm)	Photogap (μm^2)	Trapping time (ps)
PC1	G420	H-dipole (resonant)	Ti/Au 20/100	simple (5×10)	1.2
PC2	TP983	H-dipole (resonant)	Pt 100	simple (5×10)	~ 2
PC3	TP984	H-dipole (resonant)	Pt 100	simple (5×10)	~ 2
CW1 (a-d)	TP983	log-periodic (broadband)	Pt 100	$N_f=6, l_f=9, w_f=1, d=1$ (μm) fingers (10×10)	~ 2
CW2 (a-d)	TP984	log-periodic (broadband)	Pt 100	6 fingers 1×9 $N_f=6, l_f=9, w_f=1, d=1$ (μm) (10×10)	~ 2

Table B.1.: The photoconductive emitters used in the present work: the emitters denominated with PC were used mostly for THz-pulses generation while the CW emitters were used as photomixers.

C. Auxiliary publications

The following article summarizes the principle as well as key results of the additional doctoral work carried out on the *nipnip* photomixer as discussed in Chapter 1.

THz-photomixer based on quasi-ballistic transport

G H Döhler¹, F Renner¹, O Klar¹, M Eckardt¹,
A Schwanhäüßer¹, S Malzer¹, D Driscoll², M Hanson²,
A C Gossard², G Loata³, T Löffler³ and H Roskos³

¹ Institute of Technical Physics and Max-Planck-Research Group of Optics, Information and Photonics, University of Erlangen, D-91058 Erlangen, Germany

² Materials Department, University of California, Santa Barbara, CA 93116, USA

³ Institute of Physics, University of Frankfurt, Frankfurt a.M., Germany

E-mail: dohler@physik.uni-erlangen.de

Received 21 January 2005

Published 8 June 2005

Online at stacks.iop.org/SST/20/S178

Abstract

We report on a novel concept for THz photomixers with high conversion efficiency up to several THz. In contrast to the conventional pin photomixer we can overcome the trade-off between either optimizing transit-time or RC-roll-off. Using quasi-ballistic transport in nano-pin-diodes the transport path can be optimized regarding both path length and transit time. Independently, the capacitance can be kept small by using a sufficiently large number of optimized nano-pin-diodes in series. The concept is presented in detail and first experimental results are reported which corroborate our theoretical expectations.

1. Introduction

Semiconductor-based THz sources promise to be orders of magnitude more compact than conventional THz sources. Photomixing appears to represent a natural solution to bridge the THz gap, as it combines optical and microwave techniques. In fact, for many years photomixers based on 'low-temperature-grown GaAs' (LT-GaAs) represented the only solution [1]. The major disadvantages of this approach were a very low efficiency and low maximum emitted power. The maximum power observed at 1 THz is about 2 μW (with an optical conversion efficiency of about 10^{-5}), while at the (maximum) frequency of 2.7 THz it is only 0.2 μW . We will explain below why we believe that the low conversion efficiency is an intrinsic problem of LT-GaAs-based photo-conducting mixers. More recently, it was demonstrated that up to relatively high frequencies in the GHz range, pin photomixers with a special design, called the uni-travelling carrier (UTC) photomixer, [2–4] represent a promising alternative. Conversion efficiencies exceeding 10% were demonstrated and even, in spite of a roll-off with the fourth power of the THz frequency, the so far highest emitted THz power at 1 THz was demonstrated with these kinds of devices [4]. Recently, substantial progress has been achieved regarding both the purely optical as well as the purely

electrical approaches. About three years ago the first quantum cascade laser (QCL), emitting at about 4 THz and a power of 1 mW (pulsed, duty cycle 0.5%), was demonstrated [5]. For many THz applications, however, CW operation with a very low bandwidth and a wide (dynamical) tuning range of up to 20% is necessary and room temperature operation, at least, is highly desirable. By now it seems unlikely that these goals may ever be achieved with QCLs. On the other hand, within the past few years the progress in the field of multiplier sources has been remarkable. Triplers with output power of about 10 μW at frequencies of about 1.3 THz are commercially available (<http://www.virginiadiodes.com>). However, photomixers exhibit a number of unique advantages, including a wide and easily achievable tuning range and very low bandwidth of the emitted radiation, which depends on the stability of the lasers used for mixing. Therefore, novel approaches to obtain improved performance of photomixers appear highly appealing.

In this paper such an approach, based on the ballistic transport of photo-generated electrons, will be presented. We will first review the basic idea of photomixing in a somewhat unconventional and simplified form in section 2. In this section, we will also discuss the problems associated with LT-GaAs-based photomixers and pin photomixers. In section 3 we will first introduce our concept to overcome these problems

in photomixers based on ballistic flight of electrons in a special kind of superlattice. In the second part of section 3 the implementation of this concept, including model calculations and first experimental results will be presented.

2. Conventional photomixing

2.1. The concept of photomixing

The generation of high-frequency radiation by photomixing is based on periodically generating charge carriers in a semiconductor by two lasers emitting at nearly the same photon frequencies ν_0 , detuned by the beat frequency ν_{THz} . If these photo-generated carriers are subjected to a dc electric field applied between two contacts connected to an antenna, a THz current $I_{\text{THz}}(t)$ is induced by the photo-generated carriers, which, depending on the load represented by the antenna, also leads to an ac voltage $U_{\text{THz}}(t)$ at the contacts. If the beat frequency is sufficiently low, the photocurrent $I(t)$ will follow the carrier generation by the periodically modulated laser power

$$P_L(t) = P_L [1 + \cos 2\pi \nu_{\text{THz}} t] \quad (1)$$

fully in phase with the beat frequency according to

$$I(t) = I_0 [1 + \cos(2\pi \nu_{\text{THz}} t)] \quad (2)$$

with an amplitude

$$I_0 = \eta_{\text{ph}} I_0^{\text{id}} = \eta_{\text{ph}} e(P_L/h\nu_0), \quad (3)$$

provided that all photo-generated carriers arrive at the contacts. (e stands for the elementary charge; P_L is the laser power, $h\nu_0$ is the laser photon energy and η_{ph} is the fraction of incident photons absorbed in the active part of the mixer.)

If the THz frequency becomes comparable to the inverse ‘carrier transport time’ τ_t or larger, a degradation of the amplitude of the photocurrent I_0 has to be taken into account. The ‘carrier transport time’ τ_t (also called ‘response time’) is the quantity which specifies how long the contribution of a photo-generated carrier persists on average. Generally, τ_t depends on both the transit time for the carriers propagating between the contacts, τ_{tr} , and the carrier recombination lifetime, τ_{rec} . This transport time can be roughly approximated by $1/\tau_t \approx 1/\tau_{\text{tr}} + 1/\tau_{\text{rec}}$. For the photomixers discussed in the following τ_t is either specified by τ_{tr} or by τ_{rec} alone, depending on the type of photomixer. In pin-photomixer diodes the transport time is practically identical with the transit time τ_{tr} , as recombination is negligible ($\tau_{\text{rec}} \gg \tau_{\text{tr}}$). In order to get an estimate for the transit times we assume high-field drift velocities v_{dr} of electrons and holes of the order of 10^7 cm s^{-1} and contact separations L of the order of a micrometre. This yields (rather long) transit times $\tau_{\text{tr}} = L/v_{\text{dr}}$ of the order of 10 ps. In contrast, the transport time in *photo-conducting* mixers, based on LT-GaAs, e.g., is practically identical to the recombination lifetime, τ_{rec} , as τ_{rec} can become as short as 0.15 ps, i.e. about two orders of magnitude shorter than typical values for τ_{tr} .

Comparing these transport times the LT-GaAs photomixer appears, *a priori*, much more appealing for the generation of THz photocurrents, as the degradation of the THz-current amplitude starts at much higher frequencies. It can be easily shown that the periodically modulated laser power

(equation (1)) induces in the LT-GaAs photoconductor a current

$$I^{\text{pc}}(t) = I_0^{\text{pc}} [1 + (1 + i\nu_{\text{THz}}/\nu_{\text{rec}})^{-1} \cos(2\pi \nu_{\text{THz}} t)] \quad (4)$$

with a ‘3 dB roll-off frequency’ $\nu_{\text{rec}} = 1/2\pi \tau_{\text{rec}}$ for the ac part, which can become as high as about 1 THz for $\tau_{\text{rec}} = 0.15 \text{ ps}$. However, one has to bear in mind that in this case each photo-generated carrier does no longer fully contribute to the current, as its drift length $l_{\text{dr}} = v_{\text{dr}} \tau_{\text{rec}}$ covers only the fraction l_{dr}/L of the contact distance, i.e., the ‘photo-conductive gain’ $g = l_{\text{dr}}/L = (\tau_{\text{rec}}/\tau_{\text{tr}})$ becomes $\ll 1$ [6]. Thus, I_0^{pc} in equation (4) is reduced by this gain factor compared to its value I_0 from equation (3) and the amplitude of the THz current becomes

$$I_0^{\text{pc}}(\nu_{\text{THz}}) = e\eta_{\text{ph}}(P_L/h\nu_0)(\tau_{\text{rec}}/\tau_{\text{tr}})(1 + i\nu_{\text{THz}}/\nu_{\text{rec}})^{-1}. \quad (5)$$

In addition to the overall reduction of the photocurrent we should note that, while the transport roll-off frequency ν_{rec} is determined by $1/(2\pi \tau_{\text{rec}})$, for $\nu_{\text{THz}} \gg \nu_{3\text{dB}}$ the amplitude of the THz current, given by $I_0^{\text{pc}}(\nu_{\text{THz}}) = I_0^{\text{id}}/(2\pi \nu_{\text{THz}} \tau_{\text{tr}})$, no longer depends on τ_{rec} , but only on the transit time τ_{tr} .

The THz power emitted by the photo-conducting mixer can be estimated by $P_{\text{THz}} = \frac{1}{2} |I_0^{\text{pc}}(\nu_{\text{THz}})|^2 R_a$, which yields

$$P_{\text{THz}}^{\text{pc}} = P_{\text{THz}}^{\text{id}} \eta_{\text{ph}}^2 (\tau_{\text{rec}}/\tau_{\text{tr}})^2 [1 + (2\pi \nu_{\text{THz}} \tau_{\text{rec}})^2]^{-1} \quad (6)$$

where

$$P_{\text{THz}}^{\text{id}} = \frac{1}{2} (e P_L/h\nu_0)^2 R_a \quad (7)$$

corresponds to the THz power emitted by an ideal photomixer generating one electron-hole pair per incident photon. R_a is the radiative resistance of the antenna, which is typically in the order of 50 to 100 Ω . For an ideal GaAs photomixer (with $h\nu_0 = 1.43 \text{ eV} \approx E_g$), $R_a = 70 \Omega$ and $P_L = 10 \text{ mW}$ a value of $P_{\text{THz}}^{\text{id}} = 1.7 \text{ mW}$, corresponding to a conversion efficiency $\eta_{\text{THz}} = P_{\text{THz}}/P_L = 17\%$ is expected.

Similar expressions are found for the pin photomixer. The main differences result from the fact that in the pin photodiode all the photo-generated carriers contribute to the current, as $\tau_{\text{rec}} > \tau_{\text{tr}}$. Thus, the ‘gain’ is unity and, hence, the factor $(\tau_{\text{rec}}/\tau_{\text{tr}})$ does not appear in the expressions for the photocurrent amplitude $I_0^{\text{pin}}(\nu_{\text{THz}})$ and the emitted THz power $P_{\text{THz}}^{\text{pin}}$. Moreover, the transport time roll-off is now determined by the transit time τ_{tr} . The transit-time roll-off [7] depends on the design of the photodiode and does not follow a simple expression as obtained for the recombination roll-off in equation (5). To a reasonably good approximation, however, $I_0^{\text{pin}}(\nu_{\text{THz}})$ can be written as

$$I_0^{\text{pin}}(\nu_{\text{THz}}) = e\eta_{\text{ph}}(P_L/h\nu_0)[1 + i\nu_{\text{THz}}/\nu_{\text{tr}}]^{-1} \quad (8)$$

with a transport roll-off frequency

$$\nu_{\text{tr}} = 1/2\tau_{\text{tr}}. \quad (9)$$

A detailed discussion of the transit-time roll-off will be presented in section 3.2.2.

The expression for the THz power emitted by a pin photomixer then reads

$$P_{\text{THz}}^{\text{pin}} = P_{\text{THz}}^{\text{id}} \eta_{\text{ph}}^2 [1 + (\nu_{\text{THz}}/\nu_{\text{tr}})^2]^{-1}. \quad (10)$$

This expression indicates that, in contrast to the LT-GaAs *photo-conducting* mixer, for THz frequencies significantly smaller than $1/2\tau_{\text{tr}}$ close to ideal performance can be expected for a *pin-diode* photomixer provided $\eta_{\text{ph}} = 1$ (which can be

G H Döhler *et al*

achieved by using an asymmetric Fabry–Perot cavity [10]; see also section 3.2.1).

Finally, we note that in equations (6) and (10) it has been assumed that a THz current of amplitude $I_0^{\text{pc}}(\nu_{\text{THz}})$ or $I_0^{\text{pin}}(\nu_{\text{THz}})$, respectively, provided by an ideal current source is fed into an antenna with a load resistance R_a . In a real photomixer its capacitance C has to be taken into account. The resulting impedance, $1/2\pi i\nu_{\text{THz}}C$, implies that the net current flowing into the antenna is reduced by an ‘RC-roll-off’ factor $[1 + (i\nu/\nu_{RC})]^{-1}$ with

$$\nu_{RC} = 1/2\pi\tau_{RC} = 1/2\pi R_a C, \quad (11)$$

whence

$$P_{\text{THz}}^{\text{pc}} = P_{\text{THz}}^{\text{id}} \eta_{\text{ph}}^2 (\tau_{\text{rec}}/\tau_{\text{tr}})^2 [1 + (\nu_{\text{THz}}/\nu_{\text{rec}})^2]^{-1} \times [1 + (\nu_{\text{THz}}/\nu_{RC})^2]^{-1} \quad (12)$$

and

$$P_{\text{THz}}^{\text{pin}} = P_{\text{THz}}^{\text{id}} \eta_{\text{ph}}^2 [1 + (\nu_{\text{THz}}/\nu_{\text{tr}})^2]^{-1} [1 + (\nu_{\text{THz}}/\nu_{RC})^2]^{-1} \quad (13)$$

respectively.

2.2. Limitations of LT-GaAs photomixers

LT-GaAs is used in photo-conductive mixers [8], because of the short electron and hole capturing and recombination lifetime. Minimum values of $\tau_{\text{rec}} = 130$ fs have been reported, corresponding to a 3 dB frequency of 1.2 THz. In optimized LT-GaAs photomixers the photo-conductive area consists of an LT-GaAs layer with a thickness of the order of $1 \mu\text{m}$ and an interdigitated contact structure with contact separations of $L = 1.8 \mu\text{m}$, covering a quadratic area of $8 \times 8 \mu\text{m}^2$. Using again $v_{\text{dr}} = 10^7 \text{ cm s}^{-1}$ we obtain $\tau_{\text{tr}} = 18$ ps. The maximum laser power which can be applied to the photo-conductive mixer without causing thermal failure is typically about $P_L = 100$ mW. With these values and assuming $\tau_{RC} \ll 2\pi\nu_{\text{THz}}$ equation (12) yields for $\nu_{\text{THz}} = 1$ THz a value of $P_{\text{THz}}^{\text{th}} = 170 \text{ mW} \times (0.130 \text{ ps}/18 \text{ ps})^2 / (1 + 0.67) = 5 \mu\text{W}$, or an optical conversion efficiency of $\eta_{\text{THz}}^{\text{th}} = 5 \times 10^{-5}$. These values are rather close to the best reported experimental values of $P_{\text{THz}}^{\text{exp}} = 2 \mu\text{W}$ and $\eta_{\text{THz}}^{\text{exp}} = 2 \times 10^{-5}$, respectively [8]. It should be noted that, although in this case ν_{THz} is slightly smaller than $\nu_{3 \text{ dB}}$, the low efficiency at this frequency does not result primarily from the short recombination lifetime, but rather from the long transit time. For $\tau_{\text{rec}} \gg 130$ fs, equation (12) yields only a slightly higher value of $P_{\text{THz}} = P_{\text{THz}}^{\text{id}} (1/2\pi\nu_{\text{THz}}\tau_{\text{tr}})^2 = 13 \mu\text{W}$.

In fact, the real advantage of the short recombination lifetime is the reduction of the steady-state carrier density at such high laser power. A simple estimate yields an average photo-induced carrier density in the LT-GaAs layer of about 10^{15} cm^{-3} for the present example. Although this does not appear to be very high it already represents a density which tends to screen the electric fields between the contacts (if the drift velocity of electrons and holes is not the same) and, thus, to lower the photocurrent. If, however, the steady-state carrier density was determined by the (much larger) carrier transit time of about 20 ps, the photo-induced carrier density would become $>10^{17} \text{ cm}^{-3}$ (even if we base our estimate on the assumption of equal maximum drift velocity for the electrons and holes). In this case even unreasonably high external

voltages would be nearly completely screened by space charge building up near the contacts.

Inspection of equation (6) suggests that the most promising approach for improving on the performance of photomixers might be increasing the photo-conductive gain by a reduction of the transit time $\tau_{\text{tr}} = L/v_{\text{dr}}$ by reducing the contact separation L . Unfortunately, a reduction of L , while keeping the active area constant, results in an increase of the capacitance of the interdigitated contact structure approximately proportional to L^{-2} . Taking into account that the present example already represents the design where the RC-3 dB frequency $\nu_{RC} = 1/2\pi R_a C_{\text{LT}} \approx 1$ THz (C_{LT} is the capacitance of the LT-GaAs layer with the interdigitated contacts) this implies a superlinear roll-off of the ac current I_{THz} with decreasing L which overcompensates the expected linear increase.

These simple theoretical design considerations are supported by the empirical observation that in spite of significant efforts no fundamental improvement of performance has been achieved in the field of LT-GaAs photomixers during the past few years [8].

2.3. Limitation of pin photomixers

In section 2.2 it was shown that the pin photomixer may exhibit close to ideal performance if the THz frequency is less than both the transit-time and the RC-roll-off frequencies, ν_{tr} and ν_{RC} , respectively (see equation (13)). Unfortunately, the design cannot be optimized such that high values for ν_{tr} and ν_{RC} are achieved simultaneously.

The capacitance to be used in the expression for the RC-roll-off frequency ν_{RC} (equation (11)) is given by

$$C_{\text{pin}} = \epsilon_0 \epsilon_{\text{sc}} L_x L_y / L_z \quad (14)$$

(ϵ_0 is permittivity of the vacuum, ϵ_{sc} is the dielectric constant of the semiconductor material). Thus, according to equations (14) and (11)

$$\nu_{RC} = L_z / (2\pi R_a \epsilon_0 \epsilon_{\text{sc}} L_x L_y) \propto L_z \quad (15)$$

scales linearly with the i-layer thickness L_z and inversely with the sample cross section $L_x L_y$. Thus, large L_z and small cross section appear attractive for achieving high values of ν_{RC} .

On the other hand, the transit-time roll-off frequency ν_{tr} according to equation (9) increases with L_z becoming small, namely

$$\nu_{\text{tr}} = v_{\text{dr}} / 2L_z \propto L_z^{-1}. \quad (16)$$

Thus, there is a trade-off between optimizing either ν_{RC} or ν_{tr} . An optimum value of L_z for a pin photomixer can be determined from the condition

$$\nu_{RC} = \nu_{\text{tr}}. \quad (17)$$

For high fields electrons in GaAs travel at the saturation velocity $v_{\text{dr}} = v_{\text{sat}} = 10^7 \text{ cm s}^{-1}$, whereas $v_{\text{dr}} = \mu_h F$ holds for the holes. Taking $v_{\text{dr}} = 10^7 \text{ cm s}^{-1}$ for both electrons and holes for the moment and assuming a reasonable minimum value of the device cross section ($L_x = L_y = 7 \mu\text{m}$) we obtain $L_z^{\text{opt}} = 0.33 \mu\text{m}$ as the optimum i-layer thickness for which $\nu_{RC} = \nu_{\text{tr}} = \nu_{\text{opt}}$, resulting in a value $\nu_{\text{opt}} = 150$ GHz. According to equation (13) the THz power emitted at $\nu_{\text{opt}} = 150$ GHz is then expected to be a factor of 4 less than $P_{\text{THz}}^{\text{id}}$.

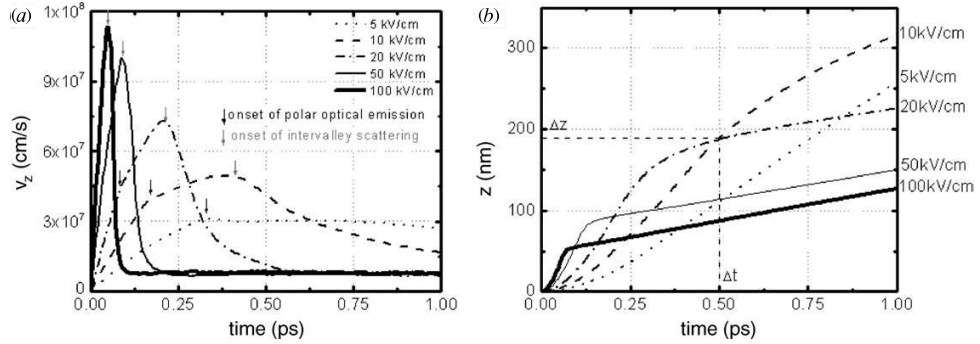


Figure 1. (a) Electron drift velocity versus time in GaAs calculated by Monte Carlo simulation for various electric fields, illustrating the ‘velocity overshoot’. (b) Drift length versus time, calculated with the data from (a). Our theoretical results from (a) agree very well with recent experimental results [13, 15, 16].

Even at 1 THz the emitted THz power should still be about 0.05% of the ideal value. For, e.g., $P_L = 100$ mW, $\eta_{\text{ph}} = 1$, and $R_a = 70 \Omega$, a value of $P_{\text{THz}} = 75 \mu\text{W}$ would still be obtained, which would represent a drastic improvement by 1 to 1.5 orders of magnitude compared to the theoretical or the best experimental LT-photomixer results, respectively. In fact, using uni-travelling carrier (UTC) pin-diodes Ito and coworkers [2] succeeded in obtaining the highest conversion efficiency for photomixers at 1 THz so far reported.

3. Ballistic niplip superlattice photomixer

3.1. Basic concept

From our discussion above we conclude that pin photomixers appear most attractive, but their high-frequency performance appears to be limited by a trade-off between the opposite effect of the thickness of the intrinsic layer on the RC-roll-off (equation (15)) and the transit-time roll-off (equation (16)), at least, if we admit that there will exist a minimum reasonable cross section ($L_x \times L_y$) for the photomixer.

An alternative, heuristic, consideration which led us to our new photomixer concept is the following. How to maximize the THz-current amplitude I_0^{pin} and at the same time avoid the RC-roll-off? The latter condition implies that the (effective) intrinsic layer thickness L_z has to be chosen according to equation (15). In order to obtain a RC-roll-off frequency of 1 THz or higher, e.g., requires $L_z > 2.3 \mu\text{m}$ for reasonable given values for the device cross section $L_x = L_y = 7 \mu\text{m}$ and the antenna impedance $R_a = 70 \Omega$.

The condition of maximized THz-current amplitude I_0^{pin} requires that all the incident photons of one THz period have to be transformed into electron-hole pairs and that these photo-generated carriers move with the highest possible speed during the first half of the THz period $T_{\text{THz}} = 1/\nu_{\text{THz}}$ and stop moving for the second half-period (roughly speaking: the argument will be refined in section 3.2.2). Thus, the distance over which the carriers propagate can be estimated as $l_z = v_{\text{av}} T_{\text{THz}}/2$, if they travel with an average speed v_{av} . As we are dealing with THz periods in the sub-ps range, the carriers, specifically the (light!) electrons, will be moving quasi-ballistically at appropriate electric fields in typical III-V semiconductors like GaAs or (even better) InGaAs. In this case the average

(ballistic) velocity v_{bal} will drastically exceed the high-field saturation drift velocity v_{sat} . A simple estimate for v_{bal} can be obtained from

$$v_{\text{bal}} = v_{\text{max}}/2 = (\Delta_{\Gamma L}/2m_c)^{\frac{1}{2}}, \quad (18)$$

assuming that the velocity increases linearly in time until the kinetic energy of the electron with effective mass m_c reaches the threshold energy $(m_c/2)v_{\text{max}}^2 = \Delta_{\Gamma L}$ (≈ 250 meV for GaAs, 510 meV for InGaAs and 590 meV for InP) for scattering into the L-side valley of the conduction band. This average velocity is about 5×10^7 cm s $^{-1}$ (for GaAs) to 10^8 cm s $^{-1}$ (for InGaAs or InP) and exceeds the corresponding saturation drift velocities v_{sat} by about a factor 5 or 10, respectively. This results in strongly enhanced values for $l_z = v_{\text{bal}} T_{\text{THz}}/2$ (in, e.g., GaAs $l_z = 250$ nm for $n = 1$ THz). Although these values are fairly large, they are much smaller than the optimized values for L_z from equation (15). Thus, except for electrons generated within a distance l_z from the n-layer, this ballistic flight is followed by a drift with the saturation velocity v_{sat} for fields exceeding 20 kV cm $^{-1}$ (figure 1). Regarding the contribution to the ac current one might argue, at first glance, that compared to the ballistic speed, the saturation velocity is negligible and the slow part of the transit does not affect the THz-current amplitude I_0^{pin} too much (see figure 1(a)), although it would imply a tolerable, though undesirable, reduction. But, in addition, each electron-hole pair would fully contribute to the dc current over many THz periods. This would not only drastically increase the Ohmic energy dissipation of the device, but also a more dramatic effect would be an unacceptable accumulation of space charge (with positive sign towards the p-layer and negative sign towards the n-layer) in the pin-diode already at low laser power P_L . This space charge would make it impossible to maintain the electric fields required for ballistic transport, as we will discuss below in connection with equation (26) and figure 4.

In order to take full advantage of the ballistic transport, to suppress all the contributions from non-ballistic transport and, at the same time, to avoid the just mentioned problems, we proposed to split the pin-diode with i-layer thickness of L_z into a superlattice consisting of an optimized number N of nano-pin-diodes with thickness $l_z = L_z/N$ (see figure 2 for an idealized version). This way, in each of the nano-pin-diodes

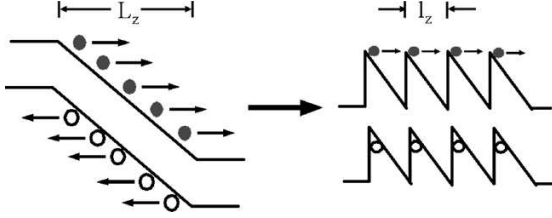
G H Döhler *et al*

Figure 2. Illustration of the basic concept of replacing a single pin-diode by N nano-pin-diodes.

the electrons generated close to the p-layer will be accelerated up to the maximum ballistic velocity by the field in the i-layer, just like in the original pin-diode. After a ballistic flight over the distance l_z , where normally they would be scattered into the L -valley and, hence, decelerated down to the saturation drift velocity, they now reach the n-layer, where they are slowed down to zero velocity. It should be noted that during this time (corresponding to $T_{\text{THz}}/2$, if correctly designed) the ac current per absorbed photon reaches the maximum possible value, i.e.,

$$I_e(t) \begin{cases} = e v_{\text{bal}} 2t / T_{\text{THz}} & \text{for } 0 < t < T_{\text{THz}}/2, \text{ whereas} \\ = 0 & \text{for } T_{\text{THz}}/2 < t < T_{\text{THz}}. \end{cases} \quad (19)$$

The THz current apparently attains the maximum possible value due to the suppression of any current during the second part of the THz period. Regarding the dc current component we note that the contribution per photo-generated carrier is only a fraction e/N , as each electron-hole pair travels only over the distance $l_z = L_z/N$ (instead of L_z , in the conventional pin-diode). It should be noted that it is crucial that all the electrons are generated close to the p-layer in order to travel ballistically the full distance l_z . This implies that the heavy and, hence, slow holes on their part can reach the p-layer within (at least) the same time (below we will explain how to meet this requirement).

Finally, the question has to be answered as to what happens to the electrons and holes after arrival at the n- and p-layers, respectively. Under photomixing conditions the same number of electrons generated within the intrinsic layer of the nano-pin-diode and within a THz period, on average, have to recombine at the ‘interface’ to the neighbouring nano-pin-diode with the corresponding number of holes from there. One might expect that this requirement can hardly be met, recalling that the extremely short recombination lifetime in the LT-GaAs photomixer leads to a roll-off for $\nu_{\text{THz}} > 1/2\pi\tau_{\text{rec}}$. Thus, the recombination lifetime of the spatially separated electrons and holes will, for sure, exceed the τ_{rec} value of LT-GaAs. Below we will actually see that this recombination lifetime may be orders of magnitude larger, if the stationary number of electrons and holes on both sides of the recombination interface is large compared to the number of carriers generated per nano-pin-diode per THz period.

For the calculation of the emitted THz power we have to take into account that the photo-generated carriers are now distributed over N superlattice periods and, therefore, the ac current amplitude I_{THz}^0 is reduced by a factor of N compared to the value for a normal pin photomixer given by equation (13). Hence, we find

$$P_{\text{THz}}^{\text{nipnip}} = P_{\text{THz}}^{\text{id}} \eta_{\text{ph}}^2 N^{-2} (1 + (\nu_{\text{THz}}/\nu_{\text{tr}})^2)^{-1} \times (1 + (\nu_{\text{THz}}/\nu_{\text{RC}})^2)^{-1}. \quad (20)$$

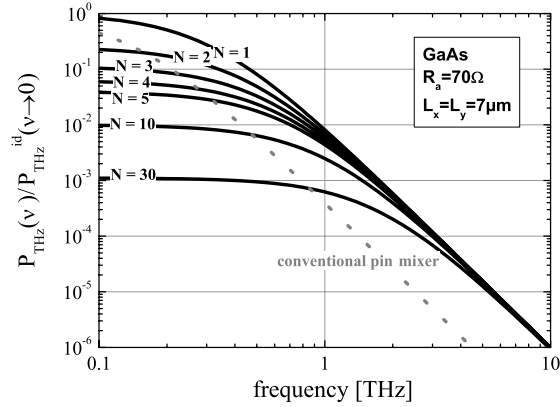


Figure 3. THz power versus frequency for the optimized N -period nipnip photomixer, normalized to the low-frequency value for an ideal pin photomixer. The corresponding results for an optimized pin-diode of the same cross section are also shown.

For a given THz frequency ν_{THz} , the optimized number of superlattice periods N^{opt} is obtained from the same condition $\nu_{\text{RC}} = \nu_{\text{tr}} = \nu_{\text{THz}}$, as already used in the case of the pin-diode. Substituting L_z in equation (15) by Nl_z with l_z adapted to the THz frequency, i.e. $l_z = v_{\text{bal}}/(2\nu_{\text{THz}})$, we obtain

$$N^{\text{opt}} = \nu_{\text{THz}}^2 R_a 4\pi\epsilon_0\epsilon_{\text{sc}} L_x L_y / v_{\text{bal}}. \quad (21)$$

Thus, for a given material and device cross section equation (21) provides the frequencies ν_N for which N^{opt} corresponds to an integer number of pin superlattice periods

$$\nu_N = \sqrt{N} \nu_1 \quad (22)$$

with

$$\nu_1 = \sqrt{v_{\text{bal}} / (4\pi\epsilon_0\epsilon_{\text{sc}} L_x L_y R_a)}. \quad (23)$$

For each value of $N = 1, 2, 3, \dots$ a frequency dependence according to equation (20), however with $\nu_{\text{RC}} = \nu_{\text{tr}} = \nu_N$, is expected (within the framework of our simplifying assumptions!). Thus

$$P_{\text{THz}}^{\text{nipnip}, N} = P_{\text{THz}}^{\text{id}} \eta_{\text{ph}}^2 N^{-2} (1 + (\nu_{\text{THz}}^2 / (N\nu_1^2)))^{-2}. \quad (24)$$

In the following we will denote $\nu_N = \sqrt{N} \nu_1$ as the 6 dB frequency. It should be noted that for $N = 1$ equation (24) also includes the conventional pin photomixer if v_{bal} is replaced by v_{sat} in equation (23). In figure 3 $P_{\text{THz}}^{\text{nipnip}, N} / \eta_{\text{ph}}^2 P_{\text{THz}}^{\text{id}}$ versus ν_{THz} is depicted in a double logarithmic plot for a GaAs ballistic nipnip superlattice photomixer with $L_x = L_y = 7 \mu\text{m}$ and $R_a = 70 \Omega$ and selected values of N as a parameter. For comparison, the corresponding graph for the ‘conventional’ pin-diode mixer, $P_{\text{THz}}^{\text{pin}} / \eta_{\text{ph}}^2 P_{\text{THz}}^{\text{id}}$ versus ν_{THz} , is also included. We note that using an optimized nipnip superlattice with ballistic instead of quasi-stationary transport leads to

- an increase of the transit-time roll-off frequency by a factor $(v_{\text{bal}}/v_{\text{sat}})^{1/2}$ for $N = 1$;
- an increase of the emitted THz power for $\nu_{\text{THz}} \gg \nu_{\text{tr}}$ by a factor of $(v_{\text{bal}}/v_{\text{sat}})^2$ (≈ 25 for GaAs and ≈ 100 for InGaAs or InP!);

- the THz power at high frequencies appears to be unaffected by using a larger number of periods, whereas it is lower by a factor N^{-2} for ν_{THz} significantly less than ν_N .

At this point one might argue that using a sufficiently small field to satisfy the condition for ballistic transport within the time $T_{\text{THz}}/2$ with $N = 1$ should yield the best results. However, we recall that the suppression of the current during the second half of the THz period requires this splitting of the i-region (otherwise the THz amplitude would be significantly reduced, as discussed in connection with equation (19)).

The far more important reason for introducing the superlattice version, however, concerns the saturation effects. In order to guarantee close to optimum ballistic transport, it is necessary to maintain more or less the ideal fields F under operation conditions.

In the following, we will present a simple estimate of the maximum laser power $P_{L,N}^{\text{max}}$ tolerable at a given THz frequency and a given number of superlattice periods N . We will see that with increasing ν_{THz} and N this power increases drastically. In particular, we will find that the conversion efficiency achievable with $P_{L,N}^{\text{max}}$ at the 6 dB frequency becomes the same, for any value of N . This implies that with increasing N not only the 6 dB frequency increases but also the absolute THz power achievable at high frequencies.

The electrons generated within a THz period in each of the nano-pin-diodes and propagating to its n-layer induce a ‘photovoltage’ $U = Q/C_{\text{pin}}$. If, ideally, $1/N$ of the incident laser power P_L is absorbed per nano-pin-diode, the charge generated per THz period per nano-pin-diode is $Q = [(eP_L/h\nu_0)/N]/\nu_{\text{THz}}$. With the condition for optimized intrinsic layer thickness of the nano-pin-diodes, $l_z = v_{\text{bal}}/2\nu_{\text{THz}}$, the capacitance becomes $C_{\text{pin}} = \epsilon_0\epsilon_{\text{sc}}L_xL_y/(v_{\text{bal}}/2\nu_{\text{THz}})$. From figure 1(b) one can see that field changes by a factor of 2 are tolerable for close to ideal ballistic transport over a given distance and time (F may vary between 10 and 20 kV cm⁻¹ for obtaining a quasi-ballistic transport distance of 200 nm within 0.5 ps in GaAs). This implies that a photovoltage swing by about $\Delta_{\Gamma L}/e$ per nano-pin-diode is tolerable. Thus, from $Q/C_{\text{pin}} = \Delta_{\Gamma L}/e$ with the values for Q and C_{pin} from above inserted and using the expression for the optimum number of superlattice periods, equation (21), we finally obtain an expression for the maximum tolerable power. This laser power $P_{L,N}^{\text{max}}$ which leads to the maximum tolerable voltage swing becomes

$$P_{L,N}^{\text{max}} = P_{L,1}^{\text{max}} N^2 \quad (25)$$

with

$$P_{L,1}^{\text{max}} = (\Delta_{\Gamma L} h\nu_0 / 2\pi e^2 R_a). \quad (26)$$

An estimate for $P_{L,1}^{\text{max}}$ for GaAs with $h\nu_0 = 1.45$ eV and with an antenna resistance of $R_a = 70 \Omega$ yields

$$P_{L,1}^{\text{max}} = 0.82 \text{ mW}. \quad (27)$$

According to equation (26) $P_{L,N}^{\text{max}}$ does not depend *explicitly* on the frequency ν_{THz} or the device cross section L_xL_y . However, as the optimum value of N for a given ν_{THz} actually does depend on the device cross section according to equation (21) the maximum power at which saturation effects

THz-photomixer based on quasi-ballistic transport

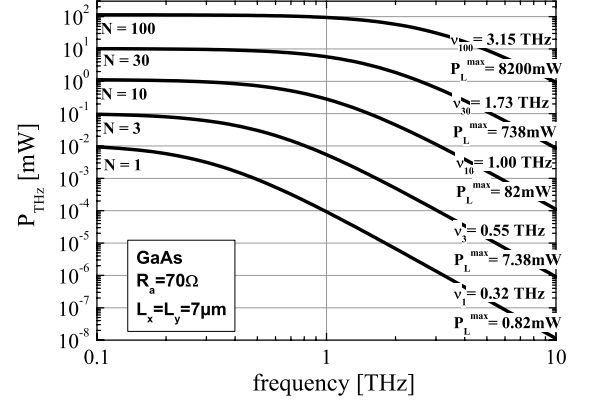


Figure 4. Expected THz power versus frequency for the optimized N -period nipip photomixer, operated at the maximum laser power which does not yet lead to excessive screening of the optimum field for ballistic transport.

do not yet yield a significant degradation depends implicitly on both ν_{THz} (with fourth power) and L_xL_y (quadratically).

With the assumption that all the incident laser power $P_{L,N}^{\text{max}}$ is absorbed, the emitted THz power is obtained by inserting the values obtained from equation (25) for $P_{L,N}^{\text{max}}$ into equation (24) and setting $\eta_{\text{ph}} = 1$, which yields

$$P_{\text{THz},N}^{\text{max}} = P_{\text{THz},1}^{\text{max}} N^2 [1 + \nu_{\text{THz}}^2 / (N\nu_1^2)]^{-2} \quad (28)$$

with

$$P_{\text{THz},1}^{\text{max}} = \frac{1}{2} \eta_{\text{ph}}^2 [\Delta_{\Gamma L}^2 / (4\pi^2 e^2 R_a)] \quad (29)$$

and ν_1 from equation (23).

In figure 4 the emitted THz power versus frequency is depicted for $R_a = 70 \Omega$ and $L_x = L_y = 7 \mu\text{m}$ for various values of N , assuming the maximum tolerable laser power $P_{L,N}^{\text{max}}$ being absorbed by the mixer in each case. We see that taking into account the maximum tolerable laser power implies that the emitted THz power increases quadratically with N for $\nu_{\text{THz}} < \nu_N$ and even with the fourth power for $\nu_{\text{THz}} > \nu_N$. (It should be noted, however, that for $\nu_{\text{THz}} \ll \nu_N$ the maximum tolerable power decreases, as equation (25) no longer strictly holds for this case.) From figure 4 we conclude that the advantages of the nipip superlattice photomixer become more and more pronounced at increasing N as both $P_{L,N}^{\text{max}}$ and $P_{\text{THz},N}^{\text{max}}$ increase $\propto N^2$ while, in addition, the 6 dB-THz frequency increases $\propto \sqrt{N}$.

The fact that saturation effects become less problematic at higher (6 dB) frequencies is immediately plausible. The optimum i-layer thickness for ballistic transport, $l_z = v_{\text{bal}}/2\nu_{\text{THz}}$, decreases with increasing ν_{THz} . This results in an increase of capacitance for the individual pin-diodes. Therefore, the tolerable voltage swing of about $\Delta_{\Gamma L}/e$ (see discussion above) implies a larger tolerable charge generated within one THz period and, hence, an increased laser power absorbed per period. In addition, generating this tolerable charge within a shorter THz period allows for a further increase of the tolerable laser power.

The fact that both $P_{L,N}^{\text{max}}$ (equation (25)) and $P_{\text{THz},N}^{\text{max}}$ (equation (29)) increase $\propto N^2$ implies that the optimum conversion efficiency at the 6 dB frequency (i.e. $\nu_{\text{THz}} = \nu_N$),

$$\eta_{\text{THz},6\text{dB}} = P_{\text{THz},N}^{\text{max}} \nu_N / P_{L,N}^{\text{max}} = \Delta_{\Gamma L} / 16\pi h\nu_0, \quad (30)$$

G H Döhler *et al*

remains the same, independent of N . For the GaAs nipnip mixer we find 0.34%, whereas for InGaAs we obtain 1.27%.

Finally, we would like to emphasize another advantage of our concept, compared with the photo-conducting LT-GaAs mixer. In the latter ones large voltages (typically about 30 V) have to be applied. This implies, in addition to the optical, a rather significant electrical power dissipation UI_0^{pc} within the mixer. The electrical power dissipation in the nipnip photomixer is negligibly small, due to much smaller voltages. Probably much more important is the fact that in the photo-conducting LT-GaAs mixer high electric fields develop directly at the metallic (Schottky) contacts at the high applied bias. These high electric fields most probably result in electromigration of contact metal atoms leading to thermal failure of the mixers at high optical power (about 100 mW) and high voltage (about 30 V). This problem is, at best, difficult to overcome. The nipnip photomixers, in contrast, exhibit (Ohmic) metallic contacts on highly doped contact layers only, implying close to zero fields at these metal contacts. Thus, the values for the maximum laser power P_L^{max} shown in figure 4 for larger values of N , exceeding a few 100 mW, should be tolerable from the point of view of thermal power dissipation as well.

3.2. Implementation of the concept

3.2.1. *Basic considerations.* For the realization of the concept one has to bear in mind the following:

- (i) The transport should predominantly be carried by the (light, and therefore fast) electrons.
- (ii) The potential drop between the starting and arrival point of the electrons should be of the order of the energy difference $\Delta_{\Gamma L}$ between Γ - and L -valleys under optimized operation conditions.
- (iii) Although after arrival in the n-contact region the velocity of the carriers is zero, the electrons at the minimum of the conduction band in the n-layer have to recombine fast enough with the holes at the valence band maximum in the neighbouring nip-diode (see figure 5) in order to avoid an excessive stationary carrier accumulation.
- (iv) In order to achieve maximum conversion efficiency it is necessary that $1/N$ of the incident photons is absorbed in each of the N nano-diodes, which also implies $\eta_{\text{ph}} = 1$.
- (v) For realistic predictions of the performance of real devices the simplified transport and roll-off models presented in section 3.1 have to be replaced by more realistic approaches, such as Monte Carlo calculations.

In figure 5 one period of the proposed ‘nipnip superlattice’ structure, designed to meet these requirements, is shown. The ‘nip transport diodes’ which are designed to have the optimum length l_e for the ballistic electron transport and a short transport length l_h for the holes at the THz frequency chosen are connected to neighbouring nip transport diodes by ‘recombination pn-junctions’. These junctions are highly doped and contain a thin electron–hole recombination layer composed of either LT-GaAs or ErAs [9] and will be discussed in more detail below. The band gap in the i-layers is asymmetrically graded close to the p-layer (see figure 5(c)); this is achieved by ramping the Al content x in the $\text{Al}_x\text{Ga}_{1-x}\text{As}$ or $\text{In}_{0.5}\text{Al}_x\text{Ga}_{1-x}\text{As}$ (lattice matched to InP) from 0 to

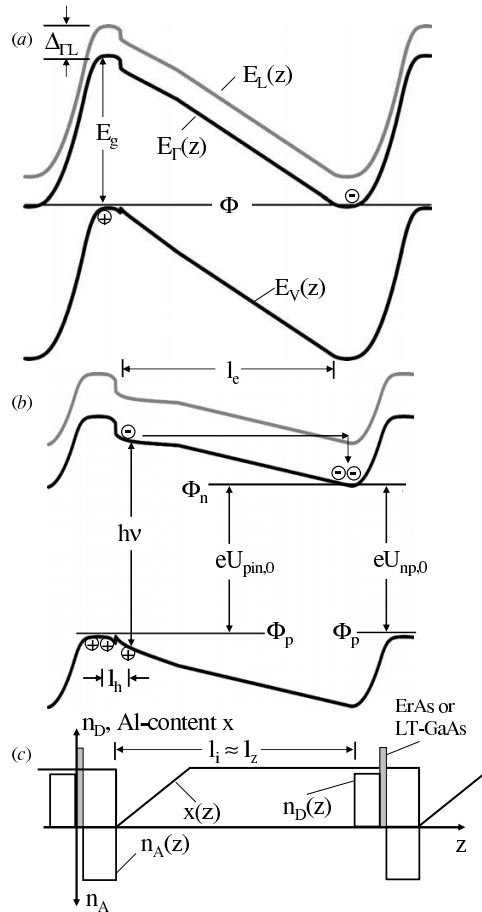


Figure 5. One superlattice period of the nipnip structure used for the implementation of our concept. (c) Doping and composition profiles; (a) Γ - and L -conduction band and valence band diagram for the ground state; (b) same, but for the excited state under (close to optimum) illumination power. $eU_{\text{pin},0}$ and $eU_{\text{np},0}$ represent the dc part or the photovoltage in the transport diode and the np-recombination diode, respectively. Note that under photomixing conditions $eU_{\text{pin}}(t)$ oscillates around the value $eU_{\text{pin},0}$. The (open circuit) amplitude of this oscillation at maximum tolerable laser power P_L^{max} (see equations (25) and (26)) amounts to about $\Delta_{\Gamma L}/2$. Similarly $eU_{\text{np}}(t)$ oscillates around $eU_{\text{np},0}$, however, with a much smaller amplitude (see the text).

a suitably chosen value as indicated in figure 5(c)). This band gap design assures that the electron generation takes place mainly at the point of minimum band gap near the p-layer as indicated in figure 5, if the laser photon energy is suitably chosen. Ideally, the fraction P_L/N of the incident laser power should be absorbed per nip transport diode. This way the same average photocurrent is generated in each nip transport diode and recombined in each recombination diode. To meet this requirement the nipnip photomixer structure can be embedded in an asymmetric Fabry–Perot structure. An optimized asymmetric Fabry–Perot structure [10] has zero reflection and zero transmission and consequently 100% absorption due to destructive interference between the light reflected at the top surface mirror and the light from the back

mirror, attenuated by the absorption of the nipnip structure in between. The standing wave inside an asymmetric Fabry–Perot cavity has a $(\lambda_0/2n_{\text{opt}})$ periodic power distribution. Fortunately, the distance of the power maxima is compatible with a reasonable choice of the superlattice period $d = d_p + d_i + d_n$ for both the GaAs and InGaAs systems. This implies that for optimum design the absorption regions can be placed at maxima of the laser radiation field.

In figure 5 the band diagrams are shown for both the ground state (a) and the excited state at illumination with close to optimum laser power P_L (b). The ground state is characterized by a common Fermi level Φ in the n- and p-layers. The residual sheet electron and hole densities in the ground state are $n_0^{(2)}$ and $p_0^{(2)}$, respectively. As the photo-generated electrons and holes recombine slowly compared to the THz period T_{THz} , an additional quasi-stationary sheet electron and hole density $\Delta n^{(2)} = \Delta p^{(2)}$ builds up under illumination. This space charge partially screens the built-in potential ($V_{\text{bi}} \simeq E_g$). This results in a splitting of the quasi-Fermi levels for the electrons in the n-layers and the holes in the p-layers $\Phi_{\text{np}} = \Phi_n - \Phi_p$ (see figure 5(b)). Under photomixing conditions the average photocurrent generated per period of the nipnip superlattice, I_0/N , flows through the recombination diodes as a (nearly constant) recombination current. The average values of Φ_{np} and, thus, also the average potential drop within the ‘pin transport diodes’ and the ‘np-recombination diodes’ correspond to eU_{pin}^0 and eU_{np}^0 , respectively, where U_{np}^0 stands for the forward bias at which only this current I_0/N flows in the ‘pn-recombination diode’. Under ideal operation conditions, the average potential drop within the pin transport diodes should be about $eU_{\text{pin}}^0 = E_g - \Delta_{\Gamma L}$ (condition (ii) from above). If this situation is realized for $\Phi_{\text{np}}^0 = eU_{\text{pin}}^0 = eU_{\text{np}}^0$, as assumed in figure 5(b), the mixer performance is optimized for zero applied bias (at the given laser power P_L). For higher laser power the recombination current and, hence, the average voltage drop at the recombination diode, eU_{np}^0 , will increase. Thus, a small compensating external bias will be required to maintain the condition $eU_{\text{pin}}^0 = E_g - \Delta_{\Gamma L}$ for optimum performance at the transport diode.

In our discussion of saturation effects preceding equation (25) we found that the periodic THz-voltage swing in the transport diodes should be of the order of $\Delta_{\Gamma L}/e$, but not exceeding this value, under optimized operation conditions. The corresponding voltage swing at the pn-recombination diodes has the opposite sign and therefore reduces the total zero-load THz-voltage swing ($\approx N\Delta_{\Gamma L}/e$) at the mixer. A simple estimate, however, shows that the U_{np} -voltage swing typically amounts to $<10\%$ of the U_{pin} -voltage swing. This results from the fact that, at the THz frequencies considered here, the U_{np} -voltage swing is reduced by the capacitance ratio $C_{\text{pin}}/C_{\text{np}}$ compared to ΔU_{pin} . In the next section we will see that the doping density in the recombination diodes is very high, which yields very narrow depletion layers, much smaller than the intrinsic layer thicknesses of the transport diodes, whence $C_{\text{pin}}/C_{\text{np}} < 0.1$.

From the estimates for optimum performance depicted in figure 4 we deduce that the current densities in the pn-recombination diodes $j_{\text{av}} = (1/N)(eP_L^{\text{max}}/h\nu_0)/(L_x L_y)$ will be in the order of 1 to 100 kA cm^{-2} for devices of typical cross section. As these values are required for a photo-induced Fermi level splitting of $\Phi_{\text{np}} = eU_{\text{np}} \approx eU_{\text{pin}} \approx$

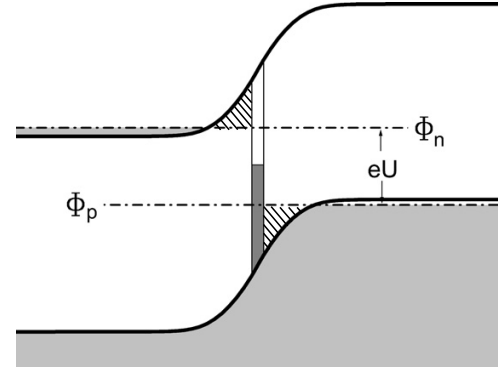


Figure 6. Schematic band diagram of a ‘recombination pn-diode’ under forward bias U . Due to high doping, electron and hole injection into the recombination layer by (inelastic) tunnelling through the barriers (shaded areas) is very efficient. For details see [9].

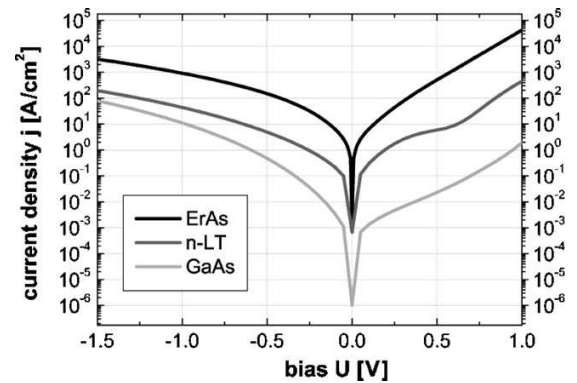


Figure 7. Comparison of measured current density versus voltage characteristics of our ‘recombination pn-diodes’ with ErAs- and n-LT-GaAs recombination layers to standard pn-junctions with the same high doping densities.

$E_g - \Delta_{\Gamma L}$ (≈ 1 eV for GaAs and ≈ 0.24 eV for InGaAs) these current density values turn out to be many orders of magnitude larger than in standard pn-junctions. Therefore, we have developed special ‘pn-recombination diodes’ which contain ErAs- or ‘low-temperature-grown’ GaAs (LT-GaAs) recombination layers, as schematically shown in figure 6. In figure 7 current density versus voltage curves for such strongly doped pn-diodes with a 1.2 monolayer thick ErAs recombination layer at the interface and $n_D = 5 \times 10^{18} \text{ cm}^{-3}$ and $n_A = 2 \times 10^{19} \text{ cm}^{-3}$ and with a highly n-doped LT-GaAs recombination layer are compared with reference diodes with the same doping densities, but without a recombination layer [9]. We see that, using this trick, the required high current densities are, in fact, accessible at the required excitation level. As explained in detail in [9] the capture of electrons and holes at the semi-metallic ErAs clusters or the deep point defects in the LT-GaAs takes place by inelastic tunnelling and is not (or only slightly) thermally activated. The high recombination current densities at 1 V, corresponding to recombination rates of about 5×10^{21} or $5 \times 10^{23} \text{ cm}^{-2} \text{ s}^{-1}$ electron and hole recombinations in the LT-GaAs layer or the ErAs layer,

G H Döhler *et al*

respectively, are rather due to the large sheet carrier densities in the range of 10^{12} to 10^{13} cm^{-2} than to particularly short tunnelling capturing times (of the order of ns for LT-GaAs to several ps in the ErAs layers). Equally favourable results have recently been obtained in InGaAs-recombination diodes [11].

3.2.2. Refined model calculations. In order to test our simple estimates from section 3.1 we have performed more detailed calculations which take into account the details regarding the electron-hole generation and the transport processes in a realistic way. This allows us to obtain amplitude and phase of the THz-current and the THz-voltage induced within the nano-diodes as a function of ν_{THz} .

In order to calculate the emitted THz power, the THz current $I_{\text{THz}}(t)$ and THz voltage $U_{\text{THz}}(t)$ in the top and bottom contact layers have to be known. Whereas $I_{\text{THz}}(t)$ is the same in each of the nano-diodes (provided the same fraction of the total laser power is absorbed), the voltage $U_{\text{THz}}(t)$ is N times the voltage $U_{\text{THz, pin}}(t)$ induced in each nano-diode. The external current is the displacement current of the electron-hole dipoles resulting from photo-generated carriers travelling through the nano-pin-diodes. It can be expressed as the time derivative of the displacement charge $Q_{\text{pin}}(t) = C_{\text{pin}}U_{\text{pin}}(t)$ induced in the n- and p-layers of the pin-nano-diode. At the time t an electron, which was generated at the position z' at the time t' , contributes

$$\begin{aligned} \delta q_{z,z'} &= e[z(t) - z']/l_z & \text{for } z(t) < l_z \\ \delta q_{z,z'} &= e[l_z - z']/l_z & \text{for } z(t) > l_z \end{aligned} \quad (31)$$

to this space charge. The position is given by

$$z(t, t') = z' + \int_{t'}^t v_e(t'') dt'' \quad (32)$$

Complementary expressions apply to photo-generated holes.

The total displacement charge originating from photo-generated electrons at the time t is obtained as the product of the local generation rate $(dn(z')/dt)_{t'}$ at z' at the time t' and $\delta q_{z,z'}(t, t')$ from equations (31) and (32), integrated over z' and all times $t' < t$. Again, complementary expressions apply to the photo-generated holes. The oscillating component of the displacement charge is obtained by taking into account the (nearly constant) rate of electron- and hole-charge recombination at the pn-recombination diodes. As this recombination rate balances the average generation rate, this means that we can calculate the oscillating part $Q_{\text{THz}}(t')$ by replacing the actual generation rate $(dn(z')/dt)_{t'} = \alpha(z')(P_L(z')/h\nu_0)[1 + \cos 2\pi\nu_{\text{THz}}t']$ with $(dn(z')/dt)_{t'} = \alpha(z')(P_L(z')/h\nu_0) \cos 2\pi\nu_{\text{THz}}t'$, whence

$$\begin{aligned} Q_{\text{THz}}(t) &= e \int_0^{l_z} dz' \int_{-\infty}^t dt' \alpha(z')(P_L/h\nu_0) \\ &\quad \times \cos 2\pi\nu_{\text{THz}}t' \delta q_{z,z'}(t, t'). \end{aligned} \quad (33)$$

Assuming ideal ballistic transport according to $v(t, t') = (e/m_c)F(t - t')$ (which represents a reasonable approximation), if $eU_{\text{pin}} = eFl_z < \Delta_{\Gamma L}$ and generation confined to $z \approx 0$, i.e., directly at the boundary to the p-layer, expression (33) can be evaluated analytically. Assuming, in addition, $eU_{\text{pin}} = \Delta_{\Gamma L}$ and that the fraction P_L/N is absorbed in each nano-pin-diode, the generation rate becomes

$(1/N)(P_L/h\nu_0)[1 + \cos 2\pi\nu_{\text{THz}}t']\delta(z' - 0)$ and $\delta q_{z,z'}(t, t')$ reduces to

$$\begin{aligned} \delta q(t - t') &= ez(t - t')/l_z = e[(t - t')/\tau]^2 & \text{for } (t - t') < \tau \\ \delta q(t - t') &= e & \text{for } (t - t') > \tau \end{aligned} \quad (34)$$

with $\tau = l_z/v_{\text{bal}}$ and we obtain for these idealized conditions the oscillating space charge

$$\begin{aligned} Q_{\text{THz}}(t) &= (1/N)(P_L/h\nu_0) \\ &\quad \times \int_{-\infty}^t dt' \cos 2\pi\nu_{\text{THz}}t' \delta q(t - t') \end{aligned} \quad (35)$$

if the potential drop within the i-layer reaches the critical value for the onset of scattering into the L -valley. For $eU_{\text{pin}} < \Delta_{\Gamma L}$ the average ballistic velocity v_{bal} no longer reaches its maximum given by equation (18). In this case the transit time has to be replaced by $\tau = l_z/v_{\text{bal}}(eU_{\text{pin}}/\Delta_{\Gamma L})^{1/2}$. For $eFl_z > \Delta_{\Gamma L}$ a similar, but slightly more complicated expression holds, which takes into account that after reaching the maximum ballistic velocity v_{max} defined in equation (18) the electrons continue their path through the i-region with the much slower saturation group velocity v_{sat} , which implies strongly enhanced transit times.

Evaluation of equation (35), under the assumption that contributions from times $t - t' \gg \tau$ do not contribute to the oscillating displacement charge, yields

$$\begin{aligned} Q_{\text{THz}}(t) &= (1/N)[(2eP_L/h\nu_0)/(2\pi\nu_{\text{THz}})^2\tau] \\ &\quad \times [\{\cos 2\pi\nu_{\text{THz}}\tau - \sin 2\pi\nu_{\text{THz}}\tau/2\pi\nu_{\text{THz}}\tau\} \cos 2\pi\nu_{\text{THz}}t \\ &\quad + \{\sin 2\pi\nu_{\text{THz}}\tau + (\cos 2\pi\nu_{\text{THz}}\tau - 1)/2\pi\nu_{\text{THz}}\tau\} \\ &\quad \times \sin 2\pi\nu_{\text{THz}}t]. \end{aligned} \quad (36)$$

The voltage oscillations and current oscillations can be easily obtained from equation (36). The total THz voltage (across the N superlattice periods) is

$$U_{\text{THz}} = (N/C_{\text{pin}})Q_{\text{THz}}(t) \quad (37)$$

and the THz current is

$$I_{\text{THz}}(t) = dQ_{\text{THz}}(t)/dt. \quad (38)$$

It should be noted that expressions (37) and (38) reduce to

$$U_{\text{THz}}(t) = (1/C_{\text{pin}})[(eP_L/h\nu_0)/2\pi\nu_{\text{THz}}] \sin 2\pi\nu_{\text{THz}}t \quad (39)$$

and

$$I_{\text{THz}}(t) = (1/N)[(eP_L/h\nu_0)] \cos 2\pi\nu_{\text{THz}}t \quad (40)$$

for low THz frequencies ($\nu_{\text{THz}}\tau \ll 1$). As expected, the THz signals decrease significantly, if the ballistic transit-time becomes comparable with half a THz period, i.e., $\tau \approx T_{\text{THz}}/2 = 1/2\nu_{\text{THz}}$. In figure 8 the expected roll-off factor for the THz power $|I(\nu_{\text{THz}})/I(\nu = 0)|^2$ is depicted as a function of ν_{THz} for $l_z = 200$ nm, whence $\tau = 200 \text{ nm}/5 \times 10^7 \text{ cm s}^{-1} = 0.4$ ps. For comparison, the simple analytical estimate according to our simplified picture from section 3.1 with $[I(\nu_{\text{THz}})/I(\nu = 0)]^2 = 1 + (\nu_{\text{THz}}/\nu_{\text{tr}})^2$ with $\nu_{\text{tr}} = v_{\text{bal}}/2l_z$ is also plotted.

In order to compare the idealized performance data with the situation in realistic photomixers we have performed Monte Carlo calculations [12]. These calculations represent a realistic numerical implementation of equations (31)–(33). They take into account the local generation rates $P_L(z', t')\alpha(z')/h\nu_0$ (where $\alpha(z')$ is the local absorption coefficient, which depends

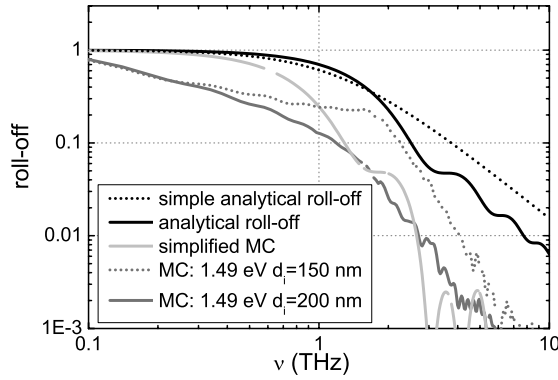


Figure 8. Transit-time roll-off factor of the emitted THz power versus THz frequency obtained for a Ga (Al) As nipnip photomixer from different analytical and numerical approaches as described in the text.

on the local electric field $F(z')$ and on the position z' , due to the band gap grading in the i-layer) as well as the initial velocity of the photo-generated electrons and holes. Furthermore, the z' -dependence of the electric field and the z' -dependence of the scattering rates of the electrons and holes for intervalley scattering and emission and absorption of acoustic and optical phonons, due to the grading, are included. We have recently demonstrated by fs-pump and probe experiments that such MC simulations provide an excellent, highly accurate, parameter-free description of the transient quasi-ballistic transport in similar pin-diodes [13]. For the calculation of the displacement charges $Q_{\text{THz}}(t)$ we have assumed that a carrier fully contributes, if it enters the flat region of the n- or the p-layer, respectively. This is expected to be a good approximation, as the short dielectric relaxation times in the n- and the p-layers ($\tau_e = \epsilon_0 \epsilon_{\text{sc}} / \sigma_e \approx 0.8 \times 10^{-15}$ s, $\tau_h = \epsilon_0 \epsilon_{\text{sc}} / \sigma_h \approx 3.6 \times 10^{-15}$ s, for our samples) do not allow for an appreciable potential drop to build up in these layers.

In figure 8 the roll-off factors resulting from such MC simulations, performed for a $\text{Ga}_{1-x}\text{Al}_x\text{As}$ -pinp-diode with $l_z = 200$ nm, with a linear grading $0 < x < 0.1$ between $0 < z < 100$ nm and $x = 0.1$ elsewhere, $d_n = 1.3$ nm, $n_D = 4 \times 10^{18} \text{ cm}^{-3}$, $d_p = 0.25$ nm and $n_A = 2 \times 10^{19} \text{ cm}^{-3}$, are depicted for (close to) optimum potential drop within the pin-diode. The grey curve is based on simplifying assumptions regarding the MC simulations (similar to those shown in figure 2) and considering only the centre of mass contributions originating from the electron ensemble, whereas the full curve includes all the details listed above, for $h\nu_0 = 1.49$ eV, including the spreading of the carrier distributions during the transport and electron reflection at the barrier formed by the recombination pn-diode. The latter example demonstrates that drastic changes compared to the more or less idealized values are observed. However, the roll-off becomes much less pronounced if l_z is reduced to 150 nm, as can be seen from the corresponding curve in figure 8. In figure 9 the results for calculations of the roll-off factor for a $l_z = 200$ nm InGa(Al)As-pinp-diode are shown. In this case the simplified MC calculation (grey curve) yields higher THz power for $\nu_{\text{THz}} > 1.5$ THz than the analytical model, and at

THz-photomixer based on quasi-ballistic transport

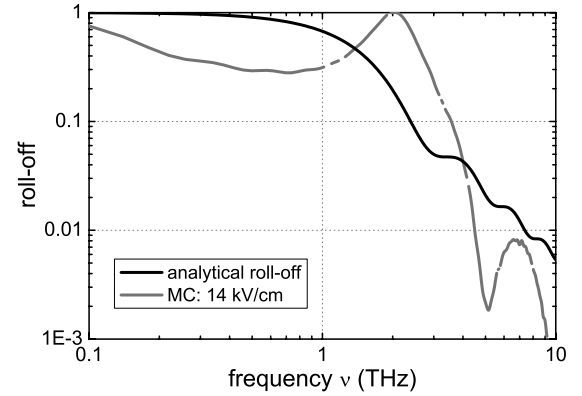


Figure 9. Same as figure 8, but for an InGa (Al) As nipnip photomixer.

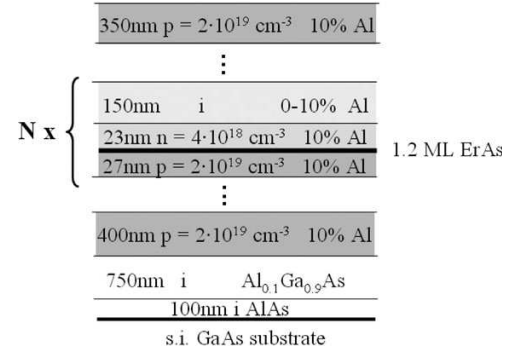


Figure 10. Schematic diagram depicting the epitaxial layer sequence of the nipnip mixer.

about 2 THz exhibits even a slightly higher THz power than at low frequencies. This perhaps surprising, but very favourable, result can be easily understood from the calculated drift velocity versus time MC results, which exhibit a pronounced oscillation with a frequency of about 2 THz. The intervalley scattering is suppressed due to the fact that the kinetic energy of the electrons remains smaller than the threshold energy $\Delta_{\Gamma L}$ for intervalley scattering everywhere. A major fraction of the electrons reaches the pn-recombination diode potential barrier and is reflected before being slowed down. Such semi-classical oscillations of an electron ensemble in wide asymmetric potential wells are theoretically expected, if their depth does not exceed $\Delta_{\Gamma L}$, and have recently been experimentally observed in Ga(Al)As wells [14].

3.2.3. Fabrication and test of nipnip photomixers. We have fabricated and tested nipnip photomixers with different numbers of periods and lengths l_z of the intrinsic layer and with both ErAs or n-LT-GaAs recombination layers contained within the recombination diodes. The samples with ErAs or n-LT-GaAs recombination layers were grown on semi-insulating GaAs substrates by molecular beam epitaxy (MBE) at UCSB and the University of Erlangen, respectively. Figure 10 depicts schematically the layer sequence. In addition to the samples with 7, 4 and 1 periods we also fabricated mixers consisting only of a pin-nano-diode with

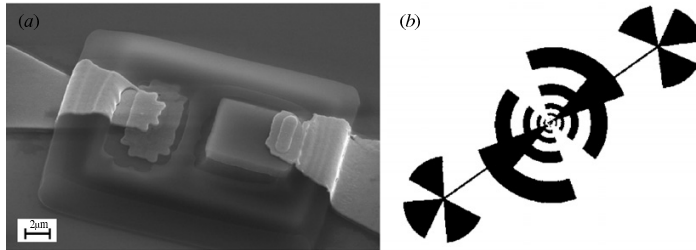
G H Döhler *et al*

Figure 11. (a) SEM picture of a processed nipnip mixer. The $7\ \mu\text{m} \times 9\ \mu\text{m}$ mesa, covered with a $4\ \mu\text{m} \times 1\ \mu\text{m}$ Au-Ge n -contact and the end of the Au antenna, is visible on the right, the bottom n -contact and the other end of the antenna on the left-hand side. (b) Diagram of the log-periodic antenna.

the same values for L_z , and n - and p -doping densities in order to compare the performance. The devices were processed using photolithography for wet-chemical etching and contact deposition via the lift-off technique. In order to keep the capacitance sufficiently low, but at the same time avoiding problems with processing of these rather high mesas and with focusing all the light onto the sample, the mesa size was varied between $7\ \mu\text{m} \times 7\ \mu\text{m}$ and $11\ \mu\text{m} \times 10\ \mu\text{m}$ (a $7\ \mu\text{m} \times 9\ \mu\text{m}$ mixer is shown in figure 11(a)). This, in combination with the rather small number of periods, resulted in rather high capacitances and low RC -3 dB frequencies. In order to minimize the effect of the frequency dependence of the antenna impedance, a log-periodic antenna, as shown in figure 11(b), was used. For testing purposes, devices of different size without antenna were also fabricated on the same wafer.

The completed devices were first tested for dc performance. The results of capacitance versus voltage (CU) measurements were in good agreement with theoretical estimates, using $L_z = N \times l_z$ in equation (14). The dark current density versus voltage ($j(U)$) characteristics showed the typical exponential behaviour with a quality factor $n = 1.87$ for forward bias (regarding the pin transport diodes) and exhibited little variation if the voltage was renormalized per superlattice period by dividing the applied voltage U by a factor N . Combining the results of measurements on single nip transport diodes and pn -recombination diodes with those on the nipnip devices, we were also able to show that the voltage drop across the np -recombination diodes was negligible within the range of interest. For optical CW characterization we performed photocurrent versus voltage measurements for photon energies close to the minimum energy gap in the i -layer over a wide range of optical power (see figure 12). The photocurrents were in excellent agreement with the theoretical responsivity values estimated from the total (z -dependent) absorption in the i -layer. In addition, the field dependence of the absorption coefficient at photon energies close to the band gap could be used to get information about the laser-power-dependent screening of the built-in field in the i -layer. The field screening deduced from these experiments was in good agreement with the behaviour expected from the studies of the dark current density versus voltage characteristics of the recombination diodes [11].

The set-up used for the study of THz emission under photomixing conditions is based on two independently tunable Ti-sapphire lasers. The linear polarized beams are combined into a glass fibre. At the end of the glass fibre the outcoming

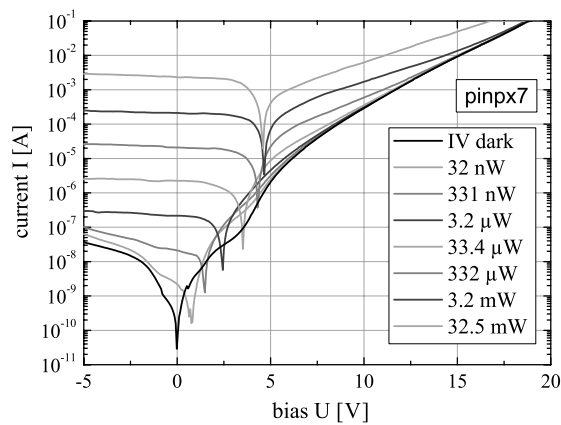


Figure 12. Dark current and photocurrent versus voltage characteristics of a ($100\ \mu\text{m} \times 100\ \mu\text{m}$!) 7-period nipnip test structure at various laser power levels, at a photon energy of 1.44 eV. At zero and reverse bias (referred to as the pin transport diode) the photocurrent is nearly constant and corresponds to the responsivity calculated from the theoretical absorption spectra, indicating that all the photocurrent generated in each nano-diode is recombining in the (forward biased) recombination diodes.

light is focused onto the mixer device, which is placed in the focus of a hyperspherical silicon lens. The THz radiation which is emitted to 90% into the substrate becomes nearly collimated by the lens and is directed either to a He-cooled InAs-bolometer or a Golay cell via parabolic mirrors. A bias U can be applied to the mixer via the contacts to the antenna and the dc component of the photocurrent can be measured.

In figure 13 results of THz power versus applied voltage are shown for different values of the laser power P_L for a mixer at 248 GHz. The fact that with increasing laser power the maximum of the emitted THz power shifts towards increasing reverse bias is a consequence of the increasing screening of the built-in field. The reverse bias compensates this reduction of the built-in field and allows for establishing of the optimum field for ballistic transport. It should also be noted that for too high a reverse bias the THz power decreases again, as the fields become too large for optimum ballistic transport. In figure 14 the THz power versus laser power is shown for both zero bias and optimum reverse bias. In the latter case the expected parabolic relation is observed within the whole range. It should also be noted that the photocurrent in these devices is a factor of 12 lower compared to the ideal values of $e/Nh\nu_0 \approx 0.67\ (\text{A W}^{-1})/N$ expected for optimum

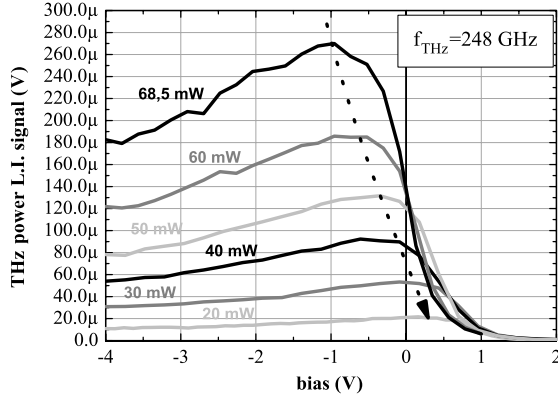


Figure 13. Emitted THz power versus applied reverse bias. At 30 mW incoming laser power, the maximum of the emitted THz power is obtained at 0 V. For increasing laser power an increasing reverse bias is needed to optimize the THz output power, since the photo-generated carriers screen the transport field inside the pin transport diode beyond the optimum value for ballistic transport (see figure 5: at zero external bias increasing laser power and, hence, increasing photocurrent results in both increased np at the recombination diode and reduced field in the pin transport diode). External reverse bias (referred to as the transport diode) at a given laser power implies increasing field in the pin transport diode.

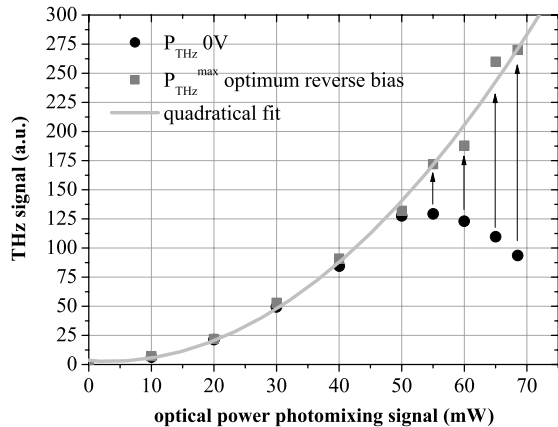


Figure 14. Emitted THz power versus the incoming laser power at 248 GHz. For optical powers below 40 mW the emitted THz power increases quadratically. For higher optical powers the transport fields are screened beyond the optimum value, and the THz power saturates and even decreases. Applying a suitable reverse bias leads to the expected quadratical increase again.

responsivity (which could be achieved by incorporating the mixer into an asymmetric Fabry–Perot cavity, as mentioned in section 3.1).

In figure 15(a) results of THz power versus THz frequency are shown for nipnip mixers with 4 and 7 periods and, for comparison, for a pin photomixer with the same design of the pin region. In figure 15(b) the same results, corrected for the RC-roll-off, are plotted again. This plot shows that no appreciable transit-time roll-off occurs, whereas the pin photomixer, which has to be operated at much too high fields for ballistic transport, exhibits a ν^{-2} transit-time roll-off with a 3 dB frequency $\nu_{tr} = 376$ GHz. This is consistent with the estimate $\nu_{tr} = 1/2\tau_{tr} = v_s/2l_z = 330$ GHz.

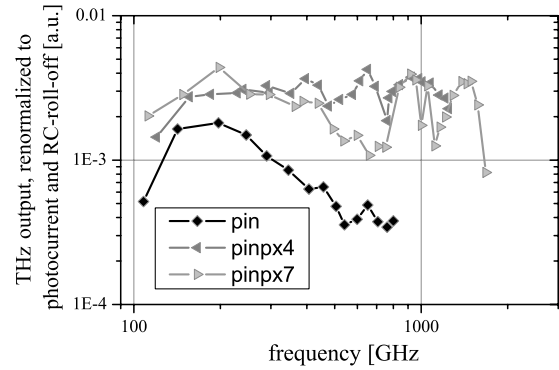
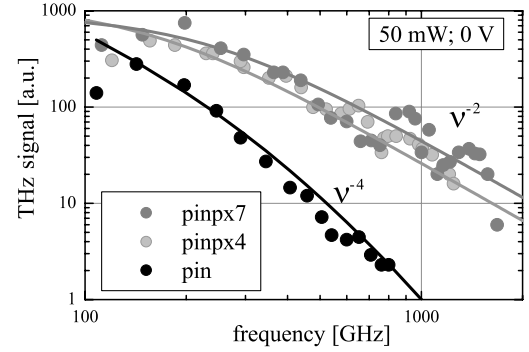


Figure 15. (a) Comparison between THz power versus THz frequency for 4- and 7-period nipnip photomixers and the conventional pin photomixer with the same design of the pin structure. As expected, the pin mixer exhibits a $1/\nu_{THz}^4$ -roll-off, whereas the nipnip devices show only a $1/\nu_{THz}^2$ -roll-off. (b) Same data, but corrected for the RC-roll-off and renormalized to $(\text{photocurrent})^2$ in order to illustrate the improvement achieved by the quasi-ballistic transport.

Presently, our attempts at determining absolute values for the emitted power are yielding values which are (nearly constant) factors between 80 and 300 lower than those expected from equation (13), depending on the growth series of the wafers from which the mixers were fabricated. We do not yet know the reason for this loss in detected power, but we are convinced that it is not related to the concept. Both the comparison of the roll-offs (ν^{-2} for the nipnip versus ν^{-4} for the nip mixer), and the voltage dependence of the measured THz power corroborate in detail the expected advantages of the ballistic transport and of the increased roll-off frequencies due to using N periods. We recall that we should observe basically the same high output power (referred to as the generated photocurrent) for our pin mixer (see figure 15) as reported by Ito and coworkers [2–4] as in both cases the same improvement compared to conventional pin photomixers is achieved due to the suppression of the hole contribution to the current. Apart from losses between the antenna and the detector we believe that the discrepancy between expected THz power may be due to Ohmic losses in the contact layers of the nipnip structures, rather than due to parasitic capacitances.

G H Döhler *et al*

4. Summary and outlook

We have presented a new photomixer concept which allows us to preserve the high intrinsic conversion efficiency of pin photomixer at low and intermediate frequencies (in the 100 GHz range) up to frequencies of several THz. Our first results on the GaAs-nipnip photomixer have confirmed that we are able to overcome the transit-time roll-off problem by reducing the transit path length and establishing optimum fields for quasi-ballistic transport. We have also been able to demonstrate that the *RC*-roll-off can be shifted independently to higher frequencies by increasing the number of superlattice periods. Our next goals are the demonstration of high absolute values of the THz power and the extension to higher frequencies. InGa(Al)-nipnip mixers are expected to exhibit particularly appealing performance data. We are also considering a modified photomixer concept where the radiation emitted coherently by the (ballistically) accelerated and decelerated electrons is directly used ('optical approach' instead of 'RF-approach').

Acknowledgments

This work was supported by the Deutsche Forschungsgesellschaft (DFG), the European Space Agency

(ESA; Far-IR-Generation) and the Bavarian-Californian-Technology Program (BaCaTeC).

References

- [1] Brown E R *et al* 1995 *Appl. Phys. Lett.* **66** 4903
- [2] Ito H *et al* 2003 *Proc. SPIE* **5246** 465
- [3] Ito H *et al* 2003 *Proc. SPIE* **4999** 156
- [4] Ito H *et al* 2005 *Semicond. Sci. Technol.* **20** S191
- [5] Köhler R *et al* 2002 *Nature* **417** 156
Rochat M *et al* 2002 *Appl. Phys. Lett.* **81** 1381
- [6] McIntosh K A *et al* 1995 *Appl. Phys. Lett.* **67** 3844
- [7] Winstel G and Weyrich C 1984 *Optoelektronik II* (Berlin: Springer)
- [8] Brown E R *et al* 2003 *Int. J. High Speed Electr. Syst.* **13** 497
- [9] Pohl P *et al* 2003 *Appl. Phys. Lett.* **83** 4035
- [10] Yan R H *et al* 1991 *IEEE J. Quantum Electron.* **27** 115
- [11] Renner F 2004 The nipnip-THz-emitter: photomixers based on ballistic transport in asymmetrical modulation-doped superlattices *Phys. Mikrostrukt. Halbleiter* **37** 169, 65
- [12] Eckardt M 2004 Aspects of high-field carrier transport in AlGaAs—towards an efficient THz-emitter *Phys. Mikrostrukt. Halbleiter* **33** 146
- [13] Schwanhäuber A *et al* 2004 *Phys. Rev. B* **70** 085211
- [14] Eckardt M *et al* 2004 *Semicond. Sci. Technol.* **19** 195
- [15] Leitenstorfer A *et al* 1999 *Phys. Rev. Lett.* **82** 5140
- [16] Leitenstorfer A *et al* 2000 *Phys. Rev. B* **61** 642

Bibliography

- [1] P.H. Siegel. Terahertz technology. *IEEE Transactions on Microwave Theory and Techniques*, 50(3):910–928, 2002.
- [2] T. Löffler, K.J. Siebertt, N. Hasegawa, T. Hahn, G. Loata, R. Wipf, M. Kress, M. Thomson, and H.G Roskos. Terahertz surface and interface characterization. *2005 IEEE MTT-S International Microwave Symposium Digest*, pages 4–, 2005.
- [3] B. Ferguson, S. Wang, D. Gray, D. Abbott, and X-C Zhang. Towards functional 3d t-ray imaging. *Phys. Med. Biol*, 47:3735–3742, 2002.
- [4] Anthony J. Fitzgerald, Vincent P. Wallace, Mercedes Jimenez-Linan, Lynda Bobrow, Richard J. Pye, Anand D. Purushotham, and Donald D. Arnone. Terahertz Pulsed Imaging of Human Breast Tumors. *Radiology*, 239(2):533–540, 2006.
- [5] William R. Tribe, David A. Newnham, Philip F. Taday, and Michael C. Kemp. Hidden object detection: security applications of terahertz technology. In R. Jennifer Hwu, editor, *Proceedings of SPIE*, volume 5354 of *Terahertz and Gigahertz Electronics and Photonics III*, pages 168–176, 2004.
- [6] D. H. Auston. Picosecond optoelectronic switching and gating in silicon. *Appl. Phys. Lett*, 26:101–103, 1975.
- [7] P. R. Smith, D. H. Auston, A. M. Johnson, and W. M. Augustyniak. Picosecond photoconductivity in radiation-damaged silicon-on-sapphire films. *Appl. Phys. Lett.*, 38:47–50, 1981.
- [8] D. H. Auston, K. P. Cheung, and P. R. Smith. Picosecond photoconducting Hertzian dipoles. *Appl. Phys. Lett*, 45(3):284–286, 1984.
- [9] D. E. Spence, P. N. Kean, , and W. Sibbett. 60-fsec pulse generation from a self-mode-locked Ti:sapphire laser. *Opt. Lett.*, 16:42–, 1991.
- [10] P.R. Smith, Auston, D.H., and M.C. Nuss. Subpicosecond photoconducting dipole antennas. *IEEE J. Quantum Elect.*, 24(9):255–260, 1988.

- [11] Martin van Exter, Ch. Fattinger, and D. Grischkowsky. High-brightness terahertz beams characterized with an ultrafast detector. *Appl. Phys. Lett.*, 55(4):337–339, 1989.
- [12] M. van Exter and D.R. Grischkowsky. Characterization of an optoelectronic terahertz beam system. *IEEE Trans. Microwave Theory Tech*, 38(11):1684–1691, 1990.
- [13] K. H. Yang, P. L. Richards, and Y. R. Shen. Generation of far-infrared radiation by picosecond light pulses in LiNbO_3 . *Appl. Phys. Lett.*, 19(9):320–323, 1971.
- [14] X.-C. Zhang, B. B. Hu, J. T. Darrow, and D. H. Auston. Generation of femtosecond electromagnetic pulses from semiconductor surfaces. *Appl. Phys. Lett.*, 56(11):1011–1013, 1990.
- [15] Karl Leo, Jagdeep Shah, Ernst O. Göbel, Theodore C. Damen, Stefan Schmitt-Rink, Wilfried Schäfer, and Klaus Köhler. Coherent oscillations of a wave packet in a semiconductor double-quantum-well structure. *Phys. Rev. Lett.*, 66(2):201–204, 1991.
- [16] Christian Waschke, Hartmut G. Roskos, Ralf Schwedler, Karl Leo, Heinrich Kurz, and Klaus Köhler. Coherent submillimeter-wave emission from Bloch oscillations in a semiconductor superlattice. *Phys. Rev. Lett.*, 70(21):3319–3322, 1993.
- [17] T. Dekorsy, H. Auer, C. Waschke, H. J. Bakker, H. G. Roskos, H. Kurz, V. Wagner, and P. Grosse. Emission of submillimeter electromagnetic waves by coherent phonons. *Phys. Rev. Lett.*, 74(5):738–741, 1995.
- [18] R. Kompfner and N.T. Williams. Back-ward wave tubes. *Proc. IRE*, 41:1602, 1953.
- [19] Jam Farhoomand, Geoffrey A. Blake, M. A. Frerking, and Herbert M. Pickett. Generation of tunable laser sidebands in the far-infrared region. *J. Appl. Phys.*, 57(5):1763–1766, 1985.
- [20] E. Schlecht, G. Chattopadhyay, A. Maestrini, A. Fung, S. Martin, D. Pukala, and I. Bruston, J. and Mehdi. 200, 400 and 800 GHz Schottky diode "substrateless" multipliers: design and results. *Microwave Symposium Digest, 2001 IEEE MTT-S International*, 3:1649–1652, 2001.
- [21] D. C. Burnham and D. L. Weinberg. Observation of simultaneity in parametric production of optical photon pairs. *Phys. Rev. Lett.*, 25(2):84–87, 1970.

- [22] Christoph Walther, Giacomo Scalari, Jerome Faist, Harvey Beere, and David Ritchie. Low frequency terahertz quantum cascade laser operating from 1.6 to 1.8 THz. *Appl. Phys. Lett.*, 89:231121–, 2006.
- [23] R. H. Pantell, M. Didomenico, Jr., O. Svelto, and J. N. Weaver. The theory of optical mixing in semiconductors. In P. Grivet and N. Bloembergen, editors, *Quantum Electronics*, pages 1811–+, 1964.
- [24] F.W. Smith, C.-L. Calawa, A.R. and Chen, M.J. Manfra, and L.J. Mahoney. New mbe buffer used to eliminate backgating in gaas mesfets. *Electron Device Letters, IEEE*, 9(2):77 – 80, 1988.
- [25] D. Nolte. Semi-insulating semiconductor heterostructures: Optoelectronic properties and applications. *J. Appl. Phys.*, 85(9):6259–6289, 1999.
- [26] E. Gerecht, C. D. Reintsema, E. N. Grossman, A. L. Betz, and R. T. Boreiko. Noise Temperature Results for Nb DHEB Mixer Receiver for Far-Infrared Spectroscopy. In MA Cambridge, editor, *Proceeding of the Thirteenth International Space Terahertz Technology Symposium*, Paper 7.3, 2002.
- [27] S.M. Duffy, S. Verghese, A. McIntosh, A. Jackson, A.C. Gossard, and S. Matsuura. Accurate modeling of dual dipole and slot elements used with photomixers for coherent terahertz output power. *IEEE Transactions on Microwave Theory and Techniques*, 49(6):1032–1038, 2001.
- [28] S. Matsuura, G. A. Blake, R. A. Wyss, J. C. Pearson, C. Kadow, A. W. Jackson, and A. C. Gossard. Design and characterization of optical-THz phase-matched traveling-wave photomixers. *Proc. SPIE*, 3795:484–492, 1999.
- [29] M. Mikulics, E. A. Michael, R. Schieder, J. Stutzki, R. Güsten, M. Marso, A. van der Hart, H. P. Bochem, H. Lüth, and P. Kordos. Traveling-wave photomixer with recessed interdigitated contacts on low-temperature-grown GaAs. *Appl. Phys. Lett.*, 88:041118–, 2006.
- [30] E. Peytavit, S. Arscott, D. Lippens, G. Mouret, S. Matton, P. Masselin, R. Bocquet, J. F. Lampin, L. Desplanque, and F. Mollot. Terahertz frequency difference from vertically integrated low-temperature-grown GaAs photodetector. *Appl. Phys. Lett.*, 81(7):1174–1176, 2002.
- [31] A. W. Jackson. *Low-Temperature-Grown GaAs Photomixers Designed for Increased Terahertz output Power*. PhD thesis, University of California, Santa Barbara, Material Engineering, October 1999.

- [32] N. Zamdmer, Q. Hu, K. A. McIntosh, and S. Verghese. Increase in response time of low-temperature-grown GaAs photoconductive switches at high voltage bias. *Appl. Phys. Lett.*, 75(15):2313–2315, 1999.
- [33] S. Gupta, Whitaker J. F., and G. A. Mourou. Ultrafast carrier dynamics in III-V semiconductors grown by molecular-beam epitaxy at very low substrate temperatures. *IEEE Journal of Quantum Electronics*, 28(10):2464–2472, 1992.
- [34] Gregor Segschneider, Frank Jacob, Torsten Löffler, Hartmut G. Roskos, Sönke Tautz, Peter Kiesel, and Gottfried Döhler. Free-carrier dynamics in low-temperature-grown GaAs at high excitation densities investigated by time-domain terahertz spectroscopy. *Phys. Rev. B*, 65(12):125205, 2002.
- [35] M. Mikulics, E. A. Michael, M. Marso, M. Lepsa, A. van der Hart, and H. Lüth. Traveling-wave photomixers fabricated on high energy nitrogen-ion-implanted GaAs. *Appl. Phys. Lett.*, 89:071103–, 2006.
- [36] F. Renner. *The nipnip-THz-emitter. Photomixers based on ballistic transport in asymmetric modulation-doped superlattices*. PhD thesis, Universität Erlangen-Nürnberg, Lehrstuhl f. Mikrocharakterisierung, 2005.
- [37] G. H. Döhler, F. Renner, O. Klar, M. Eckardt, A. Schwanhäusser, S. Malzer, D. Driscoll, M. Hanson, A. C. Gossard, G. Loata, T. Löffler, and H. G. Roskos. THz-photomixer based on quasi-ballistic transport. *Semicond. Sci. Technol.*, 20:S178–S190, 2005.
- [38] M. Kaminska, Z. Liliental-Weber, E. R. Weber, T. George, J. B. Kortright, F. W. Smith, B-Y. Tsaur, and A. R. Calawa. Structural properties of As-rich GaAs grown by molecular beam epitaxy at low temperatures. *Appl. Phys. Lett.*, 54(19):1881–1883, 1989.
- [39] J. K. Luo, H. Thomas, D. V. Morgan, and D. Westwood. Thermal annealing effect on low temperature molecular beam epitaxy grown GaAs: Arsenic precipitation and the change of resistivity. *Appl. Phys. Lett.*, 64(26):3614–3616, 1994.
- [40] Kin Man Yu, M. Kaminska, and Z. Liliental-Weber. Characterization of GaAs layers grown by low temperature molecular beam epitaxy using ion beam techniques. *J. Appl. Phys.*, 72(7):2850–2856, 1992.
- [41] X. Liu, A. Prasad, W. M. Chen, A. Kurpiewski, A. Stoschek, Z. Liliental-Weber, and E. R. Weber. Mechanism responsible for the semi-insulating properties of low-temperature-grown GaAs. *Appl. Phys. Lett.*, 65(23):3002–3004, 1994.

- [42] X. Liu, A. Prasad, J. Nishio, E. R. Weber, Z. Liliental-Weber, and W. Walukiewicz. Native point defects in low-temperature-grown GaAs. *Appl. Phys. Lett.*, 67(2):279–281, 1995.
- [43] M. R. Melloch, J. M. Woodall, E. S. Harmon, N. Otsuka, F. H. Pollak, R. M. Feenstra, and M. A. Lutz. Low Temperature Grown III-V Materials. *Annual Review of Materials Science*, 25:547–600, 1995.
- [44] P. Kordos, A. Förster, J. Betko, M. Morvic, and J. Novák. Semi-insulating GaAs layers grown by molecular-beam epitaxy. *Appl. Phys. Lett.*, 67(7):983–985, 1995.
- [45] M. R. Melloch, N. Otsuka, J. M. Woodall, A. C. Warren, and J. L. Freeouf. Formation of arsenic precipitates in GaAs buffer layers grown by molecular beam epitaxy at low substrate temperatures. *Appl. Phys. Lett.*, 57(15):1531–1533, 1990.
- [46] R. Yano, Y. Hirayama, S. Miyashita, N. Uesugi, and S. Uehara. Arsenic pressure dependence of carrier lifetime and annealing dynamics for low-temperature grown GaAs studied by pump-probe spectroscopy. *J. Appl. Phys.*, 94(6):3966–3971, 2003.
- [47] T. E. M. Staab, R. M. Nieminen, M. Luysberg, and Th. Frauenheim. Agglomeration of As Antisites in As-Rich Low-Temperature GaAs: Nucleation without a Critical Nucleus Size. *Phys. Rev. Lett.*, 95:125502–, 2005.
- [48] D. C. Look. Molecular beam epitaxial GaAs grown at low temperatures. *Thin Solid Films*, 231:61–73, 1993.
- [49] M. Kaminska and E. R. Weber. Defects in semiconductors. (Trans Tech, Pennsylvania), page 1033, 1991.
- [50] R. M. Feenstra, J. M. Woodall, and G. D. Pettit. Observation of bulk defects by scanning tunneling microscopy and spectroscopy: Arsenic antisite defects in GaAs. *Phys. Rev. Lett.*, 71(8):1176–1179, 1993.
- [51] H. Shen, F. C. Rong, R. Lux, J. Pamulapati, M. Taysing-Lara, M. Dutta, E. H. Poindexte, L. Calderon, and Y. Lu. Fermi level pinning in low-temperature molecular beam epitaxial GaAs. *Appl. Phys. Lett.*, 61(13):1585–1587, 1992.
- [52] P. Specht, S. Jeong, H. Sohn, M. Luysberg, A. Prasad, J. Gebauer, R. Krause-Rehberg, and E.R. Weber. Defect control in As-rich GaAs. In *Proc. of the International Conference of Defects in Semiconductors ICDS19, Aveiro, Portugal*, volume 951 of *Mater. Sci. Forum*, pages 258–263, 1997.

- [53] D. C. Look, J. T. Grant, and J. R. Sizelove. Shifted x-ray photoelectron peak in molecular beam epitaxial GaAs grown at 200 °C. *Appl. Phys. Lett.*, 61(11):1329–1331, 1992.
- [54] D. C. Look, D. C. Walters, G. D. Robinson, J. R. Sizelove, M. G. Mier, and C. E. Stutz. Annealing dynamics of molecular-beam epitaxial GaAs grown at 200 °C. *J. Appl. Phys.*, 74(1):306–310, 1993.
- [55] M. O. Manasreh, D. C. Look, K. R. Evans, and C. E. Stutz. Infrared absorption of deep defects in molecular-beam-epitaxial GaAs layers grown at 200 °C: Observation of an EL2-like defect. *Phys. Rev. B*, 41(14):10272–10275, 1990.
- [56] A. C. Warren, J. M. Woodall, P. D. Kirchner, X. Yin, F. Pollak, M. R. Melloch, N. Otsuka, and K. Mahalingam. Role of excess As in low-temperature-grown GaAs. *Phys. Rev. B*, 46(8):4617–4620, 1992.
- [57] M. Luysberg, H. Sohn, A. Prasad, P. Specht, Z. Liliental-Weber, E. R. Weber, J. Gebauer, and R. Krause-Rehberg. Effects of the growth temperature and As/Ga flux ratio on the incorporation of excess As into low temperature grown GaAs. *J. Appl. Phys.*, 83(1):561–566, 1998.
- [58] H. J. von Bardeleben, M. O. Manasreh, D. C. Look, K. R. Evans, and C. E. Stutz. Electron-paramagnetic-resonance study of GaAs grown by low-temperature molecular-beam epitaxy. *Phys. Rev. B*, 45(7):3372–3375, 1992.
- [59] F. W. Smith, H. Q. Le, V. Diadiuk, M. A. Hollis, , A. R. Calawa, S. Gupta, M. Frankel, D. R. Dykaar, G. A. Mourou, and T. Y. Hsiang. Picosecond GaAs-based photoconductive optoelectronic detectors. *Appl. Phys. Lett.*, 54(10):890–892, 1989.
- [60] A. Krotkus, R. Viselga, K. Bertulis, V. Jasutis, S. Marcinkevicius, and U. Olin. Subpicosecond carrier lifetimes in GaAs grown by molecular beam epitaxy at low substrate temperature. *Appl. Phys. Lett.*, 66(15):1939–1941, 1995.
- [61] S. S. Prabhu, S. E. Ralph, M. R. Melloch, and E. S. Harmon. Carrier dynamics of low-temperature-grown GaAs observed via THz spectroscopy. *Appl. Phys. Lett.*, 70(18):2419–2421, 1977.
- [62] B.R Bennett, R.A. Soref, and J. A. Del Alamo. Carrier-Induced Change in Refractive Index of InP, GaAs, and InGaAsP. *IEEE Journal of Quantum Electronics*, 26(1):113–122, 1990.
- [63] S. Gupta, M. Y. Frankel, J. A. Valdmanis, J. F. Whitaker, G. A. Mourou, F. W. Smith, and A. R. Calawa. Subpicosecond carrier lifetime in GaAs

- grown by molecular beam epitaxy at low temperatures. *Appl. Phys. Lett.*, 59(25):3276–3278, 1991.
- [64] K. A. McIntosh, K. B. Nichols, S. Verghese, and E. R. Brown. Investigation of ultrashort photocarrier relaxation times in low-temperature-grown GaAs. *Appl. Phys. Lett.*, 70(3):354–356, 1997.
- [65] H. Nemeč, A. Pashkin, P. Kuzel, M. Khazan, S. Schnüll, and I. Wilke. Carrier dynamics in low-temperature grown GaAs studied by terahertz emission spectroscopy. *J. Appl. Phys.*, 90(3):1303–1306, 2001.
- [66] E. S. Harmon, M. R. Melloch, J. M. Woodall, D. D. Nolte, N. Otsuka, and C. L. Chang. Carrier lifetime versus anneal in low temperature growth GaAs. *Appl. Phys. Lett.*, 63(16):2248–2250, 1993.
- [67] P. W. E Smith, S. D. Benjamin, , and H. S. Loka. Tailoring of trap-related carrier dynamics in low-temperature-grown GaAs. *Appl. Phys. Lett.*, 71(9):1156–1158, 1997.
- [68] S. D. Benjamin, H. S. Loka, A. Othonos, , and P. W. E. Smith. Ultrafast dynamics of nonlinear absorption in low-temperature-grown GaAs. *Appl. Phys. Lett.*, 68(18):2544–2546, 1997.
- [69] H.S. Loka, S.D. Benjamin, and P.W.E. Smith. Optical characterization of low-temperature-grown GaAs for ultrafast all-optical switching devices. *J. Quantum Electron.*, 34(8):1426–1437, 1998.
- [70] U. Siegner, R. Fluck, G. Zhang, and U. Keller. Ultrafast high-intensity nonlinear absorption dynamics in low-temperature grown gallium arsenide. *Appl. Phys. Lett.*, 69(17):2566–2568, 1996.
- [71] A. J. Lochtefeld, M. R. Melloch, J. C. P. Chang, and E. S. Harmon. The role of point defects and arsenic precipitates in carrier trapping and recombination in low-temperature grown GaAs. *Appl. Phys. Lett.*, 69(10):1465–1467, 1996.
- [72] I. S. Gregory, C. Baker, W. R. Tribe, M. J. Evans, H. E. Beere, E. H. Linfield, and A. G. Davies M. Missous. High resistivity annealed low-temperature GaAs with 100 fs lifetimes. *Appl. Phys. Lett.*, 83(20):4199–4201, 2003.
- [73] P. A. Loukakos, C. Kalpouzos, I. E. Perakis, Z. Hatzopoulos, M. Sfendourakis, G. Kostantinidis, and C. Fotakis. Role of as precipitates on ultrafast electron trapping in low-temperature-grown GaAs and AlGaAs alloys. *J. Appl. Phys.*, 91(12):9863–9868, 2002.

- [74] H. Ruda and A. Shik. Nonequilibrium carriers in GaAs grown by low-temperature molecular beam epitaxy. *Phys. Rev. B*, 63(8):085203–, 2001.
- [75] M. C. Beard, G. M. Turner, and C. A. Schmuttenmaer. Subpicosecond carrier dynamics in low-temperature grown GaAs as measured by time-resolved terahertz spectroscopy. *J. Appl. Phys.*, 90(12):5915–5923, 2001.
- [76] Roux J.F., Coutaz J.L., Siegert J., Gaarder A., Marcinkevicius S., Wolos A., Kaminska M., Adomavicius R., Krotkus A., and Bertulis K. In Proc. 3rd Symp. Non-Stoichiometric III-V Compounds. *Physik Mikrostrukturierter Halbleiter (Ed. S. Malzer and T. Marek and P. Kiesel (Erlangen, Germany))*, 23:85, 2001.
- [77] P. Grenier and J. F. Whitaker. Subband gap carrier dynamics in low-temperature-grown GaAs. *Appl. Phys. Lett.*, 70(15):1998–2000, 1997.
- [78] R. Adomavicius, A. Krotkus, K. Bertulis, V. Sirutkaitis, R. Butkus, and A. Piskarskas. Hole trapping time measurement in low-temperature-grown gallium arsenide. *Appl. Phys. Lett.*, 83(25):5304–5306, 2003.
- [79] G. Segschneider, T. Dekorsy, H. Kurz, R. Hey, and K. Ploog. Energy resolved ultrafast relaxation dynamics close to the band edge of low-temperature grown GaAs. *Appl. Phys. Lett.*, 71(19):2779–2781, 1997.
- [80] M. Stellmacher, J.-P. Schnell, D. Adam, and J. Nagle. Photoconductivity investigation of the electron dynamics in GaAs grown at low temperature. *Appl. Phys. Lett.*, 74(9):1239–1241, 1999.
- [81] J. K. Luo, H. Thomas, D. V. Morgan, and D. Westwood. Transport properties of GaAs layers grown by molecular beam epitaxy at low temperature and the effects of annealing. *J. Appl. Phys.*, 79(7):3622–3629, 1996.
- [82] D. C. Look, D. C. Walters, M. O. Manasreh, J. R. Sizelove, C. E. Stutz, and K. R. Evans. Anomalous Hall-effect results in low-temperature molecular-beam-epitaxial GaAs: Hopping in a dense EL2-like band. *Phys. Rev. B*, 42(6):3578–3581, 1990.
- [83] M. Kaminska and E. R. Weber. Low temperature GaAs: Electrical and optical properties. *Mat. Science Forum*, 83:1033–1040, 1992.
- [84] A. C. Warren, J. M. Woodall, J. L. Freeouf, D. Grischkowsky, D. T. McInturff, M. R. Melloch, and N. Otsuka. Arsenic precipitates and the semi-insulating properties of GaAs buffer layers grown by low-temperature molecular beam epitaxy. *Appl. Phys. Lett.*, 57(13):1331–1333, 1990.

- [85] J. Tersoff. Schottky barrier heights and the continuum of gap states. *Phys. Rev. Lett.*, 52(6):465–468, 1984.
- [86] M. Kaminska, E. R. Weber, Z. Liliental-Weber, R. Leon, and Z. U. Rek. Stoichiometry-related defects in GaAs grown by molecular-beam epitaxy at low temperatures. *J. Vac. Sci. Technol. B*, 7(4):710–713, 1989.
- [87] H. Yamamoto, Z-Q. Fang, and D. C. Look. Nonalloyed ohmic contacts on low-temperature molecular beam epitaxial GaAs: Influence of deep donor band. *Appl. Phys. Lett.*, 57(15):1537–1539, 1990.
- [88] J. P. Ibbetson, J. S. Speck, N. X. Nguyen, A. C. Gossard, and U. K. Mishra. The role of microstructure in the electrical properties of GaAs grown at low temperature. *J. Electron. Mat.*, 22(12):1421 – 1424, 1993.
- [89] J. P. Ibbetson and U. K. Mishra. Space-charge-limited currents in nonstoichiometric GaAs. *Appl. Phys. Lett.*, 68(26):3781–3783, 1996.
- [90] R. H. Bube. *Photoelectronic Properties of Semiconductors*. Cambridge University Press, 1992.
- [91] P. Kordos, M. Marso, A. Förster, J. Darmo, J. Betko, and G. Nimtz. Space-charge controlled conduction in low-temperature-grown molecular-beam epitaxial GaAs. *Appl. Phys. Lett.*, 71(8):1118–1120, 1997.
- [92] D. C. Look, G. D. Robinson, J. R. Sizelove, and C. E. Stutz. Electrical properties of molecular beam epitaxial GaAs grown at 300 - 450 °C. *J. Electron. Mat.*, 22(12):1425 – 1428, 1993.
- [93] J. Betko, P. Kordos, S. Kuklovsky, A. Förster, D. Gregusova, and H. Lüth. Electrical properties of molecular beam epitaxial GaAs layers grown at low temperature. *Mat. Sci. Eng. B*, 28(1-3):147–150, 1994.
- [94] M. Klingenstein, J. Kuhl, R. Nötzel, K. Ploog, J. Rosenzweig, C. Moglestue, A. Hülsmann, Jo. Schneider, and K. Köhler. Ultrafast metal-semiconductor-metal photodiodes fabricated on low-temperature GaAs. *Appl. Phys. Lett.*, 60(5):627–629, 1991.
- [95] A. Reklaitis, A. Krotkus, and G. Grigaliunaite. Enhanced drift velocity of photoelectrons in a semiconductor with ultrafast carrier recombination. *Semicond. Sci. Technol.*, 14:945–947, 1999.
- [96] P. Arifin, E. Goldys, and T. L. Tansley. Monte Carlo simulation of electron drift velocity in low-temperature-grown gallium arsenide in a Schottky-barrier model. *Phys. Rev. B*, 52(8):5708–5713, 1995.

- [97] J. K. Luo, H. Thomas, D. V. Morgan, D. Westwood, and R. H. Williams. The electrical breakdown properties of GaAs layers grown by molecular beam epitaxy at low temperature. *Semicond. Sci. Technol.*, 9:2199–2204, 1994.
- [98] V. Ortiz, J. Nagle, and A. Alexandrou. Influence of the hole population on the transient reflectivity signal of annealed low-temperature-grown GaAs. *Appl. Phys. Lett.*, 80(14):2505–2507, 2002.
- [99] C. Moglestue, J. Rosenzweig, J. Kuhl, M. Klingenstein, M. Lambsdorff, A. Axmann, Jo. Schneider, and A. Hülsmann. Picosecond pulse response characteristics of GaAs metal-semiconductor-metal photodetectors. *J. Appl. Phys.*, 70(4):2435–2448, 1991.
- [100] E. R. Brown, K. A. McIntosh, F. W. Smith, M. J. Manfra, and C. L. Dennis. Measurements of optical-heterodyne conversion in low-temperature-grown GaAs. *Appl. Phys. Lett.*, 62(11):1206–1208, 1993.
- [101] E. R. Brown, F. W. Smith, and K. A. McIntosh. Coherent millimeter-wave generation by heterodyne conversion in low-temperature-grown GaAs photoconductors. *J. Appl. Phys.*, 73(3):1480–1484, 1993.
- [102] M. Tani, O. Morikawa, S. Matsuura, and M. Hangyo. Generation of terahertz radiation by photomixing with dual- and multiple-mode lasers. *Semicond. Sci. Technol.*, 20:S151–S163, 2005.
- [103] J. Van Rudd and D. M. Mittleman. Influence of substrate-lens design in terahertz time-domain spectroscopy. *J. Opt. Soc. Am. B*, 19:319–329, 2002.
- [104] S.M. Jarrett and J.F. Young. High-efficiency single frequency cw ring dye lasers. *Opt. Lett.*, 4:176–, 1979.
- [105] C. L. Tang, H. Statz, , and G. deMars. Spectral output and spiking behavior of solid-state lasers. *J. Appl. Phys.*, 34(8):2289–2295, 1963.
- [106] G. Loata, A. Lisauskas, T. Löffler, and H.G. Roskos. Entwicklung optoelektronischer Dauerstrich-Messtechniken für die Spektroskopie im Terahertz-Frequenzbereich. *Interim Report - DFG-Projekt RO 770 / 17 - Johann Wolfgang Goethe - Universität*, 2003.
- [107] M.J.E. Golay. A pneumatic infra-red detector. *Rev. Sci. Instr.*, 18:357–362, 1947.
- [108] S.P. Langley. The Bolometer. *Nature*, 25:14–16, 1881.

- [109] M. A. Kinch and B. V. Rollin. Detection of millimetre and sub-millimetre wave radiation by free carrier absorption in a semiconductor. *Br. J. Appl. Phys.*, 14(10):672–676, 1963.
- [110] D. Rutledge and M. Muha. Imaging antenna arrays. *IEEE Transactions on Antennas and Propagation*, 30(4):535–540, 1982.
- [111] G.M. Rebeiz. Millimeter-wave and terahertz integrated circuit antennas. *Proceedings of the IEEE*, 80(11):1748–1770, 1992.
- [112] D. F. Filipovic, Gearhart S., and G. M. Rebeiz. Double-slot antennas on extended hemispherical and elliptical silicon dielectric lenses. *IEEE Transactions on Microwave Theory and Techniques*, 41(10):1738–1749, 1993.
- [113] E.K. Duerr, K.A. McIntosh, S.M. Duffy, S.D. Calawa, S. Verghese, C.-Y.E. Tong, R. Kimberk, and R. Blundell. Demonstration of a 630-GHz photomixer used as a local oscillator. *Microwave Symposium Digest, 1999 IEEE MTT-S International*, 1:127–130, 1999.
- [114] H. Quast. Untersuchungen photokonduktiver Emittter zur Erzeugung von Dauerstrich THz-Strahlung. *Diplomarbeit, Physicalisches Institut der JW Goethe Universität, Frankfurt am Main*, Juni 2001.
- [115] R. Wipf. Aufbau und Inbetriebnahme einer Meßstation zum Vermessen von THz-Photomischern. *Diplomarbeit, Physicalisches Institut der JW Goethe Universität, Frankfurt am Main*, July 2005.
- [116] E. R. Brown, K. A. McIntosh, K. B. Nichols, and C. L. Dennis. Photomixing up to 3.8 THz in low-temperature-grown GaAs. *Appl. Phys. Lett.*, 66(3):285–287, 1995.
- [117] S. Verghese, K.A. McIntosh, and E.R. Brown. Highly tunable fiber-coupled photomixers with coherent terahertz output power. *IEEE Transactions on Microwave Theory and Techniques*, 45(8):1301–1309, 1997.
- [118] E. R. Brown. A photoconductive model for superior GaAs THz photomixers. *Appl. Phys. Lett.*, 75(6):769–771, 1999.
- [119] K. A. McIntosh, E. R. Brown, K. B. Nichols, O. B. McMahan, W. F. DiNatale, and T. M. Lyszczarz. Terahertz photomixing with diode lasers in low-temperature-grown GaAs. *Appl. Phys. Lett.*, 67(26):3844–3846, 1995.
- [120] K. A. McIntosh, E. R. Brown, K. B. Nichols, O. B. McMahan, W. F. DiNatale, and T. M. Lyszczarz. Terahertz measurements of resonant planar

- antennas coupled to low-temperature-grown GaAs photomixers. *Appl. Phys. Lett.*, 69(24):3632–3634, 1996.
- [121] C. A. Balanis. *Antenna Theory: Analysis and Design*. J. Wiley & Sons, second edition, 1996.
- [122] Duffy S. M., Verghese S., and McIntosh K. A. Photomixers for continuous-wave THz radiation. In D. Mittleman, editor, *Sensing with THz Radiation*, pages 193–236. Springer, Berlin, 2003.
- [123] E. A. Michael, B. Vowinkel, R. Schieder, M. Mikulics, M. Marso, and P. Kordos. Large-area traveling-wave photonic mixers for increased continuous terahertz power. *Appl. Phys. Lett.*, 86:111120–, 2005.
- [124] G. Mouret, S. Matton, R. Bocquet, F. Hindle, E. Peytavit, J.F. Lampin, and D. Lippens. Far-infrared cw difference-frequency generation using vertically integrated and planar low temperature grown GaAs photomixers: application to H₂S rotational spectrum up to 3 THz. *Applied Physics B: Lasers and Optics*, 79(6):725–729, 2004.
- [125] V. H. Rumsey. Frequency independent antennas. *IRE National Convention Record*, 5:114–118, 1957.
- [126] Y. Mushiake. *Self-Complementary Antennas*. Berlin: Springer-Verlag, 1996.
- [127] R. H. DuHamel and D. E. Isbell. Broadband logarithmically periodic antenna structures. *IRE National Convention Record*, 5:119–128, 1957.
- [128] E. R. Brown, K. A. McIntosh, F. W. Smith, K. B. Nichols, M. J. Manfra, C. L. Dennis, and J. P. Mattia. Milliwatt output levels and superquadratic bias dependence in a low-temperature-grown GaAs photomixer. *Appl. Phys. Lett.*, 64(24):3311–3313, 1994.
- [129] P.Y. Yu and M. Cardona. *Fundamentals of Semiconductors*. Springer Verlag Berlin, 1996.
- [130] M. Marso, M. Mikulics, R. Adam, S. Wu, X. Zheng I. Camara, F. Siebe, Güsten, A. Färster R., P. Kordos, and R. Sobolewski. Ultrafast phenomena in freestanding LT-GaAs devices. *Acta Physica Polonica A*, 107(1):109–, 2005.
- [131] S.L. Teitel and J.W. Wilkins. Ballistic transport and velocity overshoot in semiconductors: Part I - Uniform field effects. *Electron Devices, IEEE Transactions on*, 30(2):150– 153, 1983.

- [132] A. Leitenstorfer, S. Hunsche, J. Shah, M. C. Nuss, and W. H. Knox. Femtosecond high-field transport in compound semiconductors. *Phys. Rev. B*, 61(24):16642–16652, 2000.
- [133] D. Birkedal, O. Hansen, C. B. Sørensen, K. Jarasiunas, S. D. Brorson, and S. R. Keiding. Terahertz radiation from delta-doped GaAs. *Appl. Phys. Lett.*, 65(1):79–81, 1994.
- [134] C. Ludwig and J. Köhl. Studies of the temporal and spectral shape of terahertz pulses generated from photoconducting switches. *Appl. Phys. Lett.*, 69(9):1194–1196, 1996.
- [135] G. M. Dunn, Alison B. Walker, A. J. Vickers, and V. R. Wicks. Transient response of photodetectors. *J. Appl. Phys.*, 79(9):7329–7338, 1996.
- [136] M. Tani, S. Matsuura, K. Sakai, and S. i. Nakashima. Emission characteristics of photoconductive antennas based on low-temperature-grown GaAs and semi-insulating GaAs. *Appl. Opt.*, 36(30):7853–7859, 1997.
- [137] Shuji Matsuura, Masahiko Tani, and Kiyomi Sakai. Generation of coherent terahertz radiation by photomixing in dipole photoconductive antennas. *Appl. Phys. Lett.*, 70(5):559–561, 1997.
- [138] A. C. Warren, N. Katzenellenbogen, D. Grischkowsky, and J. M. Woodall. Subpicosecond, freely propagating electromagnetic pulse generation and detection using GaAs:As epilayers. *Appl. Phys. Lett.*, 58(14):1512–1514, 1991.
- [139] C.-K. Sun, Y.-H. Chen, J.-W. Shi, Yi-J. Chiu, K.-G. Gan, and J. E. Bowers. Electron relaxation and transport dynamics in low-temperature-grown GaAs under 1 eV optical excitation. *Appl. Phys. Lett.*, 83(5):911–913, 2003.
- [140] L. Duvillaret, F. Garet, J.-F. Roux, and J.-L. Coutaz. Analytical modeling and optimization of terahertz time-domain spectroscopy experiments, using photoswitches as antennas. *IEEE J. Sel. Top. Quantum Electron.*, 7(4):615–623, 2001.
- [141] P. U. Jepsen and R. H. Jacobsen and S. R. Keiding. Generation and detection of terahertz pulses from biased semiconductor antennas. *J. Opt. Soc. Am. B*, 13:2424–, 1996.
- [142] Z. Piao, M. Tani, and K. Sakai. Carrier Dynamics and Terahertz Radiation in Photoconductive Antennas. *Jpn. J. Appl. Phys.*, 39:96–100, 2000.

- [143] E. Castro-Camus, J. Lloyd-Hughes, and M. B. Johnston. Three-dimensional carrier-dynamics simulation of terahertz emission from photoconductive switches. *Phys. Rev. B*, 71:195301–, 2005.
- [144] Q. Wu and X.-C. Zhang. Free-space electro-optic sampling of terahertz beams. *Appl. Phys. Lett.*, 67(24):3523–3525, 1995.
- [145] Q. Wu, M. Litz, and X.-C. Zhang. Broadband detection capability of ZnTe electro-optic field detectors. *Appl. Phys. Lett.*, 68(21):2924–2926, 1996.
- [146] Sang-Gyu Park, M. R. Melloch, and A. M. Weiner. Comparison of terahertz waveforms measured by electro-optic and photoconductive sampling. *Appl. Phys. Lett.*, 73(22):3184–3186, 1998.
- [147] Q. Wu and X.-C. Zhang. Ultrafast electro-optic field sensors. *Appl. Phys. Lett.*, 68(12):1604–1606, 1996.
- [148] C. Winnewisser, P. Uhd Jepsen, M. Schall, V. Schyja, and H. Helm. Electro-optic detection of THz radiation in LiTaO₃, LiNbO₃ and ZnTe. *Appl. Phys. Lett.*, 70(23):3069–3071, 1997.
- [149] Y. Cai, I. Brener, J. Lopata, J. Wynn, L. Pfeiffer, J. B. Stark, Q. Wu, X. C. Zhang, and J. F. Federici. Coherent terahertz radiation detection: Direct comparison between free-space electro-optic sampling and antenna detection. *Appl. Phys. Lett.*, 73(4):444–446, 1998.
- [150] J.-H. Son, T. B. Norris, and J. F. Whitaker. Terahertz electromagnetic pulses as probes for transient velocity overshoot in GaAs and Si. *J. Opt. Soc. Am. B*, 11(12):2519–, 1994.
- [151] Frank Jacob. Quellen und Detektionsverfahren für lasererzeugte intensive THz-pulse. *Dipomarbeit, JWG-Universität Frankfurt am Main*, 2001.
- [152] A. Evan Iverson, G. M. Wysin, D. L. Smith, and A. Redondo. Overshoot in the response of a photoconductor excited by subpicosecond pulses. *Appl. Phys. Lett.*, 52(25):2148–215, 1988.
- [153] (Ed.) K. Sakai. *Terahertz Optoelectronics*, volume 97 of *Topics in Applied Physics*. Springer, 2005.
- [154] T.-A. Liu, M. Tani, and C.-L. Pan. THz radiation emission properties of multienergy arsenic-ion-implanted GaAs and semi-insulating GaAs based photoconductive antennas. *J. Appl. Phys.*, 93(5):2996–3001, 2003.

- [155] N. Chimot, J. Mangeney, L. Joulaud, P. Crozat, H. Bernas, K. Blary, and J. F. Lampin. Terahertz radiation from heavy-ion-irradiated $\text{In}_{0.53}\text{Ga}_{0.47}\text{As}$ photoconductive antenna excited at $1.55\ \mu\text{m}$. *Appl. Phys. Lett.*, 87:193510–, 2005.
- [156] M. Tani, K. Sakai, and H. Mimura. Ultrafast Photoconductive Detectors Based on Semi-Insulating GaAs and InP. *Jpn. J. Appl. Phys.*, 36(9A/B):L1175–L1178, 1997.
- [157] J. T. Darrow, X.-C. Zhang, and D. H. Auston. Power scaling of large-aperture photoconducting antennas. *Appl. Phys. Lett.*, 58(1):25–27, 1990.
- [158] J.T. Darrow, X.-C. Zhang, D.H. Auston, and J.D. Morse. Saturation properties of large-aperture photoconducting antennas. *IEEE Journal of Quantum Electronics*, 28(6):1607–1616, 1992.
- [159] P. K. Benicewicz, J. P. Roberts, and A. J. Taylor. Scaling of terahertz radiation from large-aperture biased photoconductors. *J. Opt. Soc. Am. B*, 11:2533–2546, 1994.
- [160] G. Rodriguez and A. J. Taylor. Screening of the bias field in terahertz generation from photoconductors. *Opt. Lett.*, 21:1046–, 1996.
- [161] R. E. Collin. *Antennas and radiowave propagation*. McGraw-Hill, 1985.
- [162] S.G. Park, M.R. Melloch, and A.M. Weiner. Analysis of Terahertz Waveforms Measured by Photoconductive and Electrooptic Sampling. *IEEE Journal of Quantum Electronics*, 35(5):810–, 1999.
- [163] K. Siebert. Optoelektronische Erzeugung und Detektion kohärenter Dauerstrich-THz-Strahlung für bildgebende Anwendungen. *Doktorarbeit, JWG-Universität Frankfurt am Main.*, 2003.
- [164] H. Eusèbe, J.-F. Roux, , J.-L. Coutaz, and A. Krotkus. Photoconductivity sampling of low-temperature-grown Be-doped GaAs layers. *J. Appl. Phys.*, 98:033711–, 2005.
- [165] J. Montoya and Q. Hu. Low-temperature-grown GaAs coplanar waveguide single-photon/two photon absorption autocorrelator. *J. Appl. Phys.*, 95(5):2230–2237, 2004.
- [166] S. Verghese, N. Zamdmer, Qing Hu, E. R. Brown, and A. Förster. An optical correlator using a low-temperature-grown GaAs photoconductor. *Appl. Phys. Lett.*, 69(6):842–844, 1996.

- [167] S. R. Rodriguez, G. Caceres and A. J. Taylor. Modeling of terahertz radiation from biased photoconductors: transient velocity effects. *Opt. Lett.*, 19(23):1994–1996, 1994.
- [168] J. E. Pedersen, V. G. Lyssenko, J. M. Hvam, P. Uhd Jepsen, S. R. Keiding, C. B. Sørensen, and P. E. Lindelof. Ultrafast local field dynamics in photoconductive THz antennas. *Appl. Phys. Lett.*, 62(11):1265–1267, 93.
- [169] R. H. Jacobsen, K. Birkelund, T. Holst, P. Uhd Jepsen, and S. R. Keiding. Interpretation of photocurrent correlation measurements used for ultrafast photoconductive switch characterization. *J. Appl. Phys.*, 79(5):2649–2657, 1996.
- [170] Stuart D. Brorson, Jucheng Zhang, and Søren R. Keiding. Ultrafast carrier trapping and slow recombination in ion-bombarded silicon on sapphire measured via THz spectroscopy. *Appl. Phys. Lett.*, 64(18):2385–2387, 1994.
- [171] M. Tonouchi, N. Kawasaki, T. Yoshimura, H. Wald, and P. Seidel. Pump and Probe Terahertz Generation Study of Ultrafast Carrier Dynamics in Low-Temperature Grown-GaAs. *Jpn. J. Appl. Phys.*, 41(6B):L706–L709, 2002.
- [172] Karsten J. Siebert, Alvydas Lisauskas, Torsten Löffler, and Hartmut G. Roskos. Field Screening in Low-Temperature-Grown GaAs Photoconductive Antennas. *Jpn. J. Appl. Phys.*, 43(3):1038–1043, 2004.
- [173] R. Yano, H. Gotoh, Y. Hirayama, and S. Miyashita. Systematic pump-probe terahertz wave emission spectroscopy of a photoconductive antenna fabricated on low-temperature grown GaAs. *J. Appl. Phys.*, 96(7):3635–3638, 2004.
- [174] A.J. Taylor, G. Rodriguez, and D. Some. Ultrafast field dynamics in large-aperture photoconductors. *Opt. Lett.*, 22(10):715–, 1996.
- [175] Sang-Gyu Park, A.M. Weiner, M.R. Melloch, C.W. Sider, J.L. Sider, and A.J. Taylor. High-power narrow-band terahertz generation using large-aperture photoconductors. *IEEE J. Quantum Elect.*, 35(8):1257–1268, 1999.
- [176] C. W. Siders, J. L. W. Siders, A. J. Taylor, S.-G. Park, and A. M. Melloch, M. R. and Weiner. Generation and characterization of terahertz pulse trains from biased, large-aperture photoconductors. *Opt. Lett.*, 24(4):241–243, 1999.
- [177] B. B. Hu, E. A. de Souza, W. H. Knox, J. E. Cunningham, M. C. Nuss, A. V. Kuznetsov, and S. L. Chuang. Identifying the distinct phases of carrier transport in semiconductors with 10 fs resolution. *Phys. Rev. Lett.*, 74(9):1689–1692, 1995.

- [178] A. J. Taylor, P. K. Benicewicz, and S. M. Young. Modeling of femtosecond electromagnetic pulses from large-aperture photoconductors. *Opt. Lett.*, 18(16):1340–1342, 1993.
- [179] M. Thomson. *Private Communication*.
- [180] T. S. Sosnowski, T. B. Norris, H. H. Wang, P. Grenier, J. F. Whitaker, and C. Y. Sung. High-carrier-density electron dynamics in low-temperature-grown GaAs. *Appl. Phys. Lett.*, 70(24):3245–3247, 1997.
- [181] A. Othonos. Probing ultrafast carrier and phonon dynamics in semiconductors. *J. Appl. Phys.*, 83(4):1789–183, 1998.
- [182] N. Kawasaki, T. Yoshimura, M. Tonouchi, M. Tani, K. Sakai, and H. Katahama. Terahertz generation study of ultrafast carrier dynamics in polycrystalline low-temperature GaAs. *Solid State Phenomena*, 93:367–372, 2003.
- [183] I. S. Gregory, C. M. Tey, A. G. Cullis, M. J. Evans, H. E. Beere, and I. Farrer. Two-trap model for carrier lifetime and resistivity behavior in partially annealed GaAs grown at low temperature. *Phys. Rev. B*, 73:195201–, 2006.
- [184] M. Tonouchi. *Private Communication*.
- [185] D. C. Look, Z-Q. Fang, J. R. Sizelove, and C. E. Stutz. New a_{Ga} related center in GaAs. *Phys. Rev. Lett.*, 70(4):465–468, 1993.
- [186] W. Shockley and W. T. Read. Statistics of the recombinations of holes and electrons. *Phys. Rev.*, 87(5):835–842, 1952.

Curriculum Vitae



Personal

Name: Gabriel Cosmin Loață
Date of birth: 27.10.1975
Place of birth: Onești (formerly Gheorghe Gheorghiu-Dej), Bacău, Romania
Marital status: Single

Education

Pre-University education

1982 - 1990 Primary School, *Gheorghe Mocanu*, Onești, Bacău, Romania
1990 - 1994 High-school, *Grigore C. Moisil*, Onești, Bacău, Romania, Informatics Class

University education

1994 - 1999 Bachelor of Science in Physics
Faculty of Physics, Babeș-Bolyai University, Cluj-Napoca, Romania
Final grade: 8 out of 10

1999 - 2000 Master of Science Degree in Atomic and Molecular Physics
 Babeş-Bolyai University Cluj-Napoca, Romania, in cooperation
 with the Semiconductor Physics Group, Chemnitz University of
 Technology, Germany.
 Thesis title: *Electrical characterization of organic-modified Schottky
 contacts on silicon.*
 Final grade: 9.75 out of 10

Doctoral studies

Duration: 05/2002 - 01/2007
 Research group: *Ultrafast Spectroscopy and Terahertz Physics*
 Supervisor: Prof. Dr. Hartmut G. Roskos
 Institution: Physikalisches Institut, J. W. Goethe-Universität, Frankfurt am
 Main, Germany.
 Research topics: • Investigation of conventional (LTG GaAs-based) and novel de-
 sign (*nip-nip*) photomixers for CW-THz generation;
 • Implementation of pulsed THz-emission spectroscopy tech-
 niques for material and device characterization in ultrafast op-
 toelectronic applications;
 • Optical ultrafast pump-probe measurements of carrier lifetime;
 • Design and realization of CW laser sources for photomixing;
 • Design and implementation of a photomixer test-bed.
 Dissertation: *Investigation of low-temperature-grown GaAs photoconductive antennae
 for continuous-wave and pulsed terahertz generation.*

Work experience

Dates: 05/2002 - present
 Position held: Research assistant in the *Ultrafast Spectroscopy and Terahertz Physics*
 group of Prof. Dr. H. G. Roskos, Physikalisches Institut, J. W.
 Goethe-Universität, Max-von-Laue-Strasse 1 60438 Frankfurt (M),
 Germany.
 Relevant European Space Agency Project - *Optical Far IR Wave Generation.*
 projects: Deutsche Forschungsgemeinschaft - *Entwicklung optoelektronis-
 cher Dauerstrich-Messtechniken für die Spektroskopie im Terahertz-
 Frequenzbereich* and - *Effiziente CW-THz Quellen basierend auf Pho-
 tomischung in asymmetrischen Übergitterstrukturen*

- Main activities: design and development of an experimental setup (test-bed) for characterization of new photomixer structures, optical and electrical characterization of conventional and novel design photomixers, pulsed THz-emission spectroscopy.
Regular teaching activities (tutorials and practical courses in Experimental Physics).
- Dates: 03/2001 - 05/2002
- Position held: Research Assistant at the Chair of High-Frequency Techniques of the Information Technology Department, Electrical Engineering Faculty, Chemnitz University of Technology
- Relevant projects: European Space Agency Project - *Modelling of planar Schottky diodes for submillimetre-wave application*.
- Main activities: Terahertz circuits (frequency multipliers) and device (Schottky diode) simulations.
Regular teaching activities (tutorials and practical courses on Fundamentals of Microwaves).

Acknowledgments

First of all, I would like to express my gratefulness to my “Doktorvater”, Professor Dr. Hartmut G. Roskos. Thank you for taking me aboard and providing me the opportunity to work in a very dynamic, young and multinational research group. Thank you also for your continuing advice, encouragement and patience.

I am also grateful to Professor Dr. Peter Meißner who kindly agreed to become the second referee of this work.

I also owe my gratitude to Dr. Torsten Löffler for doing a great job on supervising my research. Thank you for your exceptional assistance with all the experimental issues I came across all this time, and also for all the fruitful discussions on physics, project management and so on.

I would also like to thank deeply to Dr. Mark Thomson for his help on a multitude of matters. I owe him the first pump-and-probe signal I ever measured and a great deal of the theoretical and simulation work presented in this thesis.

I am very indebted to Dr. Cezary Sydlo (TU Darmstadt), Dr. Stefan Malzer (MPI Erlangen) as well as Prof. Dr. Strasser (TU Vienna) and Mr. Hock (Uni Würzburg) for the fabrication of LTG-GaAs material and devices used in this study.

I would like to thank Professor Dr. Gottfried Döhler for offering me the exciting opportunity to work on the nipnip photomixers.

Many thanks are due to my colleagues for creating a very productive working environment: Robert Sachs, Dr. Markus Kress, Robert Wipf, Johanna Kolb, Dr. Anne Beate Hummel, Dr. Kai Rönnburg, Markus Abt, Bernhard Klug, Dr. Alvydas Lysauskas, Bernd Hils, Tobias Hahn, Claudia Blöser, Miljenko Novosel, Robert Hahn and Volker Blank.

I would also like to thank Marion Jordan for all the help with the administrative issues and bureaucracy. A great deal of respect and admiration for the craftsmanship of people in the mechanical workshop. Thank you for always delivering promptly and flawless components.

Last but not least, I would like to express my appreciation to those people outside the academic environment, especially to my family, who supported and encouraged me all throughout these years.

I cannot possibly express the depth of gratitude to my mother, Mariana. Everything I have accomplished is due to the support and love she always offered unconditionally.